

AD-A233 534



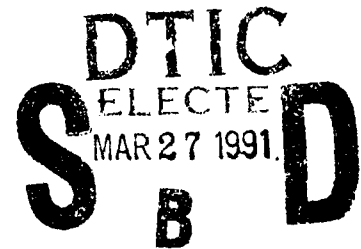
# NONLINEAR OPTICS TECHNOLOGY PHASE III FINAL REPORT

## VOLUME 2: PHASE CONJUGATED OPTICAL COMMUNICATION LINK

J. Brock, M. Caponi, A. Horwitz, L. Lembo, D. Novoseller

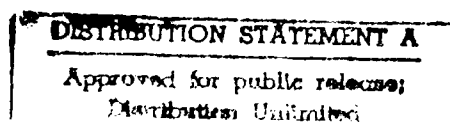
Sponsored By  
Defense Advanced Research Projects Agency

Monitored By  
Office Of Naval Research  
Contract # N00014-88-C-0228



The views and the conclusions contained in this document are those of the authors and should not be interpreted as necessarily representing the official policies, either expressed or implied, of the Defense Advanced Research Projects Agency or the U.S. Government.

TRW Space And Technology Group  
Applied Technology Division  
One Space Park Redondo Beach, CA 90278





# **NONLINEAR OPTICS TECHNOLOGY PHASE III FINAL REPORT**

## **VOLUME 2: PHASE CONJUGATED OPTICAL COMMUNICATION LINK**

**J. Brock, M. Caponi, J. Conner, A. Horwitz, L. Lembo, D. Novoseller**

**Sponsored By  
Defense Advanced Research Projects Agency**

**Monitored By  
Office Of Naval Research  
Contract # N00014-88-C-0228**

**The views and the conclusions contained in this document are those of the authors and should not be interpreted as necessarily representing the official policies, either expressed or implied, of the Defense Advanced Research Projects Agency or the U.S. Government.**

**TRW Space And Technology Group  
Applied Technology Division  
One Space Park Redondo Beach, CA 90278**

This page  
intentionally left blank

UNCLASSIFIED

SECURITY CLASSIFICATION OF THIS PAGE

## REPORT DOCUMENTATION PAGE

REPORT SECURITY CLASSIFICATION Unclassified		1d. RESTRICTIVE MARKINGS	
2a. SECURITY CLASSIFICATION AUTHORITY		3. DISTRIBUTION/AVAILABILITY OF REPORT Unclassified/unlimited	
2b. DECLASSIFICATION/DOWNGRADING SCHEDULE			
4. PERFORMING ORGANIZATION REPORT NUMBER(S)		5. MONITORING ORGANIZATION REPORT NUMBER(S)	
6a. NAME OF PERFORMING ORGANIZATION One Space & Technology Group	6b. OFFICE SYMBOL (If applicable)	7a. NAME OF MONITORING ORGANIZATION Office of Naval Research	
6c. ADDRESS (City, State and ZIP Code) One Space Park Redondo Beach, CA. 90278		7b. ADDRESS (City, State and ZIP Code) NOSC Code 843 271 Catalina Boulevard San Diego, CA 92152	
8a. NAME OF FUNDING/SPONSORING ORGANIZATION DARPA	8b. OFFICE SYMBOL (If applicable) DEO	9. PROCUREMENT INSTRUMENT IDENTIFICATION NUMBER N00014-88-C-0228	
8c. ADDRESS (City, State and ZIP Code) 1400 Wilson Boulevard Arlington, VA 22209-2308		10. SOURCE OF FUNDING NOS.	
11. TITLE (Include Security Classification) NLOT Phase III Final Report: Vol. 2: Phase Conjugated Optical		PROGRAM ELEMENT NO.	PROJECT NO.
PERSONAL AUTHOR(S) Communication Link (U) J. Brock, M. Caponi, J. Conner, A. Horwitz, L. Lembo, and D. Novoseller		TASK NO.	WORK UNIT NO.
13a. TYPE OF REPORT Final	13b. TIME COVERED FROM 03/88 TO 11/90	14. DATE OF REPORT (Yr., Mo., Day) 01/12/91	
15. PAGE COUNT			
16. SUPPLEMENTARY NOTATION			
17. COSATI CODES		18. SUBJECT TERMS (Continue on reverse if necessary and identify by block number.)	
FIELD	GROUP	SUB. GR.	
		Optical communication, laser propagation, turbulence, atmosphere, phase conjugation, four wave mixing, coherent detection, automatic tracking and pointing, holographic correction, model, system analysis	
19. ABSTRACT (Continue on reverse if necessary and identify by block number.)			
<p>A laser communication link that uses phase conjugation (PC) to correct for atmospheric aberrations due to turbulence was investigated. Significant improvements over conventional optical communication links were demonstrated through experiments and analysis.</p> <p>A 1.1 km four wave mixing (FWM) PC optical comm link propagating through the atmosphere was demonstrated and characterized over a range of atmospheric turbulence conditions and compared to the performance of a conventional link. Four wave mixing was performed in sodium vapor near the sodium D<sub>2</sub> resonance line (<math>\lambda = 589</math> nm). Signals with amplitude modulation of 10 kHz to 1 MHz were successfully transmitted and received over this link. Measurements of intensity variance demonstrated that the beam returned by the phase conjugator is corrected for atmospheric turbulence, displaying significantly less intensity variance than a beam returned by a conventional mirror.</p> <p>A 30 m FWM PC comm link was tested with a uniform turbulence generator (turbox) in the laboratory and compared to theoretical performance predictions. The intensity variance on</p>			
DISTRIBUTION/AVAILABILITY OF ABSTRACT UNCLASSIFIED/UNLIMITED <input type="checkbox"/> SAME AS RPT. <input type="checkbox"/> DTIC USERS <input type="checkbox"/>		21. ABSTRACT SECURITY CLASSIFICATION Unclassified	
22a. NAME OF RESPONSIBLE INDIVIDUAL Dr. V. Smiley		22b. TELEPHONE NUMBER (Include Area Code) (619)553-6128	22c. OFFICE SYMBOL ONR



(BLOCK 19. continued)

the phase conjugate return beam showed no increase over the variance on the beam received at the conjugator, compared with the predicted and observed intensity variance dependence of (path length)<sup>11/6</sup> for a conventional link. Phase conjugation greatly reduced the fraction of power lost over the return path compared to the outgoing path.

Both physics and system models were developed to further the understanding of FWM PC comm link physics and to determine design requirements for a fieldable system. The system model demonstrated that phase conjugation improves the performance of 2-way optical communication by reducing the transponder system size and weight and by eliminating the acquisition and tracking requirement for the transponder platform. Also, phase conjugation can have gain and can increase the power returned by the transponder to compensate for losses and further reduce transmitter requirements.

An important result of the physics model is that for large pointing errors some of the phase aberrations cannot be corrected with phase conjugation because information is lost at the small transponder aperture. Therefore, the returning beam is askew and has poor fidelity resulting in a degradation of the received power.

A holographically corrected FWM PC optical heterodyne receiver using photorefractive material was also designed, fabricated, and characterized. The efficiency of heterodyne mixing of an aberrated beacon beam was restored to the value attained for an unaberrated beam by holographically reconstructing the aberrated beacon wavefront onto a local oscillator wavefront. Correction of more than 10 waves of error and automatic tracking of the beacon beam were also demonstrated.

Accession for	
NOISY IMAGE	<input checked="" type="checkbox"/>
DTIC	<input type="checkbox"/>
Unreliable	<input type="checkbox"/>
Classification	<input type="checkbox"/>
By	
Date	
Availability Notes	
Distribution	
DIA	
A-1	

## PREFACE

This document is the second of three volumes which constitute the final report for the program entitled "Nonlinear Optics Technology (NLOT) Phase III", performed by TRW under contract No. N00014-88-C-0228 with the Office of Naval Research. Funding for the work reported in this volume was provided by Rome Air Development Center and the Defense Advanced Research Project Agency (DARPA). This volume covers the development of phase conjugated atmospheric optical communication links using four wave mixing (FWM).

The program was performed in the Applied Technology Division of TRW's Space and Technology Group, Redondo Beach, CA. The program manager was Dr. John C. Brock; project administration functioned smoothly through the efforts of Ms. Linda Meisenholder, Contracts, and Ms. Linda Tomich and Ms. Anjana Mittra, Project Control.

The work described in this volume was conducted under the technical direction of Dr. John C. Brock. Dr. Alexander B. Horwitz was responsible for the four wave mixing (FWM) phase conjugated (PC) communication link experiments, Dr. Daniel E. Novoseller was responsible for development of the FWM PC comm link system model and Dr. Maria Z. Caponi was responsible for the FWM PC physics model. Other personnel making important contributions to the technical effort were Ms. Joanna Conner who performed the mission analysis, Mr. Larry A. Dozal whose laboratory assistance was vital to both the comm link experiments and mechanical design of the artificial turbulence generator (turbox), Dr. George M. Harpole who provided the technical design of the turbox, Dr. Myung H. Lee who developed the MTF portion of the system model, Dr. Lawrence J. Lembo who designed and executed the experiments on the holographically corrected optical heterodyne receiver, Mr. Michael F. Wolff whose assistance was essential to characterizing turbox performance, and Mr. Mark E. Weber who designed and assembled the turbox power supply. The technical and managerial guidance of L. Marabella is also gratefully acknowledged along with the fine secretarial support obtained from Ms. Pamela J. Bessenbacher.

This work was administered by B. Hendrickson and N. Bernstein of Rome Air Development Center and S. Shey and L. N. Durvasula of the DARPA Directed Energy Office. The contract was monitored by V. Smiley of the Office of Naval Research. Their support and assistance contributed greatly to the success of the program.

## TABLE OF CONTENTS

	Page
I. INTRODUCTION AND SUMMARY .....	1
1. Phase Conjugated Optical Communication Links .....	2
2. Four Wave Mixing Optical Phase Conjugation .....	5
3. Program Achievements .....	7
II. SYSTEM ANALYSIS .....	12
1. Mission Analysis .....	13
a. Approach .....	14
b. Results .....	15
c. Selected Mission .....	18
2. Performance Enhancement Analysis .....	20
a. Gaussian Beam Analysis .....	21
b. Fourier Beam Analysis .....	21
c. Atmospheric Turbulence Correction .....	29
3. System Description .....	34
4. System Performance .....	39
III. PHASE CONJUGATED OPTICAL COM LINK EXPERIMENTS .....	46
1. Experimental Apparatus .....	46
a. Lasers .....	47
b. Four Wave Mixing Cell .....	50
c. Optical Layout .....	50
d. Amplitude Modulation .....	53

## TABLE OF CONTENTS (con't)

	Page
2. Artificial Turbulence Generator (Turbox) . . . . .	53
3. Diagnostics . . . . .	61
a. Com Link Intensity . . . . .	61
b. Com Link Variance . . . . .	61
c. Thermal Measurement of Local Turbulence ( $C_n^2$ ) . . . . .	62
d. Optical Measurement of Path Averaged Turbulence ( $C_n^2$ ) . . . . .	63
4. Data Reduction . . . . .	65
5. 1 km Com Link Experimental Results . . . . .	66
a. Qualitative Observations . . . . .	66
b. Amplitude Modulation . . . . .	70
c. Intensity Variance . . . . .	73
d. Power Loss . . . . .	80
6. Turbox Experimental Results . . . . .	82
a. Turbox Calibration . . . . .	82
b. Experiments . . . . .	84
IV. PHYSICS MODEL . . . . .	93
1. General Model Description . . . . .	93
2. Tests Without Turbulence . . . . .	95
a. Numerical Results . . . . .	96
b. Ad-Hoc Model . . . . .	102

## TABLE OF CONTENTS (con't)

	Page
3. Tests With Turbulence .....	106
a. Numerical Turbulence Description .....	106
b. Numerical Diagnostics .....	107
c. Model Calibration .....	108
4. PC Link Simulations .....	114
a. Rooftop Geometry .....	115
b. Turbox Geometry .....	117
V. HOLOGRAPHICALLY CORRECTED OPTICAL HETERODYNE RECEIVER .....	123
1. Introduction .....	123
2. Heterodyne Efficiency .....	126
3. General Approach .....	130
4. System Concept .....	134
5. Experimental Approach .....	136
a. Two-Beam Setup: Experimental Details .....	136
b. Two-Beam Setup: Results/Discussion .....	138
c. Three-Beam Setup: Experimental Details .....	142
d. Three-Beam Setup: Results/Discussion .....	145
6. Summary .....	149
VI. CONCLUSIONS .....	151
VII. APPENDIX A: MISSION REQUIREMENTS .....	153

TABLE OF CONTENTS (con't)

	Page
VIII. APPENDIX B: PROPAGATION EQUATION DERIVATION . . . . .	163
IX. REFERENCES . . . . .	230

## LIST OF FIGURES

		Page
I-1.	Basic concept of a FWM phase conjugated optical communication link . . .	3
I-2.	Basic FWM PC comm link power budget . . . . .	5
I-3.	Counterpropagating pump geometry for phase conjugation . . . . .	7
I-4.	Scale drawing of TRW Space Park site plan showing optical path of 1 km FWM PC comm link . . . . .	9
II-1.	Typical results of a Fourier optics calculation with a tilt of $25 \mu\text{rad}$ . . . . .	22
II-2.	Two-way power reception efficiency . . . . .	24
II-3.	Reduction in transmitted transponder power from Fourier analysis . . . . .	26
II-4.	Reduction in required transmitted transponder power versus normalized transceiver pointing error . . . . .	27
II-5.	Ratio of power received by the transponder to transmitted power versus transceiver pointing error . . . . .	27
II-6.	Ratio of power received by the transceiver to transmitted power versus transceiver pointing error . . . . .	28
II-7.	Ratio of required transponder power to transmitted power versus transceiver pointing error . . . . .	28
II-8.	Block diagrams for one- and two-way conventional and PC comm links . . . . .	35
II-9.	Spectral dependence of atmospheric transmission . . . . .	40
II-10.	Spectral dependence of atmospheric background . . . . .	41
II-11.	Typical link budget . . . . .	42
II-12.	Required transponder power versus transponder aperture diameter . . . . .	43
II-13.	Performance benefit from PC versus transceiver pointing error . . . . .	44
III-1.	Illustration of folded FWM PC comm link . . . . .	47
III-2.	Optical layout for 1 km comm link experiments (upper) . . . . .	48
III-3.	Optical layout for 1 km comm link experiments (upper) . . . . .	49
III-4.	Photograph of launch platforms above beam handling table . . . . .	52



## LIST OF FIGURES (con't)

		Page
III-5.	Optical layout employed for transmission of amplitude information over 1 km comm link (upper) . . . . .	54
III-6.	Schematic of artificial turbulence generator (Turbox) . . . . .	56
III-7.	Photograph of heater frame elements inside of turbox . . . . .	57
III-8.	Falloff of turbulence strength with downstream distance . . . . .	58
III-9.	Experimental layout employed comm link experiments with optical beam multiple passed through the turbox (lower) . . . . .	60
III-10.	Schematic of detector collection geometry . . . . .	62
III-11.	Turbox sampling port positions and nomenclature . . . . .	63
III-12.	Photographs of beacon at transceiver, beacon at transponder, and phase conjugate return beams . . . . .	67
III-13.	Photographs of beacon beam at transponder showing short and long term beam spread . . . . .	69
III-14.	Photographs of phase conjugate return and mirror return at transceiver . . . . .	71
III-15.	Results of amplitude modulation experiments . . . . .	72
III-16.	Intensity variance on FWM phase conjugated comm link . . . . .	74
III-17.	Comm link FOM for 1 km link with a mirror versus transponder aperture . . . . .	76
III-18.	Comm link FOM for 1 km link with PC versus transponder aperture size . . . . .	76
III-19.	Comm link FOM for 1 km link with PC and mirror versus transponder aperture size . . . . .	78
III-20.	Ratio of power received at the transceiver to the power reflected by a mirror at the transponder versus the ratio of the beacon power received at the transponder to the power launched at the transceiver . . . . .	81

## LIST OF FIGURES (con't)

	Page
III-21. Ratio of power received at the transceiver to the power reflected by the phase conjugator at the transponder versus the ratio of the beacon power received at the transponder to the power launched at the transceiver . . . . .	81
III-22. Calibration of thermocouple probe spacing in the turbox . . . . .	83
III-23. Typical power spectrum of turbulence in the turbox . . . . .	85
III-24. Expanded view of low frequency portion of turbox power spectrum . . . . .	85
III-25. Temperature traces for each probe during a one second test . . . . .	86
III-26. Calibration of optical turbulence diagnostic . . . . .	86
III-27. Temperature differences as a function of heating power . . . . .	87
III-28. Long term temperature difference measured on centerline at 25 kW . . . . .	88
III-29. Turbox FOM measured with a mirror versus transponder aperture . . . . .	90
III-30. Turbox FOM measured with PC versus transponder aperture . . . . .	90
III-31. Turbox FOM measured with PC and a mirror versus transponder aperture . . . . .	91
IV-1. Schematic of the geometry for aperture/tilt studies . . . . .	96
IV-2. Variation of power and peak intensity at the PC and at the receiver with tilt angle for a divergence dominated case . . . . .	98
IV-3. Variation of power and peak intensity at the PC and at the receiver with tilt angle for a collimated beam, $d_{TR} = \infty$ . . . . .	99
IV-4. Variation of power and peak intensity at the PC and at the receiver with tilt angle for a collimated beam, $d_{TR} = d_{rec} = d_{TP}$ . . . . .	100
IV-5. Intensity and phase profiles of the input and received beams for case 3 with zero tilt . . . . .	103
IV-6. Intensity and phase profiles of the input and received beams for case 3 with tilt . . . . .	104
IV-7. Configuration geometry for calibration tests . . . . .	109
IV-8. Sensitivity of the average peak intensity to the number of phase screens . . . . .	109

## LIST OF FIGURES (con't)

	Page
IV-9. Sensitivity of the average peak irradiance to the number of realizations and grid size . . . . .	110
IV-10. Sensitivity of the average power to the number of realizations and grid size . . . . .	111
IV-11. Comparison of the numerical simulation and a MCF calculation . . . . .	112
IV-12. Normalized intensity variance as a function of $C_n^2$ . . . . .	113
IV-13. Average power through an 18 cm radius receiver versus $C_n^2$ for different transceiver apertures . . . . .	113
IV-14. Configuration geometry for comm link performance predictions with a gaussian beam . . . . .	114
IV-15. Ratio of the received power to the input power versus $C_n^2$ for different transponder and receiver aperture pairs . . . . .	116
IV-16. Predictions for rooftop geometry with 2 cm diameter apertures . . . . .	118
IV-17. 3-D view of phase conjugate beams at transceiver for rooftop geometry . . . . .	119
IV-18. Phase conjugate beam profiles at transceiver for turbox geometry . . . . .	120
IV-19. 3-D view of phase conjugate beams at transceiver for turbox geometry . . . . .	121
V-1. Ideal operation of optical heterodyne receiver, with perfectly matched planar wavefronts . . . . .	124
V-2. Degradation of heterodyne signal due to relative tilt of beacon beam . . . . .	125
V-3. Degradation of heterodyne signal due to aberration of beacon wavefront . . . . .	126
V-4. General scheme for holographically corrected heterodyne receiver . . . . .	131
V-5. System concept is closely analogous to holographic image reconstruction . . . . .	135
V-6. Two-beam experimental setup for heterodyne receiver demonstration . . . . .	137
V-7. Oscilloscope trace of optical homodyne signal generated in two-beam setup . . . . .	139

## LIST OF FIGURES (con't)

	Page
V-8. Profiles of aberrated beacon beam and diffracted read beam . . . . .	140
V-9. Optical homodyne signal for aberrated beacon shown in figure V-8a . . .	141
V-10. Three-beam experimental setup for heterodyne receiver demonstration . . . . .	143
V-11. Profiles of aberrated beacons used in three-beam setup . . . . .	147
A-1 through A-42 Results of gaussian beam analysis . . . . .	186 - 229

This page  
intentionally left blank

## I. INTRODUCTION AND SUMMARY

This document is one of three volumes which constitute the final report for the program entitled "Nonlinear Optics Technology (NLOT) Phase III", performed by TRW under contract No. N00014-88-C-0228 with the Office of Naval Research. This program was devoted to the development of nonlinear optics technology for tactical applications of directed energy. Volume 1 covers the development of solid state regenerative amplifiers and is titled, "Solid State Laser Technology." Volume 2 covers the development of phase conjugated atmospheric optical communication links using four wave mixing (FWM) and is titled, "Phase Conjugated Optical Communication Link". Volume 3, entitled "Directed Energy Utility Study," is classified and investigates the utility of directed energy systems on tactical missions.

The purpose of the effort described in this volume was to study physics and engineering issues that impact the design and field performance of FWM phase conjugated optical comm links. There were four PC comm link tasks:

- Design, construct, test, and characterize a 1 km atmospheric FWM phase conjugated (PC) optical communication link and measure the improvement in link performance compared to a one-way optical link.
- Test and characterize a FWM PC optical comm link through artificially generated and controlled uniform turbulence and compare performance to model predictions.
- Develop a wave-optic propagation code with phase conjugation and turbulence for predicting performance of FWM PC comm links.
- Perform system analysis encompassing FWM PC link physics and system engineering to define design requirements for a fieldable system.

In addition, a fifth task was performed to explore other uses of nonlinear optics for improving the performance of laser communication systems. This task investigated a holographically corrected optical heterodyne receiver.

This chapter of the report summarizes the overall program objectives, introduces the subject of nonlinear phase conjugation via FWM interactions, and presents a brief list of the key results. Chapter II presents the system analysis results. The experimental results are found in chapter III and a discussion of the wave-optic code is presented in chapter IV. Characterization and performance of a holographically corrected optical heterodyne receiver is examined in chapter V.

## 1. PHASE CONJUGATED OPTICAL COMMUNICATION LINKS

The advantages of using a PC comm link are significant. The optimum performance of any optical communication system is determined by the characteristics of the diffraction limited optical system in the absence of atmospheric perturbations. This performance is usually substantially degraded in the course of atmospheric propagation by a number of phenomena such as extinction and turbulence-induced speckle. The result is increased power requirements to counter losses and reduce the effect of power fade on comm link availability.

TRW developed an optical link configuration that uses optical phase conjugation to reduce the impact of atmospheric turbulence on link operation. The basic concept is illustrated in figure I-1. A high quality optical wave, or "beacon," is sent from one station, the transceiver, to another, the transponder, where it is received, phase conjugated, and returned back to the original transceiver. Message information is added during the conjugation process. Because the return beam is the phase conjugate of the incoming beacon, it automatically retraces its path and "unravels" the distorting properties of any phase aberrations, such as turbulence, arriving back at the beacon aperture as a high quality beam with the message on it. Message information can be transmitted by amplitude or frequency modulation, or as spatial variations of phase or intensity if the phase conjugation is accomplished by FWM.

A measure of comm link performance is the normalized intensity variance,  $\sigma^2$ , defined as

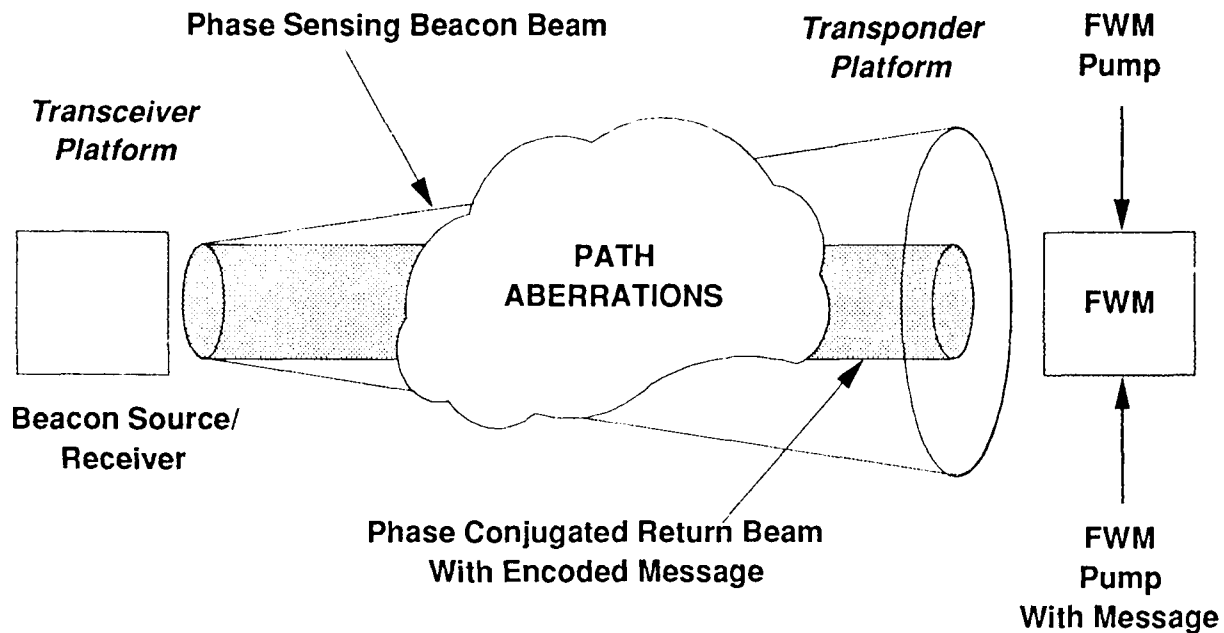


Figure I-1. Basic concept of a four wave mixing (FWM) phase conjugated optical communication link. A high quality beacon beam is transmitted by one station. It is received, phase conjugated, and returned back with message information encoded during the conjugation process by the transponder station.

$$\sigma^2 = \frac{[1 - \langle I \rangle]^2}{\langle I \rangle^2} \quad (I-1)$$

where  $I$  is the measured signal. The variance on the beam at the transmitting optic of the transceiver,  $\sigma_0^2$ , may be very small, but because of atmospheric aberrations, the variance will increase at the transponder ( $\sigma_0^2 < \sigma_{TP}^2$ ). Phase conjugation cannot itself reduce this variance on the conjugate return, but it can prevent the variance from becoming worse when the beam returns to the transceiver ( $\sigma_{TR}^2 \approx \sigma_{TP}^2$ ) by correcting the atmospheric aberrations on the return leg. Thus, this configuration of a basic PC comm link does not improve the intensity variance over that of a one-way link. However, unlike conventional links, the information on power fade is communicated back to the beacon aperture, where appropriate feedback loops operating faster than characteristic atmospheric turbulence times can alter the outgoing beacon phase front to maximize power received by the



conjugator aperture. This fade correction technique then reduces the intensity variance on the outgoing beacon as well, improving performance over a conventional link.

Results of the system study presented in section 3 show that phase conjugation does greatly reduce the size and weight of the transponder platform. In a conventional two-way optical comm link, each station requires a large laser and pointing and tracking hardware at each end of the link. But, because the phase conjugate return beam in a FWM PC link automatically tracks the path of the incoming beam exactly, transponder pointing and tracking hardware requirements are greatly reduced. Since atmospheric aberrations are corrected by the PC return beam, the power loss experienced on the transponder-to-transceiver leg (second one-way link) is also greatly decreased, thereby reducing the power requirements of the transponder laser. An additional consequence of this phenomena is that large transceiver pointing errors can be accommodated with minimal power increases. Thus, PC link power requirements will be less severe than for a conventional optical link while the availability is increased because of reduced fading.

The power reduction achieved on a two-way FWM PC link is illustrated schematically in figure I-2. There is a large power loss experienced on a one-way link resulting from diffraction- and turbulence-induced beam spread as well as pointing error between the two ends of the link. The power received at the end of the one-way link is given by the dotted line in figure I-2. This is also the beacon power that would be received by a transponder on the first leg of a two-way FWM PC link. The power loss experienced by the phase conjugate return beam is much smaller than that on the beacon beam because of the aberration correction and automatic tracking features of FWM phase conjugation. Compare the long dashed line (PC return) to the solid line (beacon beam or one-way link) in figure I-2. With unity gain in the phase conjugator, the power received by the transceiver is less than the power received on a one-way link. However, if the phase conjugator exhibits sufficient gain (greater than unity), then the power received by the transceiver can be equal to or larger than the power received on a one-way link. The phase conjugate return beam with this gain is represented in figure I-2 by the short dashed line. The difference between this line and the line with unity gain (long dashes) is the Breakeven Gain.

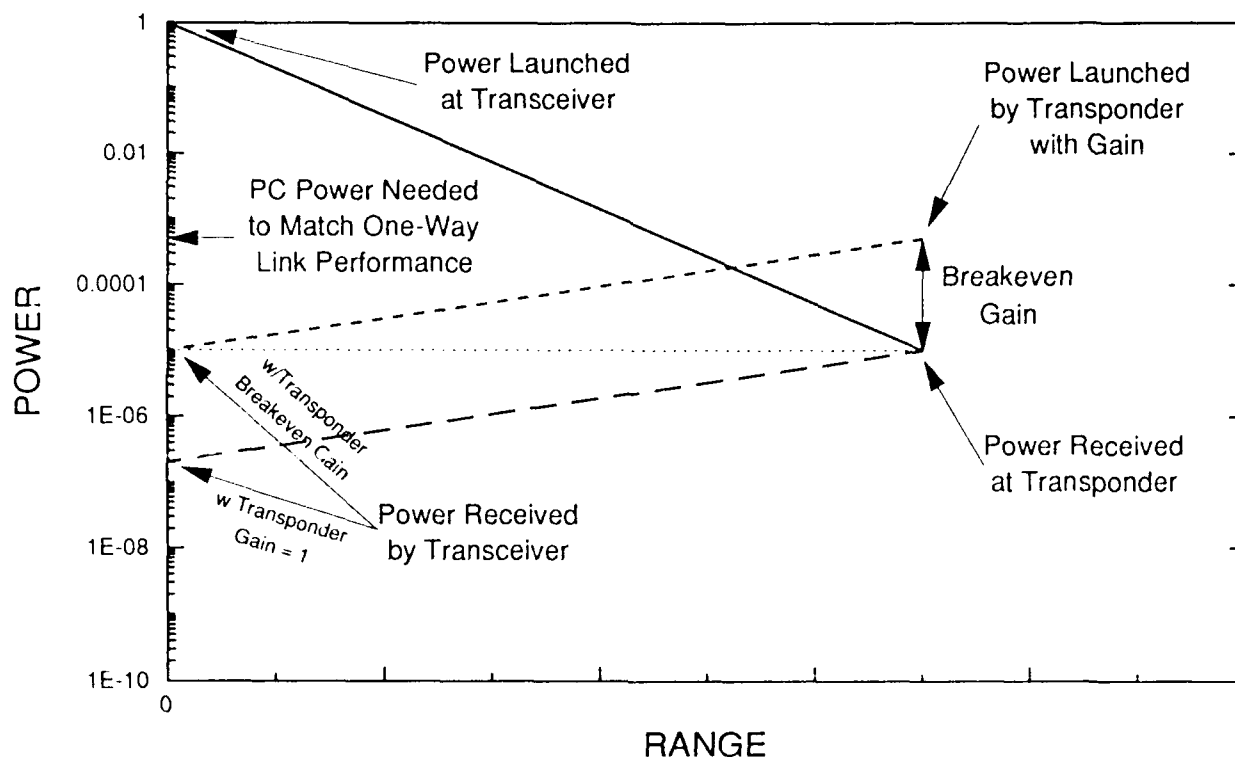


Figure 1-2. Basic four wave mixing phase conjugated comm link power budget. Power on unconjugated beacon beam (solid line) suffers power loss due to diffraction, turbulence, and pointing error. This is the one-way link power loss (represented by the dotted line). The phase conjugate return beam (long dashed line) suffers less power loss because of aberration correction and automatic tracking. In order for the PC return beam to be received with the same power as a one-way link, the phase conjugator must add gain equal to the Breakeven Gain shown in the figure. Then the PC return beam loss will be given by the short dashed line.

However, not all atmospheric-induced aberrations can be corrected equally. When a turbulent atmosphere is introduced between the transceiver and transponder platforms diffractive scales defined by the turbulence become important. For phase conjugation to cancel out the effects of turbules characterized by a spatial frequency,  $1/\epsilon$ , and located a distance  $z$  from the transponder aperture, all information about the turbules must be received by the transponder (i.e. the transponder aperture must be capable of resolving the characteristic length,  $\epsilon$ ). This requires a transponder aperture size such that

$$d_{TP} \geq 2\lambda z/\epsilon. \quad (1-2)$$

where  $\lambda$  is the wavelength. Thus, small turbules (large spatial frequencies) located far from the transponder (conjugator) aperture will cause optical aberrations that are the most difficult for the phase conjugator to correct. For example, with  $\lambda = 589$  nm, turbules on the order of 2 cm at a distance of 1 km from the phase conjugator require a 6 cm-diameter aperture. The phase conjugator material must also be fast enough to respond to temporal changes in the atmosphere. In addition, since the conjugator returns essentially a fixed fraction of the power incident upon its aperture, fade compensation requires that the phase front of the transmitted beacon beam also be modulated rapidly compared to the characteristic atmospheric turbulence time (1 - 3 ms).

## 2. FOUR WAVE MIXING OPTICAL PHASE CONJUGATION

A number of different nonlinear optical techniques have been developed for optical phase conjugation, the process in which an optical wave has its propagation direction and relative phase reversed so that it exactly retraces its path. Four wave mixing is one approach particularly well-suited for optical communication where the return or input signal is weak because the process has no threshold and because it offers a convenient way to add message information to the signal. Other phase conjugation techniques do not offer these advantages and are, therefore, not readily adapted for optical communication. Reference 1 provides an extensive review of phase conjugation, including discussions of the FWM process.

Phase conjugation by FWM is typically performed in the backward, or counterpropagating pump geometry shown in figure I-3. Three input waves incident on a material with a nonlinear response are mixed to form a fourth wave that is radiated from the medium with a frequency and direction determined by the frequencies and propagation directions of the three input waves. The nonlinear polarization that gives rise to this fourth wave is

$$P_{NL}^{(3)} = \chi^{(3)} E_T^3 \quad (I-3)$$

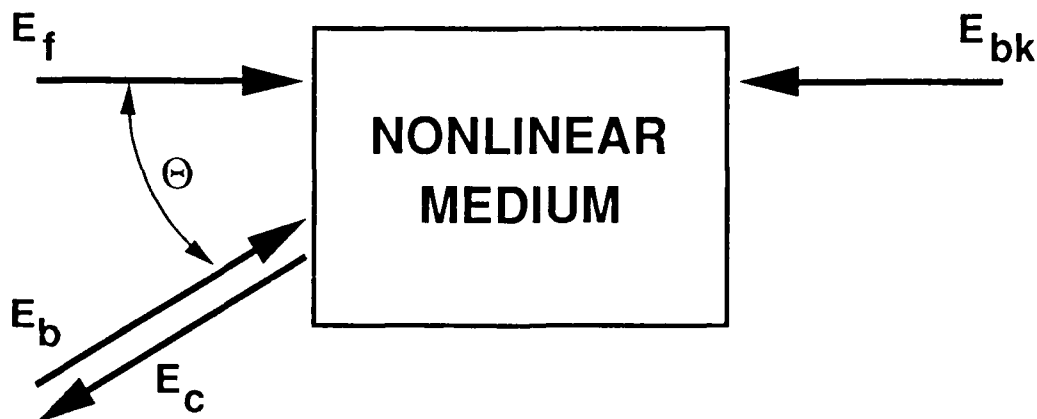


Figure I-3. Counterpropagating pump ( $E_f$   $E_{bk}$ ) geometry for phase conjugating an input beacon beam ( $E_b$ ) using four wave mixing.

where  $E_T$  is the total electric field present in the nonlinear medium and  $\chi^{(3)}$  is the third-order nonlinear susceptibility of the medium. Given input waves of the form

$$E = 0.5 E_i \exp[ i (\omega_i t - k_i z) ] + \text{complex conjugate}$$

there are many terms in the third-order nonlinear polarization, several of which have the form

$$P_{NL}^{(3)} = 0.5 \chi^{(3)} E_1 E_2 E_s^* \exp\{ i [ (\omega_1 + \omega_2 - \omega_s) t - (\vec{k}_1 + \vec{k}_2 - \vec{k}_s) \cdot \vec{r} ] \} + \text{complex conjugate} \quad (I-4)$$

If  $E_1$  and  $E_2$  are phase conjugates of one another, as they are for the two counterpropagating plane wave pumps in figure I-3, then this polarization gives rise to a field propagating in the  $-\vec{k}_s$  direction that is the phase conjugate of the input field. The interaction can be degenerate, i.e. all fields have the same frequency,  $\omega$ , or nondegenerate, with the frequency of the fourth field being the sum of the two pump fields minus the input signal field as shown in the first term of the exponential in equation (I-4). The dominant four wave mixing process out of all the terms in the third-order nonlinear

polarization is determined by the wave vector of the generated wave defined by the second factor in the exponential. This wave vector of the generated fourth wave needs to meet the phase-matching condition that  $k_4 = n\omega_4/c$  for efficient transfer of energy from the pump fields to the input signal wave and its conjugate.

The conjugate wave may be written in the form

$$E(t,x,y) = A(t,x,y) \exp[i\theta(x,y)] \exp(i\omega t). \quad (I-5)$$

where the amplitude,  $A(t,x,y)$ , is a spatially dependent temporal function,  $\exp[i\theta(x,y)]$  is a phase term representing the piston differences across the beam, and  $\exp(i\omega t)$  is the frequency term. Equation (I-5) shows that four different methods of encoding messages may be employed through FWM phase conjugation. These include amplitude modulation, spatial amplitude modulation (pictures), spatial phase modulation, and frequency modulation.

In this work, four wave mixing was performed in sodium vapor. A more detailed description of FWM physics and FWM in sodium vapor is given in chapter 3 of reference 2.

### 3. PROGRAM ACHIEVEMENTS

Significant improvements over one-way optical communication links were demonstrated with four wave mixing (FWM) phase conjugated (PC) optical communication links through experiments and analysis, providing a reliable engineering data base on the performance of FWM PC comm links.

A 1.1 km FWM PC optical comm link propagating through the atmosphere was demonstrated and characterized over a range of atmospheric turbulence conditions and compared to the performance of a one-way link. This link was established over a folded path between the rooftops of TRW buildings R1 and R8, approximately 562 m apart. A site plan of this link is shown in figure I-4. The turbulent boundary layers blowing over the rooftops near each end of the optical link and the weaker turbulence between the buildings over the length of the range made the 1 km rooftop link phenomenologically

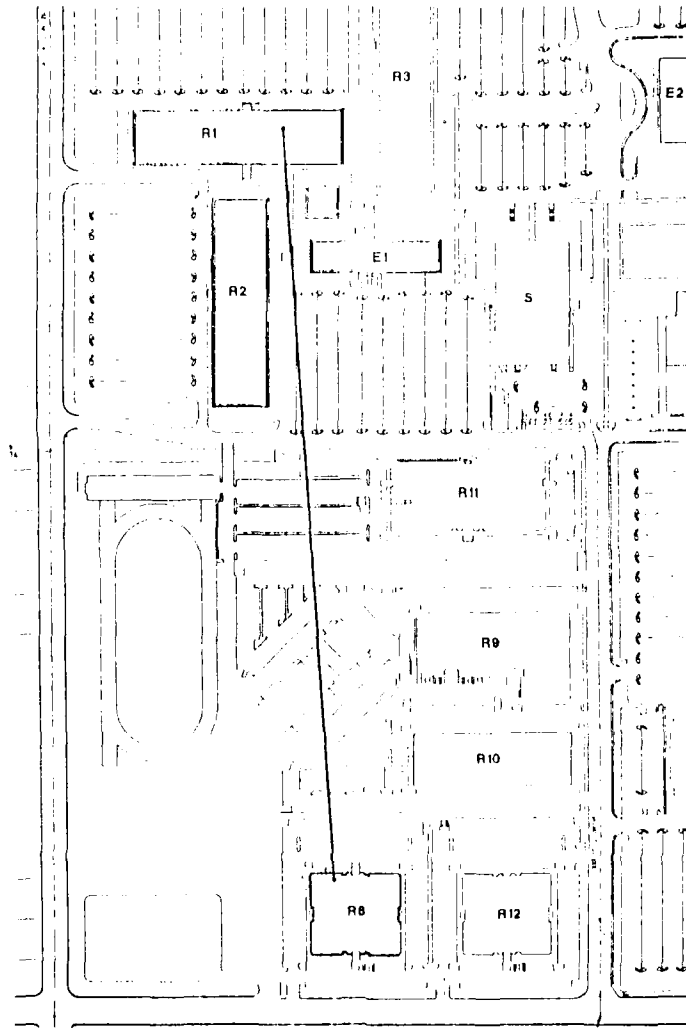


Figure I-4. Scale drawing of TRW Space Park site plan showing the optical path followed by the 1 km four wave mixing phase conjugated communication link.

similar to a real air-to-air link where a strong turbulent boundary layer exists along the surface of each aircraft. In these experiments, four wave mixing was performed in sodium vapor near the sodium  $D_2$  resonance line ( $\lambda = 589 \text{ nm}$ ). Experiments included successful transmission and reception of 10 kHz to 1 MHz amplitude modulation information and measurements of intensity variance as a function of transponder aperture size. The intensity variance on the phase conjugate return beam exhibited little or no

increase over the variance on the beam received at the transponder. The return leg received power was reduced and intensity variance increased when the phase conjugator was replaced with a mirror.

A 30 m FWM PC comm link was tested with a TRW capital artificial uniform turbulence generator (turbox) in the laboratory and compared to theoretical performance predictions. A series of experiments similar to those performed on the rooftop link were performed with the 30 m turbox link. The intensity variance on the phase conjugate return beam showed no increase over the variance on the beam received at the transponder. Without phase conjugation, the intensity variance increased as  $L^{1/6}$ , where  $L$  is the optical path length, as predicted by turbulence theory<sup>3,4</sup>. Phase conjugation greatly reduced the fraction of power lost over the return path compared to the outgoing path.

Both physics and system models were developed to further the understanding of FWM PC comm link physics and to determine design requirements for a fieldable system. The system model demonstrated that phase conjugation improves the performance of 2-way optical communication by reducing the transponder system size and weight and by eliminating the acquisition and tracking requirement for the transponder platform. With or without phase conjugation, the first leg of the comm link (beacon) suffers large power loss (e.g. assume a 20  $\mu$ rad pointing error over a 50 km range with 30 cm apertures, then 0.06% of the transmitted power is received). In a two-way link without phase conjugation, the second leg of the comm link suffers the same large power loss. However, with phase conjugation, the second leg suffers a much smaller power loss: 33% of the power returned by the second platform is received by the first platform, an overall improvement of 7 dB. Phase conjugation can have gain and can increase the power returned by the transponder to compensate for losses and further reduce transmitter requirements.

A physics wave-optics model was built from the GLAD-386 code which included turbulence and specific comm link geometries. This code was validated and compared to experimental results. An important result is that for large pointing errors some of the phase aberrations cannot be corrected with phase conjugation because information is lost

at the small transponder aperture. Therefore, the returning beam is askew and has poor fidelity resulting in a degradation of the received power.

A holographically corrected FWM PC optical heterodyne receiver using photorefractive material was also designed, fabricated, and characterized. Laboratory experiments included restoring the efficiency of heterodyne mixing of an aberrated beacon beam to the value attained for an unaberrated beam by holographically reconstructing the aberrated beacon wavefront onto a local oscillator wavefront. Correction of more than 10 waves of error and automatic tracking of the beacon beam were also demonstrated.



## II. SYSTEM ANALYSIS

Phase conjugation (PC) offers the potential of automatic high resolution compensation of aberrations in the path of a laser beam. The system study presented in this chapter explores how the phenomenon of four wave mixing (FWM) phase conjugation can be used to improve the performance of an optical communication link. This effort concentrated on defining performance advantages of the link concept illustrated in figure I-1.

Phase conjugation does not simplify the complicated initial acquisition problem. Thus, to initiate communication, one of the transmitters will have to search an uncertainty volume just as in the non-PC case. However, once the probe signal hits the receiver, phase conjugation can be used to simplify loop closure and communication. This makes most sense in an asymmetric situation, when one platform is always the transmitter, and the other is always the receiver. The platform with the phase conjugator is the transmitter, but acts as a transponder because it takes the beacon beam from the initial transmitter, and encodes a message on the beam, returning it to the platform housing the beacon transmitter and receiver.

The use of phase conjugation produces several benefits:

- reduction in the size and power of the transponder
- elimination of the acquisition and track requirement for the transponder

In this work, we have evaluated the payoff of a FWM phase conjugated optical communication link in a transponder-type mission, where phase conjugation provides a size reduction payoff to the transponder platform. A collection sentry aircraft (CSA) mission was used to define requirements associated with transferring data from a remotely piloted vehicle (RPV) to its command aircraft (CAC). The CAC probes the RPV with a beacon. The RPV modulates the beacon signal, and conjugates it, sending it back to the CAC without ever having to actually track the CAC. The PC payoff is the reduction

in size, weight, power, and complexity of the RPV-based transponder system, and the whole issue of acquisition of the CAC by the RPV is eliminated.

## 1. MISSION ANALYSIS

The mission analysis performed for NLOT attempted to identify communication missions which will benefit from the insertion of nonlinear (phase conjugation) technology. This mission analysis is anchored to real missions and stated needs. The potential improved system performance is reduced transmitter power and automatic tracking for one end of the link, thus allowing the system designer to relieve or transfer some of the burden (complexity, weight, power) from one end of a communication link to the other end.

The following criteria were used to identify missions and requirements which are currently unmet and/or would benefit from the insertion of phase conjugation technology.

- Candidates for optical communication
  - Stealthy
  - High Data Rate
- Asymmetric or 1 way communication requirement (symmetric or 2 way communication is possible, but requires duplicate hardware on each platform).
- Tactical AF missions (C<sup>3</sup>I, for example).

The top level mission and system requirements were collected (or in some cases developed) for the communication requirements, acquisition requirements and environment requirements. The communication requirements include type of link (network, 1 or 2 way communication), terminal, range(s), platform altitude(s), required data rates (DR), and the bit error rate (BER). In most cases, the stated data rates were driven by the RF technology currently used. The availability of a higher data rate will allow a mission refinement or system redesign to include more capacity or shorter communication times (thus increasing security). The acquisition requirements are mainly

the field of regard and the uncertainty angle or area for both the azimuth and elevation. The field of regard is the potential area over which the link may be required to operate. For most aircraft, the azimuth field of regard is 360 degrees (the plane may be flying in any orientation) with a 60 degree elevation field of regard. In most cases, the location of the second terminal is known within some uncertainty angle. For most applications, this is still a fairly large angle (typically 60 degrees azimuth and 2.5 degrees elevation). The uncertainty angle may be driven by a broad requirement to communicate with an aircraft somewhere to the left side of the plane. Perhaps the second terminal will have a known location and thus a smaller uncertainty angle.

The environmental requirements include an estimate of the atmospheric conditions and weather (night, fog, rain, etc.) and the dynamic environment (straight and level flight, high G maneuvers). The general system requirements for covertness, size, weight and power, and any time constraints (acquisitions and/or communication) are also stated.

a. Approach -- Candidate missions were identified through interviews with military users (Air Force, Army, Navy), defense contractors (MITRE, Aerospace, MIT/LL, TRW) and by identifying and reviewing Statements of Needs (SON).

The majority of users and contractors did not have specific needs which would require optical or phase conjugated optical communication terminals. The proposed missions were often vague and poorly defined. In general, proposed missions were based solely on the perceived "capabilities" of the laser technology. The most specific mission requirements are discussed below.

The SONs reflect real military needs and desires; however they assume a baseline of proven technology. SONs are not typically based on unproven technology and in this study, it was found that most of the user community considers laser communications to be unproven. Also, the SONs do not typically direct a contractor to use a specific technology. SONs that could use laser communication are SAC 002-79 EMP Hardened Communications, TAF 306-74 TDMA Combat Communication System (JTIDS), and TAF 321-75 Jam-Resistant Secure Voice Communications. A list of SONs potentially using lasercom include

ESC 006-83	Jam-Resistant Secure Communications
TAF 303-84	Intra-Theater Intell Comm Network
TAF 308-84	Airborne Combat Information System
TAF 321-75	Jam-Resistant Secure Voice Communications
ESC 001-77	Tactical Secure Voice
TAF 306-74	TDMA Combat Communication System (JTIDS)
SAC 012-81	Bomber Radio Update
SAC 007-79	Wideband Communications
SAC 002-79	EMP Hardened Communications
Draft MAC 03-88	Intraformation Positioning System (IFPS)

The candidate missions identified by this process are outlined in table II-1. For each candidate mission, mission requirements, description and top level system requirements were collected, as outlined in table II-2. The mission description includes the mission name and acronym, a brief statement of the mission purpose, an operating scenario, time line if appropriate, and comments on how the mission is currently accomplished, if known. Also included is an assessment of the benefits of a phase conjugated optical communication link and identification of the terminal platforms (primarily aircraft). The requirement source is also stated.

b. Results -- Most of missions listed in table II-1 are not well defined. However, detailed mission requirements, defined in table II-2, are available for the following applications and are listed in appendix A:

- Intraformation Helicopter Positioning System (IFPS)
- Situational Awareness Data Link (SADL)
- Intergroup Fighter to Fighter (IFTF)
- Airborne Command Post (ACP)
- Collection Sentry Aircraft (CSA)

Table II-1. Candidate Laser Communication Missions.

<p><b>Short Range (0 to 30 nmi)</b></p> <ul style="list-style-type: none"> <li>Helicopter Intraformation Positioning</li> <li>Intra-tank Communication</li> <li>Situational Awareness Data Link</li> <li>Ground Command Post Network</li> <li>Bomber to Bomber Refueling</li> <li>Shuttle Docking</li> <li>Space Station Free Flyer</li> <li>Fighter Squadron Communication</li> <li>Command Post Vehicles</li> <li>Aircraft to Ground</li> <li>Tank to Tank</li> <li>Robot Control</li> </ul>
<p><b>Medium Range (30 to 150 nmi)</b></p> <ul style="list-style-type: none"> <li>Airborne Command Post (ACP)</li> <li>Collection Sentry</li> <li>Remote Pilot Vehicle (RPV)</li> <li>Identification Friend-or-Foe (IFF)</li> <li>Bomber/Fighter Retargeting</li> <li>Cruise Missile Retargeting</li> <li>Intergroup Fighter</li> <li>Ship to Aircraft</li> </ul>
<p><b>Long Range (150 nmi or longer)</b></p> <ul style="list-style-type: none"> <li>Satellite Crosslink</li> <li>Satellite to Ground/Ground to Satellite</li> <li>LEO to GEO communications</li> <li>Secure Video Conference</li> <li>Submarine Laser Communications from Satellites (SLCSAT)</li> <li>Transpacific/Transatlantic</li> <li>Satellite to ship</li> <li>Deep Space Missions <ul style="list-style-type: none"> <li>-Mars</li> <li>-Outer Planets</li> </ul> </li> </ul>

Table II-2. Mission Requirements Information.

Mission Description:	Name of mission and mission objective or purpose
Operating Scenario:	How mission is accomplished, an operational time line and an estimate of how mission is currently accomplished.
Optical vs. RF:	Can an existing or proven RF technology meet these requirements?
Nonlinear Optics Use:	Can Phase Conjugation improve system design and performance?
Platform Type:	What will the terminals be mounted on?
<b>Communication Requirements:</b>	
Link:	What type of terminal configuration is required?
Range:	What is the maximum and minimum distance between terminals?
Altitude:	What is the maximum and minimum height or altitude of the terminals?
Digital Data Rate (DR) and Bit Error Rate (BER) or Analog DR and SNR:	Is the signal digital or analog? What is the current or minimum acceptable data rate (DR), bandwidth? What is the bit error rate (BER) or signal to noise ratio (SNR) required?
<b>Acquisition/Tracking Requirements:</b>	
Field of Regard:	What is the field of regard and the uncertainty angle or area for both the azimuth and elevation (the potential area over which the link may be required to operate)?
Uncertainty Angle:	How well is the location of the second terminal or transponder is known?
<b>Environment Requirements:</b>	
Weather/Atmosphere:	What is weather (clouds, rain, dust, etc.) like?
Dynamic Environment:	How stable are the platforms (high G turns, etc.)?
<b>System</b>	
Total time:	How long can the terminals spend acquiring and communicating?
Availability:	How frequently will the terminals be communicating?
Covertiness:	Is stealth or covertness important?
Size/Weight/Volume:	What are the constraints on the terminal size, weight and power allocations?

Table II-2 (con't). Mission Requirements Information.

Power:	What are the constraints on the terminal D.C. power
Cost:	Are there any unusual cost constraints?

In addition, requirements are available for IFFN. However, the existence of an ongoing program (Mark XV) that appears to meet the requirements to the satisfaction of the customer reduces its potential as an application using a nonlinear optics communication link.

c. Selected Mission -- The majority of the potential phase-conjugated optical communication applications are still in the formative stages. Requirements are generally not yet established. However, several of the proposed missions merit further consideration for a phase conjugated link. The Collection Sentry Aircraft was chosen for the NLOT system concept development. The mission requirements for the CSA is listed in table II-3. The CSA meets the NLOT criteria of tactical air-to-air missions, medium range and is primarily an asymmetric communication link, thus enhancing the potential usefulness of phase conjugated lasercom for the application. Also, covertness, stealthiness, and high data rates are major system design parameters which favor use of laser communications. This mission has an interrogation transmitter/receiver (transceiver) on a command aircraft (CAC) that probes the transponder on the sensor aircraft, a remotely piloted vehicle (RPV) or other unmanned air vehicle (UAV). The RPV operates as a long distance battlefield reconnaissance observation platform. Current mission communication is accomplished with a microwave link. Shorter (optical or infrared) wavelengths would add the advantages of covertness, jam resistance and low probability of interception (LPI). The CAC maintains communication with the RPV drone, monitoring and updating the guidance control with a low data rate "housekeeping" link. The drone, in turn, is monitoring troop movements, battle maneuvers, missile launches or other critical events and relaying the information back to the command airplane using a high data rate link. This asymmetric communications configuration is well suited to the conjugated link concept under consideration.

Table II-3. Collection Sentry Aircraft (CSA) Mission Requirements.

Mission Description:	Collection Sentry Aircraft (similar in range and data rate to Airborne Command Post Mission). Update database or transfer sensor data from a sentry aircraft or a remote piloted vehicle (RPV) patrolling over hostile territory.
Operating Scenario:	A patrol aircraft or RPV has collected a variety of sensor data. The interrogating aircraft, approximately 100 nmi. away, approaches the patrol area and initiates a data transfer. The data transfer must be very covert, not revealing the presence or location of the patrol aircraft or RPV. The interrogating aircraft is a sentry aircraft going on station and receiving the latest data or a command aircraft monitoring the RPV. A real time video relay is desired but not required (potentially an upgrade).
Optical vs. RF:	Optical communications narrow beamwidths will not betray the CSA presence or location. The CSA are vulnerable to detection during the entire data transfer (30 min.). Although data transfer time can be reduced by using a higher RF data rate, the relatively broad RF beams still reveal the CSA presence.
Nonlinear Optics Use:	The PC may reduce the fades due to jitter and the atmosphere.
Platform Type:	Large Lear Jets (between a Fighter and C135 in size).
Requirement Source:	AFWAL/ Army/ CSA Program Manager.
<b>Communication</b>	
Link	Potentially asymmetric.
Range	50 to 100 nmi, clear atmosphere - may reduce range with clouds.
Altitude	25,000 to 35,000 ft.
Digital	DR = 30 to 60 Mbps, BER = $10^{-7}$ .
Analog	DR and SNR - Not applicable.
<b>Acquisition/Tracking</b>	
Field of Regard (Transmitter and Receiver)	
Azimuth	360°
Elevation	2°
Uncertainty Angle (Transmitter and Receiver)	
Azimuth	60°
Elevation	2°
<b>Environment</b>	
Weather/Atmosphere	Very little weather at these altitudes, may have some clouds.
Dynamic Environment	Normal environment, straight flight (No dog fighting or steep turns).



Table II-3 (con't). Collection Sentry Aircraft (CSA) Mission Requirements.

<b>System</b>	
Total Time	< 1 min.
Availability	On demand.
Covertness	Very important.
Size/Weight/Volume	Keep it small, CSA aircraft are loaded with equipment.
Power	TBD
Cost	TBD

Typical communication ranges are up to 100 nautical miles (nmi), in clear atmosphere and at 10 km altitude. Data rates of 30 - 60 Mbps at  $10^{-7}$  bit error rates are highly desirable, though these capabilities are far beyond the current state of the art. Details of typical CSA mission requirements are given in table II-3. Having this capability would reduce data transfer time significantly.

The other missions for which we have detailed requirements are less suitable. Missions such as IFPS and SADL are very short range. For short propagation distances the benefit of phase conjugation is small since the beam has not diverged appreciably. For long ranges, such as with satellite crosslinks, the beams have diverged and are very large at the phase conjugator. Conjugation fidelity can be poor because such a small portion of the beam is interrogated, but this is not a factor for a crosslink where automatic tracking is the primary benefit.

## 2. PERFORMANCE ENHANCEMENT ANALYSIS

A complete analytic formulation for the performance of a FWM PC comm link has been developed. This methodology was coded into a link budget model, which was used to quantify the system payoff, as described in section II.4.

To evaluate the performance of a FWM phase conjugated comm link, gaussian beam and Fourier optics theoretical approaches were developed. The gaussian beam approach is a modulation transfer function (MTF) approach that employs gaussian beams,

apertures, etc. The details of this approach are developed in appendix B and the results are presented in section II.2.a. The Fourier optics approach replaces the gaussian apertures with hard apertures and was used to validate the gaussian approach. This is discussed in section II.2.b.

a. Gaussian Beam Analysis -- In the first approach, gaussian beam analysis was used to define the breakeven PC gain (BPG), described in chapter 1. This is the increase in power needed at the transponder so that the power received back at the transmitter is the same as that received by the transponder (see figure I-2). Expressions for the BPG are given in Appendix B for irradiance (IBPG) and for power-in-the-bucket (PBPG). Use of these gains permits us to quantify the payoff of a 2-way PC link relative to a 1-way link from the transponder platform to the receiver platform (REC). When there is no pointing error, this BPG is always greater than 1, i.e. there are always link losses in the PC link that need to be compensated relative to the performance of a 1-way direct link due, for example, to diffraction and atmospheric extinction. Under such an idealistic condition, the only value of FWM phase conjugation is automatic tracking. When there are large pointing errors, the power-in-the-bucket breakeven PC gain (PBPG) shows even larger required compensation to perform as well as an equally large transmitter on the transponder platform.

Another figure of merit quantifying the payoff of PC is described in Appendix B, section 6.0. This is the reduction in power that needs to be transmitted from the transponder in the PC link relative to that which must be transmitted in a 1-way link (see figure I-2). This parameter is greatly reduced at longer range or at larger pointing error, i.e. it shows the payoff of the PC link by assuming that the transceiver will pay the primary range loss and pointing loss penalties by providing additional laser power, and that the transponder will be able to redirect the beacon signal back to the transceiver platform with little additional loss.

b. Fourier Beam Analysis -- The gaussian analysis was validated by the use of Fourier optics to include the effect of hard, rather than gaussian, apertures. Figure II-1 shows typical calculation results. A uniform irradiance beam is centered on a 128 x 128

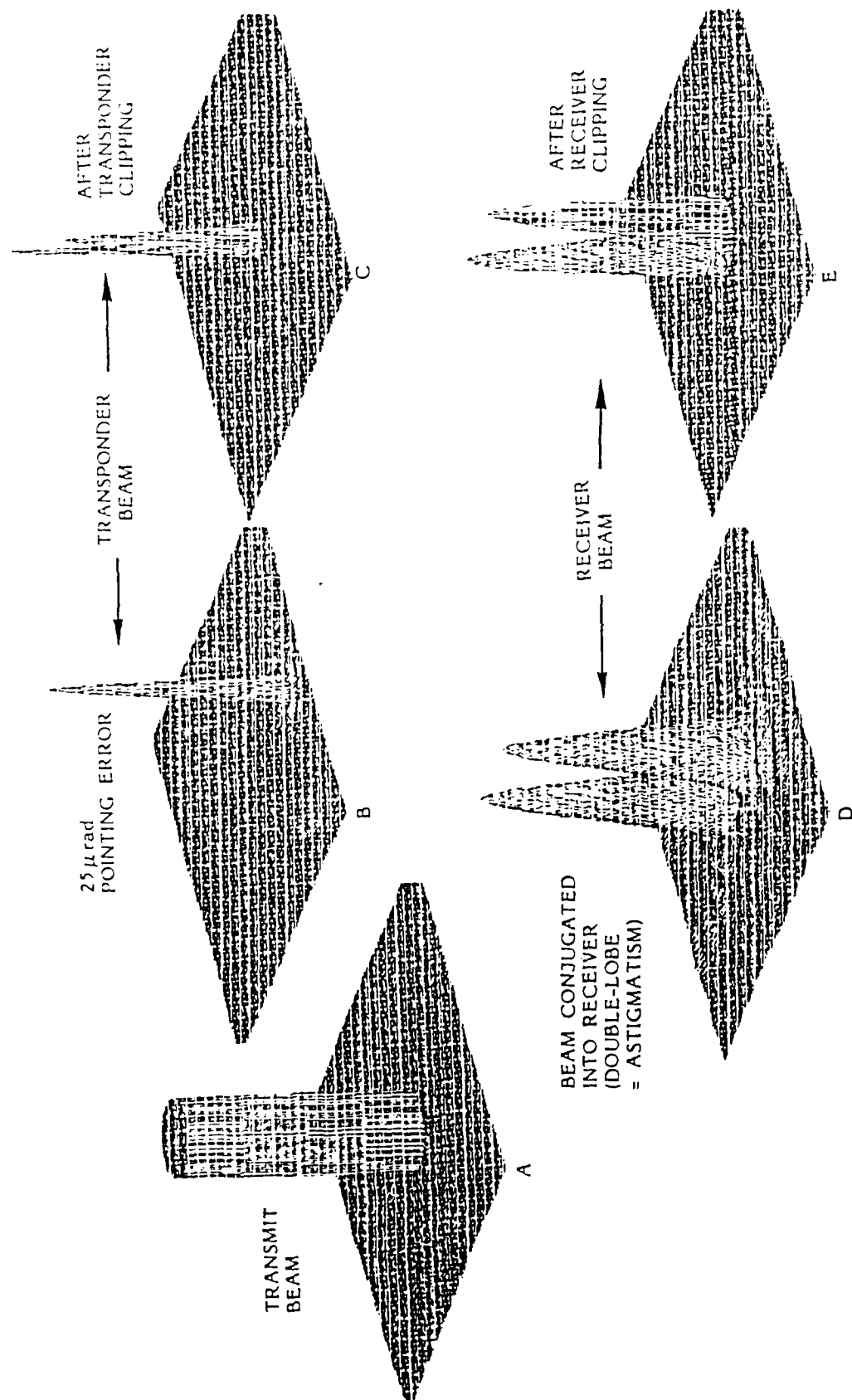


Figure II-1. Typical results of a Fourier optics calculation with a tilt of  $25 \mu\text{rad}$  placed on the beam. The x and y scales in this figure are evident by recognizing that the clipped diameters in figures A, C, and E are all 30 cm, and that figures B and D have the same scale as figures C and E, respectively. Other important parameters in the calculation are: wavelength =  $0.85 \mu\text{m}$ , range = 30 km, transmitter diameter = 30 cm, transponder diameter = 30 cm, receiver diameter = 30 cm, and atmosphere = no turbulence.

grid (figure II-1A). A pointing error (tilt phase) is placed on the beam. The beam is then propagated to the far field, producing the off-center spike shown in figure II-1B. This "received beam" is then clipped around a centered receiver, leaving a non-symmetric beam, with relatively low power (figure II-1C). Figure II-1D shows the beam conjugated and repropagated back to the transceiver. At the receiver, it is spread and somewhat out of focus. It is then clipped by the receiver and the resulting beam is shown in figure II-1E. Figure II-1C is used to evaluate the transponder power,  $P_{TP}$  (= the 1-way link received power). Figure II-1E is used to evaluate the 2-way comm link receiver power,  $P_{REC}$ .

This effect as a function of tilt angle is illustrated in figure II-2, showing by Fourier optics analysis that at large pointing error, the outgoing path suffers  $10^{-3}$  loss (30 dB), while the total 2-way loss is only about  $10^{-4}$ . In other words, the return link only costs an additional 10 dB. Thus, if the transceiver is given a large power source to compensate for the 2-way 40 dB loss, then the transponder only needs to compensate for 10 dB of loss in the second part of the 2-way link. Analysis shows that a turbulent atmosphere adds approximately  $20 \mu\text{rad}$  of pointing error to the transmitted beacon beam for a 50 km link at high altitude, an angle where there is substantial advantage for phase conjugating the second leg of the link.

Power reduction on the transponder platform can be substantial. Given

$P_{TR}$  = transmitted power

$P_{TP}$  = power received at the transponder  
= power received in a 1-way link

$P_{REC}$  = power received in the 2-way link at the receiver, assumed collocated with the transmitter

$G$  = transponder gain

The received power is then

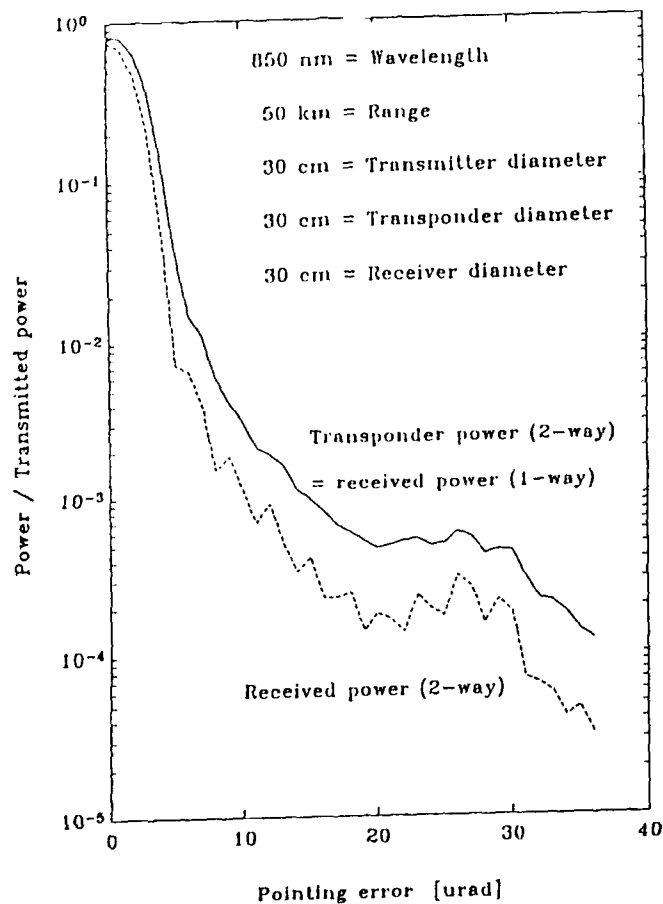


Figure 11-2. Two-way power reception efficiency. Wavelength = 0.85  $\mu\text{m}$ , range = 50 km, transmitter diameter = 30 cm, transponder diameter = 30 cm, receiver diameter = 30 cm, and atmospheric effects are accounted for in the effective tilt angle.

$G \times P_{\text{REC}} =$  power received in the 2-way link at the receiver, when  $P_{\text{TP}}$  is enhanced by  $G$ .

The gain needed to allow the 2-way link to provide the same performance as a 1-way link is given by equating these two received powers

$$P_{\text{TP}} = G P_{\text{REC}}$$

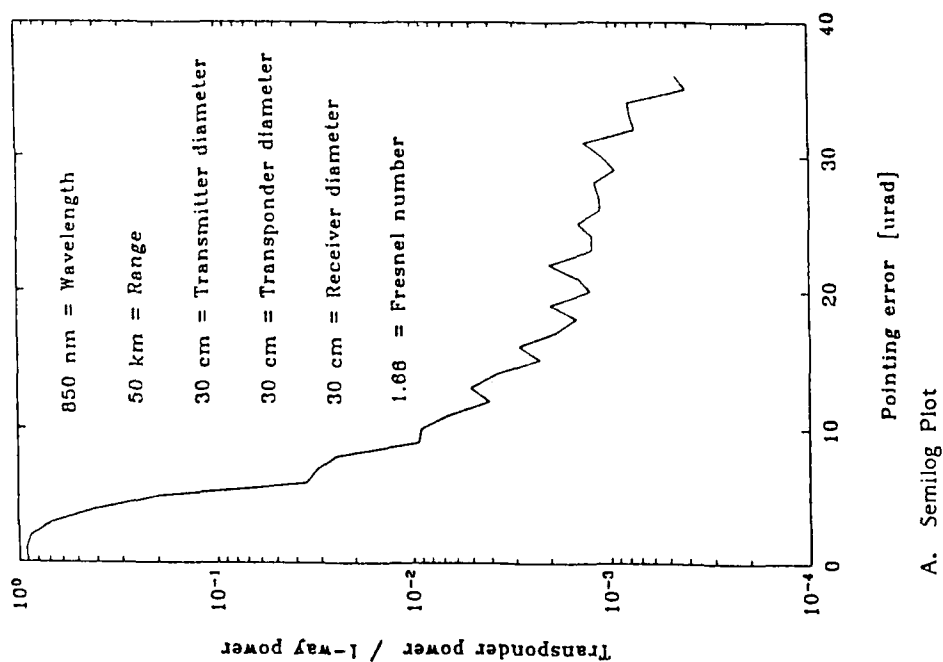
Then the power that must be transmitted from the transponder in a gain-enhanced two-way link is

$$P_{TP}' = G P_{TP} = P_{TP}^2 / P_{REC}$$

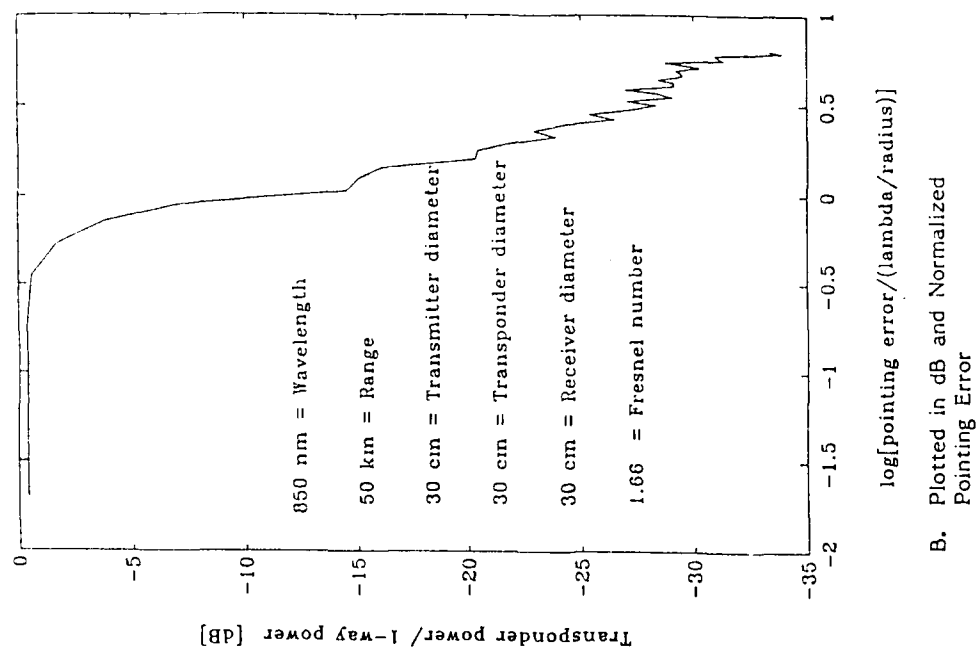
This required transponder power is reduced relative to the transmitter power,  $P_{TR}$ , that is required in a 1-way link with equal received power, and is plotted as  $P_{TP}'/P_{TR}$  in figure II-3. Far less power is needed from the transponder in a 2-way link than is needed from the transmitter in a 1-way link. For typical atmospheric turbulence-induced tilt angles over a 50 km range of 20  $\mu$ rad, the power reduction is on the order of  $10^3$  (30 dB).

Figure II-4 shows the same results as in figure II-3b, calculated using the gaussian beam formulation described in Appendix B. The comparison is not precise, as the Fresnel numbers are not quite the same, and the beam profiles are different. However, some general conclusions can be drawn. The gaussian result (figure II-4) is more optimistic in its dependence on pointing error, since it implies immense reductions in transponder power required at large pointing error. The Fourier optics result includes the sidelobes more correctly, and thus provides additional power in the 1-way (and 2-way) links, reducing the apparent performance gain. While there are quantitative differences, the similarity in form between the two cases suggests the simpler gaussian formulation can be used for evaluating PC payoff. This gaussian formulation is included in the link budgeting model discussed below.

Figures II-5 - II-7 address the accuracy expected from the Fourier optics calculations. Figure II-5 shows the transponder power (corresponding to the solid line in figure II-2), figure II-6 the receiver power (corresponding to the dashed line in figure II-2), and figure II-7 the "required power" (corresponding to figure II-3), each as a function of pointing error, for five calculation grids (8 x 8, 16 x 16, 32 x 32, 64 x 64, and 128 x 128) with the same fraction of the grid occupied by the beam as shown in figure II-1. A 256 x 256 grid exceeded the capability of the computer. The results indicate remarkable consistency from each resolution (i.e. grid size) to the next, out to 75% of the full explored



A. Semilog Plot



B. Plotted in dB and Normalized Pointing Error

Figure 11-3. Reduction in required transmitted transponder power from Fourier analysis. (a) Ratio of transmitted transponder power to power received at the transponder plotted against transceiver pointing error. (b) Ratio in (a) plotted in dB against the normalized transceiver pointing error. Normalized transceiver pointing error =  $\log_{10}[\text{transceiver pointing error}/(2\lambda/D_{TR})]$ , where  $\lambda$  is the wavelength and  $D_{TR}$  is the transceiver diameter.

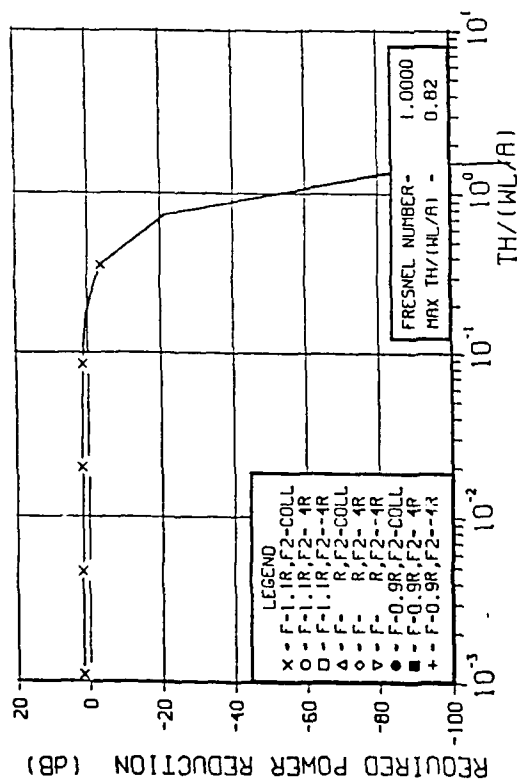


Figure II-4. Reduction in required transmitted transponder power plotted as a function of the normalized transceiver pointing error (see figure II-3) from gaussian beam analysis.

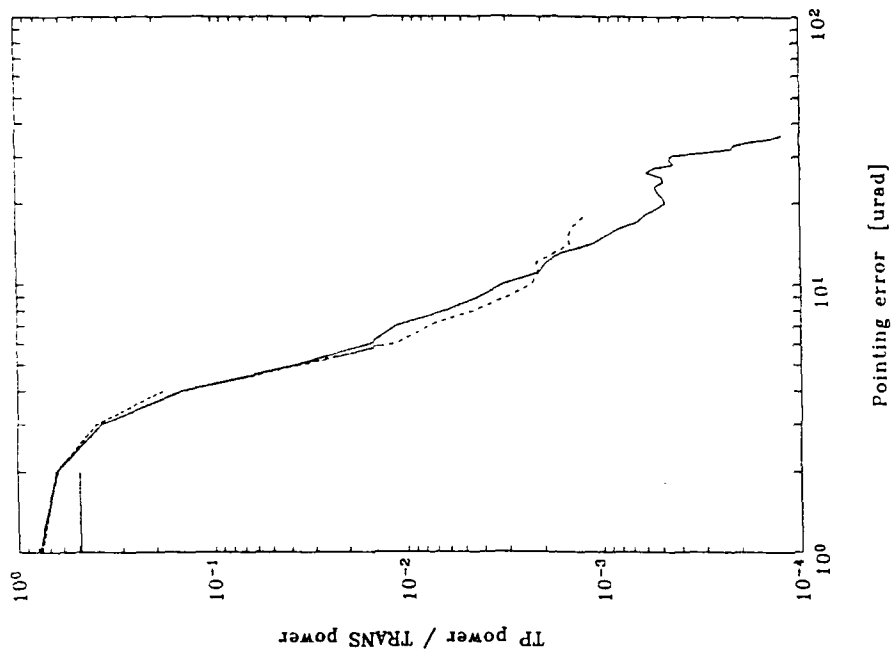


Figure II-5. Ratio of power received by the transponder (one-way power) to transmitted power plotted against transceiver pointing error. 8 x 8 grid = short solid line, 16 x 16 grid = dashed line, 32 x 32 grid = dotted line, 64 x 64 grid = dash-dot line, 128 x 128 grid = long solid line.



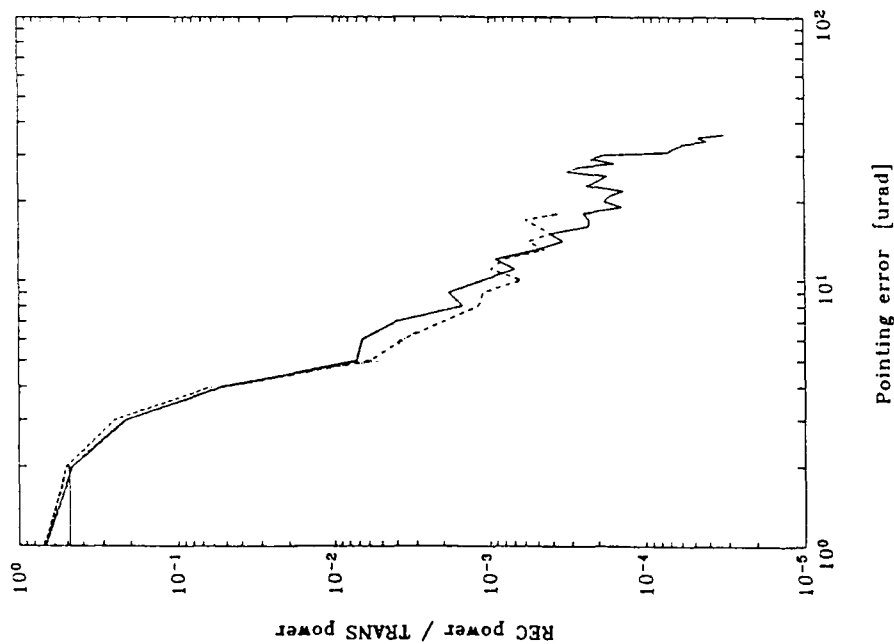


Figure 11-6. Ratio of power received by the transceiver (two-way power) to transmitted power plotted against transceiver pointing error. 8 x 8 grid = solid line, 16 x 16 grid = dashed line, 32 x 32 grid = dash-dot line, 128 x 128 grid = long solid line.

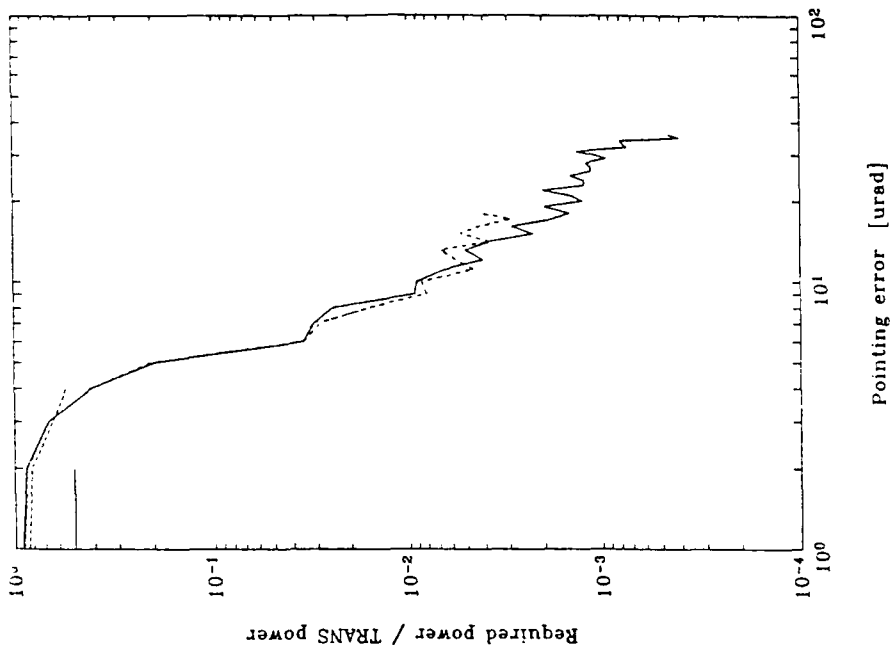


Figure 11-7. Ratio of required transponder power to transmitted power plotted against transceiver pointing error. 8 x 8 grid = short solid line, 16 x 16 grid = dashed line, 32 x 32 grid = dotted line, 64 x 64 grid = dash-dot line, 128 x 128 grid = long solid line.

range in  $P_{TP}/P_T$  (figure II-5), and somewhat less consistency in the  $P_{REC}/P_T$  calculation (figure II-6).

c. Atmospheric Turbulence Correction -- The gaussian approach provides a reasonable approximation of the effects of FWM phase conjugation on a communication link and is computationally much easier to implement than the Fourier description. However, turbulence must be added to the gaussian analysis to complete the link model. A formulation of the far-field irradiance of a turbulence-degraded laser beam is presented below.

Atmospheric turbulence factors are characterized by

$$\text{boundary layer turbulence} \quad C_n^2 L = 10^{-12} \text{ m}^{1/3}$$

$$\text{air turbulence} \quad C_n^2 = 10^{-16} \text{ m}^{-2/3}$$

where  $C_n^2$  is the atmospheric index structure constant and  $L$  is the thickness of the boundary layer.

Several turbulence-related concerns may be addressed simply. There is a point ahead requirement because of the relative speeds of the platforms. This is of order

$$\begin{aligned} \theta_{PA} &= \Delta v / c \\ &\approx 10^3 \text{ (m/s)} / 3 \times 10^8 \text{ (m/s)} \\ &\approx 3 \text{ } \mu\text{rad} \end{aligned}$$

where  $\Delta v$  is the platform relative speed and  $c$  is the speed of light. This is far smaller than the beam spread expected by diffraction, and is thus negligible in terms of the impact on conjugation fidelity.

A second concern is the effect on the fidelity of the conjugation of air motion along the path. In the time it takes for the beam to return to the transceiver, the air moves

$$\begin{aligned} \Delta z &= \Delta v [2R/c] \\ &\approx 10^3 \text{ (m/s)} [2 \times 10^5 \text{ (m)} / 3 \times 10^8 \text{ (m/s)}] \\ &= 67 \text{ cm} \end{aligned}$$

where

$R$  = the link range.

This effect should not be important if this distance is less than the Fresnel range

$$\begin{aligned} Z_F &= D^2/\lambda \\ &\approx (0.01 \text{ m})^2 / 10^{-6} \text{ m} \\ &\approx 100 \text{ m} \end{aligned}$$

where

$D$  = the aperture diameter (or point at which irradiance falls to  $1/e$  for an infinite gaussian beam) and  $\lambda$  is the wavelength.

Thus, the rays should not have deviated too far in passing through the air in the return path, and the conjugation fidelity should be good.

During times that are short relative to the characteristic atmospheric time constant, e.g. during a pulse, the irradiance delivered to a detector is assumed to be given by a gaussian form

$$I(r) = \frac{PT}{\pi \omega_{so}^2} \exp[(\vec{r} - \vec{\Delta})^2/\omega_{so}^2] \quad (II-1)$$

where

$\vec{r}$  = 2-dimensional coordinate in the detector plane

$P$  = transmitted power

$T$  = transmission factor

$$= T_o \cdot T_{ST}$$

$T_o$  = transmission factor due to losses other than turbulence (e.g. optics, atmospheric absorption and scattering)

$$\begin{aligned}
T_{ST} &= \text{transmission factor due to short-time turbulence-induced power loss} \\
&\quad (\text{e.g. wide angle scatter}) \\
\vec{\Delta} &= \text{pointing error} \\
\omega_{so}^2 &= (\text{short time averaged beam radius})^2 \\
&= \beta^2 \omega_D^2 + \omega_{ST}^2 \\
\beta &= \text{beam quality} \\
\omega_{ST} &= \text{short-time turbulence-induced beam spread} \\
\omega_D &= \text{diffraction-induced beam radius} \\
&\approx \lambda R/D \\
F &= \text{focal range}
\end{aligned}
\tag{II-2}$$

The power received by a detector of radius,  $a$ , is

$$\begin{aligned}
P(a) &= \int^a d^2\vec{r} \, I(\vec{r}) \\
&= P T Q(a/\omega_{so}, \Delta/\omega_{so})
\end{aligned}
\tag{II-3}$$

where

$$\begin{aligned}
a &= \text{detector radius} \\
Q(x,y) &= \int_0^{x^2} \exp(-z^2 - y^2) I_0(2yz) dz \\
I_0 &= \text{the modified Bessel function}
\end{aligned}
\tag{II-4}$$

In strong turbulence, the beam is broken up into hot and cold spots of characteristic radius,  $b$ , where

$$b \approx [\lambda R]^{1/2} \times (1 + 2.34 \sigma_I^{(R)})^{-6/5}$$

and  $\sigma_I^{(R)}$  is the Rytov approximation to the log intensity variance. For large  $b$  ( $b > \omega_{so}$ ), beam breakup is not important, and equation (II-3) should be used without additional  $b$ -dependence. For small  $b$  ( $b < \omega_{so}$ ), the effect of beam breakup can be included by use of a modified power in the bucket equation

$$P(a,b) = P T(a,b,\omega_{so}) Q(a/\omega_{so}, \Delta/\omega_{so}) \quad (II-5)$$

where

$$T(a,b,\omega_{so}) = T_o T_{ST}'(a,b,\omega_{so}) \quad (II-6)$$

The following arguments are developed to be used to specify the modified short time turbulence loss factor  $T_{ST}'(a,b,\omega_{so})$ .

In the near field, for  $b \gg \omega_{so}$ ,

$$\begin{aligned} \text{Fresnel Number} &\approx D^2/(\lambda R) \\ &\approx (\lambda R)/(\lambda R/D)^2 \\ &\approx b^2/\omega_{so}^2 \\ &\gg 1. \end{aligned}$$

For  $b \gg \omega_{so}$ , we are either in the near field of the transmitter or turbulence is weak. Thus, in this case we expect to have normal scintillation loss, modified only by aperture averaging, i.e.,

$$T_{ST}'(a,b,\omega_{so}) = T_{ST}(a,b) \quad (II-7)$$

where

$$T_{ST}(a,b) = \exp[ -(\sigma_t^{(ex)}/2)^2 / (1 + 4a^2/b^2) ] \quad (II-8)$$

and  $\sigma_t^{(ex)}$  is the experimental value for the log intensity variance.

For  $b < \omega_{so}$ , significant diffraction and/or beam breakup is expected, so the initial spot will be fractured into small spots. It is assumed that the irradiance is given by the profile unaffected by turbulence out to the first null (at radius  $\approx b$ ), after which the irradiance is partially scattered out of the main beam. This is approximated by assuming that the effective transmission varies as a function of beam size and averaging radius as

$$T_{ST}'(a,b,\omega_{so}) = T_{ST}(a,b) U(a,b,\omega_{so},f) \quad (II-9)$$

where U is defined to give continuity and it is represented by a simple linear fit:

$$U(a,b,\omega,f) = \begin{cases} 1 & a \leq b \leq \omega \\ (2b - a + f[a - b])/b & b \leq a \leq 2b, \omega \\ (2b - a + f[a - \omega])/(2b - \omega) & 2b \leq a \leq \omega \\ 1 & \omega \leq a \end{cases} \quad (II-10)$$

and

$f$  = scintillation fill factor

to approximate the scintillation effects. To provide continuity to the  $b <$  case, we further assume

$$f = \begin{cases} 1 & \omega \leq b \\ (2b - \omega + f_o [\omega - b])/b & b \leq \omega \leq 2b \\ f_o & 2b \leq \omega \end{cases} \quad (II-11)$$

and take

$$f_o = 0.5 \quad (II-12)$$

to model the badly broken-up beam as having a 50% "fill factor".

Equations (II-5), (II-6), (II-8), (II-9), (II-10), (II-11), and (II-12) complete the specification of our model for the scintillation-degraded power on a detector during a single pulse.

The following formulas are also used

$$\Delta^2 = 2\theta^2 R^2 \text{ for 1-sigma pointing error.}$$

$$\sigma_x^2 = 0.56 k^{7/6} \int_0^R C_n^2 r^{5/6} (1 - r/F)^{5/6} dr, \text{ with saturation as in equation (A-13) in appendix B, and aperture averaging}$$

$$b = d, \text{ to specify the aperture averaging parameter}$$

$$d = \{ \lambda R / [1 + 2.34 \sigma_t^{(R)12/5}] \}^{1/2}$$

$$\omega_{ST}^2 = 2R^2/(k^2 \rho_o^2) - 2\theta^2 R^2$$

where

$$\theta = 1.45/(kD^{1/6}\rho_0^{5/6})$$

and is the 1- $\sigma$  per axis contribution to  $r_o$ , and to jitter at the transmitter. This is root sum squared with system jitter, to produce the "average" tilt angle for inclusion in the formalism of the previous section. (Use of 3 times that angle is a more conservative approach to evaluate worst case "3- $\sigma$ " pointing-error-per-bit.)

$$\sigma_x^2 = \sigma_i^2/4$$

and is the log amplitude fluctuation variance which relates the experimental variance to the Rytov value.

### 3. SYSTEM DESCRIPTION

The use of phase conjugation in an asymmetric link reduces the complexity of the transponder, permitting it to use less power, and to have a less complicated pointing system. It does not help the transceiver, and in fact can demand a more powerful transmitter on the transceiver platform if there is no gain at the transponder.

A concept for a four wave mixing phase conjugated communication link is described in this section. Table II-4 tabulates the system functions for a 1-way system and table II-5 for a PC system. The PC payoff is evident in the elimination of the transponder scanner and mechanical slewing/pointing requirement.

Figure II-8a shows a typical block diagram for a standard 1-way air-to-air comm link. It includes a communication subsystem, pointing/tracking subsystem and possibly a separate acquisition subsystem. All of the optical elements in these subsystems must be aligned and simultaneously pointed to the opposite terminal (with point ahead compensation, as appropriate). Multiplexing and aperture sharing may allow shared use of a single telescope by the transmit, receive and tracking functions, although > 100 dB isolation is typically required between transmit and receive paths.

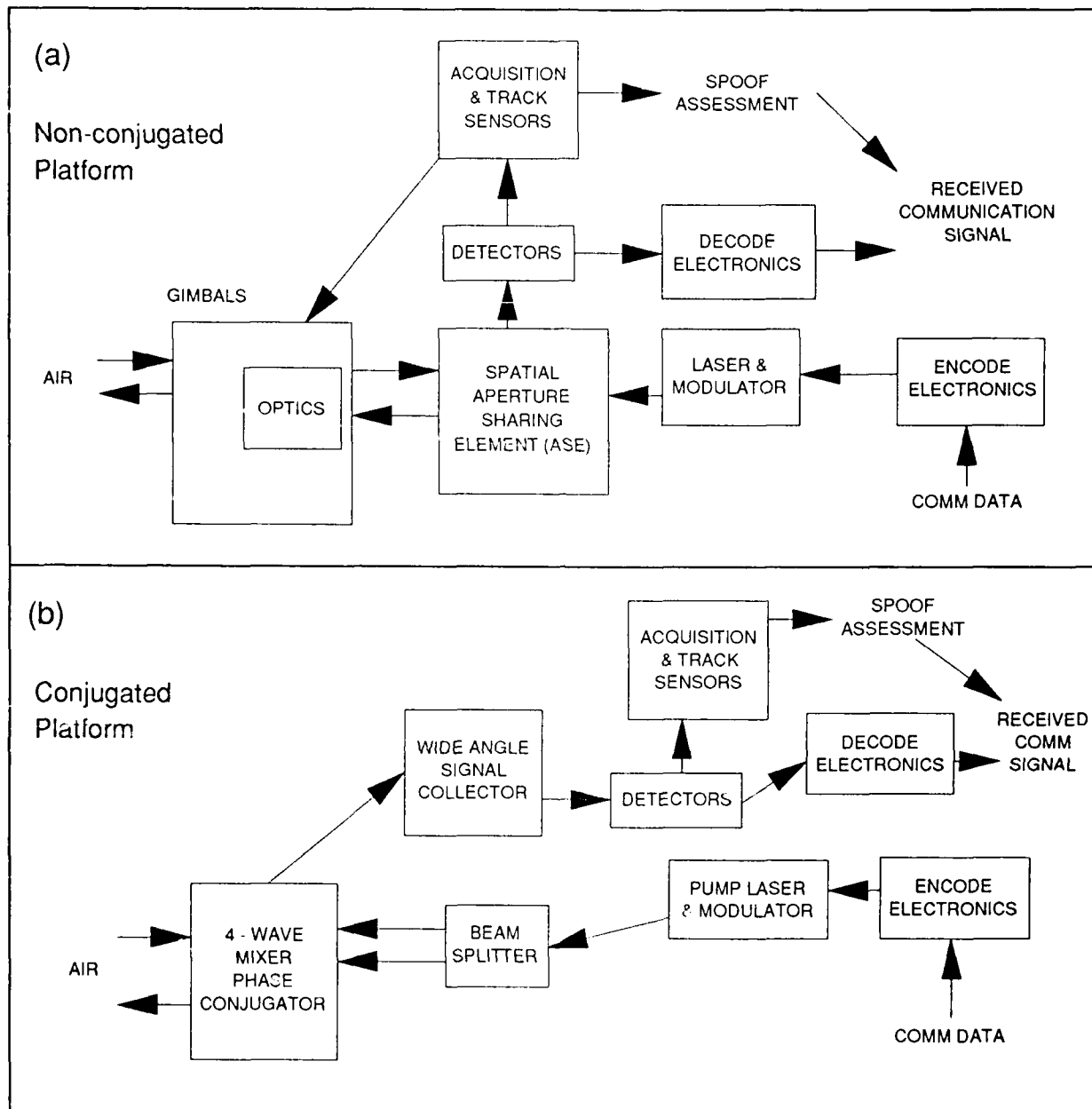


Figure II-8. Block diagram for (a) conventional one-way communication link or FWM PC comm link transceiver platform (CAC), and (b) FWM PC communication link transponder platform (RPV).



Table II-4. Conventional Air-to-Air Optical Communication System Functions.

Function	Description
TR Radar Acquisition:	A radar on the transceiver (TR) platform finds the potential transponder (TP). A radar uncertainty angle results.
TR Radar/Optics Handover:	TR radar hands over to a wide field of view (WFOV) optical sensor, narrowing down the uncertainty angle.
TP Acquisition:	
TR Laser On:	TR laser beacon sends out probe pulses to TP, hoping for the TP WFOV sensor to receive and acknowledge. This is a very slow process since the TP will probably have been silent to maintain covertness and won't know in what direction to point for the TR beacon.
TP Scan:	The TP requires a scanning mechanism to scan over its large uncertainty volume to find the TR beacon. The TP scan is over a very large fraction of $4\pi$ sr. The TR needs a large energy source to operate throughout the acquisition scan timeline.
TP Track:	On detection, the TP requires a quad cell or other sensor to measure the incoming beam angle of arrival.
TP Slew/Point:	The TP slews and points its receiver and transmitter toward the incoming signal.
TP Handover to NFOV:	The TP hands over the track signal to a narrow field of view (NFOV) sensor.
TP NFOV Track/Slew:	The TP NFOV sensor accepts handover, acquires, and tracks the incoming beacon signal.
TP Confirms:	The TP turns on its laser aimed at the TR to provide a beacon for the TR to acquire.
TR Acquisition:	
TR Scan:	The TR scans its WFOV sensor to increase its signal from the TP beam.
TR Track:	The TR uses a WFOV tracker to determine the angle of arrival (i.e. the proper pointing direction).
TR Slew/Point:	The TR slews and points to the refined incoming signal direction.
TR Handover to NFOV:	The TR hands over its track signal to its NFOV sensor.
TR NFOV Track/Slew:	The TR NFOV sensor accepts handover, acquires, and tracks the incoming TP confirmation signal.
TR Confirms:	TR sends confirmation to indicate that it has acquired the TP signal.
TP Confirms, Communication:	The TP sends a confirmation handshake and begins transmission.

\* TR = Transceiver, TP = Transponder.

Table II-5. FWM Phase Conjugated Air-to-Air Communication Link Functions.

Function	PC Link Implementation with Wide FOV Conjugator
TR Radar Acquisition:	No change.
TR Radar/Optics Handover:	No change.
TP Acquisition:	
TR Laser On:	No change. Might need more power than one-way link for two-way range loss compensation.
TP Scan:	WFOV PC catches wings of beam and returns confirmation signal automatically, independent of pointing direction. No scanner.
TP Track:	Automatic -- not required for communication, but needed for spoof detection.
TP Slew/Point:	Automatic -- gimbals and tilt mirror not required.
TP Handover to NFOV:	NFOV sensor not required for communication, but may need for spoof detection.
TP NFOV Track/Slew:	NFOV sensor not required for communication, but may need for spoof detection.
TP Confirms:	Automatic with FWM PC. Potential major reduction in required TP power. Any TP optics could be of moderate quality (potentially low observable), since TP optics aberrations are phase conjugated.
TR Acquisition:	
TR Scan:	Aperture Sharing Element (ASE) is required since outgoing beacon and incoming conjugated signal follow the same optical path.
TR Track:	Tracker will not work on PC signal since arrival angle equals the emission angle. If the PC is not saturated, tracking of the PC signal amplitude could be achieved by dithering the TR beam direction.
TR Slew/Point:	Tracker will not work on PC signal since arrival angle equals the emission angle. If the PC is not saturated, tracking of the PC signal amplitude could be achieved by dithering the TR beam direction.
TR Handover to NFOV:	Tracker will not work on PC signal since arrival angle equals the emission angle. If the PC is not saturated, tracking of the PC signal amplitude could be achieved by dithering the TR beam direction.
TR NFOV Track/Slew:	TR fine tracker and tilt mirror/scanner are not required. Tracker will not work on PC signal since arrival angle equals the emission angle. If the PC is not saturated, tracking of the PC signal amplitude could be achieved by dithering the TR beam direction.
TR Confirms:	No change.
TP Confirms, Communication:	Major power savings, especially when atmospheric transmission losses are low.

\* TR = Transceiver, TP = Transponder.

The FWM phase conjugated communication link consists of a steerable narrowband transmitter (NBT) on the CAC and a phase conjugator on the RPV. The NBT acts as the probe beacon for the phase conjugator, and is pointed or steered either mechanically, or using an electro-optical (EO) or acousto-optical (AO) mechanism, or (for a coherent diode array) by adjusting the relative phase of the array elements to meet the coarse pointing and tracking requirements. The wideband transmitter (WBT) is the phase conjugated return beam from the RPV. The phase conjugated WBT eliminates the need for a fine track subsystem on the RPV. Conceptual block diagrams of the CAC and the RPV communication systems are shown in figures II-8a and II-8b. The NBT and the wideband receiver (WBR) on the CAC use separate apertures to avoid demultiplexing the send and receive signals and to eliminate self-jamming due to atmospheric backscatter. (The simplest concept uses a single transmitter at a single wavelength, so wavelength division demultiplexing is not an option.) The frequency shifts of the return signal from the phase conjugator require a heterodyne discriminator to detect and separate the incoming and outgoing beams. Polarization demultiplexing is not a reliable technique because the atmosphere (clouds, etc.) may alter the polarization. The laser diode array directly transmits a diffraction limited beam with no intervening optics. The beamwidth is a function of the laser array dimensions (which are driven by the laser power). This beamwidth dependence complicates the system design because the beamwidth is normally independent of laser power.

The WBR collects the phase conjugate return beam with a telescope. The location (relative to the NBT) of the receiver telescope must be traded against the aircraft speed/direction and the additional pointing error (which arises because the phase conjugator returns the beam to where the transmitter was when the beacon was turned on, ignoring the CAC motion during the round trip transit time). The quadrant communication detector outputs from the four detectors sum to provide the communication signal, while sum and difference signals provide the error signals for the tracking system, which are used to steer the laser diode into the field of view (FOV) of the phase conjugator. (The coarse pointing could be provided by other technologies such as liquid crystals or AO beam deflectors.) Multiple terminals can also be used to cover

a wide (e.g.  $180^\circ$ ) field of regard. Conventional circuitry could be used in the electronic subsystems for the communication electronics and digital processing.

Figure II-8b is a block diagram for the phase conjugate drone. The NBT beam is collected by the telescope and focused into a phase conjugator. The NBT is four wave mixed in the gain medium and phase conjugated affording appreciable gain. Important phase conjugator trades that are necessary include

- Amplifier size vs. phase conjugate gain
- Phase conjugate gain vs. fidelity

The transmitted, amplified probe beam, which contains the housekeeping data, is picked off by the RPV's communication detector, the same type as used in the CAC. It could provide communication and track signals to a coarse pointing mechanism.

High frequency host disturbances (e.g. platform jitter) are compensated by the phase conjugator. The phase conjugate efficiency vs. incident angle trade still must be performed. This will ultimately determine the useful FOV of the phase conjugator. Coarse tracking and pointing is also required (resolution  $\pm 50^\circ$ , range  $360^\circ$ ) to point the NBT toward the drone. Fish eye lens, multiple receivers, AO beam steering and liquid crystals are good candidates.

#### 4. SYSTEM PERFORMANCE

Atmospheric transmission and background (sky, no sun) radiance are shown in figures II-9 and II-10, respectively, as a function of wavelength for three ranges: 10, 50, and 100 km. Transmittance drops with range, while radiance increases with range.

The performance of the system may be quantified with the link budget model. This model incorporates each of the elements discussed previously in this chapter including gaussian beam propagation and turbulence as discussed in sections II.2.a and II.2.c. Figure II-11 shows the output from a typical power budget. This link budget includes transmitter, transponder, receiver, and channel factors. Model inputs consist of the transmitter parameters including wavelength, diameter, beam quality, pointing error, and power. The description of the atmosphere is input as part of the channel parameters.

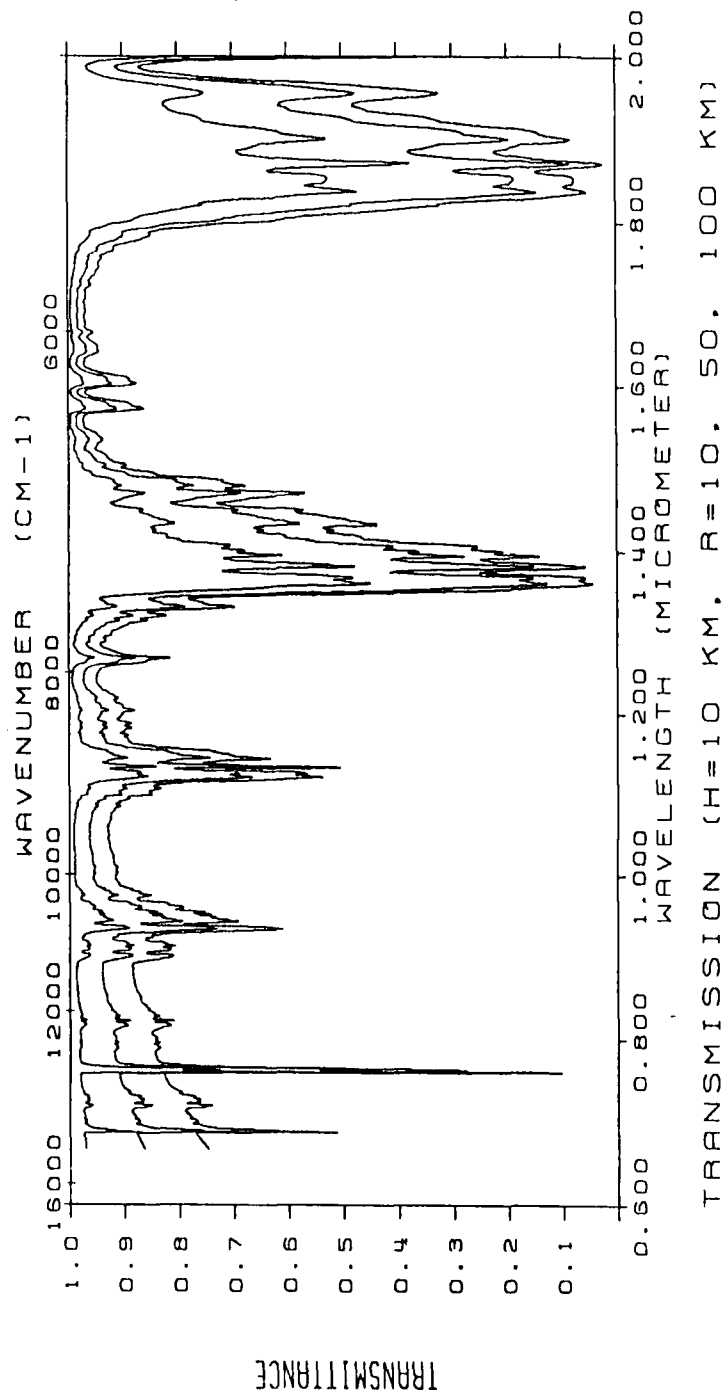


Figure II-9. Spectral dependence of atmospheric transmission over 10, 50, and 100 km ranges.

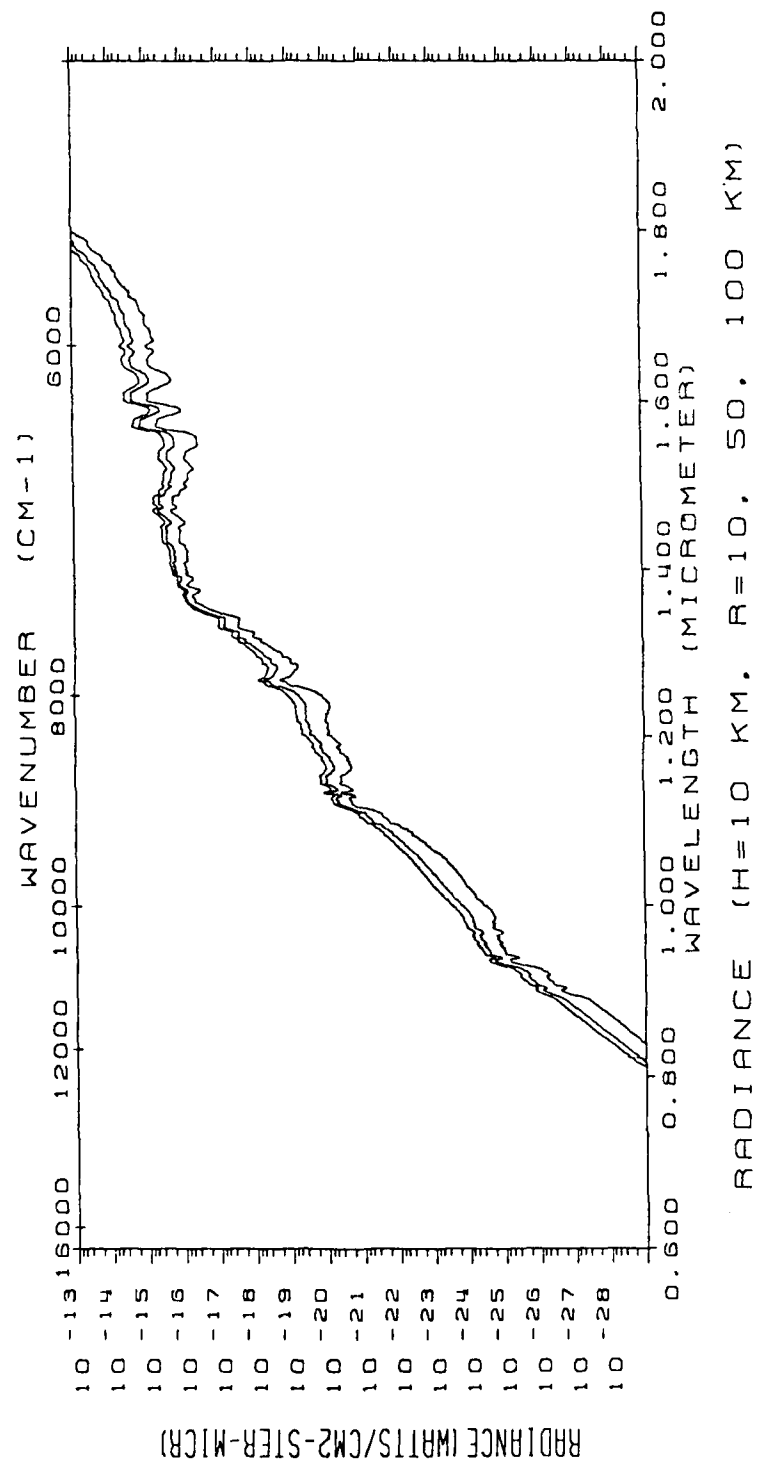


Figure II-10. Spectral dependence of atmospheric background (sky, no sun) measured through 10, 50, and 100 km optical paths.

TRANSMITTER PARAMETERS			CHANNEL PARAMETERS		
Wavelength	0.87	um	Range	100.00	km
Diameter	1.00	cm	Range Loss		-243.24 dB
Obscuration	0.00	cm	Atmospheric Extinction Loss		-1.11 dB
Beam Quality (Spread)	1.00		Cn <sup>2</sup> (atmosphere)	0.774	m <sup>-2/3</sup>
Beam Quality Loss (Fill)			Cn <sup>2</sup> x Boundary Layer	1.000E-12	m <sup>1/3</sup>
Truncation Ratio	0.70		Fried coherence diam (1-way)	3.492E-02	m
Aperture Gain	1.12		Scintillation sig <sup>2</sup> (1-way)	1.070E+01	
1/e <sup>2</sup> beamwidth	86.50	urad	Scintillation sig <sup>2</sup> (2-way)	3.218E+01	
Range / Focal Range	1.0000		Turbulence Higher Order Loss	1.000	
Pointing Error - input	100.00	urad	Fade Loss		0.00 dB
Pointing Error - turb	18.43	urad	Scint TR-TP (AP AVE) sig <sup>2</sup>	6.026E-01	-0.65 dB
Pointing Error - total	101.68	urad	Scint loss TR-TP	8.601E-01	
Wavefront Error	0.00	Np	Scint TP-REC (AP AVE) sig <sup>2</sup>	3.910E-03	
Optical Transmission	0.75		Scint loss TP-REC	9.990E-01	0.00 dB
Average Power during bit	5.000E-01	W	Beam breakup loss TR-TP	1.000E+00	0.00 dB
Peak Power during bit	1.000E+00	W	Beam breakup loss TP-REC	5.097E-01	-2.93 dB
Long term average power	5.000E-01	W			
Pulse duration	8.333E-09	sec			
RECEIVER PARAMETERS			SIGNAL PARAMETERS		
Diameter	1.00	cm	Data Rate	60.000	Mbps
Range / Focal Range	0.0000		Extinction Ratio	0.10	
Beam size into TP	5.507E+00	m			
Beam size out of TP	5.000E-03	m			
Beam size out of TP -RET	5.507E+00	m			
Beam offset at TP	3.389E-01	m			
Breakeven PC Gain=SS1/SS2	8.244E-07				
G0	1.213E+06				
G1	5.612E-06				
SS1 (1-WAY)	7.358E-04				
SS2 (2-WAY)	6.066E-10				
Transponder Power Reduction					
PC gain calc overkill					
PC + 2-way path loss factor					
Power out of transponder	8.271E-08	W			
RECEIVER PARAMETERS			RECEIVER NOISE POWER PARAMETERS		
Diameter	30.00	cm	Avalanche Gain	150.00	
Obscuration	0.00	cm	Ionization Constant Ratio	0.007	
Aperture Gain			Excess Noise Factor	3.03	
Tracking Error			Responsivity	94.06	Amp/W
Wavefront Error	0.00	Np	Background Solar Power	0.00E-01	W
Optical Transmission	0.89		Other Background Power	1.50E-12	W
Beam size into REC	5.507E+00	m	Error Function Argument (a)	5.20500	
Beam size out of REC	1.499E-01	m	Bit Error Rate	1.00E-07	K
Beam offset at REC	-6.246E-15	m	Noise Temperature	100.00	K
			Pulse Shape Factor (I2)	0.592	
			Equivalent Resistance	1.00E+09	Ohm
			Amplifier Noise Power	1.961E-22	Amp <sup>2</sup>
			Pulse Factor (I1)	0.588	
			Detector and Amplifier Noise	1.090E-10	
RECEIVER PARAMETERS			POWER REQUIREMENTS		
Diameter	30.00	cm	Quantum Efficiency	0.90	-0.46 dB
Obscuration	0.00	cm	Bit Synchronizer Loss		-1.00 dB
Aperture Gain			Intersymbol Loss		-1.00 dB
Tracking Error	0.00	Np	Received Power (on detector)	2.733E-11	W
Wavefront Error	0.89		Required Power (on detector)	1.989E-09	W
Optical Transmission	0.89		Link Margin		-105.63 dBW
Beam size into REC	5.507E+00	m	TR power needed to close link	7.217E+01	W
Beam size out of REC	1.499E-01	m	TP power needed to close link	6.019E-06	W
Beam offset at REC	-6.246E-15	m			-18.62 dB

Figure II-11. Typical Link Budget.

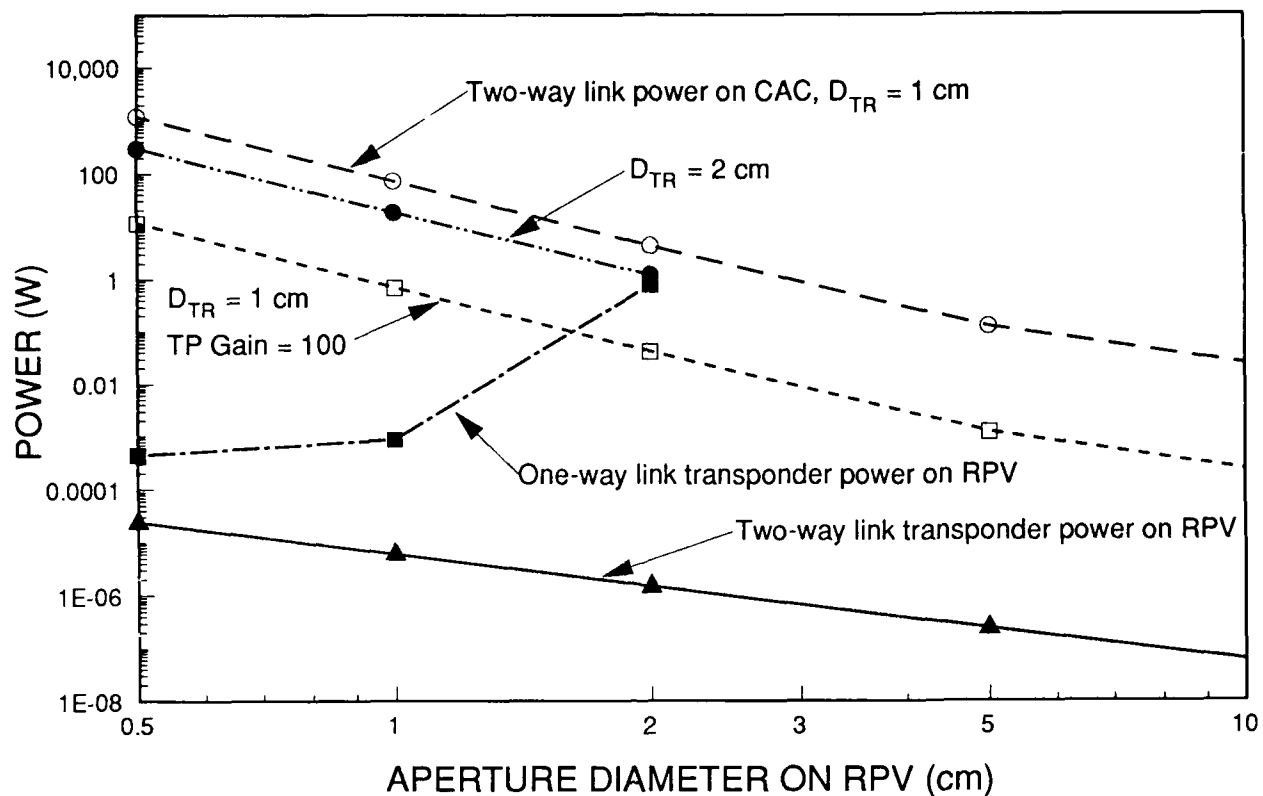


Figure II-12. Required transponder power plotted versus transponder aperture diameter on RPV. All other conditions are listed in figure II-11.

In addition, several important comm parameters are input, such as data rate, and detector quantum efficiency.

The budget items in figure II-11 shown in dB may be summed to verify the allocation. Items with units of dBxx are presented for information only, and are not part of the budget.

Figure II-12 shows key results from our link budget model. The curves show how much power is needed out of the RPV-based transponder and the CAC-based transmitter in order to close a link. An important result is that the conventional RPV-based 1-way link requires significantly more power on the RPV than in the PC-link.

For example, for 1 cm diameter transceiver and transponder apertures,  $D_{TR} = D_{TP} = 1$  cm, using a peak power from the transmitter of 73 W (long dashed line in figure II-12), the required 6  $\mu$ Watt (solid line) is generated by the transponder without



demanding any gain from the transponder (except to bring the reflectivity up to unity). Significantly, a 1-way link would have required nearly 1 mW from the transponder source (dot-dashed line), a factor of 167 more power. Alternatively, if the PC produces a gain of 100, e.g. the PC can transmit 1 mW of phase conjugated power, then the CAC transmitter power can be reduced by a factor of 100. For the case above, the CAC power is reduced from 73 W to 0.73 W (short dashed line). The simple formulation of beam break-up employed in the model breaks down when the speckle size approaches the aperture diameter. A more detailed model of beam break-up must be developed to address the effects of larger apertures on comm link performance.

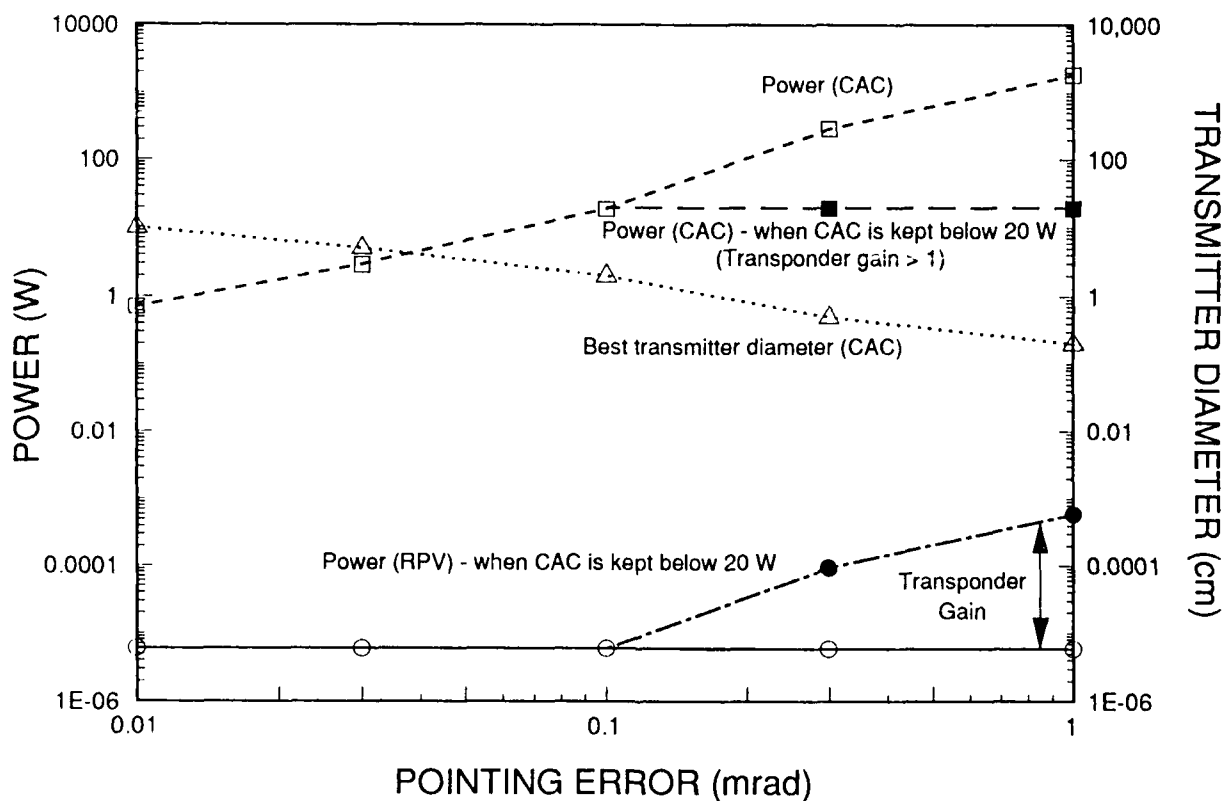


Figure II-13. Performance benefit from phase conjugation versus transceiver pointing error.  $D_{TP} = 1$  cm. All other conditions are listed in figure II-11.

An important result of this study shows that FWM phase conjugation can reduce the required CAC power for even large pointing errors. Figure II-13 shows the required

CAC and RPV power as a function of CAC pointing error for a 100 km link. The dotted line represents the CAC aperture diameter that minimizes the required power for a given pointing error. Given these apertures, the required CAC power is plotted (dashed line) as a function of pointing error. With pointing errors of 10 to 100  $\mu\text{rad}$ , a transponder gain of 1 achieves the required 6  $\mu\text{W}$  RPV transponder power (solid line) while increasing the CAC power from 0.7 to 19 W. However, if the transponder gain is kept at unity for pointing errors greater than 100  $\mu\text{rad}$ , the required CAC power can become large (dashed line). Increasing the phase conjugate gain of the transponder permits the CAC power to be reduced dramatically. When the CAC power is held below 20 W (long dashed line), the transponder gain need only be increased over a range of 1 to 100 (dot-dashed line) to provide the necessary transponder power for large pointing errors of 0.1 to 1 mrad. Thus, the stress of power production can be placed on the larger CAC platform, or balanced between the CAC and the RPV.

### III. PHASE CONJUGATED OPTICAL COMM LINK EXPERIMENTS

The following sections describe the implementation of four wave mixing in sodium vapor and the experimental apparatus necessary to operate a phase conjugated communication link over a 1 km range as well as a laboratory link through artificially generated turbulence. The experimental design for the 1 km link experiments is presented in section III.1 and the design of the artificial turbulence generator (turbox) is presented in section III.2. The diagnostics employed to measure both the turbulence and link performance are discussed in sections III.3 and III.4, respectively. In section III.5 we present the results of experiments over the 1.1 km atmospheric range, including amplitude modulation and intensity variance measurements. Section III.6 details turbox calibration and performance and presents the results of comm link experiments propagated through the artificially generated turbulence.

#### 1. EXPERIMENTAL APPARATUS

A phase conjugated communication link has two stations, a transceiving station and a transponding station. A laser is required at the transceiver to provide a beacon beam. At the transponder station, a second laser is required to provide the pump beams for phase conjugation. For simplicity, the range was folded allowing use of a single laser for the NLOT comm link experiments. This permitted all optical equipment to be set up in one laboratory, thereby reducing the required manpower and experimental complexity.

The folded PC comm link is outlined in figure III-1. A fraction of the output from a single ring dye laser ( $< 100$  mW) was split off and launched from a platform in the rooftop laboratory approximately 15 m above the ground on top of TRW building R1 toward a large mirror on top of TRW building R8 approximately 0.55 km away (measured from building site plans -- see figure I-3). The folding mirror is large enough so that the beacon beam, once aligned, never missed the mirror and was reflected back to a second platform adjacent to the first in the rooftop laboratory. The received beam was focused into the Na cell in the four wave mixing setup. The remaining laser output that was not

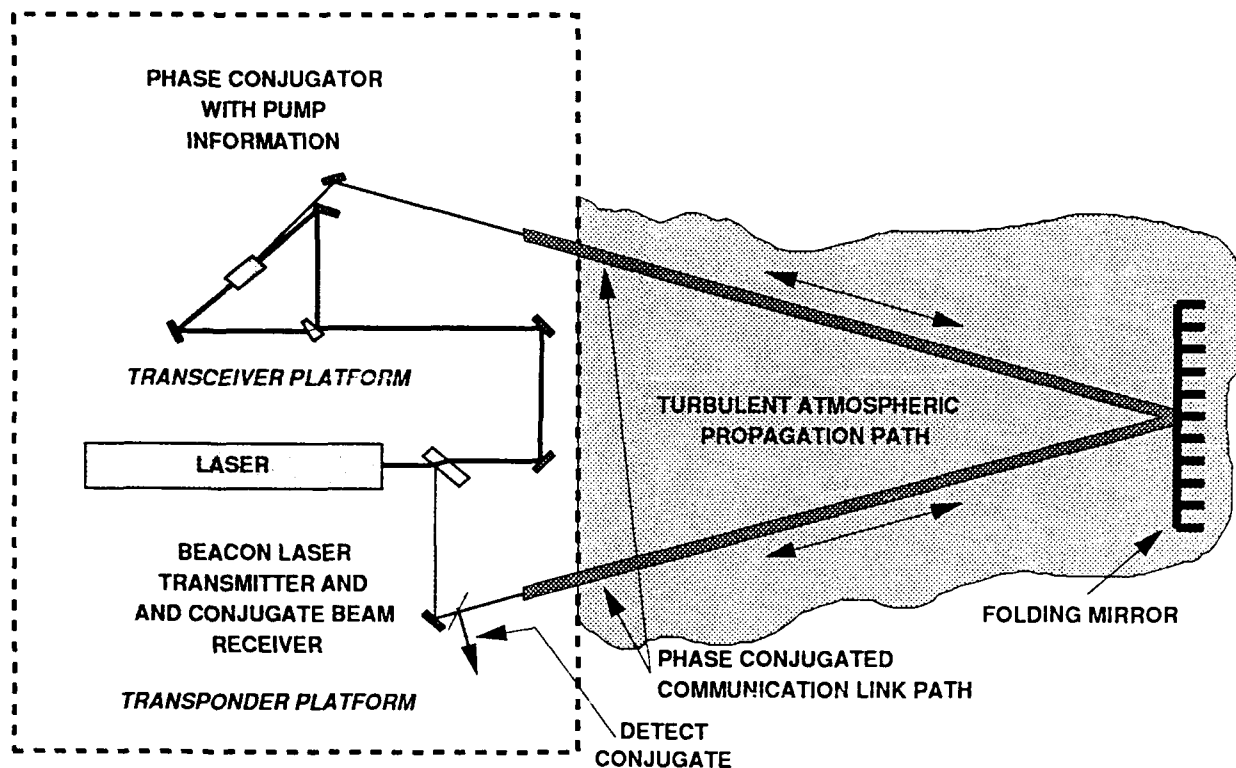


Figure III-1. Illustration of folded FWM PC comm link. A small fraction of the  $<10$  cm diameter laser output is transmitted to a 50 cm diameter mirror 0.56 km away and reflected back to a second platform. The remaining laser light serves as the FWM pump beams to phase conjugate the received beacon beam. The PC beam retraces the beacon beam path and is sampled on the transceiver table.

launched in the beacon beam was split into two beams of equal intensity and directed into the Na cell to provide counterpropagating pump beams for four wave mixing. The phase conjugated beacon beam followed the launch path back to the folding mirror and transceiver platform where a beam splitter permitted analysis of the conjugated signal. A detailed diagram of the experimental apparatus is presented in figures III-2 and III-3. The experimental apparatus consists of the lasers, four wave mixing medium, optics, and turbox. These are each described in the following subsections.

a. Lasers -- The output from a single laser system provided both the pump beams and the beacon beam for the PC comm link, discussed below. This laser system consisted of a Coherent 699-21 ring dye laser pumped by a Coherent 20 W  $\text{Ar}^+$  laser. 400 - 850 mW of single frequency light ( $\Delta\nu < 1$  MHz) was generated at the  $\text{Na D}_2$

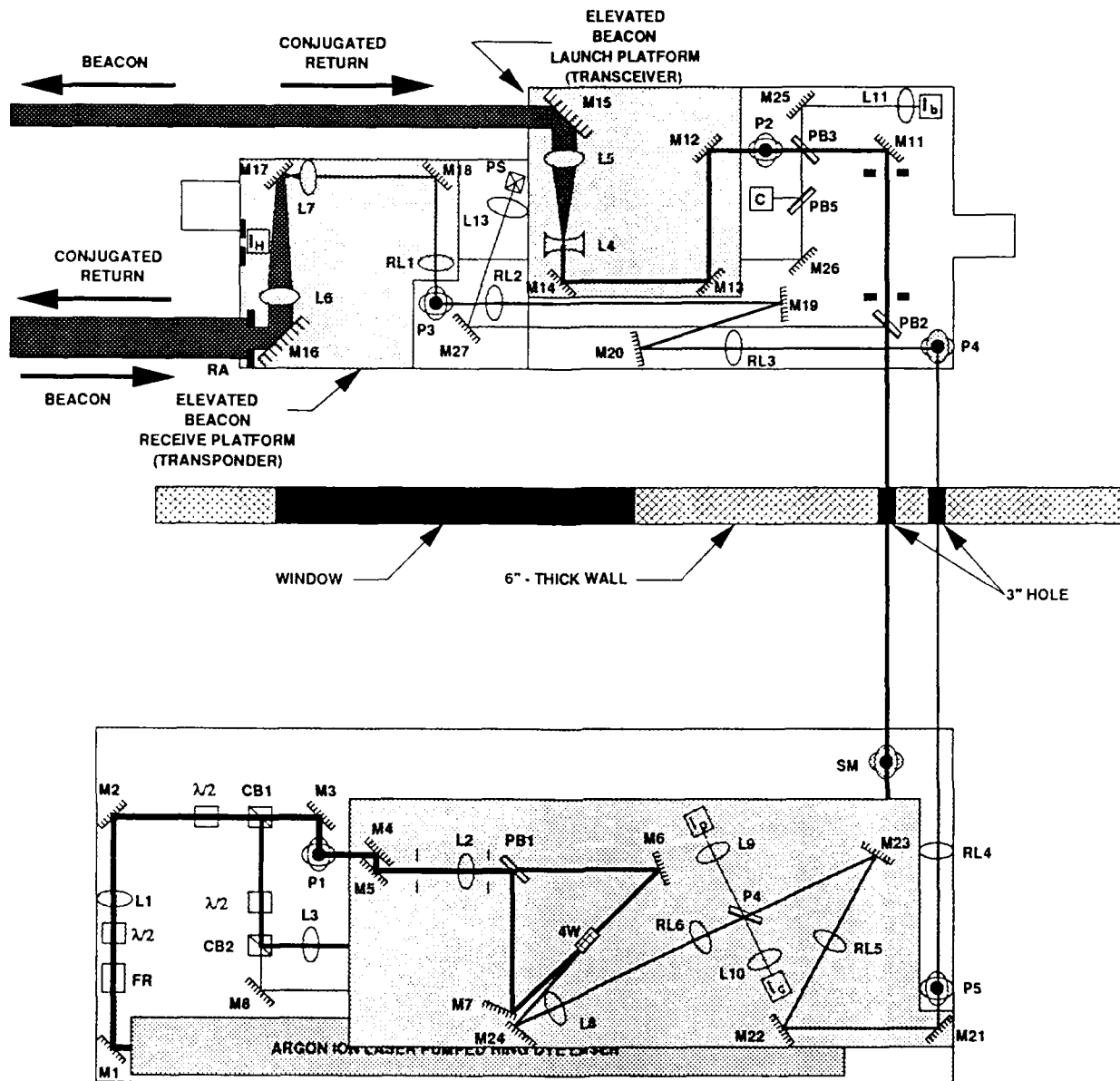


Figure III-2. Optical layout for 1 km comm link experiments. FR = Faraday rotator;  $\lambda/2$  = 1/2-wave plate; L = lens; RL = relay lens; M = mirror; CB = cube beamsplitter; PB = plate beamsplitter; P = periscope; I = 1 cm photodiode; PS = position sensing photodiode; RA = transponder aperture; c = camera; SM = steering mirrors; 4W = sodium vapor/four wave mixing cell.

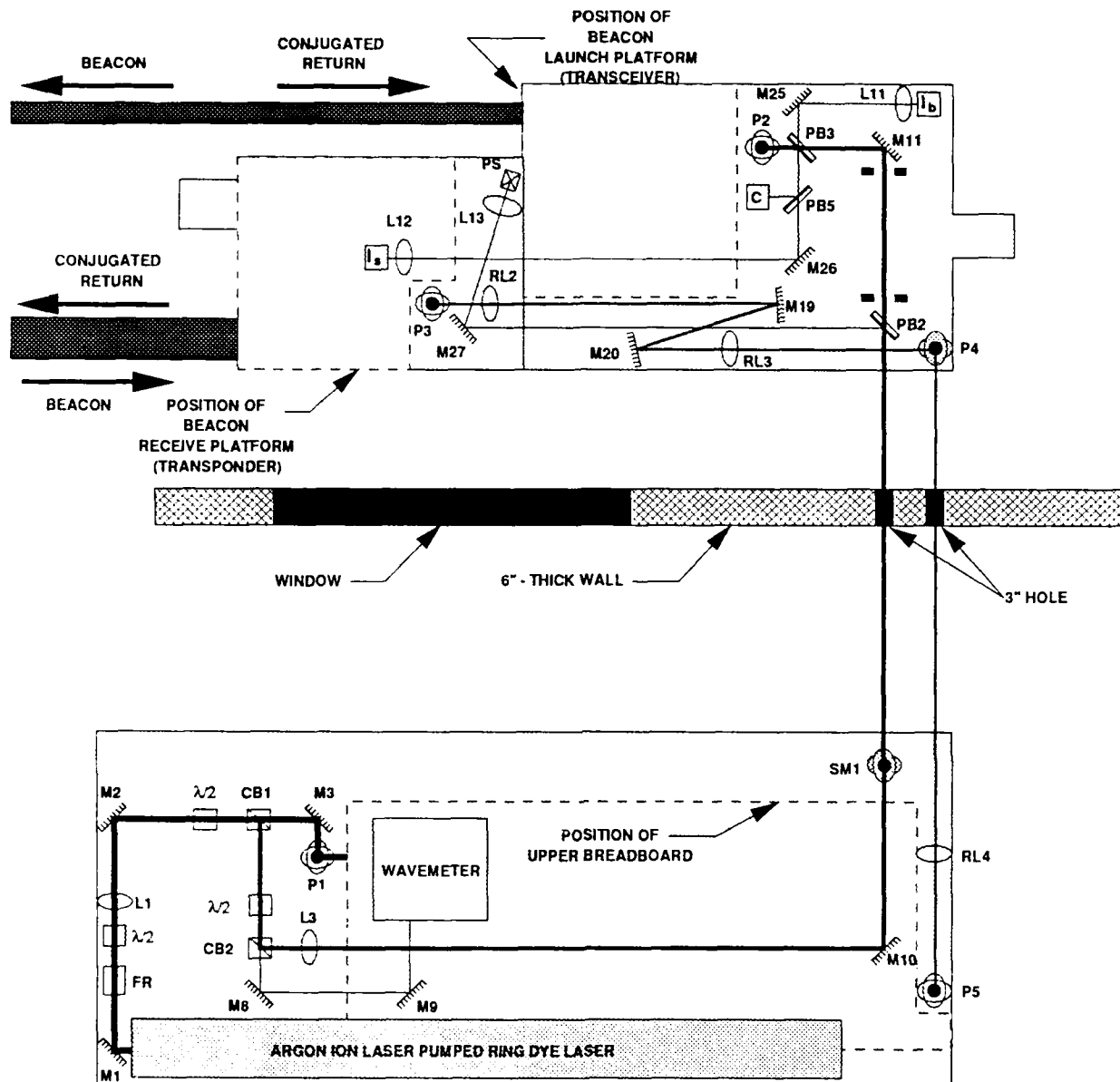


Figure III-3. Optical layout for 1 km comm link experiments. FR = Faraday rotator;  $\lambda/2$  = 1/2-wave plate; L = lens; RL = relay lens; M = mirror; CB = cube beamsplitter; PB = plate beamsplitter; P = periscope; I = 1 cm photodiode; PS = position sensing photodiode; RA = transponder aperture; c = camera; SM = steering mirrors; 4W = sodium vapor/four wave mixing cell.

wavelength (589.16 nm). The s-polarized output of the laser was rotated to p-polarized light by a Faraday rotator and a  $\lambda/2$  plate set at  $45^\circ$ . This prevented optical feedback from reaching the laser cavity and ensured laser frequency stability. The laser wavelength was typically tuned to the short wavelength side of the sodium  $D_2$  line,  $\lambda = 589.159$  nm and was monitored with a Burleigh wavemeter. However, experiments were also performed at the long wavelength side.

b. Four Wave Mixing Cell -- Phase conjugation of the optical beam was performed by four wave mixing in sodium vapor. The sodium cells used were 2.5 cm diameter x 0.5 - 2.0 cm thick and made of Pyrex. Each cell was thoroughly cleaned with acid washes, rinsed, dried, and baked on a high vacuum manifold ( $P < 10^{-6}$  torr). The clean cells were then filled with 760 torr of argon, sealed with a stainless steel valve, and transferred to a glove box purged with argon where 99.9% pure (total contaminants) sodium metal packaged under argon, was transferred to each cell. The valved cells were transferred back to the vacuum system, the argon gas pumped off, and the Pyrex side arm sealed with a torch. Cells prepared in this manner exhibited lifetimes of more than six months with temperature cycling from room temperature to the 480 - 500 K operating temperature daily over that period of time. Failure of the cell occurred when the 1 cm central aperture of the cell darkened and prevented phase conjugation.

The Na cell was heated in an oven consisting of a 10 cm long copper tube wrapped with Nicrome heater tapes and insulation. A thermocouple attached to the cell wall was used to monitor the cell temperature which was held at the set point  $\pm 1^\circ$  C.

c. Optical Layout -- Two sets of optical tables were employed in the rooftop laboratory. The first set of tables were assembled in a "bunk bed" arrangement, providing a surface for the laser and four wave mixing setup. The laser, optical isolation and beam splitting apparatus, and wavelength measurement system were on the lower, main table. An 11-cm thick breadboard supported 0.62 m above the optical table provided a larger work area for the four wave mixing setup. The second set of tables, situated directly in front of the laboratory doors, primarily served to support the transceiver and transponder platforms for the comm link. The beacon beam shown as the heavy line in figure III-3

was transmitted from the first table to the next by two scanning mirrors in a periscope configuration. Beam splitter PB2 directed some of the light received at the second table onto PS, a silicon position sensing detector. The feedback signal from PS was employed to keep the beacon beam aligned on the transceiver telescope input lens, L4 (figure III-2), and was necessary because the laser/four wave mixing table was floated on air legs while the beam handling table was not. This device will not be required in a practical system; it was required here because of the experimental design.

Beam splitter PB3 sampled the beacon beam and provided a signal for measuring the intensity and variance of the launched beacon beam at detector  $I_p$ . By selecting various combinations of lenses L4 and L5 (figure III-2) the launch beam diameter was varied over the range 1 cm to 10 cm. Collimation was achieved by inserting a 75 mm diameter shearing plate collimation tester (Continental Optical Corporation) immediately after the launch mirror, M15, and adjusting the distance between L4 and L5 until horizontal fringes were obtained. The atmospherically-aberrated beacon beam was reflected with a 50 cm diameter folding mirror 0.55 km from the launch point and directed back to the transponder platform. The received beam was reduced and collimated for easier beam steering and four wave mixing. The image of the receiving aperture, RA, which was varied from  $< 1$  to 10 cm, was relayed to the four wave mixing setup above the laser table. A high quality image of the receiving aperture was monitored on a white card at lens position, L8 to ensure that no other apertures were present in the system which might result in loss of high spatial frequencies and poor phase conjugation. Lens L8 was used to focus the beam into the center of the sodium vapor (four wave mixing) cell, 4W.

Beam splitter P4 sampled the beacon beam before it was focused into the Na cell and directed the beam through focusing lens L9 onto detector  $I_p$ . The signal on detector  $I_p$  measured incoming aberrations on the received beacon beam in the form of power loss and intensity variance. The phase conjugate beam was also sampled by P4 and detected at  $I_c$ . Comparing the signals on  $I_p$  and  $I_c$  permitted us to measure any degradation in the power or intensity variance of the phase conjugate beam due solely to the phase conjugator. In the experiments reported here the intensity variance were identical



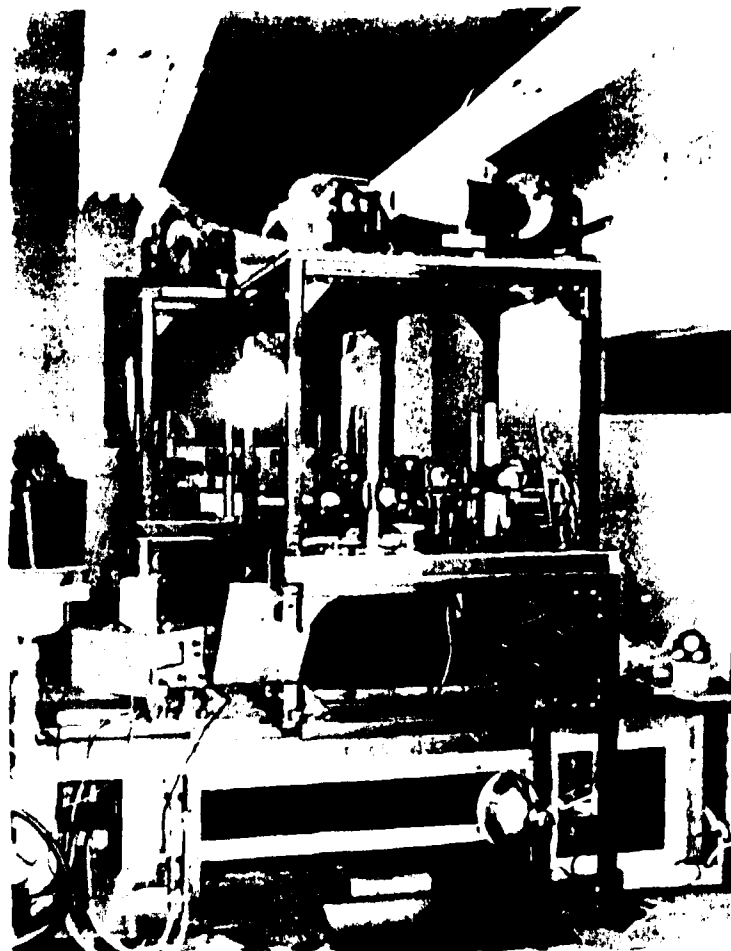


Figure III-4. Photograph of launch platforms above beam handling table. The beam steering transponder mirror can be seen on the top of the near platform next to the 10-cm input optic. The transceiver platform and similar optics can be seen behind and to the left of the transponder platform. The turbox sits on the floor supporting the launch platforms and beam handling tables.

$(\sigma_c^2 - \sigma_p^2)$ , indicating no degradation from the phase conjugator. The phase conjugate beam retraced the incoming beacon path and sampled the same turbulence as the launched beacon (time for one round trip to the folding mirror and back is  $3.7 \mu\text{s}$ ). The received conjugate beam was then sampled by PB3, visually displayed by a CCD camera with PB5, and detected with lens L12 and silicon detector  $I_s$  (figure III-3). Light detected at  $I_b$ ,  $I_c$ ,  $I_p$ , and  $I_e$  was first focused so that the total beam was swallowed by the detector and the variance of the total intensity could be determined. Figure III-4 shows a view of the transceiver and transponder platforms taken from outside the laboratory with the

doors open. However, the eight-inch diameter transceiver and transponder mirror mounts are apparent on top of their respective platforms as well as one of the ten centimeter diameter telescopes employed for the experiments. The structure supporting the tables is the frame for the artificial turbulence generator discussed in section III.1.e.

d. Amplitude Modulation Over 1 km Link -- Experiments in which amplitude information was transferred over the comm link were performed using the above apparatus with the addition of an acousto-optic modulator placed between cube beam splitter CB1 and turning mirror M3 in figure III-5. This served to deflect and misalign the pump beams sufficiently to be attenuated by the edge of the two iris diaphragms between M5 and PB1. The result was modulation of the pump intensity in the beacon/pump interaction region in the Na cell with a frequency equal to the driver frequency on the AO modulator (0 - 4 MHz). Beam splitter PBS sampled the forward pump beam and detector  $I_a$  detected the intensity with a time response of 40 kHz.

## 2. ARTIFICIAL TURBULENCE GENERATOR (TURBOX)

In order to determine the effects of uniform turbulence on the performance of an optical PC comm link, TRW designed, fabricated, and assembled with capital fabrication funds a device capable of generating turbulence equivalent to that experienced on the 1 km rooftop range. It was designed to have uniform turbulence with  $[C_n^2 L]^{3/5}$  similar to that on an air-to-air link.

To establish design requirements for turbox operating conditions, the ratio of the transverse coherence length,  $\rho_0$ , to the Fresnel length,  $(\lambda L)^{1/2}$  is an indication of the degree of irradiance scintillation at the receiver. The transverse coherence length,  $\rho_0$ , is the turbulence-induced counterpart to the Fresnel length (diffraction-induced). It is the transverse distance at which the coherence of a beam propagating over a distance,  $L$ , falls to  $1/e$  of its peak value in a plane perpendicular to the plane of propagation and is given by the expression<sup>5</sup>

$$\rho_0 = [1.45 k^2 L C_n^2]^{-3/5} \quad (\text{III-1})$$

for a plane wave and<sup>5</sup>

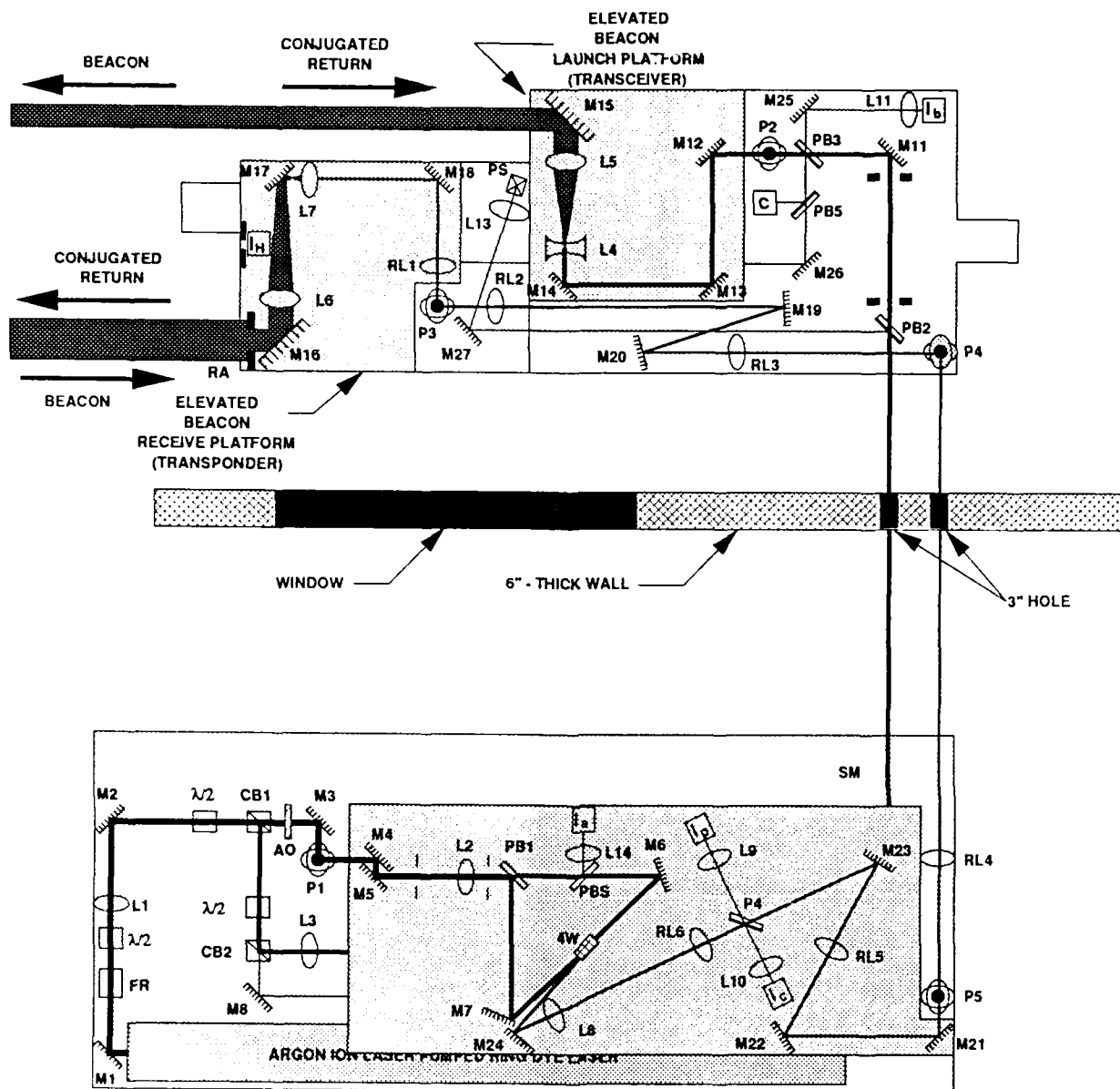


Figure III-5. Optical layout employed for transmission of amplitude information over 1 km comm link. Components are described in figure III-2. AO = acousto-optic modulator; PBS = pellicle beamsplitter. Lens L14 and detector Ia were used to monitor amplitude of forward pump leg.

$$\rho_0 = [0.544 k^2 L C_n^2]^{-3/5} \quad (\text{III-2})$$

for a spherical wave, where  $k = (2\pi)/\lambda$  is the free space wavenumber and  $L$  is the optical path length. In order to simulate either the rooftop link or an air-to-air link, the ratio,  $\rho_0/(\lambda R)^{1/2}$ , must be similar for the turbox and the link of interest.

$$\rho_0/(\lambda L)^{1/2} = [0.544 k^2 L C_n^2]^{-3/5} (\lambda L)^{-1/2} \quad (\text{III-3})$$

The wavelength,  $\lambda$ , is 589 nm. If we assume a 1 m thick turbulent boundary layer along the skin of an aircraft of  $C_n^2 = 10^{-11} \text{ m}^{-2/3}$  and turbulence of  $C_n^2 = 10^{-16} \text{ m}^{-2/3}$  over a 10 km long link, then the air-to-air link will experience (assume a planar wavefront over 10 km)

$$\begin{aligned} \rho_0/(\lambda L)^{1/2} &= [1.45 k^2]^{-3/5} \times [(2)(10^{-11}) + (10^4)(10^{-16})]^{-3/5} \times [\lambda \times 10^4]^{-1/2} \\ &= 0.10 \end{aligned}$$

On the rooftop link we typically measured the atmospheric index structure constant as  $C_n^2 = 10^{-16} - 10^{-15} \text{ m}^{-2/3}$ . There is a boundary layer over the roof at the exit and entrance to the rooftop laboratory which we assumed to be on the order of  $10^{-14} \text{ m}^{-2/3}$ . Thus, we may calculate for the rooftop link (assume mostly planer wavefront over 1 km)

$$\begin{aligned} \rho_0/(\lambda L)^{1/2} &= [1.45 k^2]^{-3/5} \times [(2)(30)(10^{-14}) + (10^3)(10^{-15})]^{-3/5} \times [\lambda \times 10^3]^{-1/2} \\ &= 1.45 \end{aligned}$$

Thus, our range of interest is  $0.10 < \rho_0/(\lambda L)^{1/2} < 1.45$ . The comm link beam may be multiple passed eleven times through the turbox (total optical path = 27 m) along a small downstream distance over which the turbulence varies less than 15%. Then in order to simulate both the rooftop and air-to-air links, the turbox must be able to generate turbulence over the range  $1.2 \times 10^{-12} < C_n^2 < 1 \times 10^{-10} \text{ m}^{-2/3}$ . TRW's capital artificial turbulence generator is capable of achieving  $C_n^2 \leq 3.3 \times 10^{-11} \text{ m}^{-2/3}$  and therefore can simulate all of the rooftop conditions, and within a factor of 3 of the 10 km air-to-air link.

A schematic of the device is shown in figure III-6. The artificial turbulence generator, nicknamed the turbox, has internal dimensions of 1.22 m wide x 2.44 m long x 0.15 m high. It is a hot wind tunnel. Air at ambient temperature (generally 15 to 22°C)

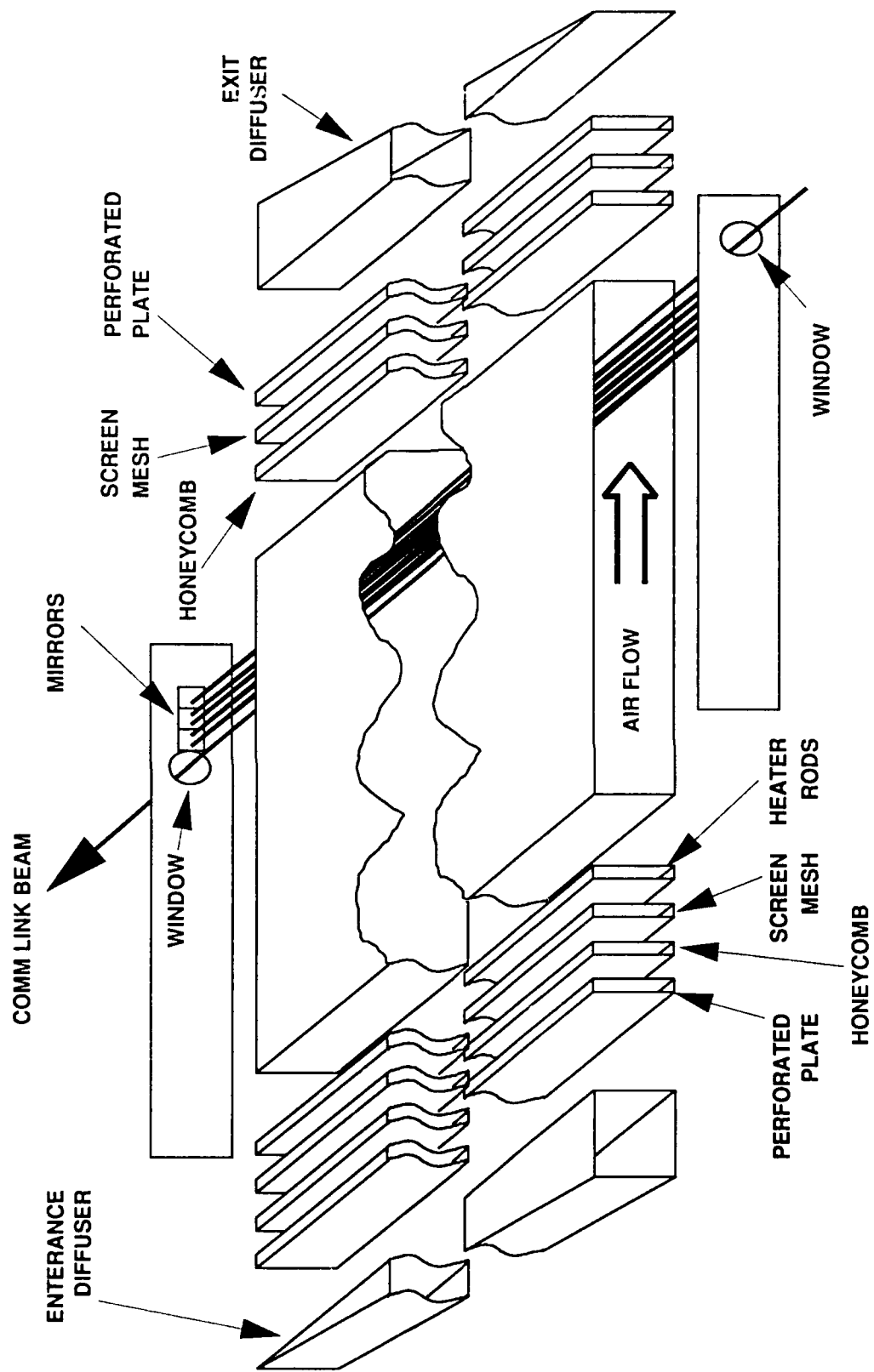


Figure III-6. Schematic of artificial turbulence generator (Turbobox).

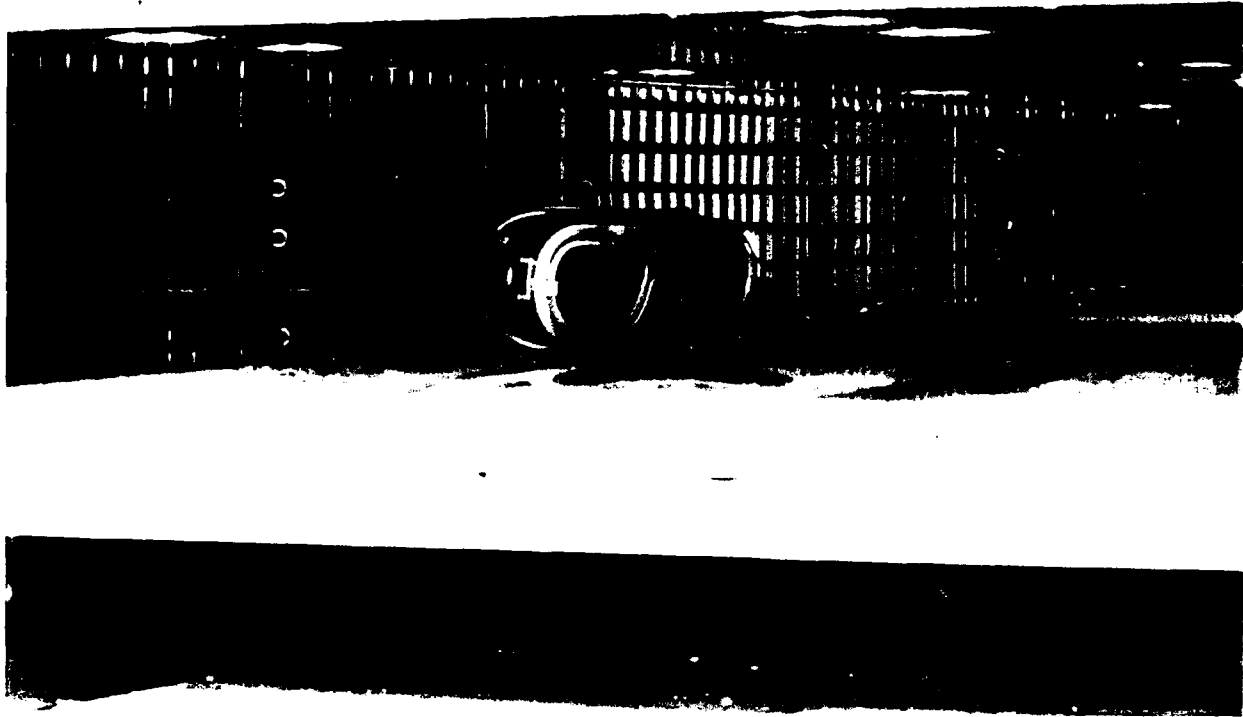


Figure III-7. Photograph of heater frame elements inside of the turbox. Rods are 5 mm in diameter and 2.44 m long. Vertical rods are 15 cm long. Heater rod spacing is 2.54 cm, center-to-center.

is drawn in through the entrance diffuser. Because of the angle at which the diffuser tapers off and because of the pressure drop induced by the perforated plate immediately following the diffuser, the mass flow of air across the turbox is uniform at any point along the length of the entrance diffuser. The honeycomb serves to ensure that the flow is perpendicular to the plane of the honeycomb frame over the entire length of the turbox and the two layers of screen mesh assure that the air flow is uniform.

The key to the performance of the turbox is the heater rod matrix pictured in figure III-7. A steel frame supports six horizontal rows of 5.0 mm diameter x 2.44 m long heater elements running the length of the turbox, with a center-to-center spacing of 2.54 cm. Perpendicular to these are 96 individual 15 cm long heater elements of the

same diameter, each spaced 2.54 cm apart, center-to-center. Air is drawn through the grid of hot elements and turbules approximately 2 cm square (the spacing between heater elements) are established that are hot around the edges and cold in the center. As the air moves downstream (across the turbox) the turbules break up into turbules of various smaller sizes. The inner and outer scales of turbulence were not measured but were predicted to be outer scale,  $L_0 \approx 1.2$  cm, (one-half the grid spacing) and the inner scale,  $\ell_0 \approx 0.14$  mm. When the air reaches a distance about 57 cm downstream of the heater elements (28 times the element spacing<sup>6</sup>), a Kolmogorov<sup>7</sup> distribution of turbule sizes has been established. This downstream distance is important because the optical comm link beam must be passed through the turbox eleven times (26.8 m optical path) in order for the beam to experience  $C_n^2 L^{8/3}$  similar to the roof top link. From the heater element frame to this downstream position, the turbule size distribution changes very rapidly. However, as figure III-8 shows, at a position equal to approximately 28 grid spacings downstream of the heater elements, the turbule distribution changes very slowly, permitting multiple passes of the optical beam through the length of the turbox over many centimeters in the downstream direction (see figure III-6) with nearly uniform turbulence.

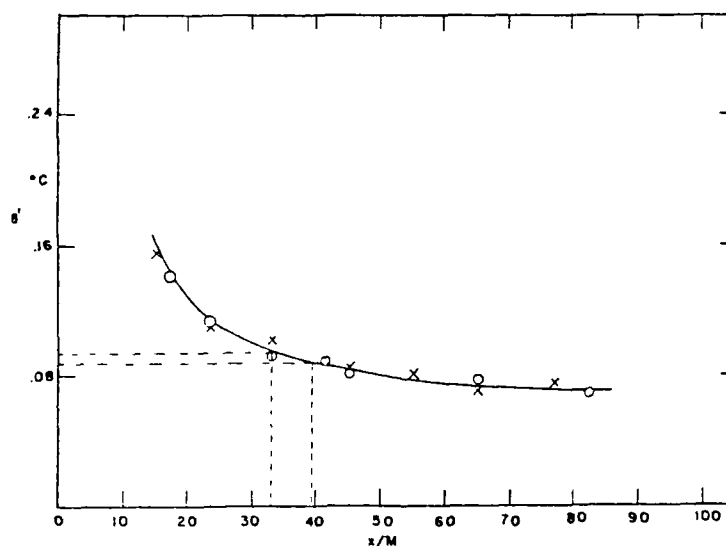


Figure III-8. Falloff of turbulence strength with downstream distance. Abcissa is the downstream distance in units of heater grid spacings. Over range where the comm link beam was multiple passed ( $x/M \approx 33$  to  $39$ ) the temperature falls off only 8% ( $C_n^2$  falls off 15%). From Mills, et al.

The final sheet of honeycomb material, the perforated plate, and exit diffuser help to ensure that the flow does not turn while crossing the turbox perpendicular to the optical beam (see figure III-6). The wind velocity in the turbox can be varied by adjusting a gate valve between the turbox and the pump. However, in all of the experiments discussed in this report, the wind velocity was held constant at approximately 0.5 m/s. The turbulence strength can be varied up to  $C_n^2 = 3 \times 10^{-11} \text{ m}^{-2/3}$  by varying the input power on the heater elements from zero to 28 kW. In order to achieve values of  $C_n^2 L^{8/3}$  that are similar to an air-to-air link, a substantially larger device than the one fabricated by TRW must be built with some combination of stronger heaters and a longer optical path.

Because of the large size of the turbox and space limitations of the laboratory, the turbox was assembled in an aluminum and steel frame on the laboratory floor. This frame served as a solid base for the comm link launch, transceiver, and transponder tables, which were bolted to the frame. The assembled system is pictured in figure III-4. The optical apparatus employed for the turbox comm link experiments is illustrated in figure III-9. After the optical beam arrived on the launch table from the laser table, half of the beam was split off with plate beam splitter PB3 and directed onto detector  $I_b$ , as in the 1 km link experiments. The rest of the beam was periscoped down to the level of the turbox, where it was expanded and collimated with lenses L15 and L16. The beam radius,  $\omega$ , must be greater than the turbulence inner scale,  $\ell_0$ , and smaller than the outer scale,  $L_0$ . From above,  $0.014 < \omega < 1.2 \text{ cm}$ . A beam radius of 0.5 cm was employed for the tests. The total optical path of the beam through the turbox,  $L$ , must fall within the inertial subrange where the effects of the turbulence are described by turbulence theory<sup>5,7</sup>.

$$Z_c < L < Z_i \quad (\text{III-4})$$

where

$$Z_c = (0.39 C_n^2 k^2 L_0^{8/3})^{-1} \quad (\text{III-5})$$

$$Z_i = (0.30 C_n^2 k^2 \ell_0^{8/3})^{-1} \quad (\text{III-6})$$

so that  $2.5 \text{ m} < L < 4 \text{ km}$  for weak turbulence and  $0.06 \text{ m} < L < 106 \text{ m}$  for strong turbulence. Consequently, the beam was multiply passed through the turbox with mirrors



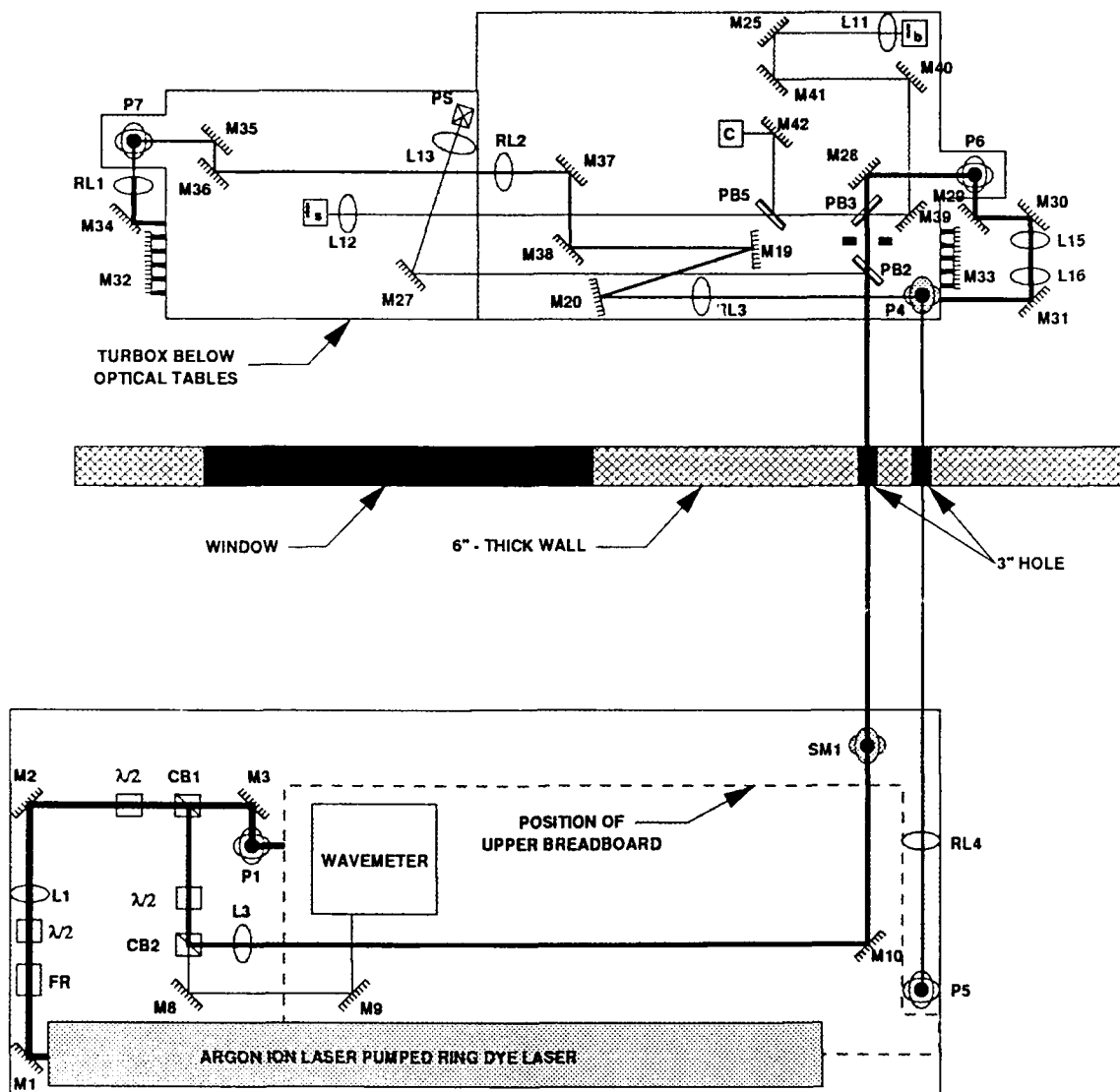


Figure III-9. Experimental layout for comm link experiments with optical beam multiple passed through the turbox. Components are described in figure III-2.

M32 and M33, making eleven passes through the turbox for a total path length of 26.8 m. This optical path length lies within the inertial subranges calculated above for all expected turbulence conditions. The image of the beam exiting the turbox was then relayed to the four wave mixing table, shown in figures III-2 and III-5, where it was focused into the sodium cell and phase conjugated. The phase conjugate reflection retraced the path of the incoming beam, shown in figure III-9, back through the turbox and up to the launch table where it encountered plate beam splitter PB3. This beam splitter split half the beam and directed the light to detector  $I_s$  and to a CCD camera, C.

### 3. DIAGNOSTICS

Diagnostics were developed to permit analysis of the comm link performance either through the atmosphere or through the turbox, and to determine the level of atmospheric or artificially generated turbulence. These diagnostics are discussed in the following sections.

a. Comm Link Intensity -- Intensity on the comm link was measured at various positions shown in figures III-2,3,5, and 9. In all cases, the beam was collected and focused with a lens much larger than the beam through a narrow band interference filter ( $\Delta\nu = 10$  nm [FWHM]) to block the solar and laboratory background and then onto a 1 cm diameter detector so that all light in the beam was detected. The response time of these detectors was  $> 1$  kHz so that speckle-induced variations could be detected. This is illustrated in figure 10. For the experiments described in section III.1.d above, 0.2 cm diameter fast silicon photodiodes were employed with a time response of 40 kHz.

b. Comm Link Variance -- The primary measure of comm link performance was the normalized intensity variance. This quantity was determined by first detecting and measuring the intensity as described in section III.2.a, and then storing this information in a computer at a rate of 0.1 to  $>10.0$  kHz. After a sufficient number of data points were acquired over a period of time ranging from seconds to minutes, the computer then computed the normalized variance by the formula

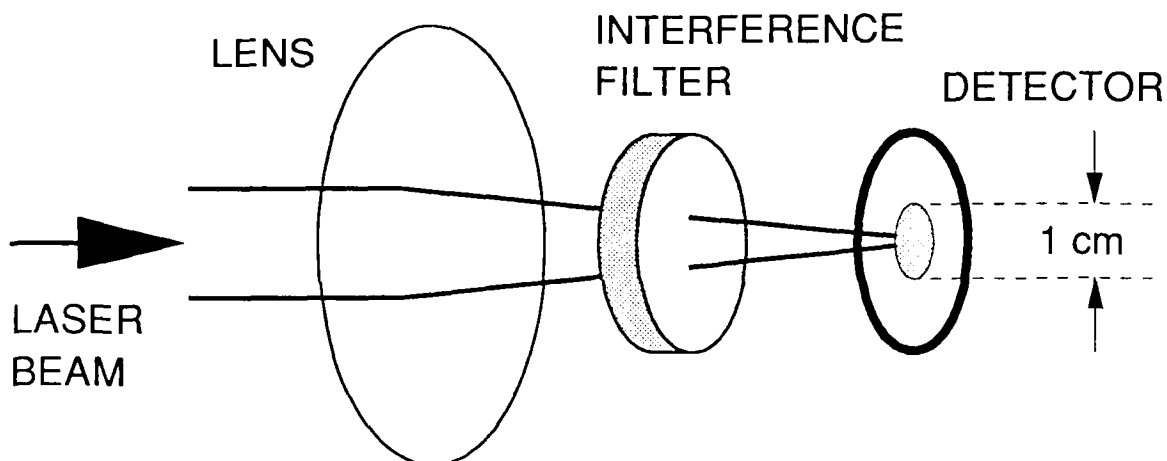


Figure III-10. Schematic of detector collection geometry. Laser beam diameter is much smaller than collecting lens. Beam is focused through an interference filter and detected with a 1 cm diameter silicon photodiode.

$$\sigma^2 = \frac{\langle [I - \langle I \rangle]^2 \rangle}{\langle I \rangle^2} \quad (\text{III-7})$$

where  $I$  is the measured signal.

c. Thermal Measurement of Local Turbulence ( $C_n^2$ ) -- A simple and accurate technique for determining the refractive index structure constant is to measure the temperature difference between two points with extremely fine wire probes<sup>7</sup>. This measurement leads directly to a value for the temperature structure constant<sup>4</sup>

$$C_T^2 = \langle (T_1 - T_2)^2 \rangle r^{-2/3} \quad (\text{III-8})$$

where  $T_1$  and  $T_2$  are the temperature measurements and  $r$  is the separation between the measurement probes. From this quantity, the refractive index structure constant may be inferred<sup>8</sup>.

$$C_n^2 = \left[ \frac{77.6 P}{T^2} \left( 1 + \frac{0.00753}{\lambda^2} \right) \times 10^{-6} \right]^2 C_T^2 \quad (\text{III-9})$$

where  $P$  is the pressure,  $T$  is the temperature, and  $\lambda$  is the wavelength of interest.

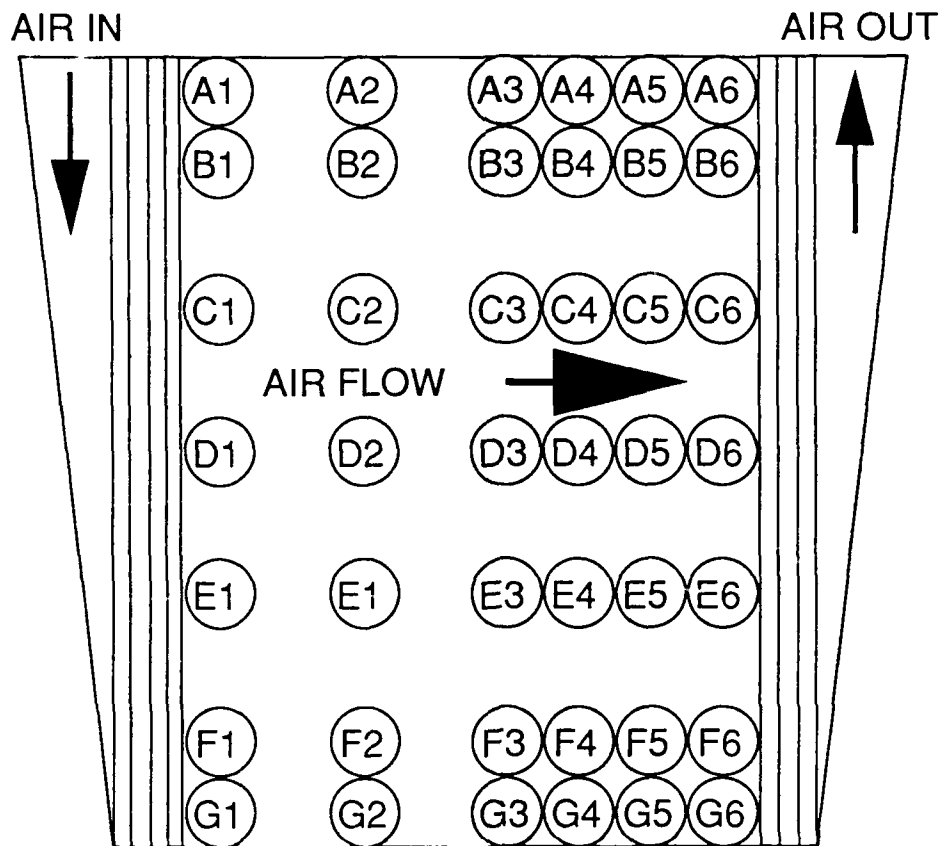


Figure III-11. Turbox sampling port positions and nomenclature. Not to scale.

This technique was applied to the turbobox where it is possible to sample regions of air everywhere the optical beam interacts with the air. An assembly was fabricated to hold two hot wire probes of 4  $\mu\text{m}$  diameter tungsten wire with variable separation. This holder could be attached to any of the 42 sampling ports on the top of the turbobox (see Figure III-11). The results of calibrating the turbobox in this fashion are presented in section III.5.a.

It was not reasonable to measure the turbulence over the 1 km rooftop link in this way. Instead, an optical diagnostic was developed to measure the path averaged value of the index structure constant. The next section gives a description of this diagnostic.

d. Optical Measurement of Path Averaged Turbulence ( $C_n^2$ ) -- In order to evaluate the performance of the comm link over the 1 km range or through the turbobox, it was

necessary to determine the strength of the turbulence integrated over the optical path,  $\int_L C_n^2(L)$ . Applying the temperature measurement method described in the preceding section would have provided very accurate data when all measurements were performed simultaneously. However, making in situ measurements with probes supported 15 meters above streets, parking lots, trees, and buildings and wiring the probes to one central location would have been an extremely complex and costly task to implement. Instead, the variance on an optical beam was employed to determine the refractive index structure constant,  $C_n^2$ , averaged over the optical path.

A 5 mW Melles Griot (model 05LHR151) multimode HeNe laser ( $\lambda = 632.8$  nm) was mounted next to the folding mirror and aimed at the entrance of the rooftop Laboratory. A 1.5 mm diameter pinhole, 632.8 nm narrow band pass ( $\Delta\lambda = 10$  nm [FWHM]) interference filter, and 1 cm diameter Si detector were mounted on top of the transponder platform ( $I_H$  in figures III-2 and III-5). The direction of the collimated output of the HeNe laser was adjusted so that the detector was in the center of the beam 563 m away. A computer was employed to sample the intensity at 0.3 to 10 kHz and to compute the normalized variance in the natural logarithm of the intensity. The log intensity variance is related to the refractive index structure constant by the relationship

$$C_n^2 = \frac{1}{1.228} \frac{1}{k^{7/6} L^{11/6}} \sigma_{\ln I}^2 \quad (III-10)$$

This technique for measuring  $C_n^2$  has been used and improved upon by many workers<sup>9-18</sup>. There are two concerns when measuring  $C_n^2$  in this manner. The first is that the detector aperture be small compared with the correlation distance of the wave so that aperture averaging does not occur. In the absence of turbulence this would be the Fresnel length,  $[\lambda L]^{1/2}$ . However, in the presence of turbulence, this length may be reduced to the transverse coherence length,  $\rho_0$ , given in equations (III-1) and (III-2) for plane and spherical waves, respectively. The second requirement is that the measured variance does not saturate ( $\sigma_{\ln I}^2 < 0.3$ ). For our folded range,  $L_{\text{HeNe}} \approx 563$  m,  $\lambda = 632.8$  nm, and for  $10^{-16} \leq C_n^2 \leq 10^{-14}$ ,  $\rho_0 \geq [\lambda L]^{1/2} = 1.9$  cm. The 1.5 mm aperture employed in the diagnostic is sufficiently less than the correlation distance of the optical beam. A measured value

of  $\sigma_{in/}^2 = 0.3$  implies a value for  $C_n^2$  of  $1.5 \times 10^{-14} \text{ m}^{-2/3}$ . This is the strongest turbulence that was expected on the rooftop range. Stronger atmospheric turbulence would have saturated the measured variance and resulted in incorrectly inferred values of  $C_n^2$ . However, the measured  $\sigma_{in/}^2$  was always  $< 0.3$ .

#### 4. DATA REDUCTION

All data was acquired with an IBM PC-XT through a Strawberry Tree data acquisition card. Up to eight channels of data could be sampled simultaneously and stored in the computer at varying rates depending on the number of channels in use. It was expected that data would need to be sampled at 1 kHz since that is approximately the atmospheric time constant for turbule movement. An initial set of experiments were performed at  $10^4$  Hz in which data was reduced using all points, every other point, every third point, etc. to determine the minimum sample rate required to duplicate the results of the fastest sampling rate. It was determined that data acquired at sampling rates  $> 300$  Hz all gave the same result within  $2\sigma$  error limits. Typically, 6 channels were employed and data was acquired at approximately 400 Hz. Sample periods were typically 3 to 6 seconds at the end of which, the mean and normalized variance were computed by the computer for each channel and/or derived quantity. The detectors that were always monitored included:

- $I_b$  Beacon power launched at transceiver -- Serves as monitor of laser fluctuations, and permits comparison with  $I_p$ .
- $I_p$  Beacon power focused into the Na cell -- Measures one-way extinction and one-way variance,  $\sigma^2$ ; Can be calibrated to give power received through transponder aperture.
- $I_c$  Conjugate power immediately reflected from the Na cell -- measures variance added to conjugate reflection by conjugation process.
- $I_s$  Conjugate power received at transceiver -- Provides measure of two-way (round trip) variance. Can be calibrated to give power received through transceiver aperture for comparison with  $I_c$ .

- $I_c/I_b$  Normalized conjugate power received at transceiver -- Removes effects of laser fluctuations on  $\sigma_c^2$  by providing  $\alpha_{cb}^2$ .
- $I_H$  Pinhole signal for optical measurement of  $C_n^2$

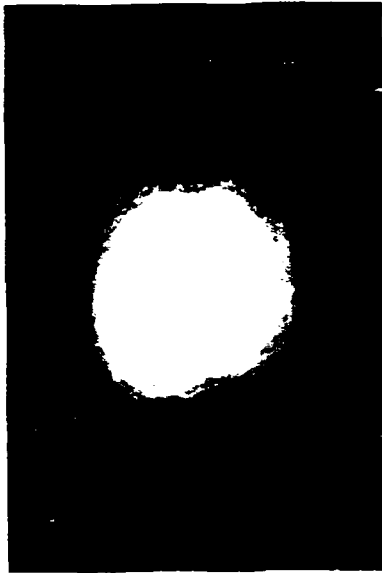
In preliminary tests, the quantities,  $I_{np} = I_p/I_b$  and  $I_{nc} = I_c/I_b$  were monitored simultaneously with  $I_b$ ,  $I_p$ , and  $I_c$  to determine the effects of laser fluctuations on the variance. Laser fluctuations occurred for a variety of reasons including bad dye, temperature changes, and alignment drift. When the laser was steady ( $\alpha_c^2$  was small), there was virtually no difference between the measured variances  $\alpha_p^2$  and  $\alpha_{pb}^2$  or between  $\alpha_c^2$  and  $\alpha_{cb}^2$ . However, when the laser became slightly unstable ( $\alpha_c^2$  increased) then  $\alpha_p^2$  and  $\alpha_c^2$  both increased similarly while the corresponding normalized variances exhibited negligible increases. For simplicity of data acquisition, only the quantity  $I_{nc} = I_c/I_b$ , the normalized conjugate, was typically measured as a monitor of laser fluctuations in later experiments. Strong deviations between the variance measured for  $I_c$  and  $I_{nc}$  indicated that the laser was unstable and the data for that test was disregarded.

The phase conjugate reflectivity was calculated by the computer as  $I_c/I_p$  and was typically kept between 15 and 35% to minimize self-focusing effects observed at higher reflectivities<sup>2</sup>.

## 5. 1 km COMM LINK EXPERIMENTAL RESULTS

Two sets of experiments were performed over the 1 km comm link. In the first set of experiments, the intensity of the four wave mixing counterpropagating pump beams were modulated with an A-O modulator as described in section III.1.d. In the second set of experiments the diameter of the beacon beam and transponding aperture was varied and the variances on the detectors were recorded. These experiments are detailed in the following sections.

a. Qualitative Observations -- Photographs of the comm link beam are presented in figure III-12. A 5 cm diameter (approximately) beacon beam launched through the 10 cm transceiver output aperture is shown in figure III-12a. At 10 cm diameter, the collimated beacon beam exhibits a similar Gaussian intensity distribution across the beam



(a)



(b)



(c)



(d)

Figure III-12. (a) Photograph of 5 cm diameter beacon beam two meters after launch from transceiver aperture. (b) Photograph of aberrated beacon beam at transponder aperture after travelling 1.1 km through atmosphere. Photograph shows an instantaneous beam position which changes on the time scale of the turbulence. (c) Photograph of phase conjugate beam arriving back at transceiver for 1.1 km atmospheric link. (d) Phase conjugate beam arriving at transceiver for 4 m laboratory comm link for comparison to photograph in (c).



but has a hard aperture. Figure III-12b shows the aberrated beam at the transponder aperture after it traveled 1.1 km (Beacon beam was collimated 10 cm diameter) as it was captured on video tape. Since the video camera and recorder scan faster than 25 Hz, the spot in the photograph may include a small amount of averaging of short term beam spread and aberration. Since turbulence is dynamic, local changes occur on millisecond timescales; beam spread and aberration, therefore, will change on a similar timescale. The photos in figure III-13 illustrate this effect. These are a series of frames taken from videotape of a focused 5 cm diameter beam over half of the link (563 m). In each frame atmospheric turbulence aberrates the beam in a different way. This is the short term beam spread and aberration (i.e. the instantaneous beam shape resulting from turbulence-induced distortion). On a longer time scale the beam wanders around a central region. The two effects contribute to the long term beam spread. This can be described by

$$\langle r_L^2 \rangle = \langle r_s^2 \rangle + \langle r_c^2 \rangle \quad (\text{III-11})$$

where  $r_L$  is the long term beam spread,  $r_s$  is the short term beam spread, and  $r_c$  is the beam wander. Observing the videotape at normal speed or averaging many frames of the videotape presents a good picture of the long term beam spread. A photograph of the long term beam spread for the photos shown in figure III-13 was obtained by averaging several videotape frames and is presented in figure III-13d.

Figure III-12c shows the reconstructed phase conjugate spot detected by a CCD array after it has completed the 1.1 km return trip. For comparison a 4 m comm link was established by mounting a folding mirror on the wall inside the rooftop laboratory. The phase conjugate spot detected with this short comm link is shown in figure III-12d. This spot is much brighter and more round than the spot detected over the 1.1 km link. Much of the intensity is lost on the transponder aperture over the first leg (beacon) of the 1.1 km link. Certainly some of the spatial frequency information is lost on the transponder aperture as well. These photographs result after the beam travels 2.2 km through the atmosphere, but do not indicate on which leg of the trip the aberrations and extinction



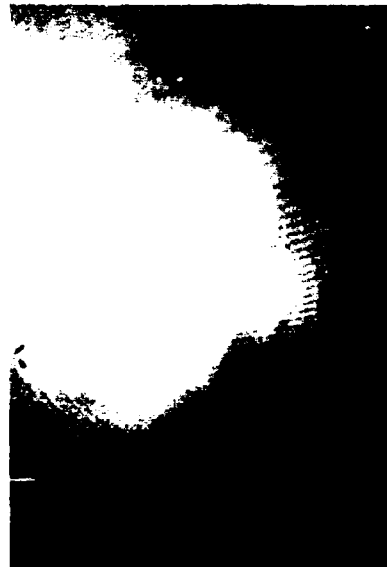
(a)



(b)



(c)



(d)

Figure III-13. Photographs of beacon beam at transponder after travelling 1 km through atmospheric turbulence. (a) - (c) are single frames from video tape demonstrating turbulence-induced instantaneous (short term) beam spread and beam steering. (d) is a 1 second average of video tape frames illustrating the long term beam spread induced by turbulence induced beam steering (wandering) and beam spread.

occurred. Experiments measuring the effect this has on the intensity variance and received power demonstrate that virtually all of the damage to the beam occurs on the first leg (beacon) as the beam travels from the transceiver to the transponder. Because the return beam is phase conjugated, it experiences only a small extinction loss. These results will be discussed in the following sections.

Finally, when a mirror is placed in front of focusing lens L8, blocking the four wave mixing cell, the detected return beam on the CCD camera is doubly aberrated. A photograph of the detected spot is shown in figure III-14b. This beam is strongly aberrated and moves very rapidly in contrast with the phase conjugate return shown in figure III-14a.

b. Amplitude Modulation -- The frequency of the AO modulator was varied from 0 to 4 MHz. Results from experiments with the AO modulator operating at 100 kHz and 1 MHz are presented in figure III-15. Three traces are displayed in each oscilloscope photograph. The lowest trace is the DC component of the beacon signal received at the sodium cell ( $I_b$ ) after travelling 1.1 km through the atmosphere. In both photographs this trace is flat, exhibiting no amplitude modulation. The center trace is the modulated pump beam signal ( $I_a$  in figure III-5) and displays the frequency of the AO modulator, 100 kHz DC coupled in figure III-15a and 1 MHz AC coupled in figure III-15b. The 1 MHz signal is not sinusoidal because the detector response is insufficient to follow the signal accurately. However, the AC component does represent the frequency correctly and is displayed for that purpose. The top trace in each photograph is the received phase conjugate signal at detector  $I_b$  in figure III-5. In figure III-15a it is the DC component; in figure III-15b it is the AC component.

In all tests, from 0 to 1 MHz, the frequency of the pump beam amplitude modulation was successfully transferred to the phase conjugate beam and read at the transceiver station. With frequency modulation slower than the detector response time ( $\approx 40$  kHz), the phase conjugate signal always dropped to zero between pulses.

The upper two traces in each photograph in figure III-15 exhibit a phase shift. Careful analysis of this shift using the 100 kHz data gives a delay time of  $t_d = 3.66 \mu s$ .

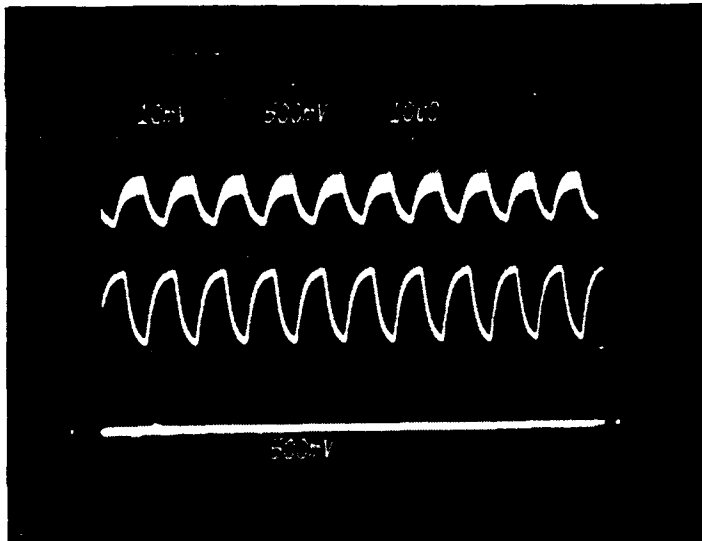


(a)



(b)

Figure III-14. Photographs of (a) phase conjugate return beam on 1.1 km comm link taken at transceiver and (b) return beam detected at transceiver on 1.1 km comm link with a mirror placed in front of focusing lens, L8, (see figure III-2) blocking the phase conjugator.



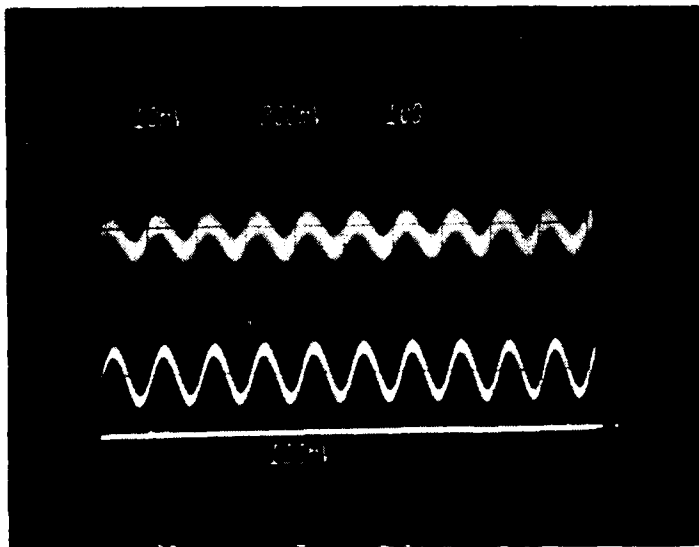
(a)

$\nu = 100 \text{ kHz}$

Phase Conjugate ( $I_s$ ).

Modulated Pump ( $I_a$ ).

Beacon Beam ( $I_b$ ).



(b)

$\nu = 1 \text{ MHz}$

Phase Conjugate ( $I_s$ ).

Modulated Pump ( $I_a$ ).

Beacon Beam ( $I_b$ ).

Figure III-15. Results of amplitude modulation experiments. Modulation of rear pump beam at (a) 100 kHz and (b) 1 MHz. There was no signal on the beacon beam launched at the transceiver ( $I_b$ ). The pump beams on the transponder ( $I_a$ ) were modulated at frequencies up to 1 MHz. The phase conjugate return beam ( $I_s$ ) carries the same frequency as the pump beam read onto it during the FWM process.

Using a value for the speed of light of  $c = 2.9979 \times 10^8$  m/s gives a range distance of  $1.098 = 1.1$  km. This corresponds to the value extracted from site plans (see section III.1.c).

c. Intensity Variance -- The primary diagnostic for determining comm link performance was the normalized variance of the received intensity on the phase conjugate return beam,  $\sigma_s^2$ . The ratio of  $\sigma_s^2$  to the one-way normalized variance,  $\sigma_p^2$  (no phase conjugation), was found to be an important figure of merit (FOM) for overall comm link performance since it readily compares the PC link performance to the that of a one-way link. This is illustrated in figure III-16. A beacon beam is launched at the transceiver with some initial intensity variance,  $\sigma_b^2$ . As this beam travels through the atmosphere, turbulence distorts the beam and adds intensity variance to it. The beam received by the transponder has a larger variance,  $\sigma_p^2$ , due to this atmospheric turbulence ( $\sigma_p^2 > \sigma_b^2$ ). At the transponder, the beam is phase conjugated and reflected back to the transceiver. If the phase conjugating material imparts no additional variance to the beam, then the variance on the phase conjugate return,  $\sigma_c^2$ , is equal to  $\sigma_p^2$  as it leaves the transponder station. As discussed in sections I.1 and I.2, phase conjugation cannot reduce the variance on a beam. However, it can prevent the variance from increasing further. Since the return beam is the phase conjugate of the incoming beam, it compensates for atmospheric aberrations on the return leg and receives little or no additional intensity variance. If phase conjugation corrects *all* of the atmospheric aberrations on the return leg then the received conjugate variance,  $\sigma_s^2$ , will exhibit the same variance as the beam at the transponder ( $\sigma_s^2/\sigma_p^2 = 1$ ). If a mirror is used to return the beam from the transponder in place of the phase conjugator, the atmosphere will add intensity variance to the beam on the return leg and  $\sigma_s^2 > \sigma_p^2$ . Thus, a FOM greater than 1 indicates poor aberration correction of the phase conjugated link. The ratio of  $\sigma_s^2/\sigma_p^2$  was used as the figure of merit for all comm link experiments.

It is important to compare results of these experiments to those without phase conjugation. Consequently, a mirror was placed immediately in front of focusing lens L8 in figure III-2 and carefully aligned for maximum signal at  $I_s$ . If the turbulence over the

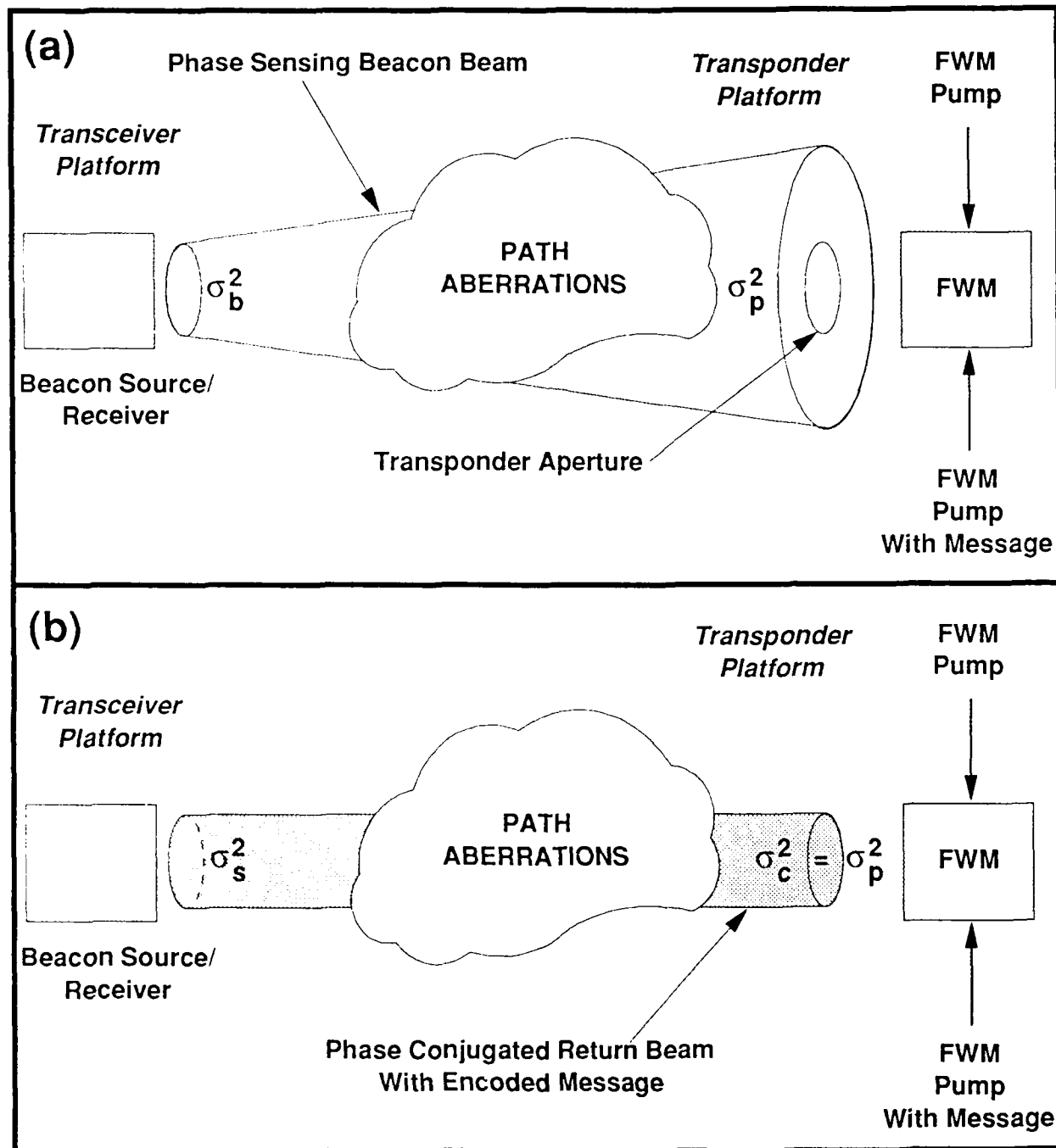


Figure III-16. Intensity Variance on a FWM phase conjugated communication link. The beacon beam leaves the transceiver with some minimal variance,  $\sigma_b^2$ . The atmosphere adds variance to the beam so that when it reaches the transponder, it has variance,  $\sigma_p^2$ . The FWM cell may or may not add variance also, so the reflected beam has variance,  $\sigma_c^2$  which may be equal to  $\sigma_p^2$ . If the atmosphere adds variance to the return beam (mirror used instead of phase conjugator) then the signal beam arriving back at the transceiver will have variance,  $\sigma_s^2$ .

1 km range is uniform, the figure of merit measured in these experiments,  $[\sigma_s^2/\sigma_p^2]_M$ , can have a minimum value of  $2^{11/6}$  since

$$\sigma^2 = C_0 k^{7/6} L^{11/6} C_n^2, \quad (\text{III-12})$$

where  $C_0$  is a constant (equal to 1.23 for a plane wave and 0.496 for a spherical wave),  $k = (2\pi)/\lambda$  is the free wavenumber,  $L$  is the optical path length, and  $C_n^2$  is the refractive index structure constant throughout the link propagation path. For the one-way link,  $L = 2 \times 563$  m and the variance will have some value,  $\sigma_p^2$ . With the mirror in place,  $L = 4 \times 563$  m, the atmospheric turbulence (and therefore,  $C_n^2$ ) remains frozen on the return leg 3.8  $\mu$ s later, and  $\sigma_s^2$  can be expected to increase by the range increase (i.e.  $\sigma_s^2 = 2^{11/6} \sigma_p^2$ ). Comparing the figure of merit for experiments performed with phase conjugation,  $[\sigma_s^2/\sigma_p^2]_{PC}$ , to that measured for experiments performed with the mirror,  $[\sigma_s^2/\sigma_p^2]_M$ , gives a measure of the improvement in intensity variance gained by employing phase conjugation in the optical communication link.

A series of experiments were performed with aperture sizes ranging from 1 to 10 cm to determine the effects of capturing light with a subaperture of the beam at the transponder. The experiments were performed with the phase conjugator and repeated with the mirror in front of focusing lens L8 (no phase conjugation). Results of the experiments performed with the mirror in front of focusing lens L8 are presented in figure III-17 for transponding apertures of 1, 2, 3, 5, and 10 cm diameter. A straight line is drawn at

$$[\sigma_s^2/\sigma_p^2]_M = 2^{11/6} = 3.56.$$

The data at the four lower apertures exhibit scatter around this line suggesting that the turbulence over the 1 km range is not uniform. There is no correlation between the measured  $C_n^2$  values and the magnitude of the scatter in figure III-17. The data measured for a transponder aperture diameter of 10 cm exhibits a large degree of scatter.

The largest output lens available was 10 cm in diameter and was always employed as the final collimating optic, L5 (see figure III-2), for all experiments. Different beacon



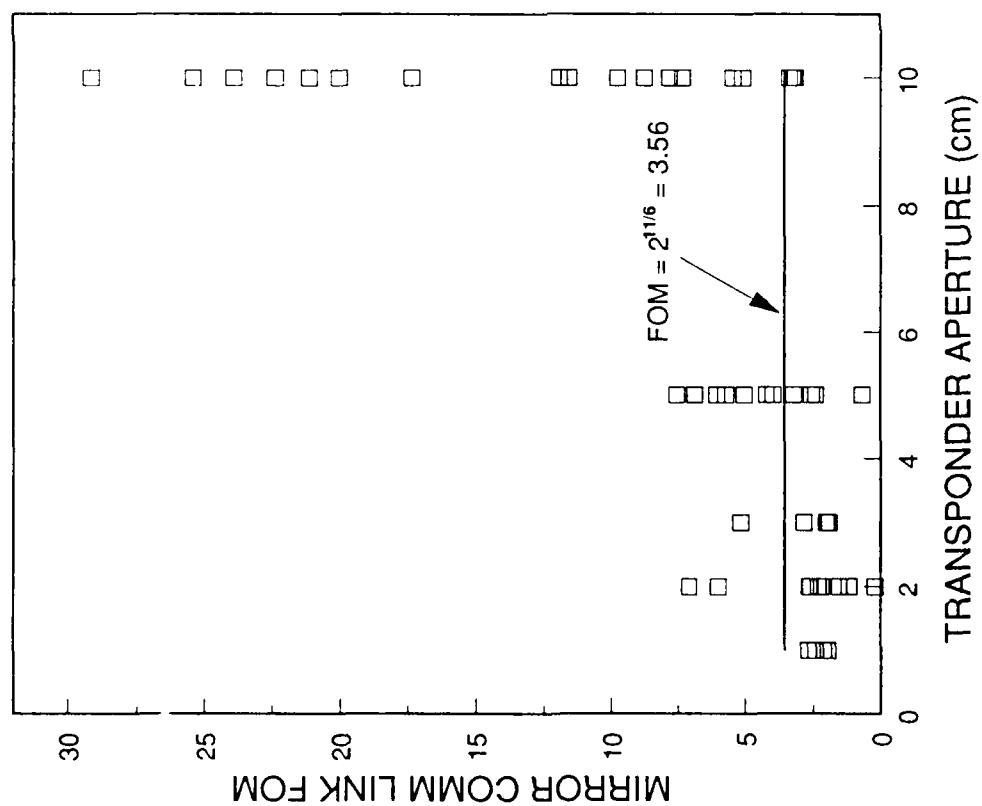


Figure III-17. Comm link FOM for 1 km link with a mirror as a function of transponder aperture diameter.

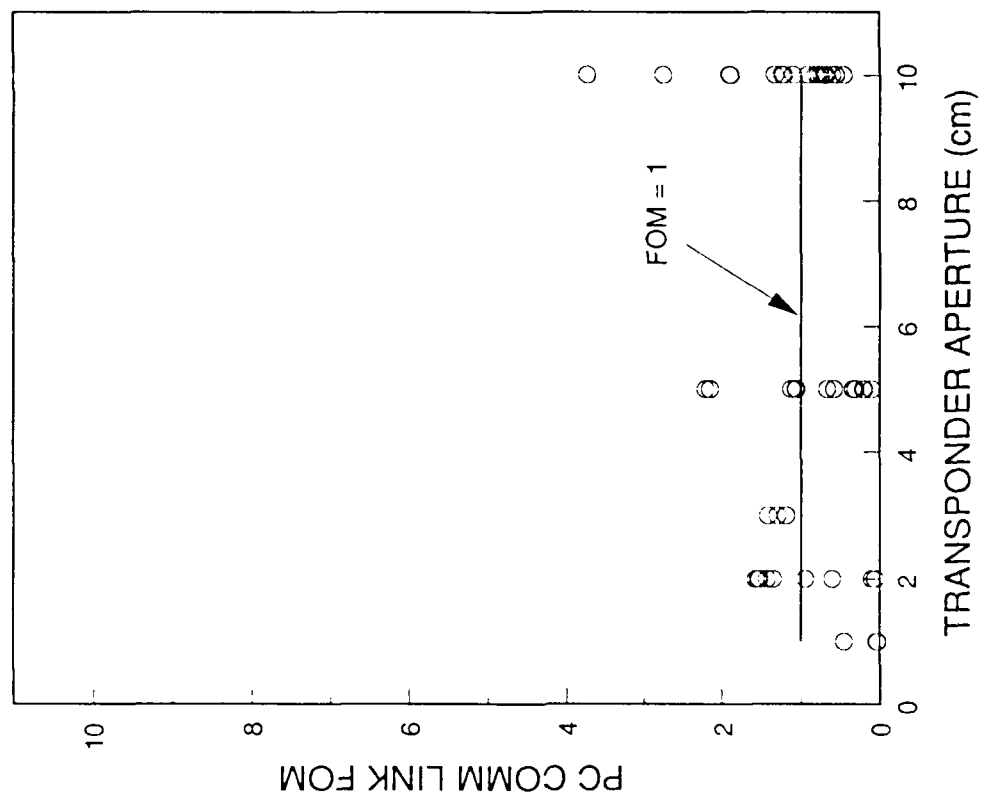


Figure III-18. Comm link FOM for PC 1 km link as a function of transponder aperture diameter. (Note the factor of three scale change compared to figure III-17.)

beam diameters were achieved by changing the input optic, L4. A lens identical with the collimating optic, L5, was used as the transponder receiving lens, L6. An adjustable iris (0.2 to 11 cm diameter) served as the transponder aperture and was used to determine the fraction of light received by the transponder receiving lens, L6. When the light was reflected by the mirror in front of focusing lens, L8, the transponder aperture established the amount of light returned. However, the amount of light received by the transceiver was always determined by the 10 cm aperture lens. Without phase conjugation, the beam received at the transceiver wanders around a central region (as it always does at the transponder aperture since the one-way path has no phase conjugation). This wander can exceed the ten centimeter aperture and is larger for larger diameter beams and transponder apertures. When the beacon beam and transponder aperture diameters are 1 - 5 cm, the centroid of the returned beam is nearly always on the 10 cm optic, but some of the light is lost as it flickers around the edge of the 10 cm aperture. This changing intensity on the transceiver optic contributes to the scatter in the data for those apertures in figure III-17. However, with the 10 cm beam and transponder aperture of 10 cm, the centroid of the returned beam moves over and off of the transceiver optic. This creates a much larger variance in the intensity at  $I_c$ , as exhibited by the 10 cm aperture data in figure III-17.

Data for experiments performed with the phase conjugator were performed under the identical conditions as the mirror experiments. The results are plotted in figure III-18. A straight line is drawn in figure III-18 at  $[\sigma_s^2/\sigma_p^2]_{PC} = 1$ . There is very little scatter in the data, compared with the mirror data, and it centers around the value of 1, indicating that the intensity variance on a phase conjugated link is no worse than that on a one-way comm link. These data are replotted together with the mirror data in figure III-19. The data taken with phase conjugation are better than the data with the mirror in all cases. The scatter in the data for a transponder aperture of 10 cm with the phase conjugator is also much improved over the scatter in the 10 cm aperture data taken with the mirror. This result is expected because the reflected phase conjugated beam is not affected by atmospheric turbulence and does not spread dramatically. However, the transponder aperture is sampling only a portion of the beacon beam because of diffraction and

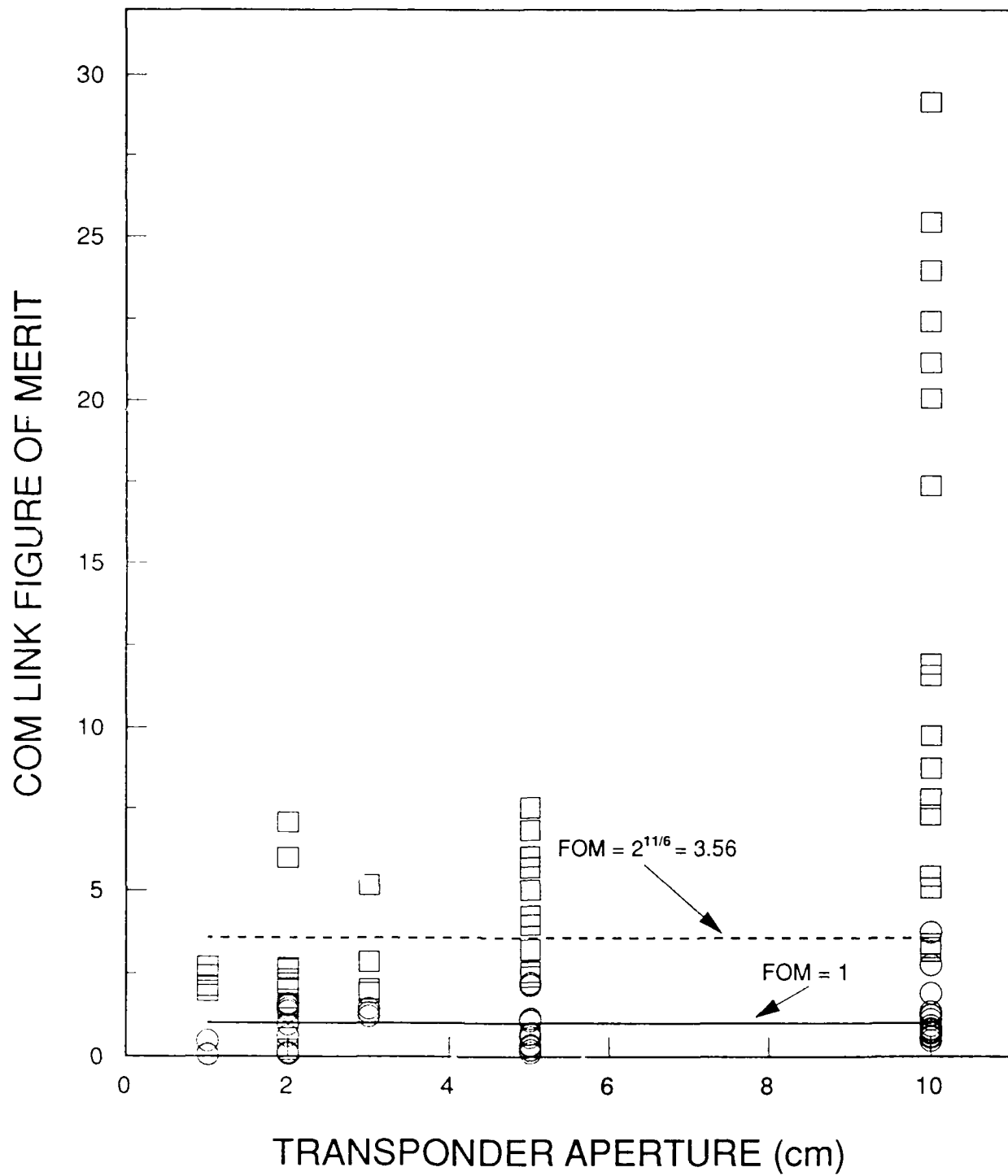


Figure III-19. Comm link FOM for PC 1 km link (circles) and 1 km link with mirror (squares) as a function of transponder aperture diameter.

turbulence on the beacon link. This should mean that the ability of phase conjugation to correct the returned beam is diminished. The phase conjugated return spot as viewed on the CCD camera is circular with some Airy rings, suggesting that phase conjugation does a good job of correcting and reconstructing the beam. The Airy rings are the result of diffraction somewhere on the link, either at the transponder or transceiver.

Table III-1. Beam spread over 1.1 km with  $C_n^2 = 1 \times 10^{-14} \text{ m}^{-2/3}$ .

Collimated Launch Diameter	Spot Size At L = 1100 m
1 cm	8.3 cm
2 cm	4.6 cm
3 cm	4.1 cm
5 cm	5.3 cm
10 cm	10.0 cm

It is not clear why the scatter increases for the 10 cm aperture data. In weak turbulence, the spot size of a collimated beacon beam 1 to 10 cm in diameter at a distance of 1100 m is dominated by diffractive spreading. The spot size at 1100 m of each of the beam/aperture sizes tested is given in table III-1 for  $C_n^2 = 1 \times 10^{-14} \text{ m}^{-2/3}$ . The spot sizes for the 1, 2, and 3 cm diameter beacon beams at 1.1 km are all larger than the transponder aperture diameter (which is equal to the beacon beam launch diameter). Under the influence of atmospheric turbulence the beacon beam wanders around the transponder aperture. Since the beam is much larger than the transponder aperture, the aperture always remains completely filled by the beam. However, the spot size of the 5 and 10 cm diameter beacon beams at the transponder is about equal to the launch diameter. Consequently, when these beams wander around the transponder aperture, the aperture is filled and then only partially filled as the beam moves on and then off of the aperture. If data were acquired for a period long enough to average out all of this

movement, then the data in figures III-17 through III-19 should all exhibit very little scatter. The scatter in the data for the 5 and 10 cm diameter apertures in these figures suggests that at least for those experiments, the averaging period of 3 to 6 seconds was not sufficient.

d. Power Loss -- An important result of the system study discussed in chapter II is that phase conjugation can significantly reduce the power required on the second leg of a two-way communication link. We have experimentally demonstrated the validity of this conclusion on the 1 km link.

The only experiments in which the beacon beam diameter, the transceiver aperture diameter, and transponder aperture diameter were all identical was with a 10 cm diameter beam and apertures. The average beacon power at the transceiver,  $I_b$ , and power received at the transponder,  $I_p$ , were measured. Each detector was calibrated to give the power at the respective aperture and the ratio of the measured powers,  $I_p/I_b$ , was computed. This ratio represents the fraction of the launched beacon power received at the transponder in a one-way comm link. Simultaneously, the average power returned at the transponder,  $I_c$ , and the power received back at the transceiver,  $I_s$ , were measured. Each detector was calibrated to give the power at the respective aperture and the ratio of the measured powers,  $I_s/I_c$ , was computed. In a conventional two-way link, the two ratios are expected to be similar since diffraction, atmospheric extinction, and turbulence-induced losses are experienced equally on each leg. Experiments with a mirror in front of focusing lens, L8 (see figure III-2) on top of the FWM table simulate a conventional link. Figure III-20 is a plot of the ratio measured on the return leg in these experiments plotted against the ratio measured for the beacon beam. The data range from less than 0.05 to more than 0.2 as a result in variations in  $C_n^2$ . The straight line in Figure III-20 has a slope of one. The data are scattered around and to the right of this line indicating that the power loss on the second leg may be slightly greater than on the first leg. This result is expected since the return beam is not collimated as it exits the transponder aperture; the beam should have the same diffraction, etc. parameters as the beacon beam that arrived at that aperture and so be diverging on exit.

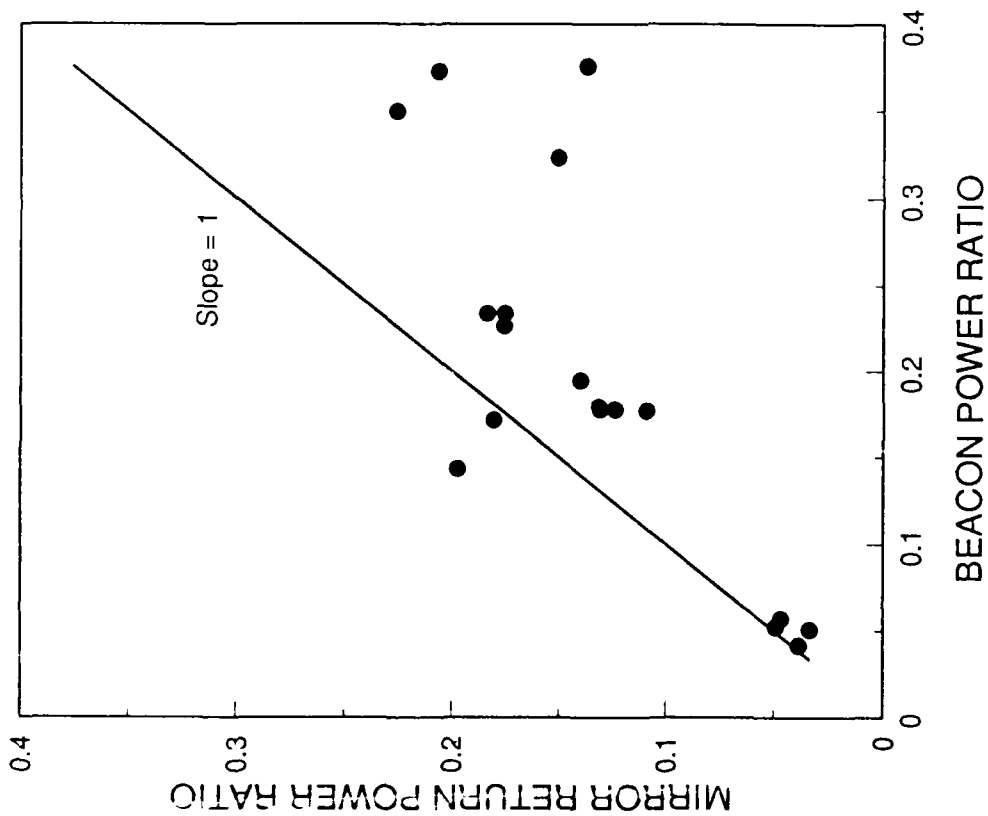


Figure III-20. Ratio of power received at the transceiver to the power reflected by a mirror at the transponder plotted against the ratio of the beacon power received at the transponder to the power launched at the transceiver. Experiment mimics a conventional two-way comm link. Apertures and beam diameters are 10 cm.

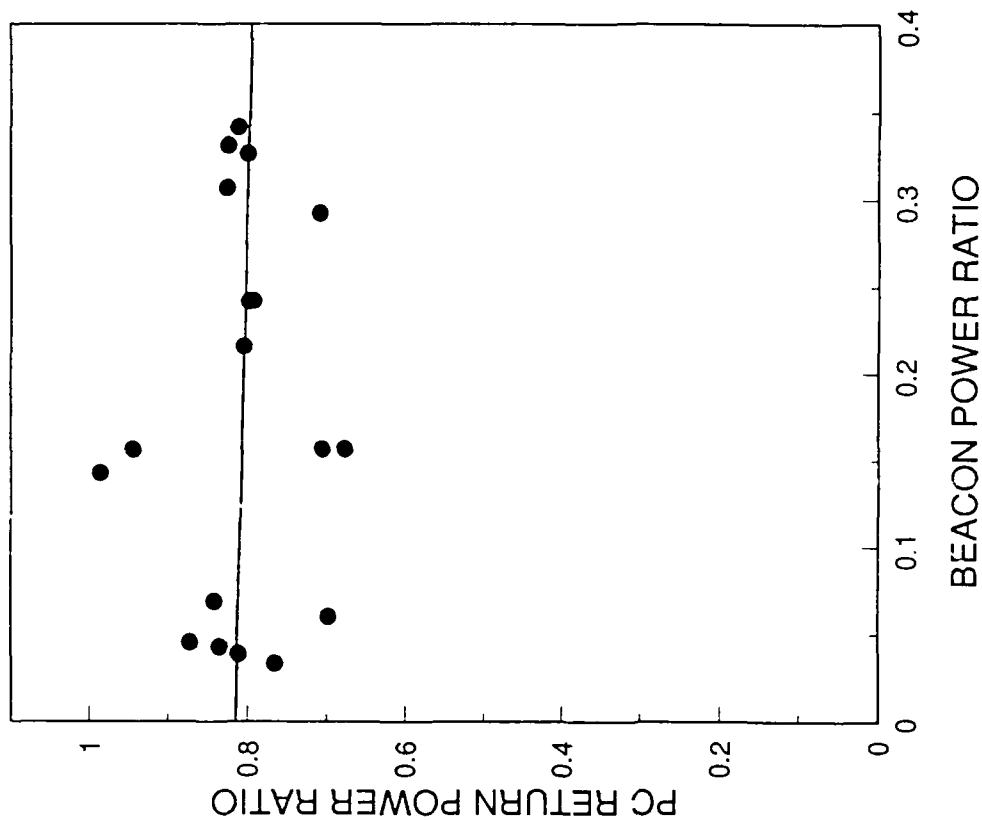


Figure III-21. Ratio of power received at the transceiver to the power reflected by the phase conjugator at the transponder plotted against the ratio of the beacon power received at the transponder to the power launched at the transceiver. Apertures and beam diameters are 10 cm. Note factor of >2.5 scale change compared to figure III-20.

Data measured in experiments with phase conjugation are plotted similarly in Figure III-21. These data appear to be clustered around a more horizontal line with a value approximately equal to 0.8. Thus, over the very narrow range of turbulence strengths experienced on this link, and over a range of 1 km, phase conjugation reduces the power lost on the second leg of a two-way link compared to the power lost on the second leg of a conventional link by a factor of 4 to 16.

## 5. TURBOX EXPERIMENTAL RESULTS

In this section we present the results of comm link studies performed with the turbox, a device capable of artificially generating and controlling uniform turbulence. Section III.5.a describes the turbulence calibration technique and results. Comm link experimental results are presented in section III.5.b.

a. Turbox Calibration -- Turbulence artificially generated in the turbox was measured by direct temperature measurements at various positions along the optical beam path and as a function of downstream air flow distance as described in section III.2.c. Temperature data was acquired at 10 kHz and stored in the computer for analysis. It is always important that the  $\Delta T$  between the probes be measured with a separation greater than the inner scale of the turbulence,  $\ell_0$ , but less than the outer scale,  $L_0$ . Rearranging equation (III-8) and taking the ln gives

$$\ln \langle (T_1 - T_2)^2 \rangle = \frac{2}{3} \ln(r) + \ln C_T^2 . \quad (\text{III-13})$$

Plotting  $\ln \langle \Delta T^2 \rangle$  against  $\ln(r)$  will result in a straight line with a slope representative of the turbulence power distribution. If the turbulence is Kolmogorov-like, the slope will be equal to 2/3. Varying the probe separation at fixed power and wind velocity settings on the turbox results in the data presented in figure III-22. These data fit a straight line with a slope of 2/3 indicating that the turbulence generated in the turbox follows the two-thirds law and can, therefore, be treated as having a Kolmogorov spectral distribution.

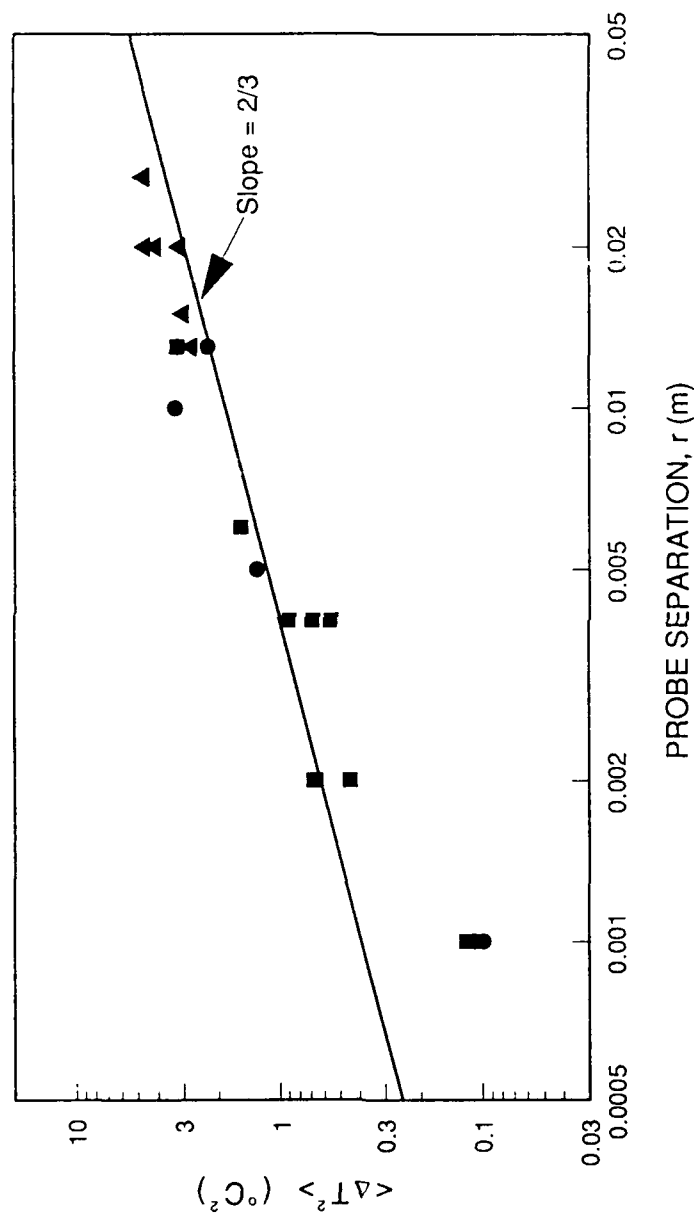


Figure III-22. Calibration of thermocouple probe spacing for measurement of turbulence strength in the turbobox. Data acquired with  $T = 110 - 115^\circ\text{C}$  ( $\Delta H = 20 \text{ kW}$ ). Data exhibits a slope of 2/3 and can be treated as having a Kolmogorov spectral distribution. Inner scale of turbulence is probably less than  $r = 1 \text{ mm}$ . Probe spacing was kept fixed at  $r = 4 \text{ mm}$  for all subsequent measurements.



The data is expected to roll off when the probe separation approaches the inner scale size,  $\ell_0$ . This effect is not observed in figure III-22 probably because we could not achieve a probe separation small enough to observe it (predicted  $\ell_0 = 0.14$  mm). With our apparatus it was very difficult to achieve a probe separation of less than about a millimeter and to accurately know the small separation.

Figures III-23 and III-24 are typical examples of the power spectrum of the temperature fluctuations measured with the turbox set near maximum heat load (maximum  $C_n^2$ ). The spectrum is nearly flat from 100 to 500 Hz, but exhibits some increase at low frequency ( $< 50$  Hz). The absolute temperatures measured by each probe are displayed in figure III-25 as a function of time. The two probes track each other very well. There are two spikes, one at about 0.28 s and the second near 0.93 s, which are present on the signal detected by one probe only. The source of these spikes are uncertain; they may be due to hot particles of dust striking the wire probes. However, they were eliminated before the data was reduced.

For all subsequent measurements the probe separation was held at  $r = 4$  mm, a value clearly within the range  $\ell_0 \leq r \leq L_0$ , and less than the optical beam waist, 1 cm. Using this value of  $r$ , equations (III-8) and (III-9), and the measured pressure and temperature, the measured values of  $\langle \Delta T^2 \rangle$  were converted to values of the refractive index structure constant,  $C_n^2$ . This was first employed to calibrate the optical  $C_n^2$  diagnostic described in section III.2.d. A 100  $\mu$ m pinhole was employed on the detector in place of the larger one used on the 1 km range. The thermally measured values of the refractive index structure constant are plotted in figure III-26 against the optically measured values. The agreement is very good. However, the slope is not equal to 1 indicating a nonlinearity in the optical diagnostic in this range. Reproducibility of the  $\Delta T$  temperature probe data was good to about  $\pm 40\%$  and was therefore used to determine the value of  $C_n^2$  for all turbox experiments.

b. Experiments -- The average value of the square of the temperature difference between the two thermocouples,  $\langle \Delta T^2 \rangle$ , was computed for a series of tests over a variety of turbox conditions and at several sample ports. Figures III-27a - III-27c present this

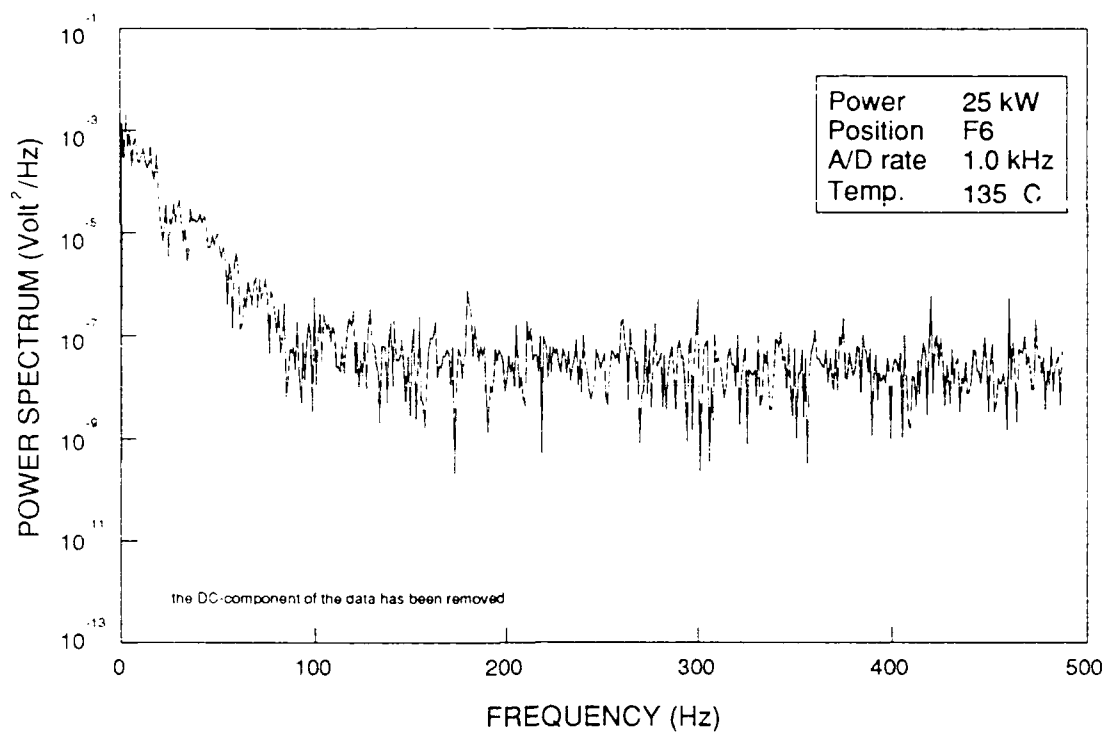


Figure III-23. Typical power spectrum of turbulence in turbofan measured with temperature probe technique.

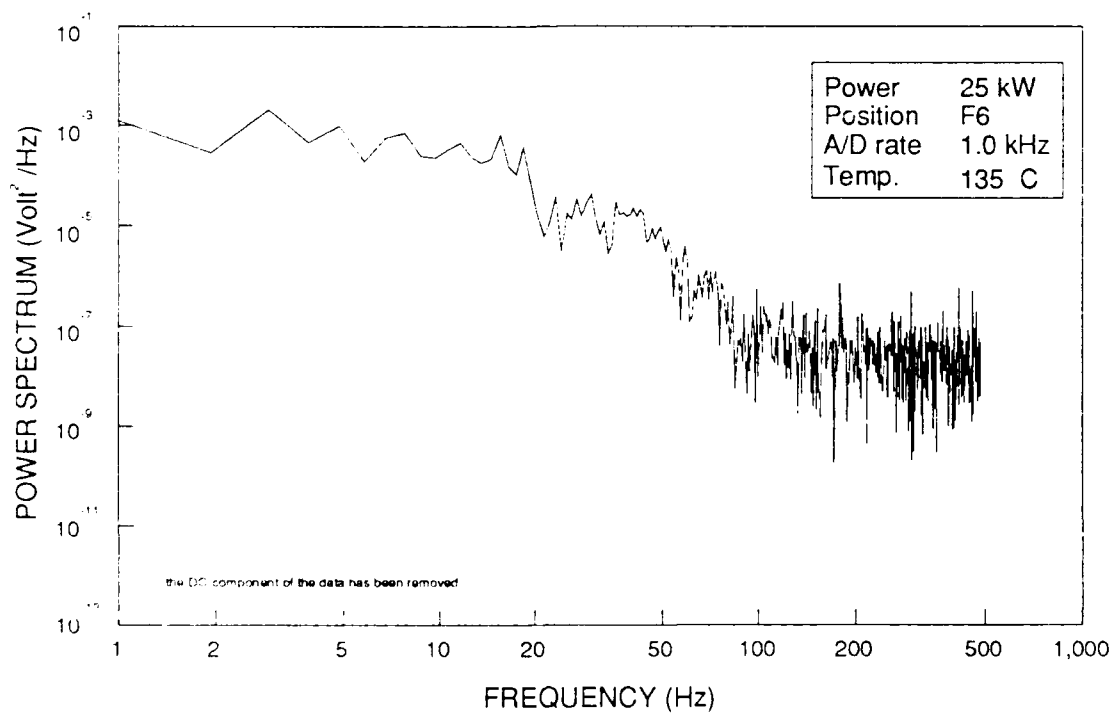


Figure III-24. Expanded view of low frequency portion of power spectrum.

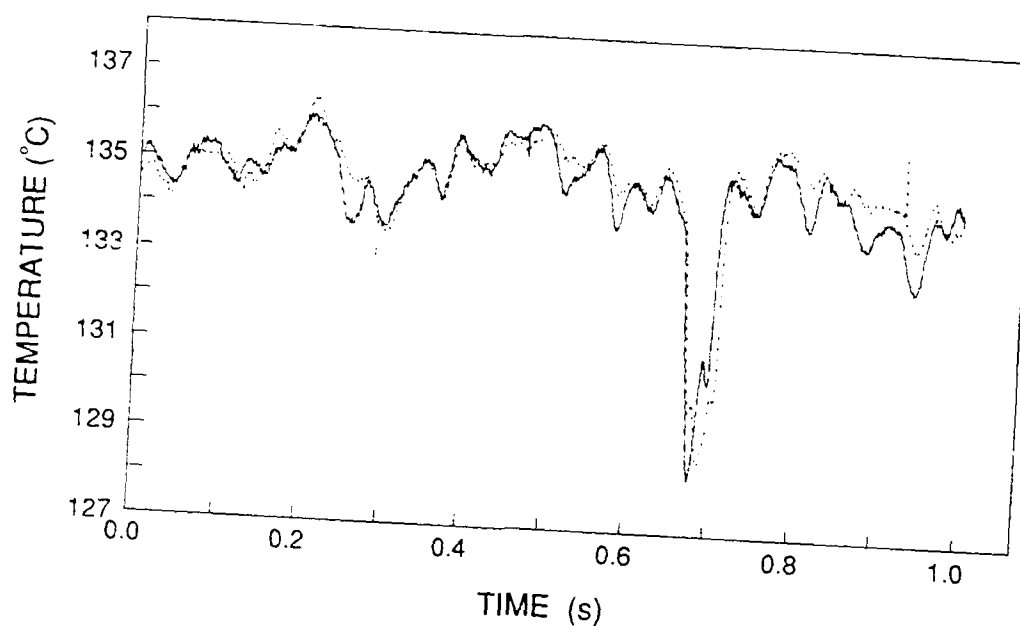


Figure III-25. Temperature traces for each thermocouple during a one second test. Probe separation is  $r = 4$  mm. Occasional spiking is thought to result from dust particles striking probe.

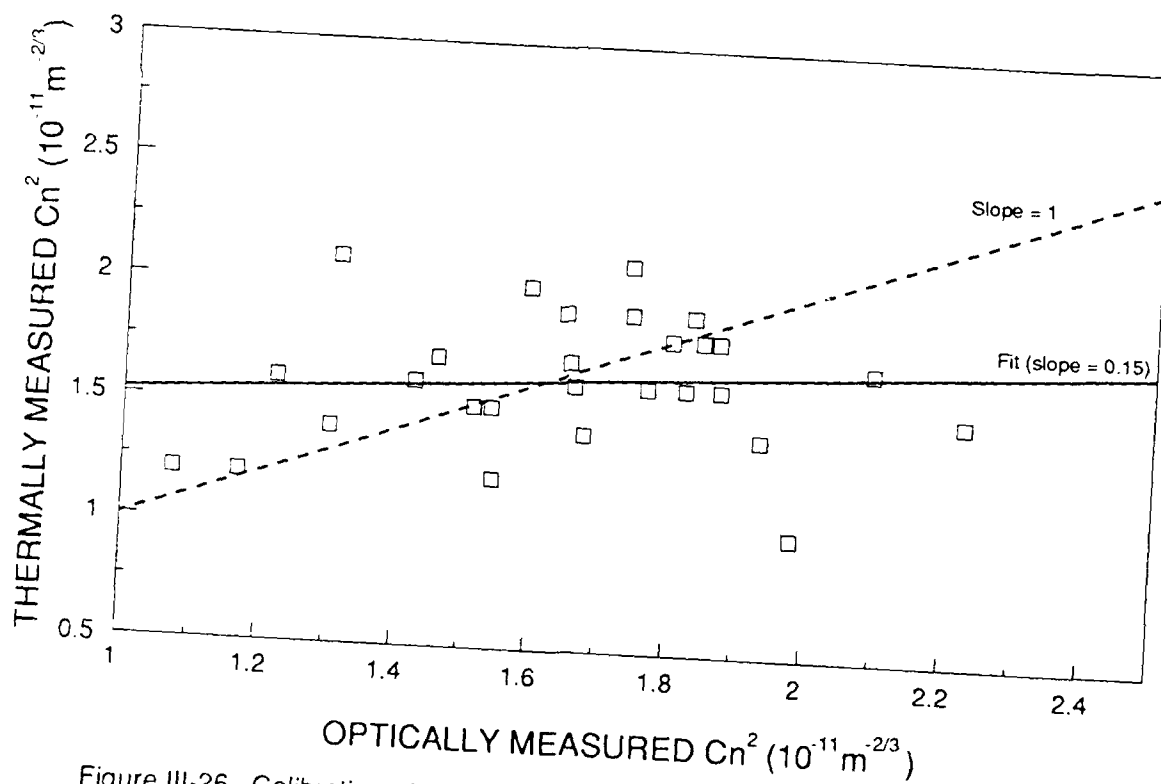


Figure III-26. Calibration of optical turbulence diagnostic against thermal diagnostic. Agreement with line of slope = 1 is good. But scatter is large and fit has slope = 0.15. Thermal diagnostic was employed for all experiments.

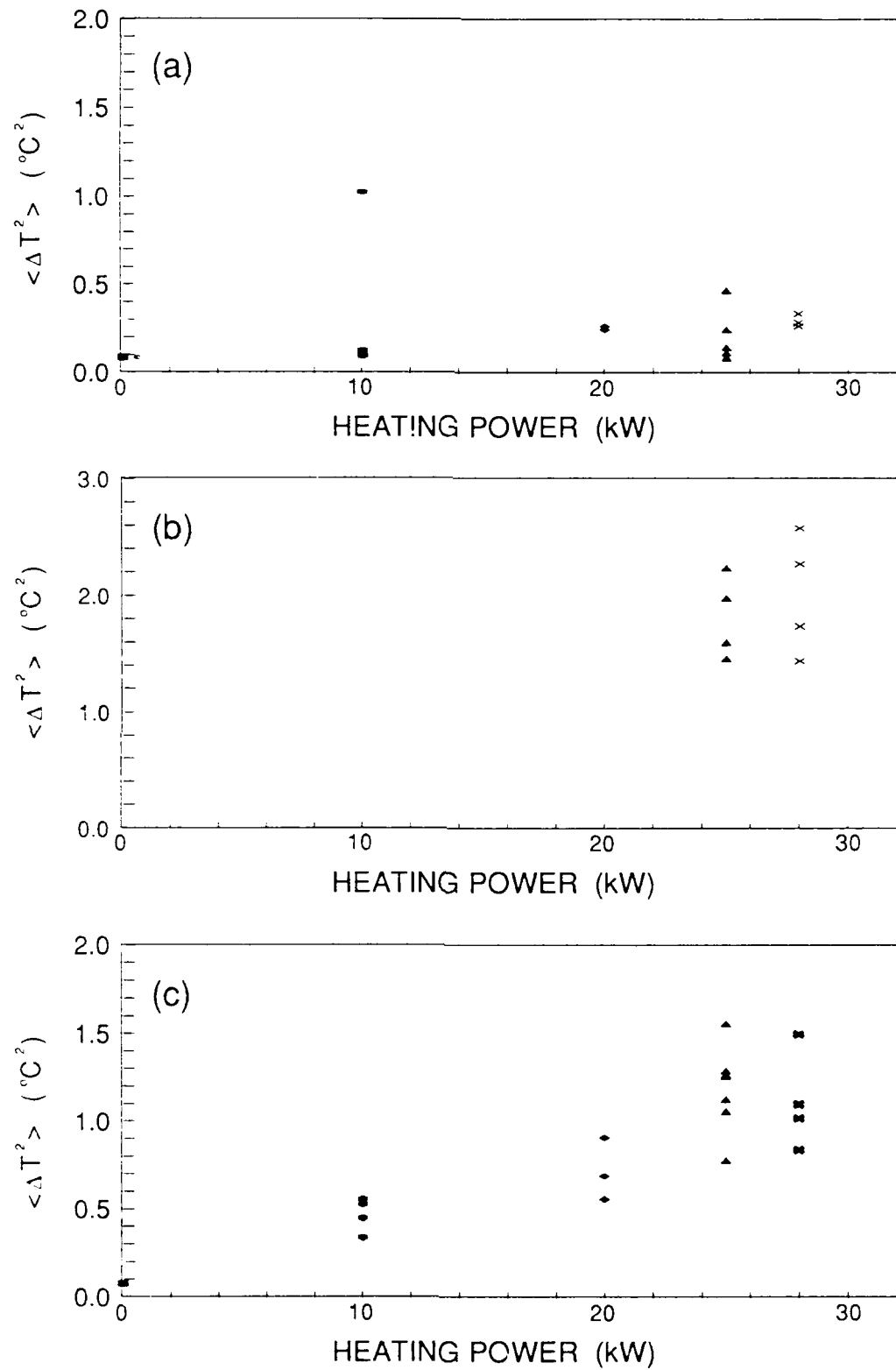


Figure 27. Temperature differences as a function of heating power (turbulence strength). (a) Position F6, near the wall; (b) Position D5, on centerline; (c) Position D6, on centerline further downstream.

data as a function of electrical heating power at three turbox positions. The data in figure III-27a was collected with the temperature probes at position F6 (see figure III-11) near one wall of the turbox and at the extreme downstream end. The measured values of  $\langle \Delta T^2 \rangle$  at this position are substantially lower than those measured on the center line (D5 and D6 in figures III-27b and III-27c, respectively). However, data measured symmetrically on the other side of the turbox (B4 - B6) and at the next inside positions, C3 - C6 and E3 - E6, were very similar to the center line data, indicating that the artificially generated turbulence is uniform over more than 80% of the turbox width. In addition, the data plotted in figures III-27b and III-27c are virtually identical, indicating that the turbulence is uniform over the region sampled by the multiple-passed optical comm link.

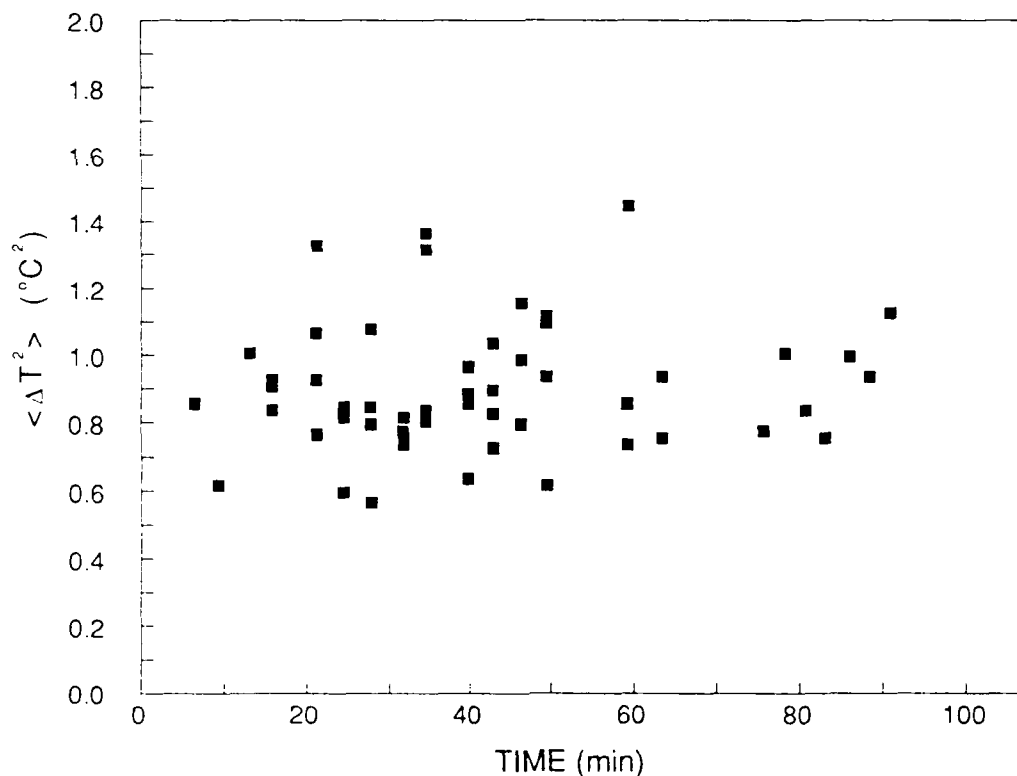


Figure III-28. Long term temperature difference measured on centerline in turbox at position D5 with 25 kW of power.

$\langle \Delta T^2 \rangle$  is plotted in figure III-28 as a function of time over 90 min. This data indicates that the turbox is able to hold one of its most severe conditions stable within  $\pm 40\%$  of the average value over very long periods of time. This is important since experiments are repeated several times over at least 10 minutes to ensure reproducibility. Reproducibility of a particular turbulence condition is therefore  $\pm 40\%$ .

With a 0.3 to 1 cm diameter optical comm link optical beam propagating through the turbox as shown in figure III-9, the variance on the different detectors was measured both when conjugating and with a mirror in front of the sodium cell and with several different transponder apertures. The turbulence strength was also varied over the range  $10^{-16} \leq C_n^2 \leq 3.3 \times 10^{-11} \text{ m}^{-2/3}$ . In each case, the comm link figure of merit was computed. These data are plotted in figure III-29 and III-30 for the experiments performed with a mirror and with phase conjugation, respectively. The data in figure III-30 is excellent and fits our performance expectations very well. Both sets of data are plotted together in figure III-31 for comparison.

As expected with the three transponder apertures tested, the non-conjugated (mirror) comm link exhibits a minimum FOM value of  $[\sigma_s^2/\sigma_p^2]_M = 2^{11/6} = 3.56$ , and a high degree of scatter with the largest aperture tested. The transceiver aperture (1.3 cm) was only slightly larger than the largest launched beam diameter (1 cm). The transverse coherence diameter for the turbox experiments is about 3 mm. With this beam the centroid of the returned beam moves on and off of the aperture. Consequently, the observed larger variances on the 1 cm diameter aperture experiments should be expected.

The phase conjugated comm link exhibits well corrected behavior (figure III-30). All of the data is clustered around  $[\sigma_s^2/\sigma_p^2]_{PC} = 1$ , and with very little scatter. There appears to be no correlation between the strength of the turbulence and the ability of the link to correct it.

The four wave mixing phase conjugated optical communication link exhibits reduced intensity variance compared to a one-way link, both over the 1 km open air link and through the turbox, an artificial turbulence generator. This improvement is as little as a factor of 3.56 ( $2^{11/6}$ ), but may be much larger depending on how much larger the

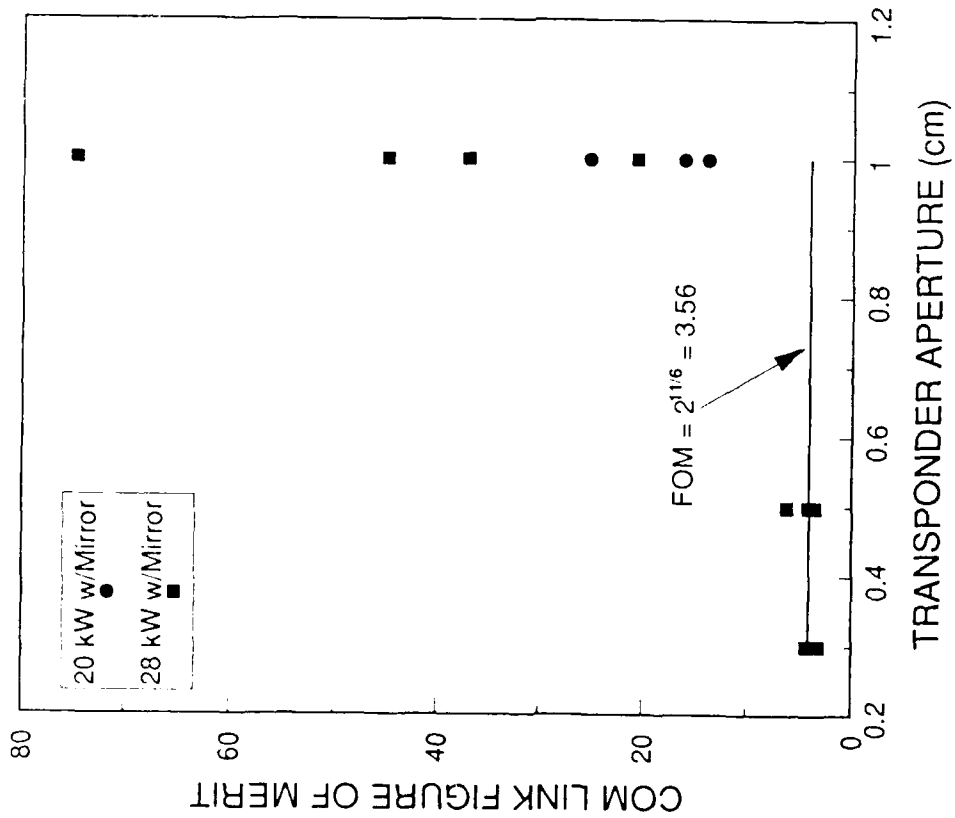


Figure III-29. Turbox figure of merit measured for experiments performed with a mirror. Straight line is at  $FOM = 2^{11/6}$ . Initial collimated beam diameter is 1 cm; transceiver aperture diameter is 1.3 cm.

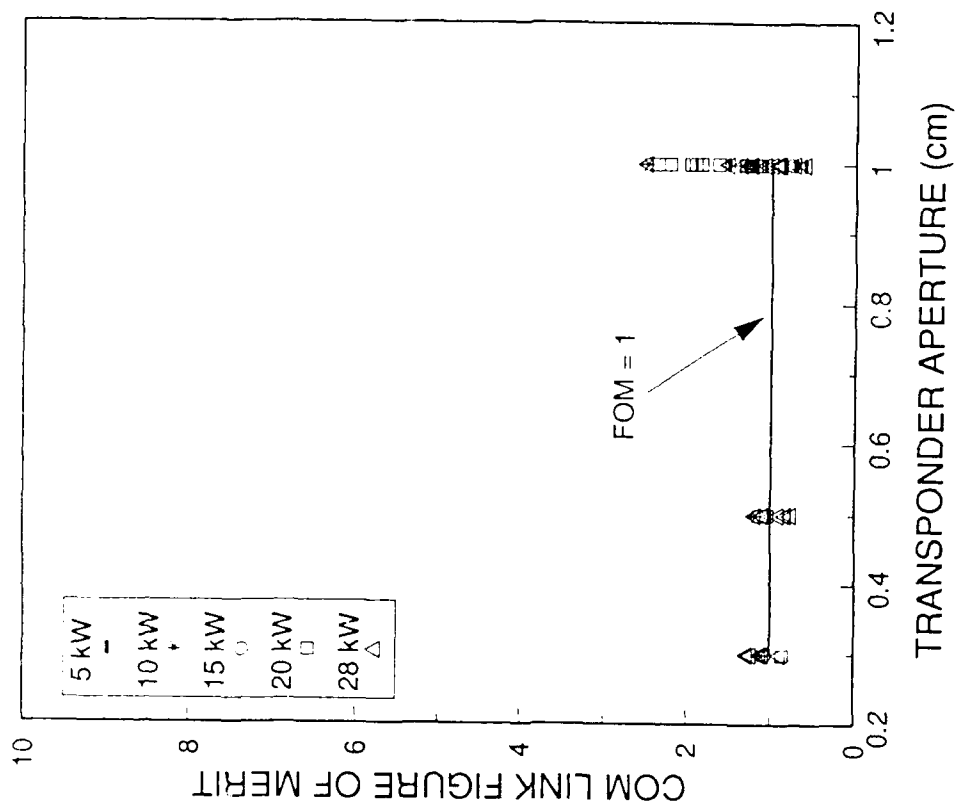


Figure III-30. Turbox figure of merit measured for experiments performed with phase conjugation. Straight line is at  $FOM = 1$ . Initial collimated beam diameter is 1 cm; transceiver aperture diameter is 1.3 cm. Note factor of 8 scale change compared to figure III-29.

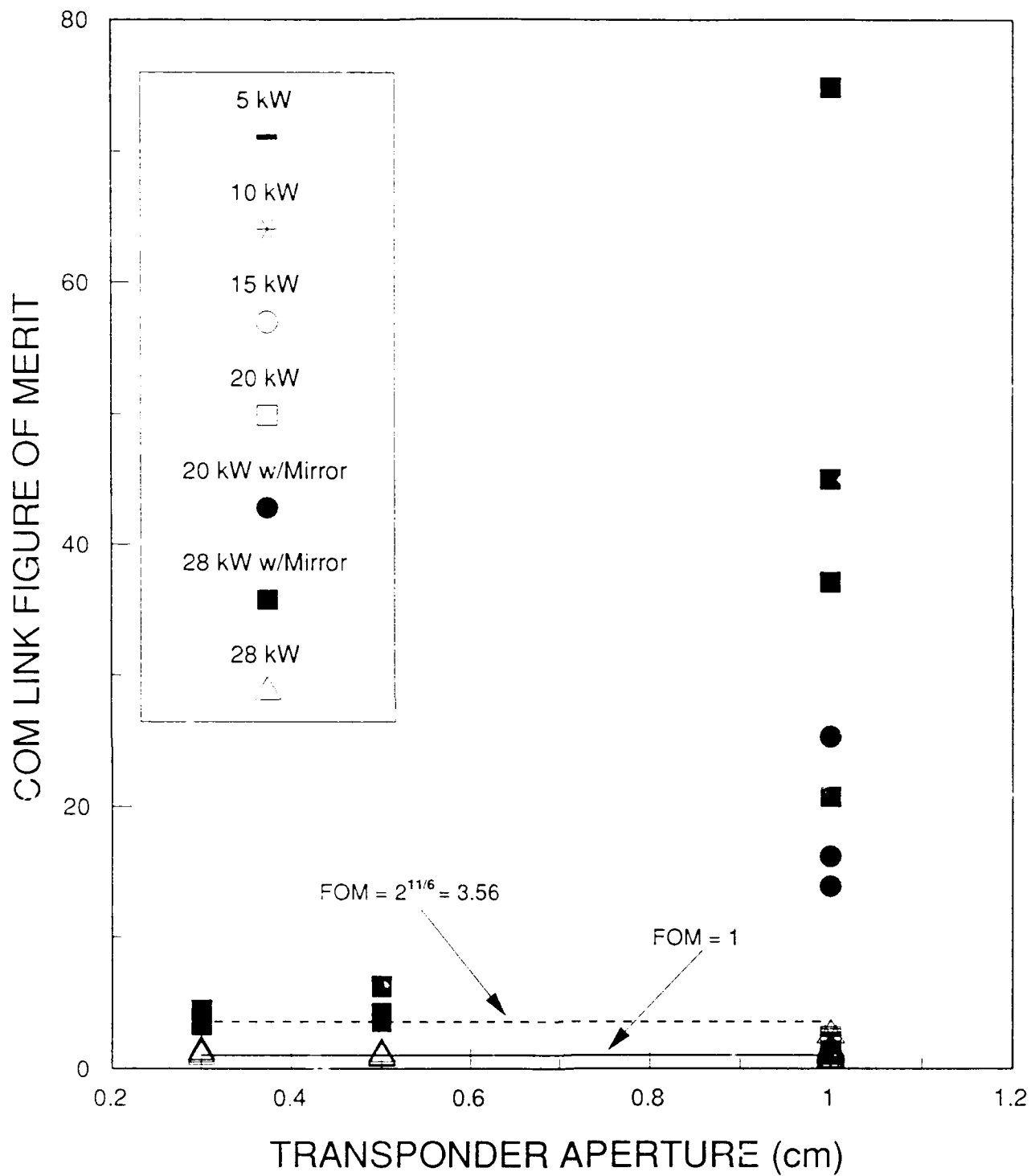


Figure III-31. Turbox figure of merit measured for experiments performed with phase conjugation and a mirror. Straight lines are at FOM = 1 and  $2^{11/6}$ . Initial collimated beam diameter is 1 cm; transceiver aperture diameter is 1.3 cm



transceiver aperture is compared to the launched beam and how the turbulence is distributed over the link.

## IV. PHYSICS MODEL

The overall objective of the phase conjugated optical link physics modeling task was to increase our understanding of the interactions of atmospheric turbulence with phase conjugated optical comm links. Specifically, we want to be able to predict PC optical link performance for a given geometry and environment. In order to satisfy that objective, a PC optical link physics (POLIP) model has been developed and utilized to calculate the influence of apertures, overall optical comm link geometry and random inhomogeneities of the propagation medium on the PC reflectivity, fidelity and FOV. The values of relevant statistical properties obtained with the numerical simulation were compared with those obtained from analytical calculations for model calibration. The model was then employed to predict the performance of geometries and environments similar to the rooftop 1 km comm link and laboratory turbox experiments.

### 1. GENERAL MODEL DESCRIPTION

In order to address the physics issues associated with a PC optical communications link, a numerical wave optics code, GLAD-386, that runs on a 80386-based personal computer was used.<sup>19</sup> The design of GLAD allows the user to perform optical calculations by entering, through a set of commands, detailed information about the starting conditions, optical configuration, propagation geometry, and active medium.

The set of commands, POLIP, was created and processed to simulate the relevant PC link physics characteristics: optical configuration, focussing lenses and PC, propagation geometry and turbulence. This detailed wave optics description was supported with analytical calculations that make use of a modulation transfer function approach (see chapter 2) to calculate the relevant statistical quantities.

GLAD-386 is a fully 3-dimensional wave-optics code, where the optical beam is represented by a 2-dimensional complex amplitude array. The optical field is propagated along a given path by numerically solving the inhomogeneous wave equation.<sup>20</sup> The propagation path can include several optical elements: lenses, with or without

aberrations, mirrors, phase conjugators, etc., and turbulence.

In order to numerically solve the wave equation in the presence of optical elements and an active medium, a finite difference solution algorithm is applied to the calculation that consists of a small diffraction step in free space followed by a small propagation step in the medium. The numerical free space solution is performed with a Fast Fourier Transform (FFT) and is valid for either near or far field propagation. This technique is not only very efficient and can be applied to propagation steps of any length, but is also relatively insensitive to the nature of the medium or distribution to be propagated.

The main inaccuracies introduced by the model are all related to the discrete sampling and finite array size associated with the transverse spatial dimensions of the optical beam. Use of the FFT algorithm keeps errors in the propagation direction small and independent of the propagation step. In addition, energy is conserved to better than a factor of  $10^{-6}$ .

To reduce the magnitude of errors in the transverse spatial dimensions, the minimum array size and the sampling intervals or units can be chosen for each particular case by minimizing the aliasing errors and maximizing the resolution in the beam center or shadow depending on the case of interest.

The aliasing errors arise mainly because as the beam propagates and diffracts, energy is forced outside the bounds of the array but is folded back into the array by the FFT process. An approximate expression for these errors in the near field is:

$$\epsilon_b = (\lambda z)^{1/2} / (2M\Delta x) \quad (\text{IV-1})$$

for the bright regions inside the geometric aperture areas, and

$$\epsilon_d = \lambda z / [5(M\Delta x)^2] \quad (\text{IV-2})$$

for the dark regions in the shadow. In these expression,  $M$  is the number of array points,  $\Delta x$  is the interval size in any of the transverse directions,  $\lambda$  is the wavelength and  $z$  is the effective propagation distance. Hence, for a typical case where the wavelength is  $0.59 \mu\text{m}$  and  $z = 1 \text{ km}$ , intensity errors smaller than 1% in the bright region require  $M\Delta x \geq 1.2 \text{ m}$ . On the other hand, resolving the beam center requires  $\Delta x \leq \lambda z/a$ , where

a is the aperture size. Thus, for  $a = 5 - 10$  cm,  $\Delta x \leq 1 - 0.5$  cm, and  $M > 100 - 200$  to satisfy the 1% error requirement. This value of  $M$  is a reasonable array size.

The atmospheric turbulence is modeled by inserting appropriate random phase aberrations or "screens" in the propagation path to simulate the random refraction index fluctuations. The random aberrations are distributed in spatial frequency  $k$  according to a given spectrum. For the current code version, the random phase aberrations are distributed according to a Von Karman<sup>7,21</sup> spectrum, and the inner and outer length are input parameters. This turbulence description is instantaneous (single realizations) and multiple runs are necessary to obtain averaged statistics and measurable diagnostics.

The turbulence aberrations are characterized in the code by the autocorrelation diameter,  $r_0$ , sometimes known as Fried's parameter. This parameter is twice the transverse coherence radius for a plane wave.

$r_0 = 2 \rho_0$ , where

$$\rho_0^p = [1.45 R k^2 \int_0^1 C_n^2(v) dv]^{-3/5} \quad (\text{IV-3})$$

where  $R$  is the total propagation length and the variable  $v$  is the ratio of the variable propagation distance  $z$  to  $R$ . The particular turbulence characteristics utilized in the numerical simulation of the PC comm link are summarized in section IV.3, where the results obtained with POLIP are described in detail.

## 2. TESTS WITHOUT TURBULENCE

The high and low spatial frequencies of the outgoing beacon beam and returning conjugate wave are filtered by the combination of apertures, lenses, potential tilts and diffraction. This filtering decreases the conjugated power, alters the spatial wavefront of the returning beam and is independent of the turbulent aberrations although it is compounded by them. In order to understand the ultimate limitations of a PC comm link, it is necessary to investigate the influence of the aperture/tilt combination on the received power and peak intensity. The next two subsections describes the results of such an investigation.

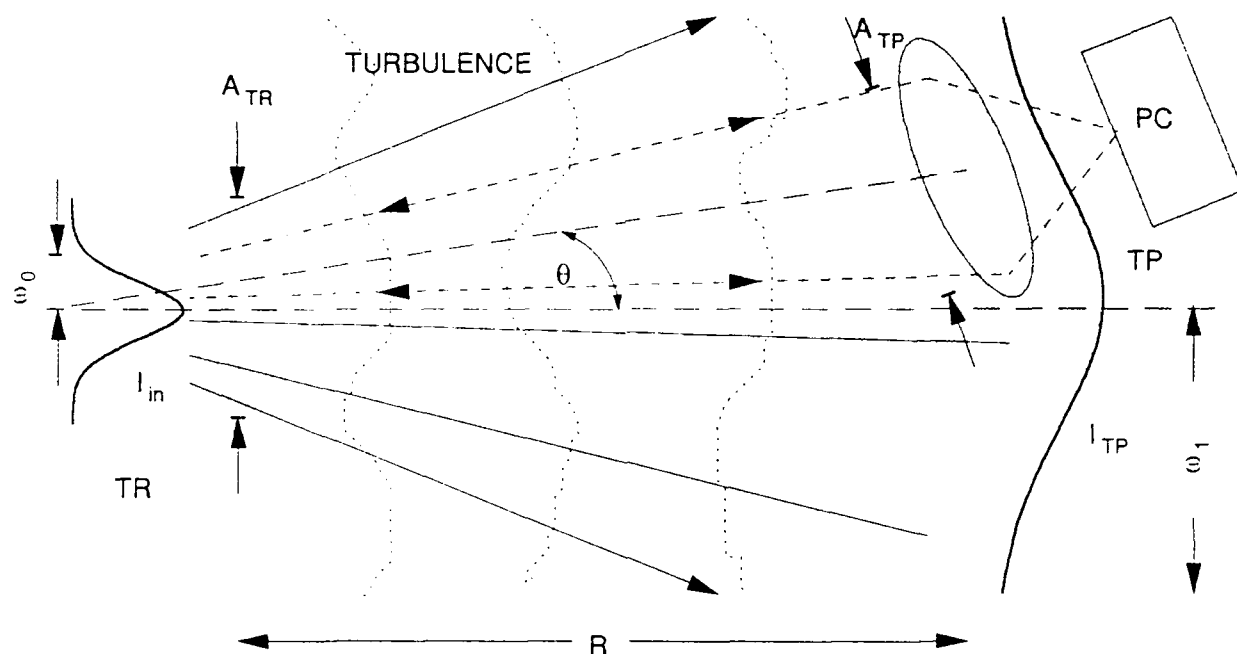


Figure IV-1. Schematic of the geometry for aperture/tilt studies.

a. Numerical Results -- A schematic of the geometry used for the aperture/tilt studies in the absence of turbulence is shown in figure IV-1. The input (beacon) optical beam of waist radius  $\omega_0$  and wavelength  $\lambda$ , is propagated through the transmitter aperture of diameter  $d_{TR}$  and is received after a propagation distance  $R$  by the transponder (TP) with aperture  $d_{TP}$ . After phase conjugation the beam is propagated back to the transceiver (TR), and through the receiver aperture,  $d_{TR}$ .

The angle between the transceiver/transponder optical axis and the beacon direction is  $\theta_i$ . For simplicity the phase conjugator and transponder apertures are the same (no further degradation occurs between the transponder and the conjugator). The ratio of the optical beam waist radius,  $\omega_1$ , at the transponder to the propagation length  $R$  is defined by the beam angle  $\theta_b$ , and the ratio of the aperture radius  $d/2$  to the propagation length  $R$  is defined by the aperture angle  $\theta_a$ .

The ratio of the power received at the transponder,  $P_{TP}$ , and at the transceiver,  $P_{TR}$ , to the input power,  $P_{in}$  as well as the ratio of the received to input peak intensity  $I_p^{TP}/I_p^{in}$ , depend on the ratio of the total beam angle plus tilt to the aperture angle and were evaluated numerically for different initial conditions. A focused or collimated Gaussian

(input) beam was propagated through hard circular apertures defined at the transceiver and transponder positions and phase conjugated. The input beam waist, the tilt angle and the aperture radius were varied in a consistent manner to evaluate the influence of the various relevant parameters on the received power. An ad-hoc model was subsequently developed based on this numerical parametric study. This model is discussed in section IV.2.b.

Three specific cases illustrate the numerical results in the absence of turbulence. The overall geometry is shown in figure IV-1. The initial beam conditions and the transmitter aperture were the adjustable parameters:

Case 1: Gaussian input beam of waist radius  $\omega_0 = 1$  mm, with an infinite transmitter aperture and a propagation length of 600 m. This case is dominated by beam divergence up to tilt angles on the order of 1 to 2  $\theta_d^{TP}$  (see figure IV-2).

Case 2: Collimated input beam with waist radius  $\omega_0 = 5$  cm, and infinite transmitter aperture, with a propagation length of 1.1 km. This case is illustrated in figure IV-3 and is basically tilt dominated for  $\theta_t > \theta_b \approx 23$   $\mu$ rad if  $\theta_b \geq \theta_d^{TP}$ .

Case 3: Collimated input beam with a finite transmitter aperture of the same diameter as the transceiver aperture. This case, outlined in figure IV-4, results in smaller received powers due to diffraction.

Results are presented for three different transponder and transceiver aperture diameters: 30 cm, 10 cm and 5 cm. For simplicity the transponder and transceiver apertures are identical. Figures IV-2, IV-3 and IV-4 illustrate the variation in the receiver power and peak intensity at the transponder and at the transceiver with increasing tilt angle. For zero tilt, the received power at the transponder has to be proportional to the ratio of the beam waist at the transponder to the aperture radius. It is straightforward to calculate the power ratio  $r_{TP} = P_{TP}/P_{in}$  for zero tilt, a Gaussian beam and no diffraction effects from the transmitter. This has the form:

$$r_{TP}^0 = (P_{TP}/P_{in})^0 = 1 - \exp[-2(\theta_d^{TP}/\theta_b)^2] \quad (IV-4)$$

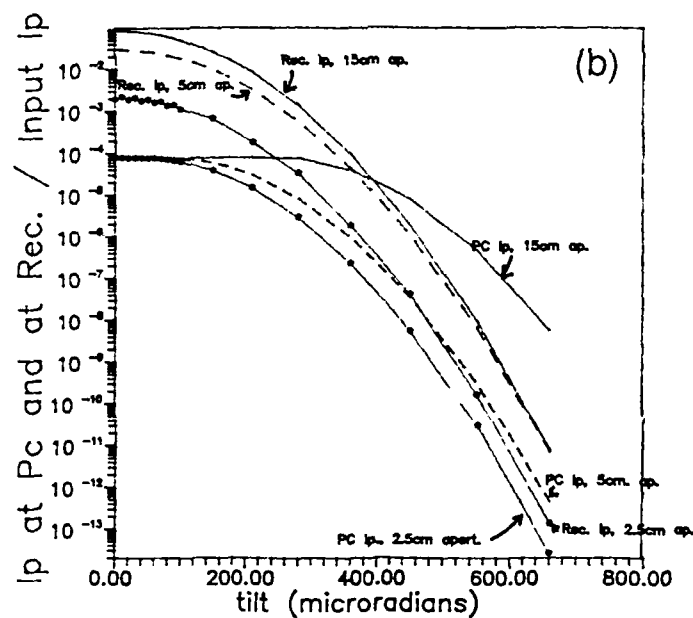
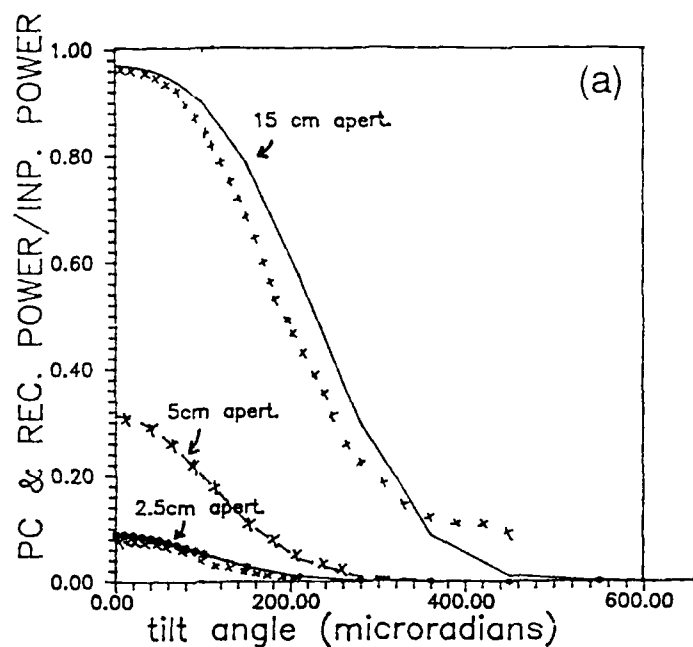


Figure IV-2. Variation of power and peak intensity at the PC and at the receiver with tilt angle for a divergence dominated case. Gaussian input beam,  $\omega_0 = 1$  mm,  $d_{trans} = \infty$ ,  $d_{rec} = d_{TP} = 5, 10$ , and  $30$  cm,  $R = 600$  m.  $x$  is from ad-hoc model.

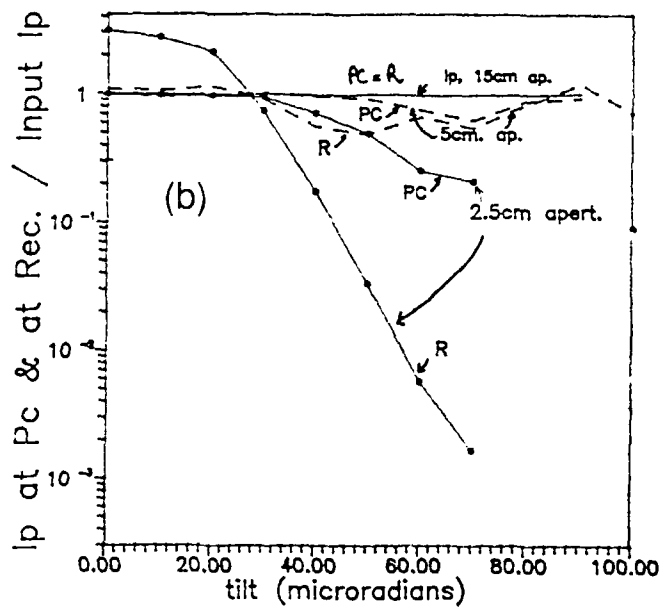
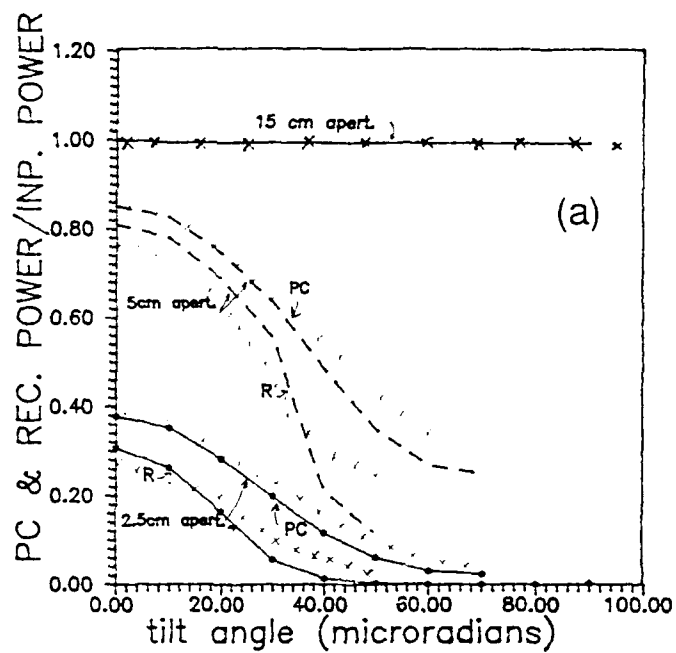


Figure IV-3. Variation of power and peak intensity at the PC and at the receiver with tilt angle for a collimated beam.  $\omega_0 = 5$  cm,  $d_{\text{trans}} = \infty$ ,  $d_{\text{rec}} = d_{\text{TP}} = 5, 10$ , and 30 cm,  $R = 1.1$  km. x is from ad-hoc model.



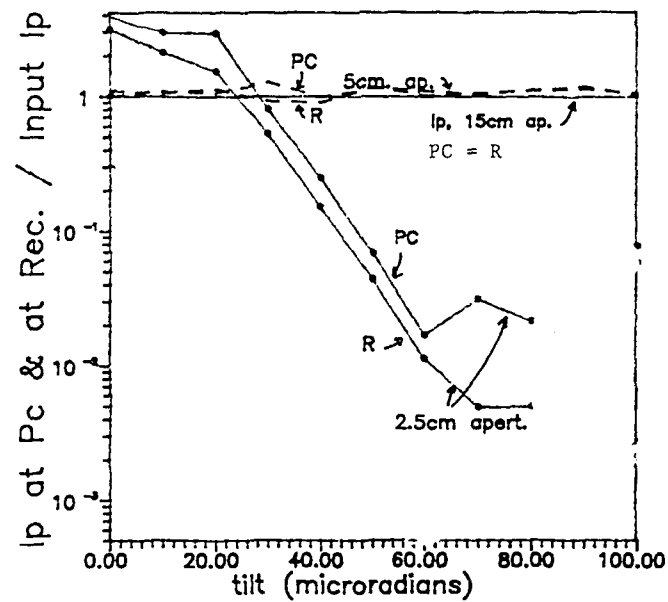
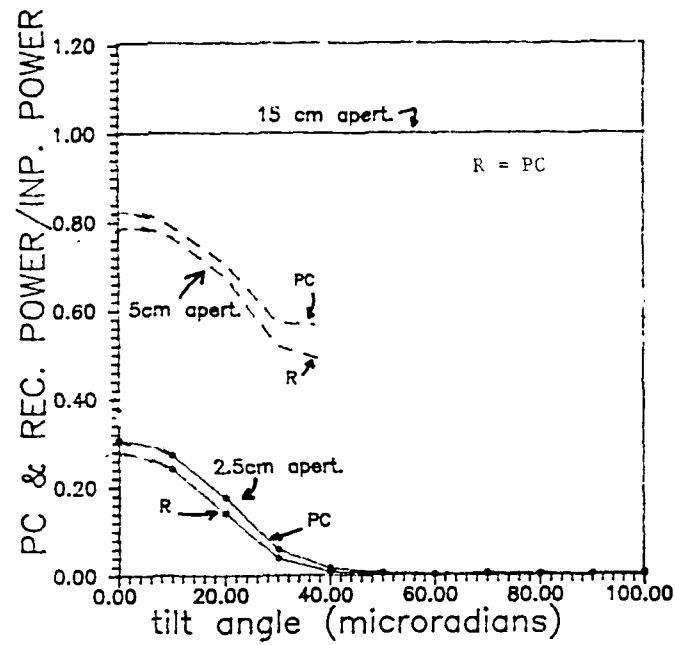


Figure IV-4. Variation of power and peak intensity at the PC and at the transceiver with tilt angle for a collimated beam.  $\omega_0 = 5$  cm,  $d_{\text{trans}} = d_{\text{rec}} = d_{\text{TP}} = 5, 10, \text{ and } 30$  cm,  $R = 1.1$  km.

In case 1, the beam diverges to a waist radius of  $\omega_1 = 11.25$  cm at the transponder. This is equivalent to a divergence angle  $\theta_b = \omega_1/R = 186 \mu\text{rad}$  and for  $\theta_i = 0$ , the numerical result agrees with equation (IV-4). The power received at the transponder decreases to  $1/e$  of its initial value for  $\theta_i \approx 2 \theta_d^{TP}$  for  $\theta_b > \theta_d^{TP}$  and for  $\theta_i \approx \theta^{TP}$  when the beam radius is smaller than the transponder aperture radius.

Figure IV-2 shows that no power is lost on the return leg between transponder and transceiver. The return beam waist is smaller than any of the modeled receiver apertures even for large tilts because the input beam waist is more than one order of magnitude smaller than the smallest transceiver aperture. For large tilts there is loss of fidelity in the PC and the return beam spreads and distorts due to the transponder aperture diffraction effects. However, the maximum spread is smaller than 2.5 cm. This result is consistent with the decrease in peak intensity between phase conjugator and transceiver also shown in figure IV-2. As the beam spreads due to finite diffraction effects, the peak intensity decreases.

The received peak intensity also decreases with tilt as expected since the beam is Gaussian and only the tail end is eventually received by the finite PC aperture as the tilt increases. Note that the tilt angle for which the peak intensity received at the PC starts to decrease (indicating that half of the beam is lost) coincides with the tilt for which the received power decreases to  $1/e$  of its maximum. The three orders of magnitude difference between peak intensity at the PC and at the transceiver is due to phase conjugation of a divergent beam.

A collimated beam is modeled in case 2, with a 5 cm beam waist. In this case transponder diffraction effects degrade the power received from the transponder for transceiver aperture radii on the order of or smaller than 5 cm. Figure IV-3 shows that for the large aperture case ( $d = 30$  cm), no power is lost for tilts smaller than  $100 \mu\text{rad}$ , compared to almost exponential power decrease with the smaller apertures. The larger propagation length modeled in this case translates to smaller aperture angles whereas collimation results in a beam angle on the order of the smallest aperture angle. Hence, there is an increase in received power for small tilts and a stronger tilt angle dependence than in the previous case.

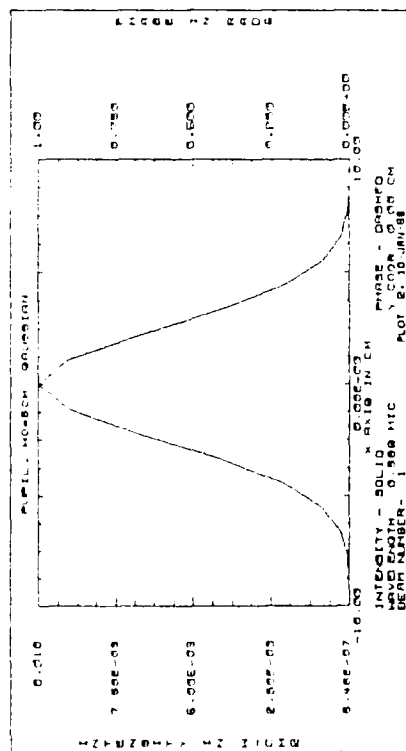
In case 2, the peak intensity remains fairly constant up to 100  $\mu$ rad tilts for apertures on the order of or smaller than the collimated beam radius (5 cm), indicating that more than half of the beam is received by the PC. In fact, the power received does not fall below 1/e for the range of tilt angles shown. This is not the case for the smaller 2.5 cm radius aperture, where the peak intensity starts decreasing for tilt angles larger than 40  $\mu$ rad. With this small aperture the ratio of received peak intensity at the transceiver to input peak intensity is larger than for small tilts, indicating main lobe focussing due to finite aperture diffraction effects.

The effect of diffraction due to a finite transmitter aperture is shown in figure IV-4. For a collimated beam, this effect translates into a degradation of power received at the phase conjugator. Also, the finite transmitter aperture deforms the beam received at the PC. The reduction in beam waist of the center lobe, increase in central intensity but overall beam spreading (Airy pattern) is consistent with a ratio of peak intensity received at the PC to input intensity larger than one and a ratio of total power received at the PC to input power much smaller than one. Focusing increases the number of higher frequencies received by the PC, thereby increasing its fidelity and reducing degradation between PC and transceiver.

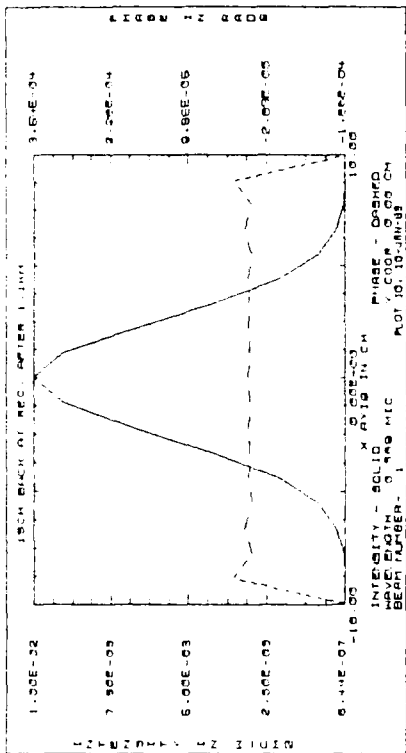
Changes in beam shape at the PC and at the transceiver with aperture diameter are illustrated in figures IV-5 and IV-6 obtained with the numerical simulation for case 3 with zero tilt. Figure IV-5 shows the input beam and the beam after the receiver aperture; figure IV-6 shows the optical beam at the PC. The solid lines correspond to the beam intensity and the dashed lines to its phase.

b. Ad-Hoc Model -- An analytical model was developed that predicts the ratio of power received at the PC and/or at the transceiver to the input power. This model is based on the results from the numerical simulations and although approximate it can be used for quick estimates of the effect of apertures in a PC link system.

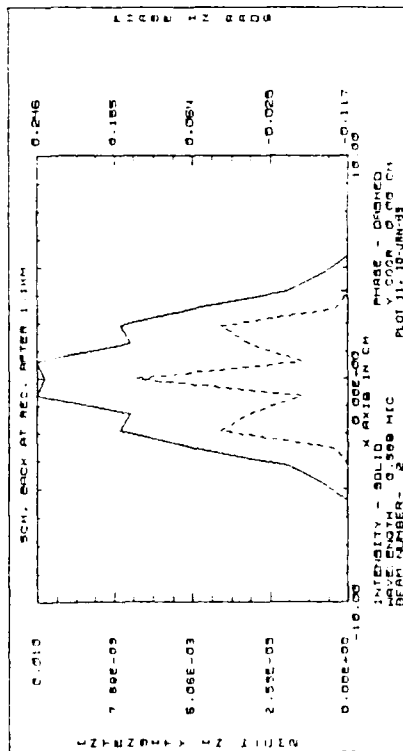
The ratio of the power received at the transceiver to the input power ( $r_{TR}$ ) is proportional to the ratio of the power received at the PC to the input power ( $r_{TP}$ ) reduced by a function that depends on how much optical beam is lost at the PC. This determines



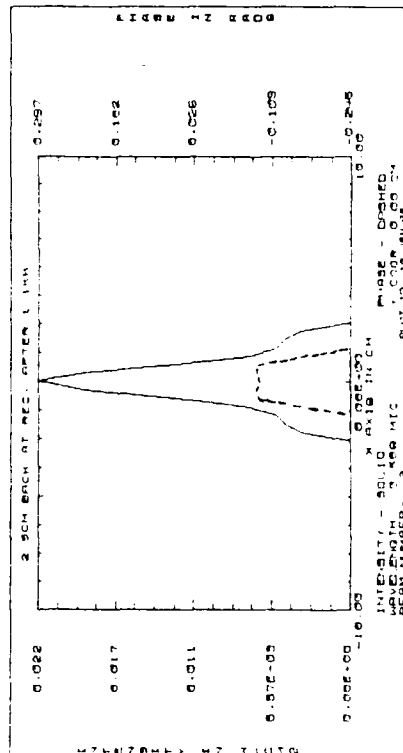
### INPUT BEAM



### 15 cm APERTURE RECEIVER

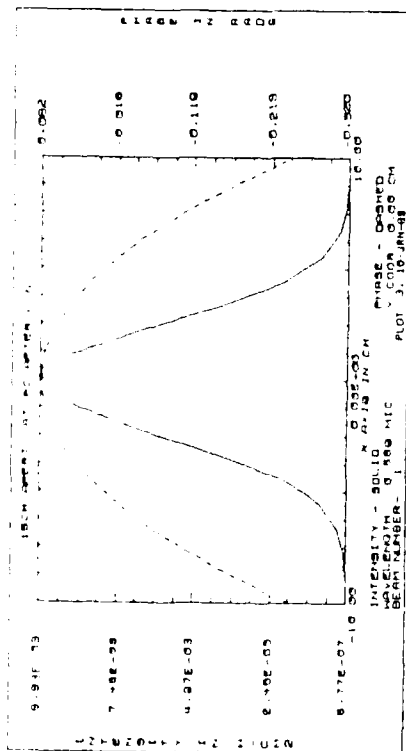


### 5 cm APERTURE RECEIVER

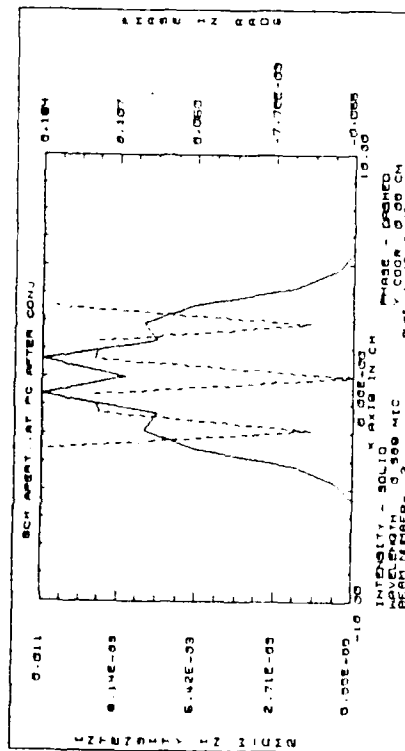


### 2.5 cm APERTURE RECEIVER

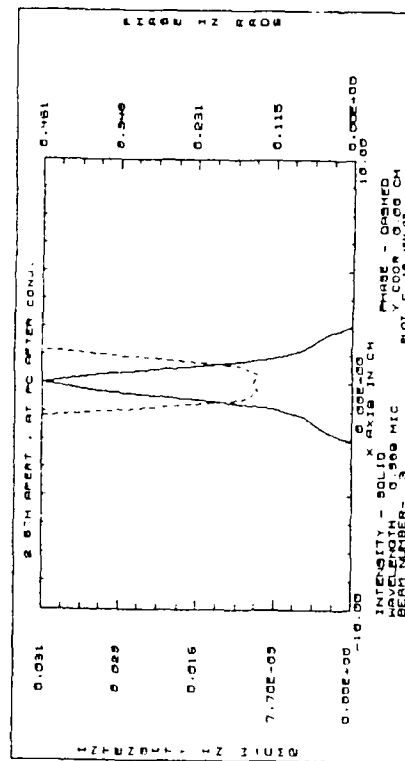
Figure IV-5. Intensity and phase profiles of the input and received beams for case 3 with zero tilt.



15 cm APERTURE



5 cm APERTURE



2.5 cm APERTURE

Figure IV-6. Intensity and phase profile of the beam received at the phase conjugator for case 3 with tilt.

the influence of finite transponder aperture effects and hence optical beam lost at the transceiver due to the resulting beam spreading. The  $r_{TP}$  is basically the power received for zero tilt reduced by tilt effects and diffraction effects. These ratios can be analytically described by the following ad-hoc formulas:

$$r_{TP} = 4\{1 - \exp[-2(\theta_d^{TP}/(\theta_b + \alpha_1 \theta_{dif}^{TR} + \alpha_2 \theta_i^n))^2]\} / \{3 + \exp[(\theta_i/\alpha_3 \theta_d^{TP})^3]\} \quad (IV-5)$$

where

$$\alpha_1 = \theta_b / (3 * \theta_d^{TR})$$

$$\alpha_2 = [2 \theta_d^{TP} / (\theta_b + \theta_{dif}^{TR})]^4$$

$$\alpha_3 = 1 + \theta_b / (\theta_d^{TP} + \theta_b)$$

and where the beacon beam divergence,  $\theta_b$ , and the finite diffraction angle,  $\theta_{dif}$ , are defined as:

$$\theta_b = \omega_o [(1-R/f)^2 + R^2/(\pi\omega_o^2/\lambda)^2]^{1/2}/R$$

$$\theta_{dif} = 1.2 \lambda/d$$

and  $f$  is the focal length of the transmitted beam. In general the beacon beam will be collimated ( $R < f$ ,  $R < (\pi\omega_o^2/\lambda)$ ) or focussed at the transponder,  $R = R_{TP}$  and the initial waist  $\omega_o$  chosen to avoid any effects due to the transceiver finite aperture and therefore  $\alpha_1 \rightarrow 0$ .

The power at the transceiver to input power ratio  $r_{TR} = P_{TR}/P_{in}$  was found to satisfy the following beam, diffraction, and aperture angular dependence:

$$r_{TR} = r_{TP} \{ [\exp(-(\theta_d^{TP}/\theta_{tot})^4) \exp(-(\theta_{dif}^{TP}/2\theta_d^{TR}) - \beta(\theta_i / \theta_d^{TR})) + 2 \exp(-(\theta_{tot}/\theta_d^{TP})^4)] / [1 + \exp(-(\theta_{tot}/\theta_d^{TP})^4)] \}$$

where  $\beta$  and  $\theta_{tot}$  are given by

$$\beta = \theta_i / (2 \theta_d^{TR} + 3 \theta_{dif}^{TR})$$

$$\theta_{tot} = 0.5 (\theta_i + \theta_b) + \theta_{dif}^{TR}$$

An analysis of the expression above shows that if most of the beacon beam goes through the transponder aperture,  $\theta_{\text{ta}} < \theta^{\text{TP}}$ , the first term in that expression can be neglected and no power is lost between the transponder and the transceiver. If  $\theta_{\text{ta}}$  is sufficiently larger than  $\theta^{\text{TP}}$ , the second term becomes small and the power lost between transponder and transceiver depends on the conjugated beam diffraction relative to the transceiver aperture.

The results obtained using this ad-hoc model are illustrated in figures IV-2 through IV-4, with a cross symbol line.

### 3. TESTS WITH TURBULENCE

In order to use the model described in section IV.1 to simulate the effect of turbulence on a PC link, it was necessary to calibrate the numerical effects of the turbulence and to develop appropriate numerical diagnostics. This numerical calibration was performed by comparing the results of the code with the results obtained using an analytical modulation coherence function (MCF) model.

a. Numerical Turbulence Description -- The problem of atmospheric turbulence characterization is separated into three parts: (1) determination of the effects of the various levels of turbulence (phase screens) in terms of the transverse coherence diameter,  $r_o = 2p_o$ , for each level [see equations (III-1) and (III-2)], (2) summation of the  $r_o$ 's, and (3) implementation of aberration using the  $r_o$  parameter. The wavefront is calculated in terms of Fried's parameter  $r_o$  and the inner and outer scale as input parameters (see reference IV-1). Because  $r_o$  depends on the integrated value of the structure function along the propagation path, its value can be determined from optical measurements for a given experimental configuration.

The number of levels is determined from either a physical reason, such as nonuniform turbulence (e.g. stronger near the ground or in the boundary layer of an aircraft), or from a numerical one, such as the need to use more than one turbulence screen or phase aberration as the beam diffracts to simulate a given turbulence strength.

The summation of  $r_o$ 's for different levels takes the form:

$$r_{\text{total}} = [r_1^{-5/3} + r_2^{-5/3} + \dots]^{-3/5}$$

Thus, propagation through N layers of equivalent aberration of  $r_o$ , which occurs in horizontal propagation, will result in  $r_{\text{total}} = r_o / N^{3/5}$ . In order to take into account the effect of turbulence in the beam diffraction (or the reverse), propagation over considerable distances is accomplished either by taking short steps of simple diffraction in vacuum alternating with short steps of aberration or by adding accumulated phase to the beam phase. The number of steps or "turbulence screens" depends on the magnitude and spatial frequencies of the aberration and the system configuration.

In general, a good measure of the minimum  $r_o$  per screen is given by the requirement that  $r_o$  be larger than the Fresnel length of propagation for that particular screen,  $r_o > (z_i \lambda)^{1/2}$ , with  $z_i$  the length propagated before the introduction of another screen. In section IV.3.c this problem is illustrated and the number of necessary screens is calibrated by comparison with the MCF model results and by numerical convergence.

b. Numerical Diagnostics -- A set of GLAD-386 commands were developed to either calibrate the model or numerically simulate the experimental diagnostics. The numerical diagnostics developed to predict performance are:

- Instantaneous (single realization) peak intensity and power through a given aperture.
- Averaged peak intensity and power through a given aperture (including a pinhole).
- Aperture averaged log amplitude variance,  $\sigma_x$ ,

$$\sigma_x^{2s} \approx 0.56 k^{7/6} R^{11/6} \int_0^1 C_n^2(v) (1-v)^{5/6} v^{5/6} dv,$$

where  $k$  is the wavenumber ( $2\pi/\lambda$ ),  $C_n^2$  is the index structure constant,  $R$  is the total propagation length and the variable  $v$  is the ratio of the variable propagation distance  $z$  to  $R$ .



- Aperture averaged intensity variance  $\sigma_I^2 = [\langle I \rangle^2 - \langle I^2 \rangle]$  and hence the log intensity variance,  $\sigma_I^2$ ,

$$\sigma_I^2(I) \approx \langle [\ln I(r) - \langle \ln I(r) \rangle]^2 \rangle = \langle [\ln(I/\langle I \rangle) - \langle \ln(I/\langle I \rangle)]^2 \rangle.$$

The average quantities were obtained by running the code a large number of times with the same configuration and turbulence coherence parameter, but different random phase screens. In order to determine the number of runs necessary to obtain a "statistically meaningful" result, the model was calibrated for different configurations, as discussed in the following section.

c. Model Calibration -- The following numerical quantities were calibrated by parametric studies and comparison with the MCF model:

- Resolution along the propagation direction.
- Resolution normal to the propagation direction.
- Sensitivity to number of realizations
- Sensitivity to different aperture truncation for specific cases.

In order to compare the numerical results with MCF calculations that had already been performed in other projects<sup>22</sup>, the geometry utilized to perform most of these tests was similar to an actual field test rather than to the laboratory or the brassboard experiment PC link. This geometry is illustrated in figure IV-7: a 100 W Gaussian beam with full waist of 30 cm is propagated to its focus at 100 km. A further number of limited simulations were performed with the laboratory PC link geometry, with similar overall results lending credibility to the overall calibration conclusions.

Resolution along the propagation direction -- the number of phase screens was calibrated by performing simulations where the number was varied from 1 to 30 along the propagation path for a fixed overall transverse coherence diameter  $r_0$ . The average peak intensity and power through an aperture was then plotted as a function of screen number, and the numerical experiment was carried out for different turbulence strengths.

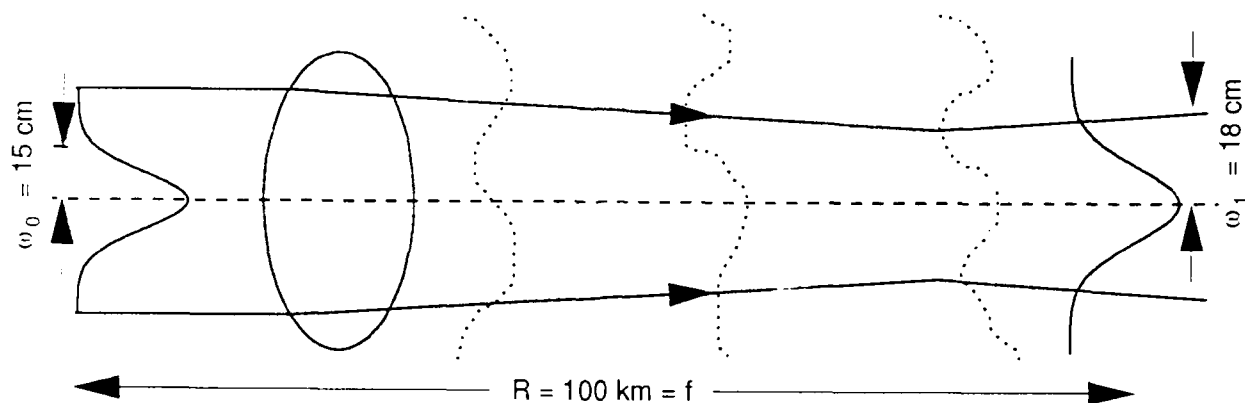


Figure IV-7. Configuration geometry for calibration tests.

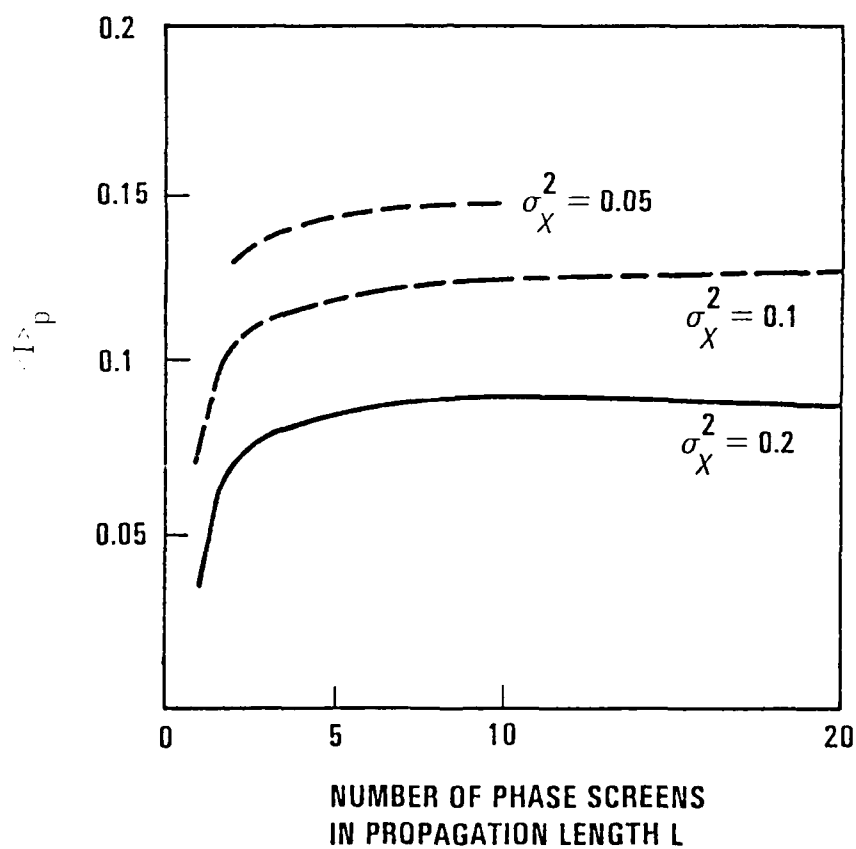


Figure IV-8. Sensitivity of the average peak intensity to the number of phase screens

The results are illustrated in figure IV-8 where the different turbulence strengths are expressed in terms of the log amplitude variance [ $\sigma_\chi = 0.124 k^{7/6} R^{11/6} C_n^2$ ]. The average peak intensity and power are expected to be independent of the number of screens when the effective  $r_o$  per screen ( $r_o^i$ ) is larger than the Fresnel length associated with the diffraction step  $z_i$  [ $r_o^i > (\lambda z_i)^{1/2}$ ] so that the scintillation per diffraction step is small. Assuming diffraction steps of identical length,  $R = N z_i$ , with a constant turbulence strength along the path, the transverse coherent length per screen is  $r_o^i = r_o N^{3/5}$ . Assuming "much greater" to be on the order of 10, an appropriate number of screens is

$$N \approx 10 \text{ Integer}[(\lambda R)^{1/2} / r_o]^{10/11},$$

which for the cases shown in the figure corresponds to  $N \approx 9, 13$  and  $18$  for  $\sigma_\chi \approx 0.05, 0.1$ , and  $0.2$  respectively. The figure shows that this is a factor 2 overestimate of the simulation results (4, 5, and 10 respectively).

Resolution normal to the propagation direction -- the optical beam is described by a complex field defined on an  $M \times M$  grid. This finite grid size limits the high and low spatial frequency resolution and hence the spatial frequency of turbulence that can be modeled. For an area  $A = X^2$ , only frequencies  $f$  within the interval  $1/X < f < M/X$  can be well resolved.

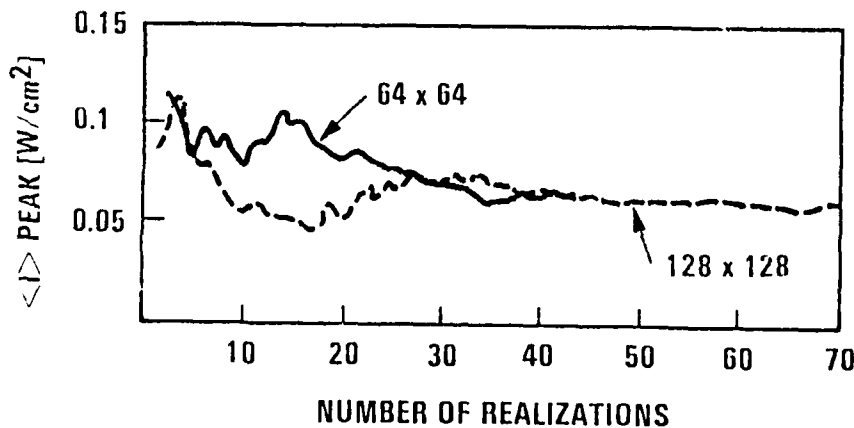


Figure IV-9. Sensitivity of the average peak irradiance to the number of realizations and grid size.

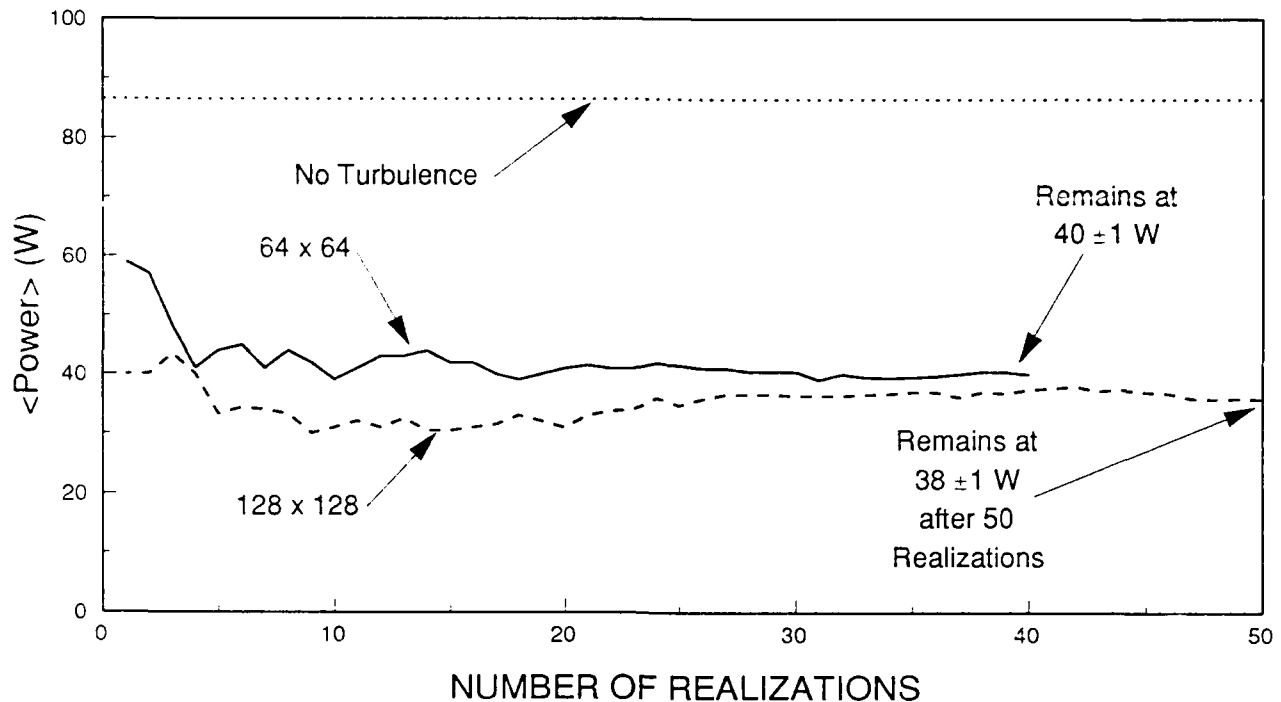


Figure IV-10. Sensitivity of the average power to the number of realizations and grid size. Power is average power in the bucket through an 18 cm radius receiver.

Typical atmospheric turbulence spectrums are expected to have contributions in spacial frequency down to 1 mm, and loss of accuracy should be expected when  $M \leq X/1$  mm. For the case illustrated in figure IV-9,  $X \approx 30$  cm and  $M$  should be  $\geq 300$  to avoid loss of accuracy. Figure IV-9, however shows that this is also an overestimate since for an appropriate number of realizations the loss of accuracy for  $M \approx 64$  is small compared to 128 (and 256 not shown in the figure). This was also found to be the case for the laboratory PC link geometry.

Sensitivity to the number of realizations -- Comparison with MCF models or experimental PC link measurements require the average of a large number of single physical propagation runs. The sensitivity of the results to the number of realizations was investigated by measuring the average peak intensity (see figure IV-9), average power in the bucket (see figure IV-10) and variance as a function of the number of realizations. It was found that for most cases 50 realizations provided adequate average values.

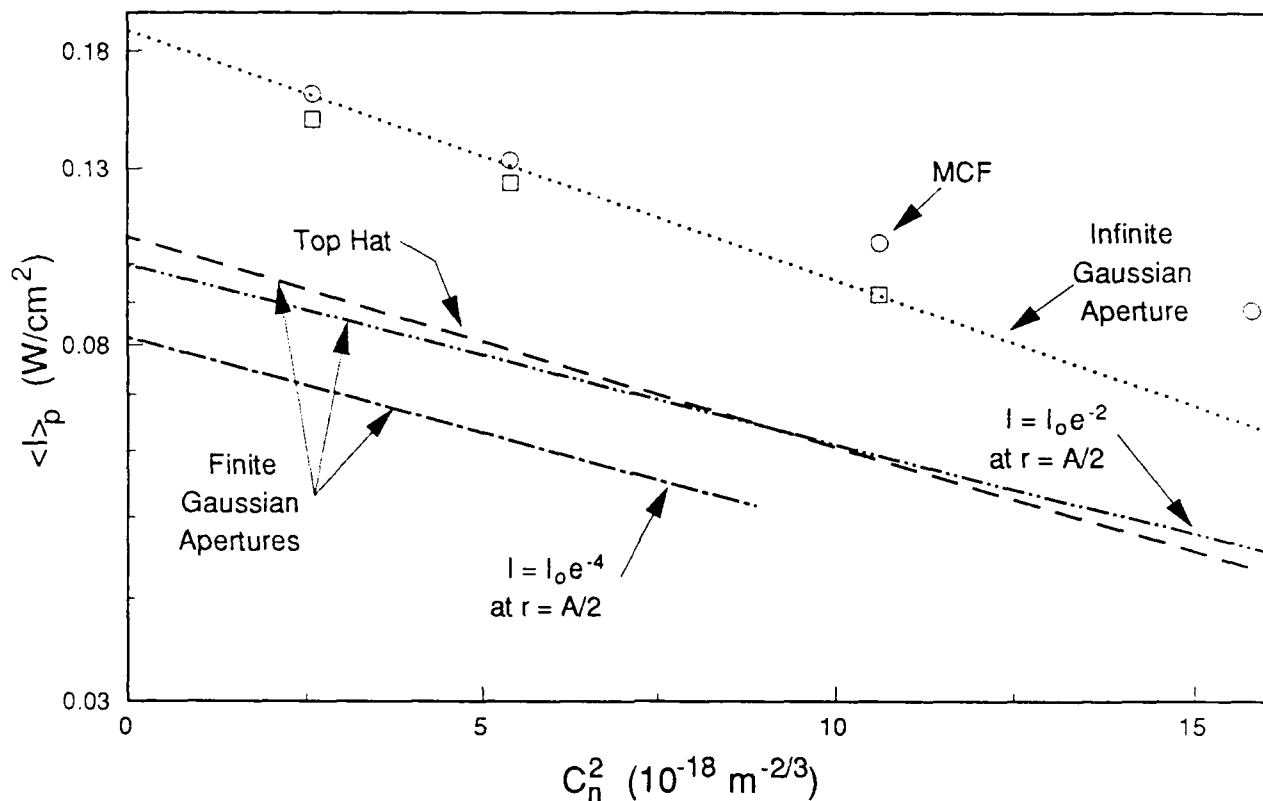


Figure IV-11. Comparison of numerical simulation and MCF calculation. Average peak irradiance versus index structure constant for different transceiver apertures.  $A = 30$  cm.

MCF model comparison -- The numerical simulations were compared with the results obtained with an MCF model described in chapter 2 and reference IV-3. This permitted evaluation of the turbulence strength necessary for failure of standard MCF calculations. In figures IV-11 and IV-12, the average peak irradiance and the intensity variance are plotted as a function of the turbulence structure function. These plots show that the MCF model is optimistic for strong turbulence. In particular as  $C_n^2$  varies from  $2 \times 10^{-18} \text{ m}^{-2/3}$  to  $2 \times 10^{-17} \text{ m}^{-2/3}$ , the intensity variance reaches the saturation value of 1.2 and departs from the analytical approximation of 4 times the amplitude log variance.

Sensitivity to transmitter aperture -- Numerical simulations were performed for different transmitter apertures. Results were obtained for the average peak irradiance, power in the bucket, and the intensity variance as a function of turbulence strength for an infinite Gaussian (usual analytical MCF model), a finite Gaussian aperture, a finite

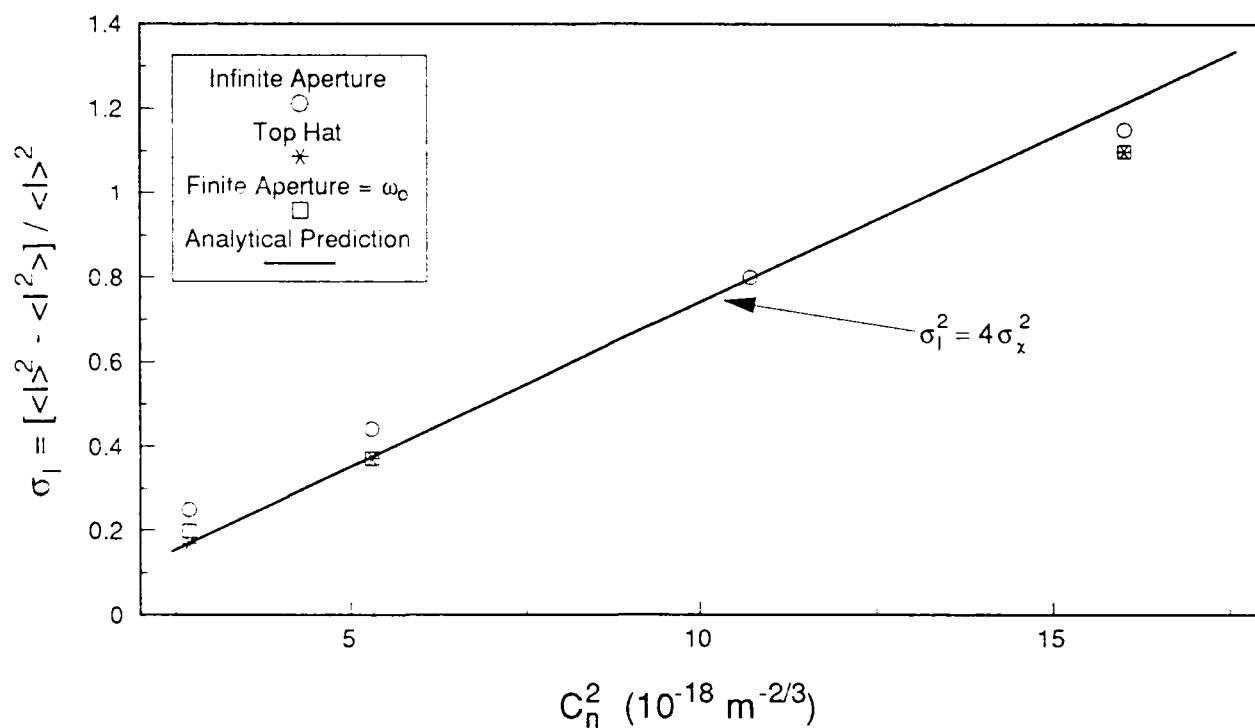


Figure IV-12. Normalized intensity variance as a function of the index structure constant.

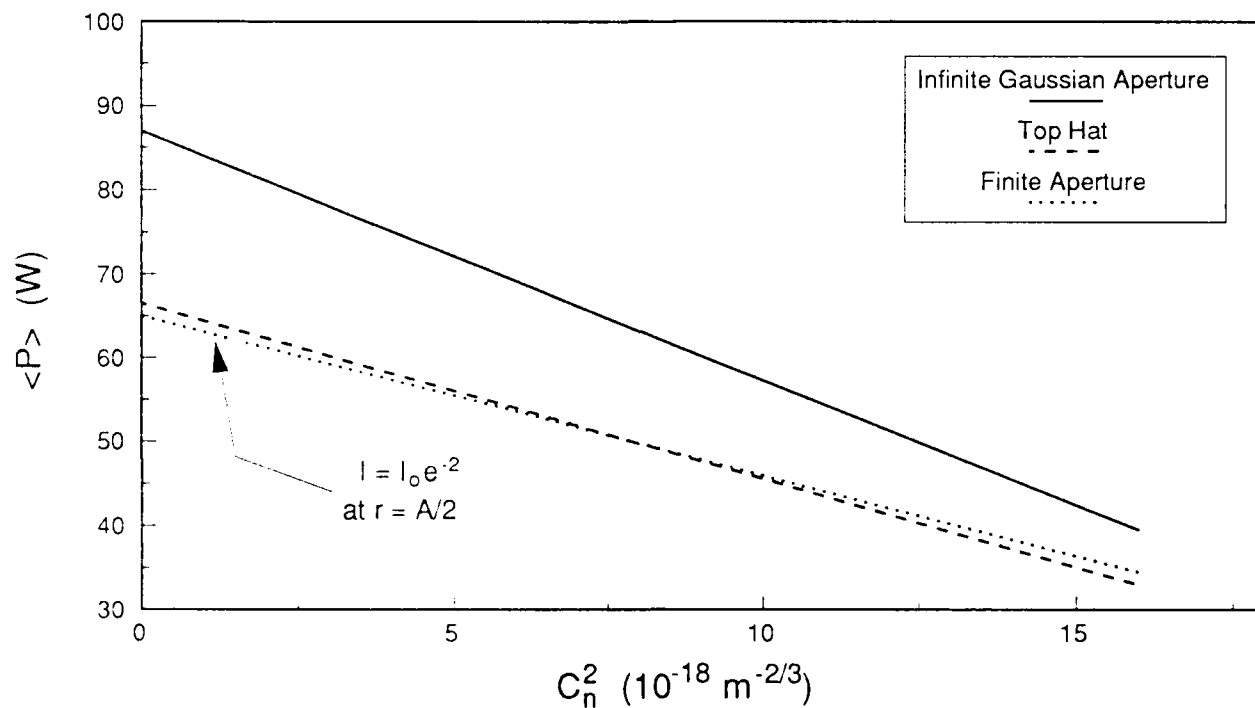


Figure IV-13. Average power through an 18 cm radius receiver as a function of the index structure constant for different transceiver apertures.

super Gaussian [decreases faster than  $\exp(-r^2/w_o^2)$ ], and a top hat. The results are illustrated in figures IV-11, IV-12, and IV-13, respectively. Although the peak intensity and power in the bucket decrease for a finite transmitter aperture due to finite diffraction effects, the slope is similar for the various cases yielding a linear power law for  $\ln(I/I_o)$  with  $1/r_o$ . ( $\ln(I/I_o) \approx -0.2 (d/r_o)$ , where  $I_o$  is initial peak intensity and  $d$  the transmitter aperture diameter.

#### 4. PC LINK SIMULATIONS

The numerical model was utilized to predict the performance of a PC optical link with a geometry similar to that utilized for the roof top experiment and for the turbox. The overall geometry is illustrated in figure IV-14. An optical beam of waist  $w_o$  is propagated through a telescope of apertures  $d_1$  and  $d_{TR}$ , and through a region of turbulence of length,  $R$ . It is then received by the transponder telescope of aperture  $d_{TP}$  and  $d_2$  and propagated to a PC or a mirror with aperture  $d_3 = d_2$  for most cases. The beam is phase conjugated and returned through the same transponder telescope and received by the transceiver telescope.

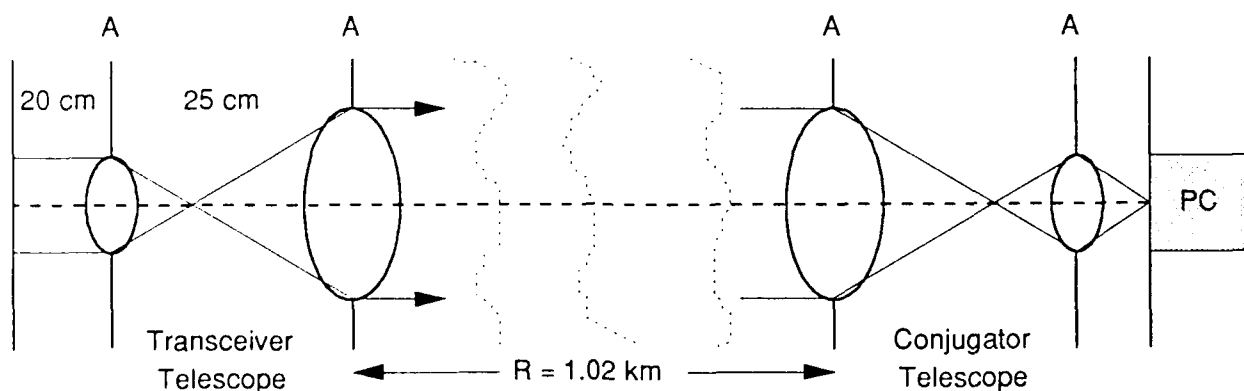


Figure IV-14. Configuration geometry for comm link performance predictions with a Gaussian beam,  $I = 10 \text{ mW/cm}^2$ ,  $w_o = 1 \text{ mm}$  (Characteristic of rooftop geometry. A = aperture, PC = phase conjugator.

a. Roof-Top Geometry -- A sufficient number of cases were simulated with turbulence and configuration characteristics of the roof-top experiment to predict the comparative performance of average power received at the transceiver. No numerical predictions of log intensity variance were obtained for comparison with experimental results. The optical beam, collimated by the transceiver telescope, is assumed to have an initial beam intensity of  $10 \text{ mW/cm}^2$  and an optical beam waist of  $w_0 = 1 \text{ mm}$ . The collimated beam size at the transceiver telescope output is  $2.5 \text{ cm}$ . The transceiver-to-transponder propagation length is  $1.02 \text{ km}$  and the inner and outer length scales are assumed to be  $1 \text{ mm}$  and  $1 \text{ m}$ , respectively.

Table IV-1. Rooftop geometry. Received power for different apertures and turbulence strengths.

TURBULENCE STRENGTH $C_n^2 \text{ (m}^{-2/3}\text{)}$	CONJUGATOR APERTURE (cm)	$P_{\text{REC}}/P_{\text{INP}}$
0	4.0	1.0
0	2.5	0.94
0	1.0	0.27
$10^{-14}$	2.5	0.93
$10^{-13}$	4.0	0.75
$10^{-13}$	2.5	0.67
$10^{-13}$	1.0	0.13

Table IV-1 shows a comparative chart of the ratio of the power received back at the transceiver to the input power for different apertures at the conjugator telescope (which are the same as for the transceiver), and various turbulence strengths,  $C_n^2$ . Results were also obtained with a mirror in place of the phase conjugator for the medium aperture. Figure IV-15 illustrates the degradation in received power with turbulence and for smaller apertures. For  $C_n^2 \approx 10^{-14} \text{ m}^{-2/3}$ ,  $r_0 \approx 2.5 \text{ cm} \approx (\lambda R)^{1/2}$  so that turbulence effects are expected to be negligible. In fact for almost any aperture that we simulated, (diameters 2, 5 and 8 cm) the differences in the results between no turbulence and



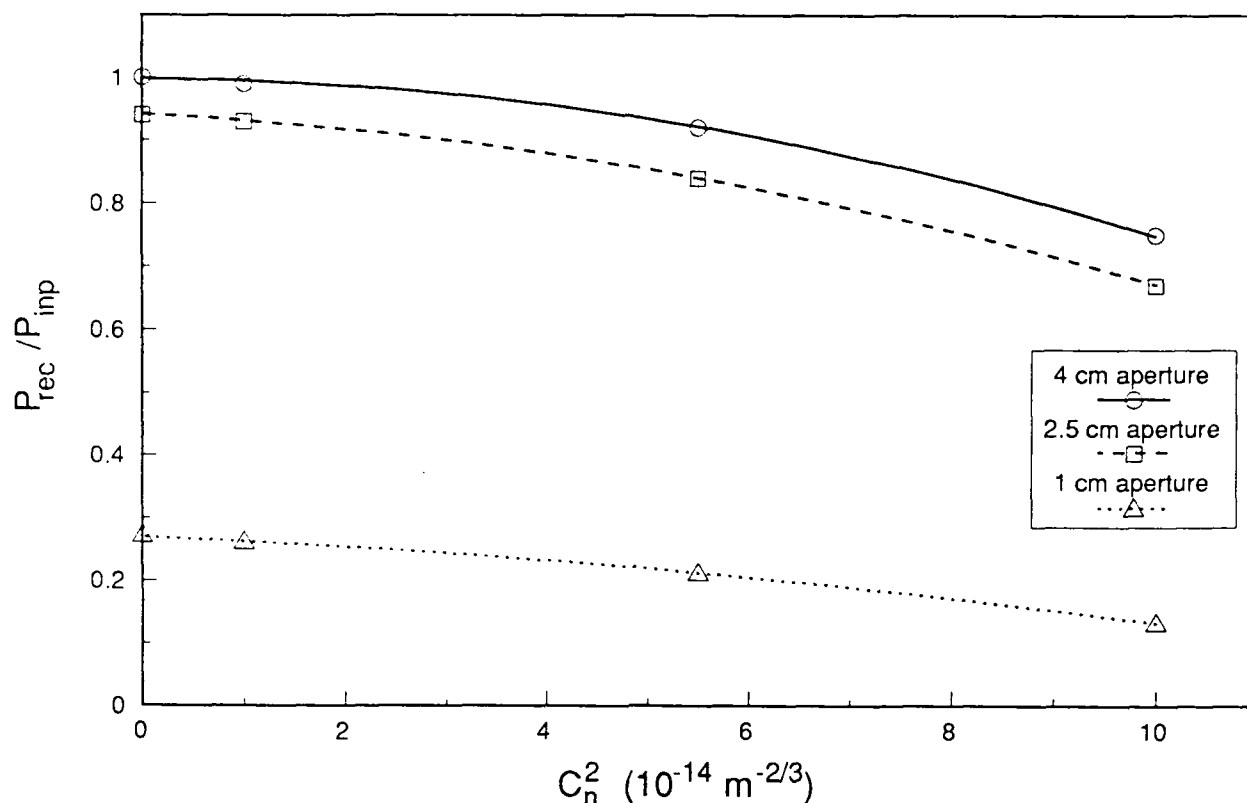


Figure IV-15. Ratio of received power to input power versus index structure constant for different transponder and receiver aperture pairs.

$C_n^2 \leq 10^{-14} \text{ m}^{-2/3}$  were very small. As the structure constant value is increased one order of magnitude the transverse coherence length becomes  $6.3 \text{ mm} < (\lambda R)^{1/2}$  and the received power decreases accordingly.

It is also of interest to note that the degradation effect is similar (on the order of 20%) for apertures much greater than  $r_0$  and it is stronger as the aperture size nears the transverse coherence length. For aperture diameters on the order of  $2 \text{ cm} \approx 3 r_0$ , the degradation is 50%. Importantly, the strong degradation that occurs for aperture radii of about 1 cm without turbulence occurs because the input collimated beam radius (kept fixed at 2.5 cm) is much larger than the transponder aperture radius.

Table IV-2 compares the results of a PC link with and without turbulence with the results obtained by substituting a mirror for the phase conjugator. The case shown corresponds to an aperture size that is similar to the collimated input beam. For a PC link, transponder diffraction effects are negligible (see section IV.3). However, for a mirror

Table IV-2. Rooftop geometry. Comparison of phase conjugation (PC) and a mirror (M) at the transponder.

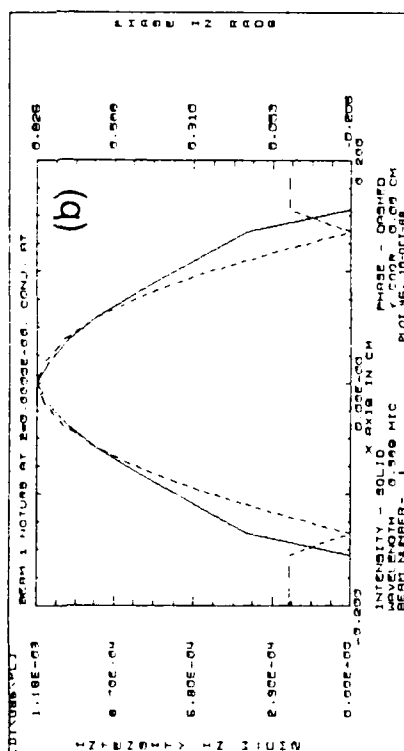
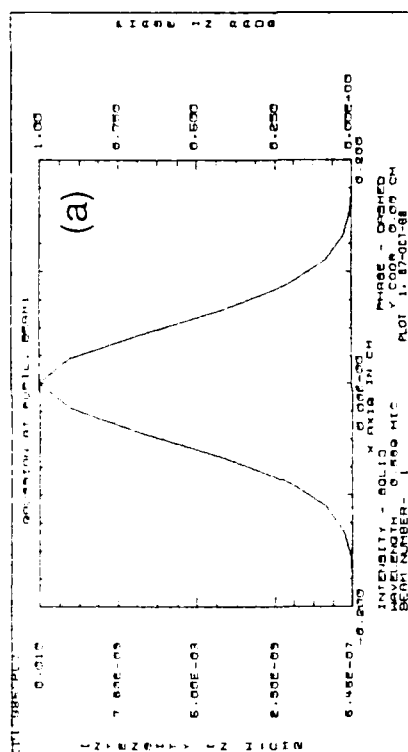
CONJUGATOR	TURBULENCE STRENGTH $C_n^2 \text{ (m}^{-2/3}\text{)}$	CONJUGATOR APERTURE (cm)	$P_{\text{REC}}/P_{\text{INP}}$
PC	0	2.5	0.94
M	0	2.5	0.74
PC	$10^{-13}$	2.5	0.67
M	$10^{-13}$	2.5	0.26

link, these effects degrade the power received even in the absence of turbulence. This may be quantified by (degradation of mirror link)/(degradation of PC link)<sub>w/o turb</sub> which is about 20% for the data in Table IV-2. In the presence of turbulence this ratio increases to 60%.

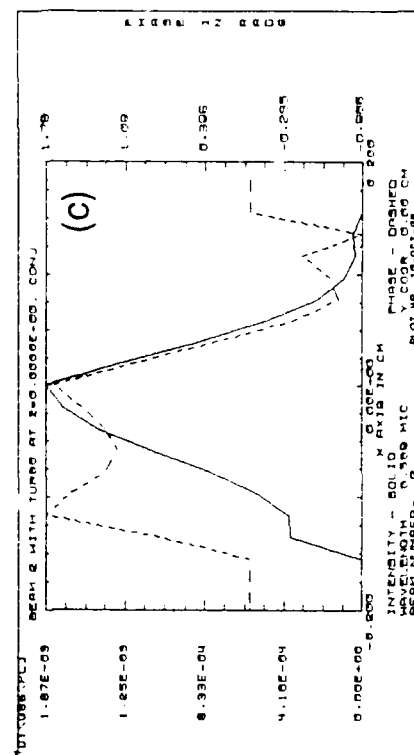
Figures IV-16 and IV-17 illustrate the changes in the optical beam profile at the transceiver in the presence of turbulence for the case of a 2 cm diameter aperture and  $r_o = 2.5$  cm. When the turbulence is turned off, the PC is able to conjugate the returning beam with fairly good fidelity. When the turbulence is turned on, some of the phase aberrations cannot be corrected with phase conjugation because information is lost at the small transponder aperture. The returning beam is askew and has poor fidelity resulting in a degradation of the received power as indicated in Tables IV-1 and IV-2.

b. Turbox Geometry -- Time and resource limitations restricted the number of cases for which numerical predictions for the turbox geometry were obtained. In particular, a configuration with  $C_n^2 \approx 10^{-10} \text{ m}^{-2/3}$  and an equivalent  $r_o = 3.5$  mm for a propagation length  $R \approx 2.5$  m was simulated. The results are shown in figures IV-18 and IV-19. These results are presented primarily to illustrate the model performance since the propagation length chosen is 10 times smaller than that used for most of the experiments.

In this example the input beam has a 1.1 cm radius at the output of the transceiver telescope and due to a poor optical configuration, diffracts without turbulence to 2 cm at

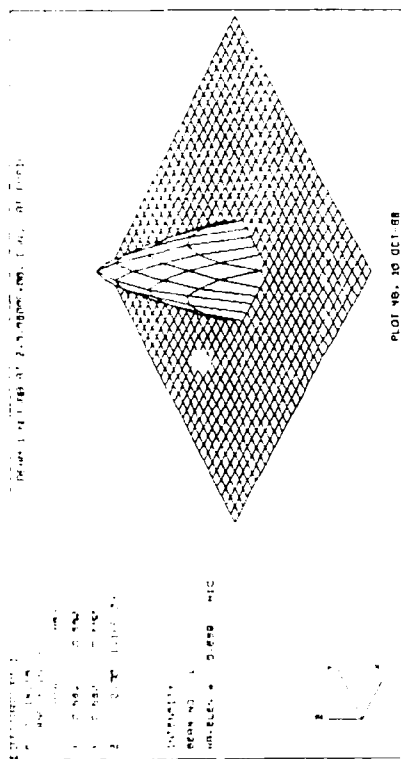


TURBULENCE OFF

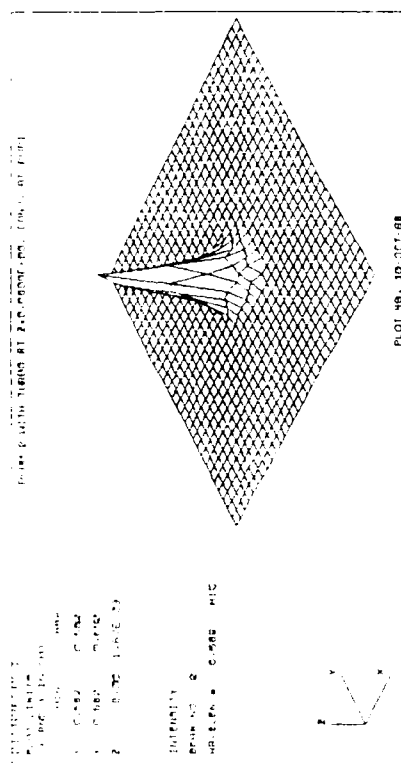


TURBULENCE ON

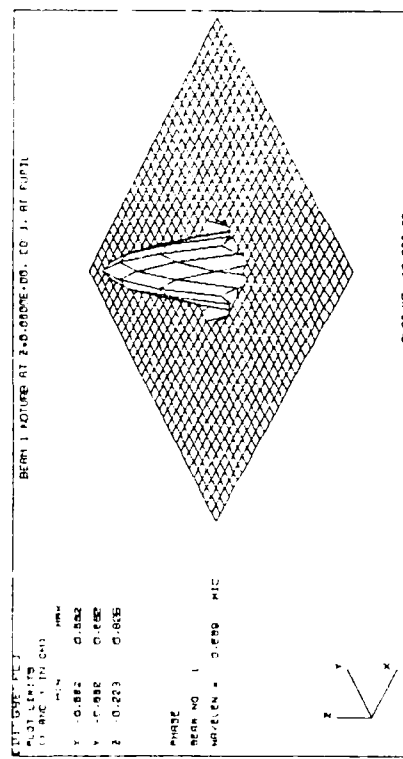
Figure IV-16. For rooftop geometry with 2 cm diameter apertures at PC and receiver. Solid line = intensity, dashed line = phase. (a) Input beam profile, (b) and (c) PC profiles at transceiver.  $C_n^2 = 10^{-14} \text{ m}^{-2/3}$ .



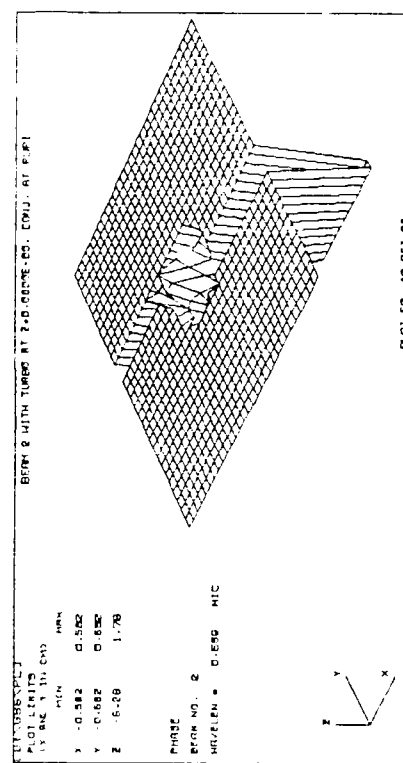
INTENSITY -- NO TURBULENCE



# INTENSITY -- TURBULENCE ON

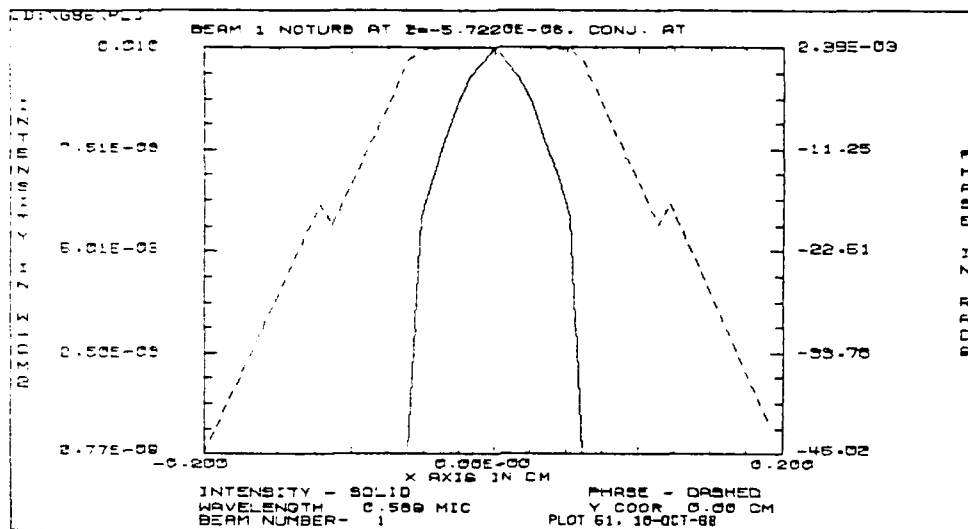


PHASE -- NO TURBULENCE

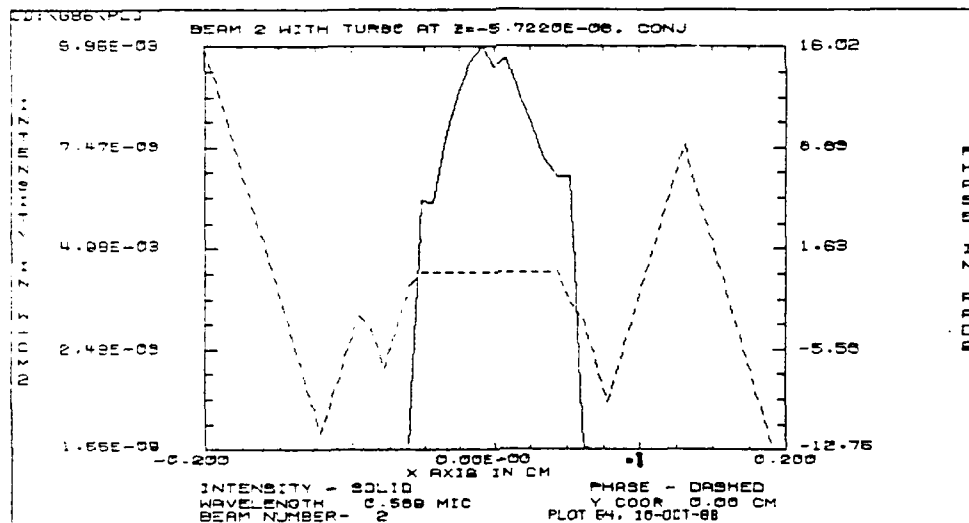


PHASE -- TURBULENCE OFF

Figure IV-17. 3-D view of phase conjugate beams at transmitter for rooftop geometry and 2 cm diameter apertures.  $C_n^2 = 10^{-14} \text{ m}^{-2/3}$ .

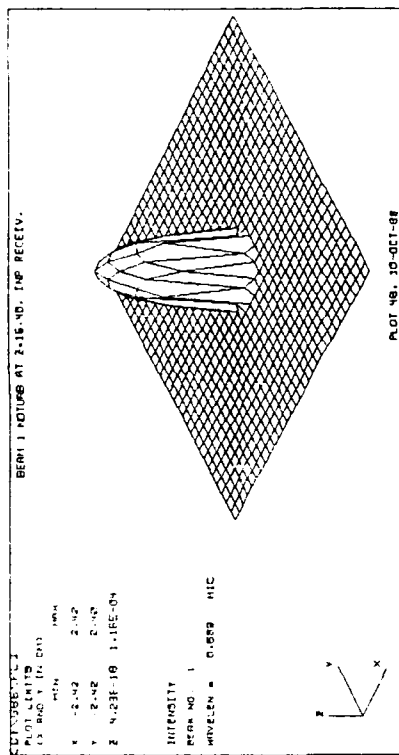


TURBULENCE OFF

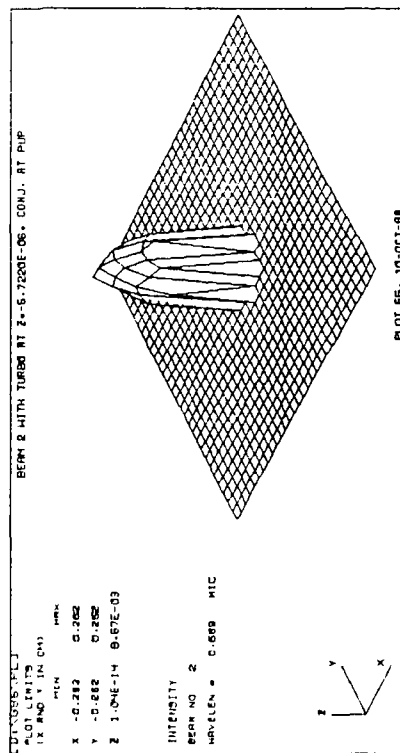


TURBULENCE ON

Figure IV-18. Phase conjugate beam profiles at transceiver for geometry similar to turbox.  $C_n^2 = 10^{-14} \text{ m}^{-2/3}$ .



# INTENSITY -- TURBULENCE OFF



# INTENSITY -- TURBULENCE ON

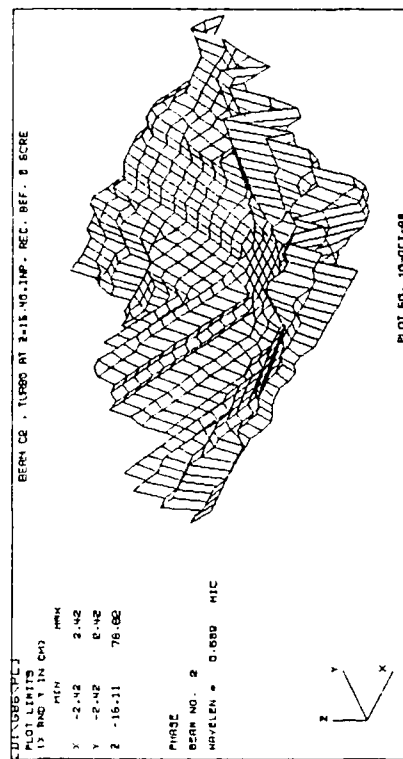


Figure IV-19. 3-D view of phase conjugate beam at receiver for the same case as figure IV-18.  $C_n^2 = 10^{-14} \text{ m}^{-2/3}$ .

the entrance to the transponder telescope. The transponder aperture radius is taken to be 1.1 cm and therefore part of the optical beam is lost at this end. The resulting conjugated beam cannot completely correct all the phase aberrations in a fashion similar to the roof-top experiment with 1 cm radius apertures. The ratio of the received power to the input power is 0.39 and is independent of turbulence being present or not, indicating that most of the degradation is due to finite aperture effects.

## V. HOLOGRAPHICALLY CORRECTED OPTICAL HETERODYNE RECEIVER

The advantages of coherent detection for any communication system are well known. These include the ability to increase the signal-to-noise detection ratio with the use of a strong local-oscillator beam. Optical communication systems are also coming into increased use, primarily over fiber-optic links. Such links are obviously not feasible for certain space-based communication applications, such as satellite uplinks and downlinks. The drawback of such a free-space system is the atmospheric wavefront aberration introduced in the link. Some correction scheme must be implemented to compensate for such aberrations if the advantages of coherent detection are to be realized. The methods discussed elsewhere in this document for compensating communications link aberrations make use of a receiver that is equipped with a laser, and a transmitter that employs a four wave mixing cell. Here, we report the results of an experimental study to demonstrate the feasibility of an aberration-corrected, optically coherent communications receiver that places no special demands on the capabilities of the transmitter.

### 1. INTRODUCTION

In an optical coherent detection system, two wavefronts are combined on a nonlinear detector. A heterodyne system carries information on a beacon wavefront whose central frequency is displaced from that of the second wavefront, referred to as the local-oscillator beam. A homodyne system carries the information on a beacon whose frequency is equal to that of the local-oscillator beam. For either scheme, aberrations are an especially critical problem for the optical implementation, because any mismatch of the two wavefronts will cause the phase difference between the two optical wavefronts to vary with position within the detector's active area. The effect of optical aberration will thus be a reduction in the coherent signal.



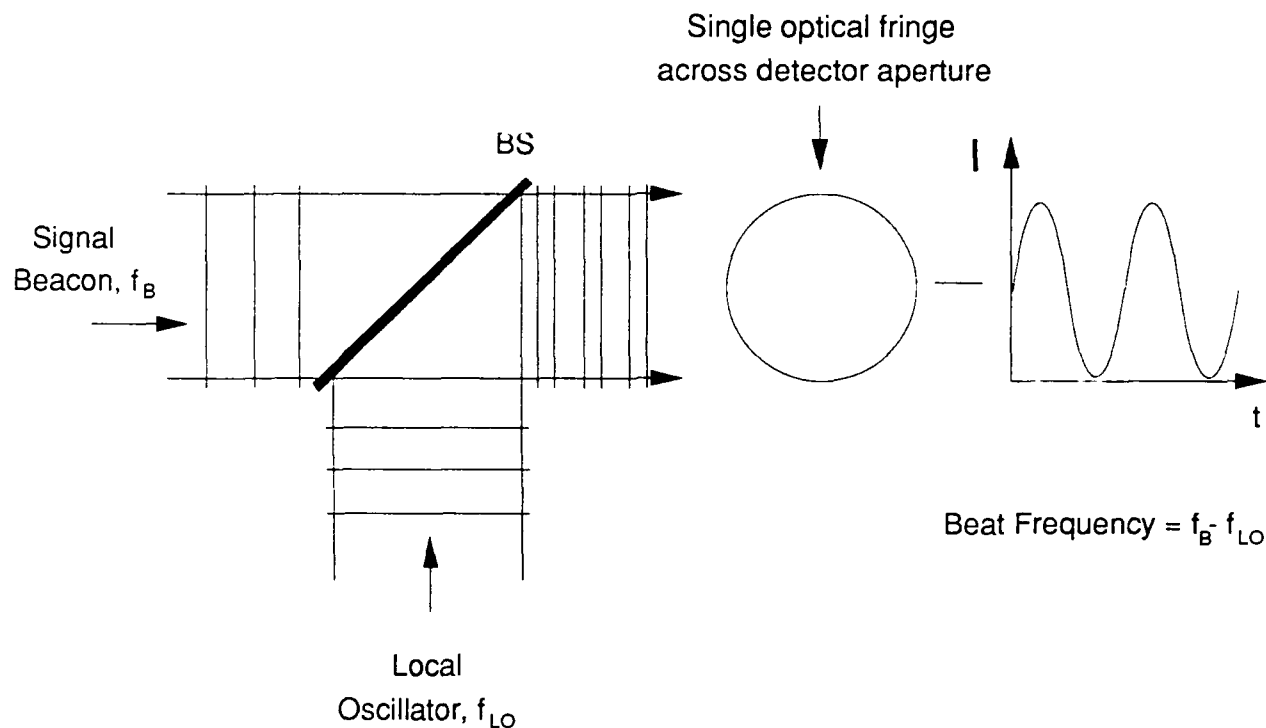


Figure V-1. Ideal operation of optical heterodyne receiver, perfectly matched planar wavefronts. Intensity oscillates with equal phase everywhere within detector aperture, at a frequency equal to the difference between the beacon and local-oscillator frequencies.

In an ideal optical heterodyne receiver, two planar wavefronts whose optical frequencies are offset by an interval, called the beat, or heterodyne frequency,  $\omega_h$ , are combined with a beamsplitter on the surface of a nonlinear detector (see figure V-1). With perfect wavefront matching of the two beams, the result is a pattern that varies sinusoidally in time with the same phase everywhere in the detector aperture. The integrated detector signal is proportional to the effective area of the detector.

An actual system will be subject to wavefront mismatch, which causes the integrated heterodyne signal to be degraded relative to the ideal situation. The field-of-view limitation in a coherent communication system has long been recognized; this limitation results from the fact that, as the beacon source moves, the beacon and local-oscillator wavefronts become tilted unless measures are taken to track the beacon

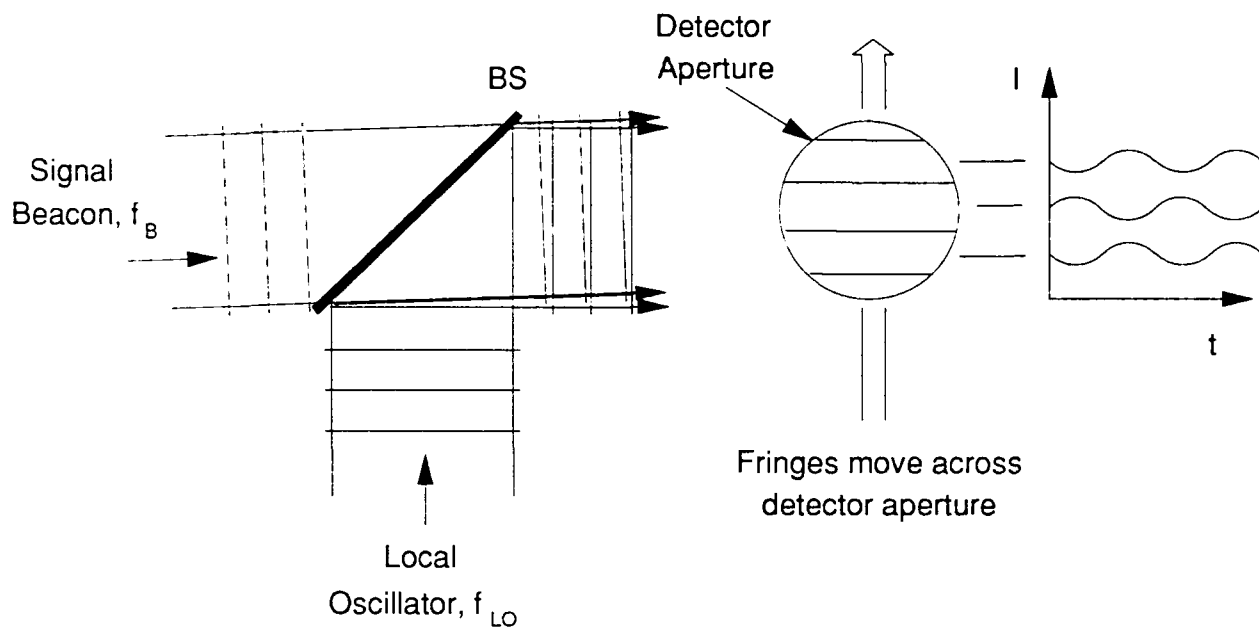


Figure V-2. Degradation of heterodyne signal due to relative tilt of beacon beam. Optical beat signal is shown for various positions within the detector aperture.

direction with the local-oscillator beam. This misalignment is a particular type of wavefront mismatch problem. As illustrated in figure V-2, misalignment of the local-oscillator and signal beams results in a set of moving intensity fringes in the detector plane; the phase of the oscillating intensity pattern varies within the detector aperture. The beat signal in various portions of the detector aperture add destructively, reducing the overall signal. The integrated detector signal thus decreases as the relative tilt of the two wavefronts increases, varying inversely with the number of optical fringes appearing across the detector plane.

In general, the beacon wavefront will possess wavefront aberrations in addition to simple tilt (tracking) error. As illustrated in figure V-3, the detector plane fringes will no longer be straight. Once again, portions of the intensity pattern oscillate with different phases; hence, the integrated detector signal is degraded relative to the ideal case. Intuitively, one expects this reduction factor to be given approximately by the ratio of the area of the largest fringe in the pattern to the total area of the intensity pattern. In lieu

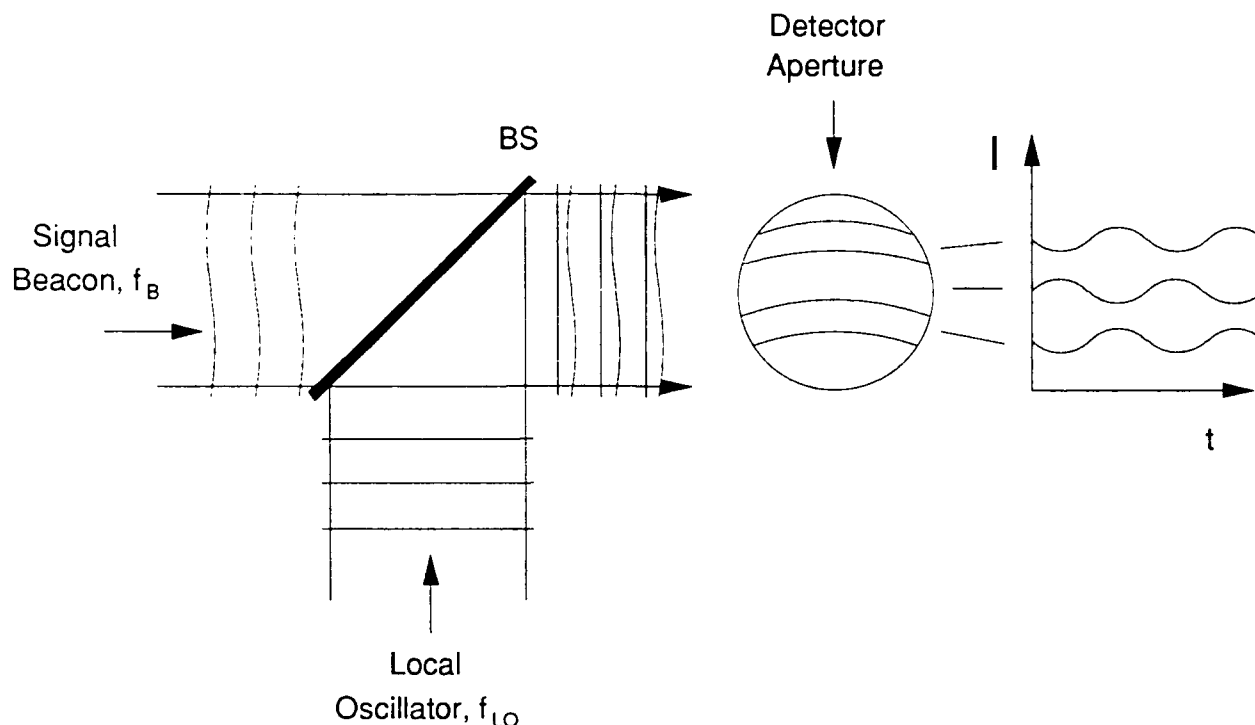


Figure V-3. Degradation of heterodyne signal due to aberration of beacon wavefront. Cancellation in the beat signal occurs among various positions within the detector aperture.

of an ability to correct for the optical aberrations in the link itself, what is needed is some method whereby the local oscillator and beacon wavefronts can be matched for optimum coherent mixing. This strategy constitutes the core of our general approach, which employs holographic recording and reconstruction of the beacon wavefront.

## 2. HETERODYNE EFFICIENCY

Consider the mixing of two optical wavefronts of frequency  $\omega_{lo}$  and  $\omega_b$  on a square-law detector. The total electric field in the detector plane is given by:

$$E_T = 1/2 E_{lo} \exp[i(\omega_{lo}t + \phi_{lo}(r))] + 1/2 E_b \exp[i(\omega_b t + \phi_b(r,t))] + cc \quad (V-1)$$

where  $E_{lo}$  and  $E_b$  are the amplitudes of the local oscillator and beacon fields, respectively,

and cc denotes complex conjugation. It is assumed here that the magnitudes of the electric fields are uniform across the active area of the detector. The position-dependent phases  $\phi(r,t)$  account for aberration or relative tilt of the beacon and local-oscillator beams. An additional time dependence is included in the beacon phase term to allow for the possibility of phase modulation of the beacon beam. This will be relevant for one of the experimental demonstrations, where the phase of the beacon beam is modulated by a PZT-mounted mirror. The time-averaged intensity seen by a square-law detector will be given by:

$$\begin{aligned} I_T &= c/(4 \pi) \cdot |E_T|^2 \\ &= I_{lo} + I_b + 2 [I_{lo} I_b]^{1/2} \cos[\omega_h t + \Delta\phi(r,t)], \end{aligned} \quad (V-2)$$

where

$$\Delta\phi(r,t) = \phi_{lo}(r) - \phi_b(r,t). \quad (V-3)$$

The first two terms are simply the sum of the local oscillator and beacon intensities, without interference. The final term is the interference term, and is responsible for the heterodyne signal;  $\omega_h$  is the heterodyne frequency, i.e., the difference of the local oscillator and beacon frequencies. It is convenient to define the heterodyne signal intensity as:

$$I_h(r,t) = 2 [I_{lo} I_b]^{1/2} \cos[\omega_h t + \Delta\phi(r,t)]. \quad (V-4)$$

Consider first the case of a pure beat-note signal, where the time dependence in the phase term is linear, and hence is already implicit in the difference frequency,  $\omega_h$ . The total power contained in the heterodyne signal is given by the integral of the heterodyne intensity over the active area of the detector:

$$P_h(t) = 2 [I_{lo} I_b]^{1/2} \iint \cos[\omega_h t + \Delta\phi(x,y)] dx dy \quad (V-5)$$

In general, the phase of the heterodyne signal will be position dependent, as described

by the phase  $\Delta\phi(x,y)$ ; this is the mathematical expression of the situation illustrated in figures V-2 and V-3, where several fringes coexist within the active area of the detector.

Variations in  $\Delta\phi$  across the active area of the detector will result in an oscillatory behavior of the integrand in equation (V-5) and decrease the net signal as a result. If the beacon and local oscillator wavefronts are perfectly matched, then  $\Delta\phi(x,y)$  is a constant, and the signal will attain its maximum possible value. In particular, the power contained in the heterodyne signal is in this case simply  $I_h$  times the total effective area of the detector:

$$\begin{aligned} P_h(t) &= 2 [I_{lo} I_b]^{1/2} A_{eff} \cos[\omega_h t] \\ &= 2 [P_{lo} P_b]^{1/2} \cos[\omega_h t] \end{aligned} \quad (V-6)$$

This result shows that under ideal circumstances, the maximum amplitude of the heterodyne signal is given by  $2 [P_{lo} P_b]^{1/2}$ :

$$P_h(\text{Ideal}) = 2 [P_{lo} P_b]^{1/2} \quad (V-7)$$

This provides a convenient reference for defining the heterodyne efficiency as the ratio of the experimentally observed heterodyne amplitude to this ideal amplitude:

$$\eta_{het} = P_h(\text{Exp}) / P_h(\text{Ideal}) \quad (V-8)$$

Consider next the case of pure phase modulation, where the time-averaged frequencies of the beacon and local oscillator beams are equal. This is the optical implementation of homodyne detection. As an example, the local oscillator beam's phase could be modulated by sinusoidally dithering the position of a PZT-mounted mirror. In this case, the time-varying component of the signal becomes

$$I_h(r,t) = 2 [I_{lo} I_b]^{1/2} \cos[ m \cos(\omega_d t) + \Delta\phi(r)], \quad (V-9)$$

where  $\omega_d$  is the dither frequency of the mirror, and  $m$  is the modulation depth, determined in our example by how far the PZT mirror is physically moved. In general, this expression can lead to complex time behavior, described in frequency space with the typical

Bessel-function sidebands. For example, a modulation depth,  $m$  equal to 10, would create a beat signal that undergoes 10 oscillations every period of the mirror's motion. Nonetheless, the maximum possible amplitude of the homodyne signal is still  $2 [P_{lo} P_b]^{1/2}$ , and is attained when the spatial wavefronts of the local oscillator and reference beams are identical [ $\Delta\phi(r) = 0$ ]. The definition of coherent detection efficiency is thus the same as for the heterodyne case, and will be referred to as the heterodyne efficiency.

As a particular case of wavefront mismatch, consider a simple tilt error between two planar wavefronts, such that the  $k$ -vectors of the two beams both lie in a plane arbitrarily designated the  $y$ - $z$  plane; then the phase term  $\Delta\phi(x,y)$  is equal to  $k_x x$  where  $k_x$ , the grating constant of the optical interference pattern, which equals the optical wavevector times one half the tilt angle. Substitution of this term into equation (V-5) results in the expression

$$P_h(t) = 2 [I_{lo} I_b]^{1/2} \int \cos[\omega_h t - k_x x] dx dy, \quad (V-10)$$

for the integrated heterodyne signal. If it is further assumed that the intensity pattern is square with dimension  $L$ , then integration over the area of the beam yields the result

$$P_h = 2 [P_{lo} P_b]^{1/2} \sin(kL/2)/(kL/2) \quad (V-11)$$

for the amplitude of the heterodyne signal. The number of fringes appearing across the detector aperture is given by  $N = kL/2\pi$ , so that this result may be recast in the form

$$P_h = 2 [P_{lo} P_b]^{1/2} \sin(\pi N)/(\pi N) \quad (V-12)$$

verifying the earlier claim that the integrated signal in the case of simple wavefront tilt varies inversely as the number of fringes across the detector aperture.

In the more general case of beacon wavefront aberration, the optical interference pattern displays more irregular sets of fringes, where the term "fringe" refers to an area of the interference pattern where the beat signal is oscillating with equal phase. The degradation of the heterodyne signal with the number of fringes is not as straightforward as in the case of a simple relative tilt, since in general, not all fringes will have the same

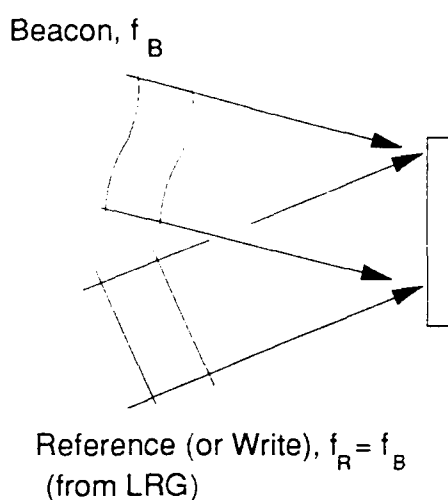
size. As suggested in the previous section, the heterodyne signal will be degraded approximately by the ratio of the largest fringe in the interference pattern to the total area of the pattern. Using this guideline, the heterodyne signal is thus still expected to degrade inversely with the number of "fringes" in the interference pattern.

In conclusion, the strength of the signal obtained using an optical coherent detection technique degrades as the wavefronts of the beacon and local oscillator beams exhibit position-dependent phase deviations due to either beacon tracking error or comm link aberrations. Techniques for reconstructing the wavefront of a subject beam from a stored holographic record are commonly employed in holographic interferometry. Such a technique has been used in this study to create a local-oscillator beam whose wavefront is a holographic replica of the beacon, effectively eliminating the phase deviations that limit the strength of the integrated coherent signal. This approach will now be described in detail.

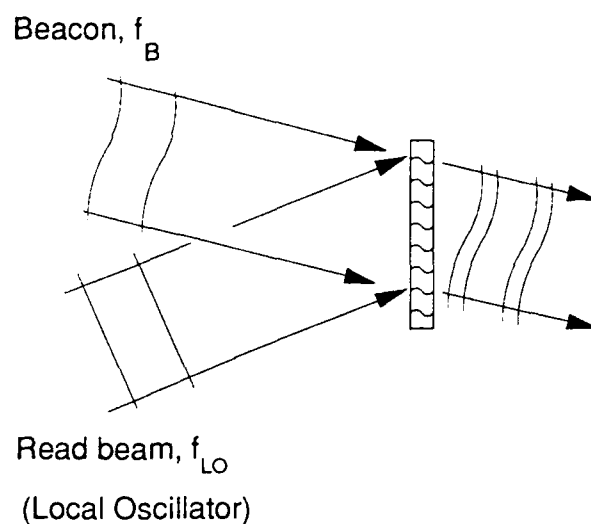
### 3. GENERAL APPROACH

The approach taken to the problem is to use a holographic method to match the beacon and local-oscillator beams. Here, matching is required in the most general sense, where it implies both tracking and aberration-correction ability. The concept is elucidated in figure V-4. The correction process is illustrated as a two step procedure. In the first step, a hologram of the beacon wavefront is recorded with a planar reference beam, or write beam, which must have a frequency equal to that of the beacon.

In the second step, this hologram is read by a beam that is collinear with the reference beam, but frequency shifted by the desired heterodyne frequency. For frequency shifts in the radiofrequency (RF) range, the read beam will still be Bragg matched to the hologram that was written by the reference beam. It will therefore be diffracted, with an efficiency determined by the hologram written in step 1, into a beam whose wavefront matches that of the beacon. The relative phases of the beacon and read beams will thus be independent of transverse position, and the optical intensity



Step 1: Write hologram  
of beacon beam



Step 2: Read hologram with  
frequency-shifted beam

Figure V-4. General scheme for holographically corrected heterodyne receiver.

A record of the beacon wavefront is written using the reference beam; this hologram is read by a frequency-shifted local-oscillator beam, which is combined with the beacon to generate a heterodyne signal.

pattern will fluctuate at the beat frequency with the same phase everywhere in the detector plane. The heterodyne efficiency should thus recover its ideal value of unity.

The holographic correction scheme for the optical heterodyne receiver has been illustrated above as a two step procedure. If the system is to track the beacon and compensate for link aberrations in real time, then it may be necessary to maintain continuous illumination of the hologram by the reference beam. It is therefore more probable in practice that the writing and reading of the hologram take place simultaneously, with the read beam possibly operating in a pulsed mode (see discussion below).

It is useful to compare the amplitude of the integrated heterodyne signal for the direct mixing of two mismatched wavefronts with the signal expected from the holographic correction scheme. For the sake of illustration, consider the direct mixing of two planar



wavefronts whose mismatch consists of a tilt error, for which the result of equation (V-12) is appropriate. Assuming that the holographic scheme results in perfect wavefront matching, and given a holographic diffraction efficiency  $\xi$ , the integrated ("corrected") heterodyne signal is given by:

$$P_h(\text{corr}) = 2 [\xi(1-\xi)]^{1/2} [P_o P_b]^{1/2}. \quad (\text{V-13})$$

By equating the expressions (V-12) and (V-13), one finds the diffraction efficiency required for the corrected heterodyne signal to equal the signal that would result without correction:

$$[\xi(1-\xi)]^{1/2} > \sin(\pi N)/(\pi N) \approx 1/(\pi N), \quad (\text{V-14})$$

where it may be recalled that  $N$ , the number of fringes appearing in the detector aperture, characterizes the strength of the aberration even for the more general case. As expected, the more severe the aberration strength, the lower the diffraction efficiency required for the holographic method to result in signal enhancement.

In the context of an optical comm link, coherent detection is attractive because the signal of interest is likely to be a very weak one. The main appeal of coherent detection lies in the ability to amplify a weak signal by mixing it with a strong local-oscillator beam; by its very nature, any heterodyne receiver thus involves waveforms of quite disparate intensities. For the optical receiver described in the foregoing paragraphs, this disparity in strength results in substantial dynamic-range requirements on practical real-time holographic materials. It is important to understand these requirements and what approaches might be considered to satisfy them.

Consider for the moment a receiver in which the read, write, and beacon beams are all present simultaneously. The quasi-stationary intensity grating formed by the (equal frequency) beacon and write beams is superimposed upon a set of rapidly moving fringes created by the superposition of the beacon and read beam. The latter fringe pattern is modulated at the RF frequency; if this period is short compared with the response time

of the recording material, the result is effectively a dc background intensity level upon which the fringe pattern recorded by the beacon and reference beams is superimposed.

The effect of this large background intensity depends upon the nature of the holographic material, and in particular, whether the amplitude of the holographic grating is proportional to the absolute depth or to the relative modulation depth of the optical intensity grating. For some recording materials, such as photorefractive crystals, the strength of the holographic index grating is determined by the contrast ratio of the optical intensity grating and will, therefore, be decreased in response to the presence of a strong, frequency-shifted local oscillator. In other words, the readout of the beacon-wavefront hologram by the local-oscillator beam is a destructive process.

At least two approaches may be taken to address this problem. First, one can imagine a comm link for which the specifications allow the read beam to be operated in a pulsed mode, keeping its optical duty cycle to a minimum. Such a receiver would not be practical for high data-rate systems. Second, the problem may be approached from the standpoint of the holographic material itself. In the foregoing description, the hologram for the beacon wavefront was written in the conventional optical manner. If a separate wavefront sensor could be used to probe the beacon wavefront, then the appropriate computerized hologram may be written onto an electronically addressed spatial light modulator (SLM); this hologram could then be used to diffract a planar local-oscillator beam into a replica of the beacon beam as in the previously proposed scheme. Finally, the destructive readout problem could also be solved by a holographic material/technique that permits strong discrimination in writing efficiency between the local-oscillator and beacon frequencies, while maintaining strong diffraction (reading) efficiency for the local-oscillator beam. The radio-frequency proximity of the two corresponding optical frequencies makes this a formidable challenge, but potentially addressable with atomic media, such as the sodium vapor employed in a degenerate four wave mixing cell in other parts of this effort.

The dynamic range of optical intensities inherent in a real-world heterodyne receiver thus places demanding requirements on the holographic material that probably could not be met by presently available photorefractive materials. A breadboard

demonstration is not the goal of the present study. The purpose of this experiment is rather a proof-of-principle demonstration for the ability of a holographic reconstruction to enhance the heterodyne efficiency of an optical detector receiving an aberrated signal wavefront. To this end, the use of a photorefractive crystal is ideal because of the facility with which holograms of various beacon beams may be erased and rewritten.

A related practical issue is the recording speed of the holographic material, which is in this case dependent upon the intensities of the beams. In practice, the recording material should be fast enough to track changes in the beacon wavefront; this, in turn, will depend upon the atmospheric turbulence in the link and the speed of the beacon source. Note also that for homodyne detection, the holographic material should actually be slow in comparison with the beacon phase modulations that one wishes to detect; otherwise, the material will simply write a new hologram corresponding to the new phase rather than read the new phase with a quasi-fixed hologram. Again, these issues are not important for the proof-of-principle demonstration we are attempting. In any case, dynamic-range requirements will probably prove far more difficult to satisfy than speed requirements in practical utilization of a real-time holographic material.

#### 4. SYSTEM CONCEPT

In order to write a hologram, one requires a reference beam matched in frequency to the wavefront to be recorded. With a remote source located on a moving platform and subject to a significant Doppler shift, some method is required for generating a planar optical reference matched in frequency to the received beacon. One common method for doing this consists of using a portion of the beacon to injection lock a laser; the difficulty with this approach is that the beacon powers are expected to be weak, resulting in a rather narrow injection-locking range. Figure V-5 shows a system configuration that incorporates a different local-reference-generator concept, the spatial filter with gain (SFWG)<sup>1</sup>.

The SFWG is a single mode semiconductor device operated above threshold, lasing at a frequency close enough to the beacon frequency to provide gain at that

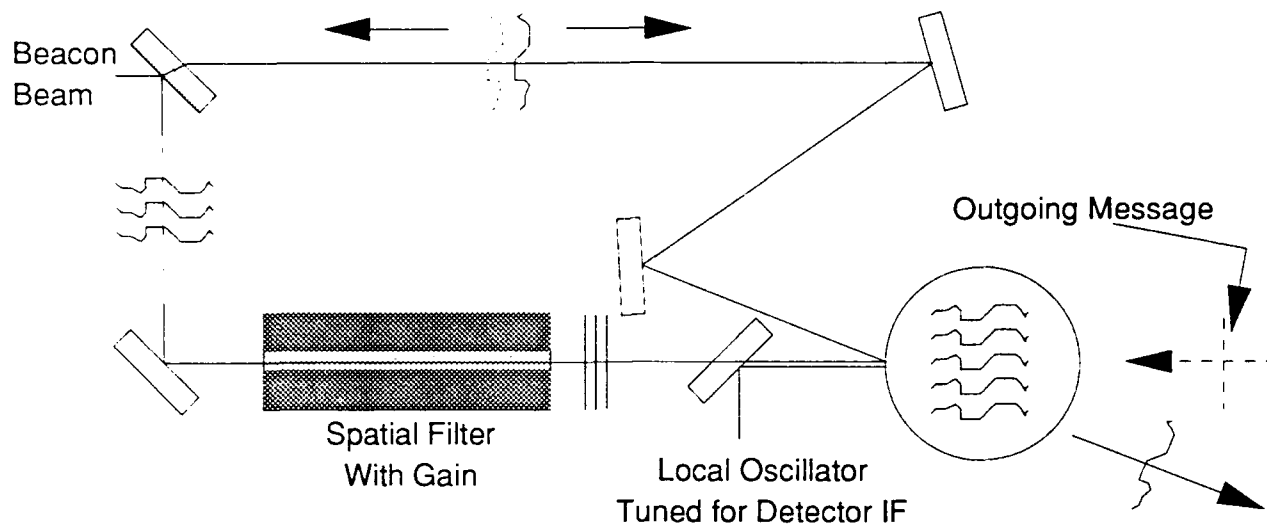


Figure V-5. System concept is closely analogous to holographic image reconstruction. System can be automatically aligning and the return beam can be phase conjugated. The outgoing message can be phase conjugated and tuned for Doppler shifts.

frequency by four wave mixing. A portion of the beacon wavefront is injected into the SFWG; the output consists of single spatial mode radiation at the lasing frequency,  $\omega_o$ , the beacon frequency,  $\omega_b$ , and an image frequency,  $2\omega_o - \omega_b$ . The  $\omega_b$  component is filtered with an etalon and allowed to mix with the remainder of the beacon wavefront in the holographic recording plane. The local oscillator beam reads this hologram and diffracts into a reconstructed version of the beacon wavefront, with which it mixes for coherent detection.

As shown in figure V-5, this system has the capacity for a two-way conjugated communications link. To accomplish this, a plane-wave beam carrying the desired temporal information is transmitted through the hologram in a direction counterpropagating to the local-reference/local-oscillator beams. This plane wave will diffract into a phase conjugate replica of the beacon wavefront and propagate back to the beacon source.

Note that if one were to require only one-way coherent detection of a stationary beacon, e.g., from a geostationary transmitter, the SFWG would alone be sufficient for the task. Since the SFWG output emits an amplified plane wave whose instantaneous

frequency equals that of the beacon, it would remain simply to mix this with the local oscillator beam on a nonlinear detector. The holographic technique offers the additional capabilities of tracking a moving beacon and conjugated two-way communication for any beacon propagating over an aberrated link.

## 5. EXPERIMENTAL APPROACH

Two experimental approaches were taken for the holographically corrected heterodyne receiver. For the purposes of this demonstration, both experiments proceeded in separate writing and reading stages. In the writing stage, the hologram of the beacon beam was recorded by exposure of the holographic medium to the beacon and a plane-wave write beam; in the reading stage, the local-oscillator beam was turned on. The differences in the two experiments consisted in the method of obtaining the local-oscillator beam: in the first demonstration, the local oscillator was simulated simply by dithering a PZT-mounted mirror, while in the second demonstration, the local oscillator was simulated with an acousto-optic frequency shifter.

a. Two-Beam Setup: Experimental Details -- Figure V-6 depicts the first experimental arrangement, called the two-beam setup. A Coherent CR-3 argon ion laser was operated on the 514.5 nm line at a power level of 1 W. The beam passed through a rotatable half-wave plate/polarizing beamsplitter pair for intensity control and then through a telescopic spatial filter, from which a collimated 13 mm beam emerged. A beamsplitter divided the beam into a beacon path and a second path that serves the double role of a local oscillator ( $I_o$ , or read) beam and a holographic reference (write) beam. The beacon and  $I_o$ /read beams were both steered to an Fe-doped LiNbO<sub>3</sub> crystal, which served as the holographic medium; the two beams intersected inside the crystal at an angle of 0.1 radians, which for this wavelength of operation and unaberrated plane-wave beams corresponds to a grating spacing of 5  $\mu\text{m}$ . An aberrator consisting of a heat-warped glass microscope slide was inserted into the beacon beam to test for aberration-correction ability. A lens was employed to image the photorefractive crystal

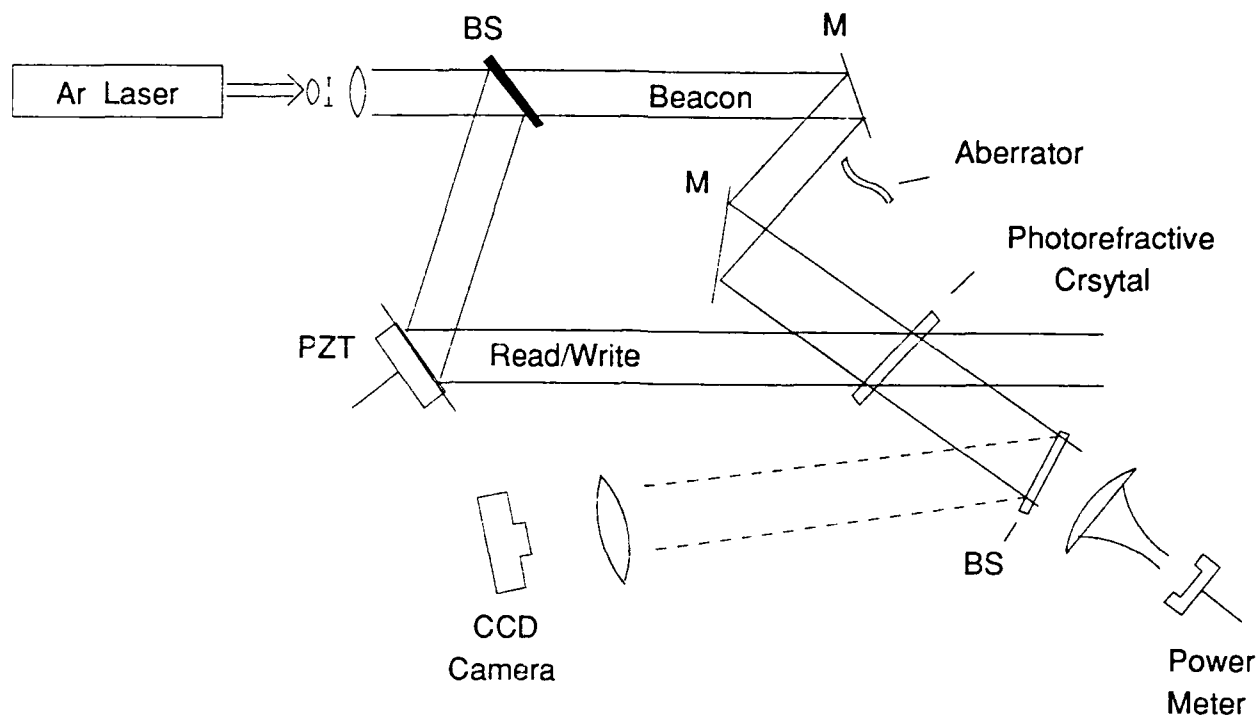


Figure V-6. Two-beam experimental setup for heterodyne receiver demonstration. Superposition of transmitted beacon and diffracted read beams are monitored for homodyne power; photorefractive crystal plane is imaged onto a ccd camera to monitor beam profiles.

onto the active surface of a CCD camera to record the near field intensity patterns of the beacon beam.

The local oscillator/read beam path contained the PZT-mounted mirror, which provided the phase modulation needed for coherent signal generation. The PZT mirror was driven by a Kepco OPS 2000B high voltage operational amplifier, the input for which was provided by a Hewlett-Packard 3310 B function generator. The function generator could be used to supply a sinusoidal waveform to the PZT or to manually adjust the mirror to a fixed position (i.e., a fixed optical phase for the read beam).

A Newport power meter equipped with a Model 850 silicon sensor head was used to make power measurements and a lens was used to collect light in the aberrated beams onto the active surface for power readings. The temporal response of the detector was sufficient for the beat frequencies generated in this part of the experiment. The

analog output of the power meter head was fed to an oscilloscope for monitoring the optical signal waveforms.

b. Two-Beam Setup: Results and Discussion -- To record the hologram of a given beacon wavefront, the PZT mirror was kept stationary and the lithium niobate crystal was illuminated simultaneously by the (identical frequency) beacon and reference beams. As the photorefractive grating was written, two-beam coupling occurs from one beam into the other. Typical beam intensities are  $15 \text{ mW/cm}^2$  for the reference and  $2 \text{ mW/cm}^2$  for the beacon; at these power levels, diffraction efficiencies of approximately 10% are obtained after 10 minute writing times. The reference beam was diffracted into a direction coincident with the transmitted beacon beam, and under conditions of good holographic fidelity, with an identical wavefront. The coherent superposition of the diffracted reference beam and the transmitted beacon beam was directed onto the power meter head.

In order to generate a coherent optical signal, the position of the PZT mirror was modulated sinusoidally, thereby modulating the phase of the local oscillator beam and thus the intensity of the aforementioned coherent superposition. Note that since the phase modulation impressed upon the local oscillator beam was periodic rather than linear in time, this particular experiment is more closely analogous to homodyne than heterodyne detection. (Of course, in a real communications link, it is the beacon phase that is modulated and not the local oscillator.) As the phase of the reference beam was dithered, the fringe pattern of the optical interference pattern in the photorefractive crystal oscillated from side to side, and began to modify the index grating. The 10 minute writing times required at these intensity levels, however, gives one ample time to record the pertinent beam intensities. In this sense, the long response time characterizing the photorefractive recording material was an advantage in this experiment.

To gain a feeling for the heterodyne efficiencies one can expect from the holographic beam combination, we began by writing a hologram for a planar, unaberrated beacon. Figure V-7 is a photograph of the oscilloscope trace monitoring the output of the power meter. The phase of the local-oscillator beam was modulated at a frequency of

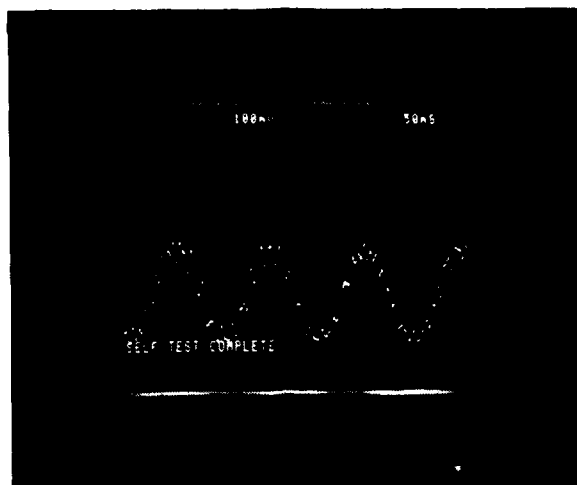


Figure V-7. Oscilloscope trace of optical homodyne signal generated in two-beam setup. Signal is generated by dithering the position of a PZT-mounted mirror; small 90-Hz ripple is attributable to mechanical vibrations. Beacon beam is an unaberrated plane wave.

7 Hz, with a total displacement of one-half wavelength in order to give the maximum possible constructive and destructive interference between the beacon and diffracted local-oscillator wavefronts. The more rapid ( $\approx 90$  Hz) oscillations in the intensity are attributable to mechanical vibrations transmitted from the laser cooling supply to the optical table.

The individual powers of the diffracted reference and transmitted beacon beams measured 2.36 and 0.82 mW, respectively. The amplitude of the time-varying signal as displayed on the oscilloscope trace in figure V-7 should, according to equation (V-7), equal 2.78 mW if the holographic reconstruction of the beacon were perfect. The experimental amplitude of the signal was measured by applying a fixed voltage to the PZT, and manually adjusting the mirror position to record the minimum and maximum intensities. These were found to equal 0.91 mW and 3.45 mW, giving a signal amplitude of 1.27 mW ( $= \text{one-half max} - \text{min value}$ ). The result is a "heterodyne" efficiency, defined according to equation (V-8), of 46%.

The most likely reason that the heterodyne efficiency for the unaberrated beacon falls short of its ideal value is that the optical interference pattern is affected by the short



and long-term motions in the system. The mechanical vibrations evinced in figure V-7 imply that the optical fringe pattern that writes the beacon hologram jitters during the 10 minute writing phase. In addition, the optical path difference (OPD) of the two arms of the experiment is subject to long-term drift. The holographic index grating is determined by the intensity pattern time averaged over the characteristic photorefractive response time. Both the rapid and slow OPD changes will result in an index grating that is not a perfect holographic record of the beacon beam.

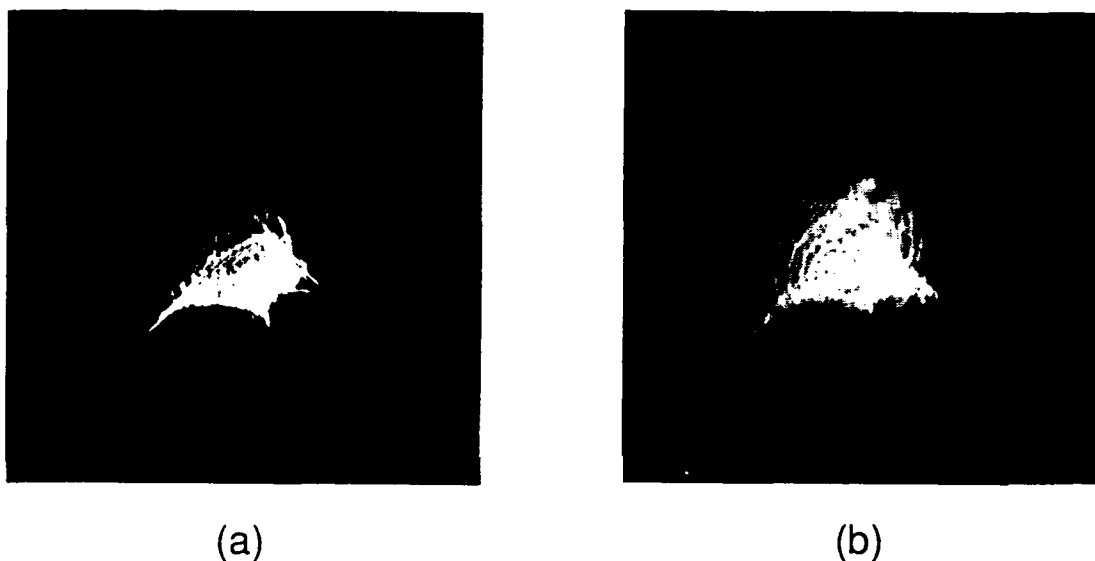


Figure V-8. Profiles of (a) aberrated beacon beam used in two-beam heterodyne demonstration and (b) corresponding diffracted read beam.

Once the performance of the system was established for a clean beacon, the glass aberrator (see figure V-6) was inserted to test the system with various degrees of wavefront distortion. Figure V-8a is a photograph of the intensity profile of the beacon beam for one such trial. The aberrator was inserted while the hologram for the plane-wave grating, written as described in the foregoing paragraphs, was still present inside the photorefractive crystal; because of the writing times required to write a new hologram for the aberrated beacon, the reference beam diffracts into a plane wave with

the direction of the beacon and can be used to measure the coherent signal that would result in the absence of holographic correction. This corresponds to the signal one would obtain by simple combination using a beamsplitter. For the beacon beam shown in figure V-8a, the amplitude of the coherent (phase modulation) signal is unobservable without holographic correction; the corresponding oscilloscope trace reveals only the rapid 90 Hz ripple and no indication of a 7 Hz modulation signal. Given the amplitude of the 90 Hz noise, we estimate an upper limit of 2% for the uncorrected ("direct mixing") heterodyne efficiencies in these two-beam experiments.

The photorefractive crystal was then rotated so that the plane-wave grating was no longer Bragg-matched to the reference beam. A hologram of the aberrated beacon was then written in the  $\text{LiNbO}_3$ . Figure V-8b shows the profile of the diffracted reference beam following a 15 minute writing period; this is a reasonable (though not perfect) replica of the beacon beam shown in figure V-8a. Dithering the PZT mirror revealed a recovery of the heterodyne signal, illustrated in the oscilloscope trace shown in figure V-9. Following the same prescription described above for the unaberrated beacon, the

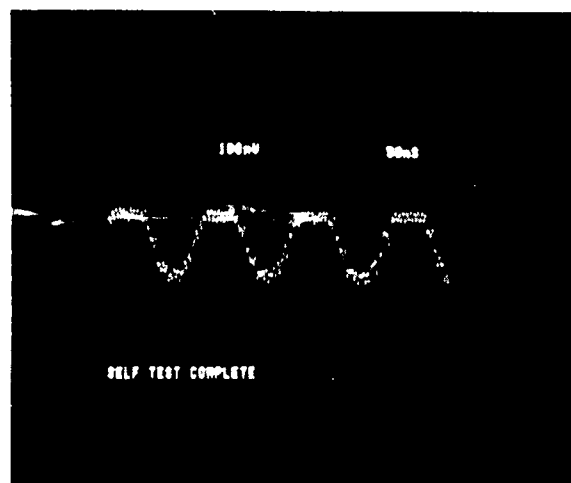


Figure V-9. Optical homodyne signal for aberrated beacon profile shown in fig V-8a. Heterodyne efficiency recovers to half the value obtained for an unaberrated beacon. Asymmetry in the waveform is due to dc drift in the total optical path length difference between beacon and read-beam paths.

measured heterodyne efficiency for the aberrated case was equal to 27%. (The asymmetry evident in the signal in figure V-9 was caused by a slow drift in the OPD of the two beams; the average position of the PZT mirror could be adjusted to give a trace resembling that in figure V-7.)

The heterodyne efficiency for the aberrated beacon (27%) did not fully recover to the value observed for the clean, plane-wave beacon (46%). The beacon used in this trial was severely aberrated, and therefore required a range of spatial frequencies in the corresponding holographic grating. Any optical fringe motion present during the writing phase will have a more severe impact on the recording efficiency of the higher spatial frequencies. In addition, the efficiency of a photorefractive grating is well known to vary with spatial frequency. Either of these two effects will create a diffracted beam that is not a true reproduction of the original beacon. This discrepancy is evident upon comparison of figures V-8a and V-9b. It should be emphasized that this is a severely distorted beacon. According to equation (V-12), the recovery of the heterodyne signal from a value of less than 2% to 27% indicates the ability to reproduce a beacon wavefront with more than 16 waves of distortion to within 1 wave of average deviation across the wavefront.

Although this discussion has focussed on the demonstration of wavefront aberration correction, it should be noted that the ability of the scheme to track the direction of a beacon was also demonstrated. This was accomplished by employing a microscope slide containing a wedge error as the aberrator. For this type of "aberrator", the heterodyne signal recovered to the 46% level, as one would expect. The demonstration described in this section is similar to previous work by Davidson and Boutsikaris,<sup>24</sup> investigating the use of photorefractive barium titanate as a beam combiner to maintain beacon tracking for homodyne detection. The work described herein carries that scheme one step further, in demonstrating the ability of a holographic approach to correct beacon aberrations as well.

c. Three-Beam Setup: Experimental Details -- Figure V-10 depicts the three-beam setup for the holographic correction demonstration. The arrangement is similar to the previously described two-beam experiment. The beacon and reference

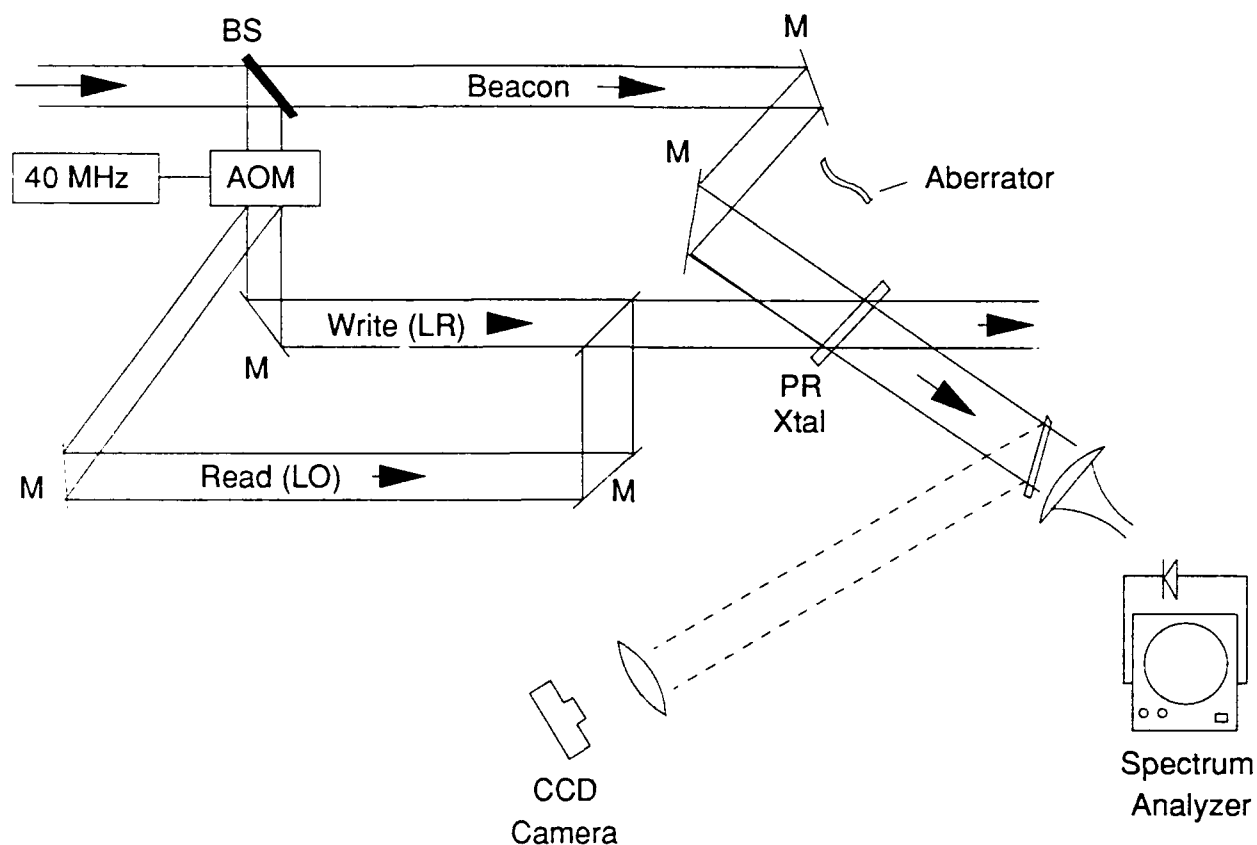


Fig. V-10. Three-beam experimental setup for heterodyne receiver demonstration. Diffracted local-oscillator and transmitted beacon beams are combined on the surface of a fast photodiode, and the resulting beat signal observed on an RF spectrum analyzer.

(write) beams served the same function as in the two-beam experiment; the local oscillator now consisted of a separate frequency-shifted reading beam. This beam was provided by deflecting a portion of the laser beam with an Intra-Action model 40N acousto-optic modulator (AOM). The AOM transducer was driven by a 40 MHz RF carrier; the RF driver has a video input, which could be used to optionally modulate the intensity of the AO-shifted beam. The intensities of the beacon, reference, and local reference beams were 2, 10, and 9 mW/cm<sup>2</sup>, respectively; the beams were collimated with an approximate  $1/e^2$  full width of 13 mm.

The laser was operated multimode with an approximate 1 GHz linewidth; hence, some care was taken to equalize all path lengths to within 1 cm, which is much shorter than the 19 cm coherence length of the laser. This ensures that, although the instantaneous frequency of the laser is uncertain to within 1 GHz, the instantaneous frequency of the AO-shifted beam is always downshifted from that of the reference and local oscillator beams by 40 MHz when compared (mixed) at the same point in space (e.g., the surface of a detector).

For the detection of a 40 MHz beat note, the power meter deployed for the two-beam (homodyne) setup was no longer sufficient. To detect this signal, the light from the beacon path was passed through a 10% neutral density filter and focussed onto the surface of a Motorola MRD 721 photodiode. The detector was reversed biased to 30 V; at this quiescent point, the intrinsic rise time of the device is 2 ns, sufficient to detect a 40 MHz signal. The photodiode was ac-coupled to a United Detector Technology UDT-700 transimpedance amplifier (TIA), which provided a current-to-voltage gain of 3500 ohms over a bandwidth of 500 kHz to 400 MHz. The output of the TIA was fed into a Hewlett Packard 8557A RF spectrum analyzer, where the amplitude of the 40 MHz heterodyne signal was recorded.

The drawback to this electronic arrangement is that it was not possible to obtain a direct reading of the 40 MHz signal amplitude in terms of optical intensity, since the electronics described above cannot record a dc intensity level, which could be compared with a power meter reading. To measure heterodyne efficiencies, it is therefore essential to obtain some optical intensity calibration for the spectrum analyzer readings. In order to obtain such a calibration, a 500 kHz square wave was applied to the video input of the RF driver, resulting in a frequency-shifted beam that was chopped on and off at a 500 kHz rate. From Fourier analysis, it is known that the amplitude of the 500 kHz component of a square waveform equals  $2/\pi$  times the amplitude of the waveform; in this context, the amplitude of the waveform equals the intensity of the unmodulated beam, which was measured with the Newport power meter.

To illustrate, a beam with an intensity of 590  $\mu\text{W}$  is chopped at a rate of 500 kHz; the spectrum analyzer reads a 500 kHz amplitude of 0 dBm. This is interpreted to mean

that the combination of photodiode and TIA generate a 0 dBm (224 mV) signal for a sinusoidal optical signal with a  $590 \mu\text{W} \times 2/\pi = 373 \mu\text{W}$  amplitude. The linearity of the spectrum analyzer readings with respect to optical beam intensity was verified. As the frequency of the square wave modulation was increased beyond 1 MHz, the spectrum analyzer readings began to decrease; this is because the AO modulator does not have the required switching time to modulate the intensity of a beam this rapidly, a fact which was readily apparent by monitoring the modulated optical beam on an oscilloscope. It is thus, unfortunately, not at all clear that the overall electronic response of the system (photodiode, TIA, and spectrum analyzer) is the same at 500 kHz and 40 MHz. Therefore, the heterodyne efficiencies to be cited in the following section must be regarded as subject to an overall systematic calibration error. The relative values, however, are valid.

Note that with a local oscillator that is truly frequency shifted, this three-beam experiment is more closely analogous to true heterodyne detection than the foregoing two-beam arrangement, which bears more similarity to a homodyne scheme. The use of a 40 MHz heterodyne beat note has certain advantages over the slow phase modulation possible with the PZT mirror. For one, the 90 Hz mechanical ripple seen in the two-beam experiment (figures V-7 and V-9) does not obscure the beat-note amplitude; for another, slow phase drifts do not affect the qualitative nature of a heterodyne signal in the same way as they would a homodyne signal (the asymmetry of the waveform evident in figure V-9). One must bear in mind, however, that both of these effects will still cause optical fringe motion during the holographic writing stage and thus affect the ability to write a faithful hologram of the beacon beam in the slow photorefractive medium. The heterodyne efficiencies are therefore not expected to exceed those observed in the two-beam experiment.

d. Three-Beam Setup: Results and Discussion -- The experiment proceeded in separate write and read stages as in the (homodyne) two-beam experiment. The read beam was blocked during the first stage, while a photorefractive hologram of the beacon beam was recorded. In the reading stage, the read beam was unblocked and allowed

to diffract into a replica of the beacon beam. A heterodyne tone may be generated by two different beam combinations: the transmitted beacon and diffracted local-oscillator pair, or the diffracted reference and diffracted local oscillator pair may be mixed to form the beat signal. Of the two, the beat signal for the transmitted beacon and diffracted local oscillator pair is a better indicator of the ability of the holographic scheme to reproduce the wavefront of an aberrated beacon.

In principle, all three beams (diffracted reference, diffracted local oscillator, and beacon) may be allowed to mix at once, and the superposition of both beat signals observed. There are two practical difficulties with this approach. First, the relative OPD drift between the reference and beacon arms translates into a phase drift between the two beat-notes and hence an erratic superposition. Second, the heterodyne efficiency as defined in equation (V-7) is far more straightforward to interpret with only two beams mixing at a time. The heterodyne signals were thus recorded by blocking the reference (write) beam and allowing the diffracted local oscillator and transmitted beacon beams to mix.

The heterodyne efficiencies were measured for various beacon beams in accordance with the procedure described for the two-beam experiment and the definition of equation (V-7). The efficiency was first measured for an unaberrated plane-wave beacon as a standard of comparison for the results obtained with the aberrated beacons. The results of these measurements are summarized in table V-1 and figures V-11a - V-11d. Figure V-11 shows the near field intensity profiles for four aberrated beacon beams; for the first three beams, the profiles shown are actually interferograms of the beacon beam with the plane-wave reference (an interferogram was not recorded for the beacon shown in figure V-11d).

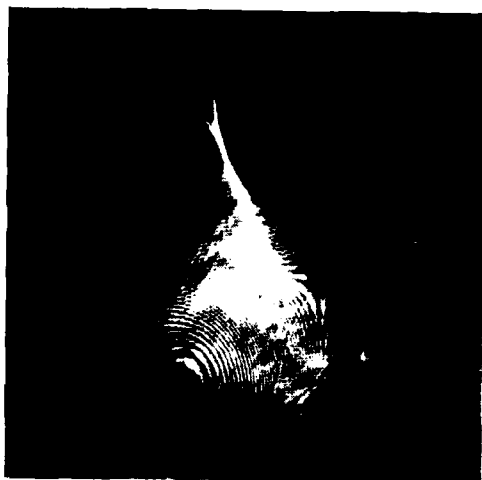
Table V-1 lists the heterodyne efficiencies measured for the four beacon beams in figure V-11, as well as the result for an unaberrated beacon. Table V-1 also lists the "uncorrected" heterodyne efficiencies,  $\eta_{unc}$ , obtained by mixing each of the aberrated beacons with a plane-wave local oscillator, produced by diffraction of the local oscillator from a plane-wave hologram stored in the photorefractive crystal. The final column constitutes the figure of merit for the correction scheme; it compares the magnitude of the



(a)



(b)



(c)



(d)

Figure V-11. Profiles of aberrated beacons used in three-beam setup. Table V-1 lists corresponding corrected and uncorrected heterodyne efficiencies.



heterodyne signal obtained by using holographic correction with the signal obtained by mixing the beacon wavefront directly with a plane wave.

Table V-1. Corrected and uncorrected heterodyne efficiencies, three-beam setup.

Beacon	$\eta_{\text{cor}}^{\dagger}$	$\eta_{\text{unc}}^{\dagger}$	Improvement
Plane wave	16%	N/A	N/A
#1	13%	0.9%	14
#2	14%	0.04%	350
#3	10%	< 0.01%	> 1000
#4	6%	< 0.01%	> 600

\* Beacons #1 - #4 correspond to the profiles shown in figures V-11a - V-11d.

<sup>†</sup> Subject to overall systematic error (see text).

The heterodyne efficiency for the plane-wave case (16%) is significantly lower than the 46% efficiency measured in the two-beam experiment. With only a 40 MHz frequency shift, the local oscillator beam in the three-beam experiment should diffract from the hologram with a wavefront virtually identical to the wavefront diffracted by an unshifted beam. It is almost certain that the low value of heterodyne efficiency quoted here is a consequence of the previously discussed difficulty of calibrating the 40 MHz spectrum analyzer signal to an optical intensity. The efficiency in the two-beam experiment comes from a straightforward, static measurement of the matching of the beacon and diffracted reference wavefronts, and is free from any calibration uncertainties; it should be regarded as the more reliable absolute measurement. The actual values of the heterodyne efficiencies in table V-1 are probably all too low by a factor of approximately 3 (i.e., 46%/16%). This implies that the actual heterodyne efficiencies for the aberrated beacons #1 - #4 are 37%, 40%, 29%, and 17%, respectively.

The uncorrected heterodyne efficiencies are less than 1% for all aberrated beams that were investigated. The extent of wavefront aberration and the concomitant decrease in heterodyne efficiency can be correlated somewhat to the corresponding fringe patterns

in the interferograms. For example, in figure V-11a, approximately 15 fringes appear in the pattern; the uncorrected heterodyne efficiency is thus expected, on the basis of equation (V-12), to be smaller than the unaberrated beacon efficiency by a factor of 50. The observed efficiency decreases by a factor of 18. Since equation (V-12) was derived for the case of a simple tilt error, one cannot expect it to be any more than a rule of thumb for beams such as those seen in figure V-11. The holographically corrected heterodyne efficiencies are always a marked improvement over the uncorrected values, and by three orders of magnitude for the two most severely aberrated beams.

For the two less severely aberrated beacons (#1 and #2), the corrected heterodyne efficiency recovers to better than 80% of the efficiency observed for the unaberrated beacon. The heterodyne efficiencies for mixing the beacon with the diffracted local-oscillator beam decrease as the wavefront quality of the beacon degrades. The holographic reconstruction fidelity for the aberrated beacon wavefront will never be perfect; hence, the diffracted reference and beacon beams will never have exactly identical wavefronts. As the data bear out, this effect becomes more pronounced as the wavefront quality of the beacon becomes poorer (i.e., carries higher spatial frequencies). An additional cause for the decrease in efficiency of the two beacons shown in figures V-11c and V-11d is the fact that these beams are so severely aberrated that they cannot be entirely collected onto the small active surface of the fast-response photodiode.

## 6. SUMMARY

We have shown that the holographic reconstruction of an aberrated beacon wavefront onto a local-oscillator wavefront can substantially improve the efficiency of heterodyne mixing over the value attained by employing a plane-wave local-oscillator beam. Correction of more than 10 waves of error has been demonstrated; this is probably limited by the fidelity of the holographic recording material and optical path length fluctuations that occur during the (long) writing times needed for the material used in this particular demonstration. As a trivial case of wavefront correction, beacon tracking was also demonstrated, at the speeds allowed by the photorefractive crystal.

A practical implementation of this technique will require an efficient real-time holographic recording material that is fast compared with the time scale characterizing the beacon wavefront fluctuations. The most demanding requirements for the real-time holography arise from the disparate intensities of the beacon and local-oscillator wavefronts, a property that is intrinsic to any coherent detection system. The holographic medium must have very high write sensitivity in order to operate with the low writing intensities that will characterize almost any signal beacon. Furthermore, the beacon hologram must remain intact while being read by a local-oscillator beam whose intensity, by design, is orders of magnitude larger than that of the beacon. Possible approaches to this problem include operation of the local-oscillator beam in a low duty cycle, pulsed mode of operation and the utilization of an appropriate holographic medium, such as an electronically addressed spatial light modulator.

## VI. CONCLUSIONS

The experimental, modeling, and systems analysis results of the NLOT program prove that significant improvements over one-way optical communication links can be achieved with four wave mixing (FWM) phase conjugated (PC) optical communication links. A two-way FWM PC comm link requires a substantially smaller transponder platform than required in a conventional two-way link. This reduction in size and weight of the transponder platform is the result of two benefits: the automatic tracking and atmospheric aberration correction features of the phase conjugation process. Thus, the pointing and tracking hardware required in a conventional system may be eliminated. Since the measured power loss on the second (phase conjugate return) leg of the comm link was shown to be vastly reduced compared to the first (beacon) leg, the power requirements on the transponder laser are also greatly reduced. In addition, large transceiver pointing errors can be accommodated with minimal power increases. However, model results indicate that there is a limit to the ability of FWM PC to generate a PC return with good fidelity if the pointing error is too large. In this extreme, some of the phase aberrations cannot be corrected because information is lost on the small (compared to the beam tilt) transponder aperture.

A basic FWM phase conjugation communication system does not reduce the intensity variance,  $\sigma^2$ , on the comm link over that on a one-way link. However, the experimental results demonstrate that it can prevent the variance on the conjugate return leg from becoming worse. The ratio of the measured variance on the PC return received by the transceiver to the measured variance on the beacon beam received at the transponder,  $\sigma_s^2/\sigma_p^2$ , was 1 for the range of apertures studied. When the FWM cell was replaced with a mirror, the measured variance on the return leg increased and the ratio increased to  $\sigma_s^2/\sigma_p^2 = 2^{11/6} = 3.56$ , the value predicted by turbulence theory for uniformly distributed turbulence. Importantly, unlike conventional links, the information on power fade is communicated back to the beacon aperture via FWM phase conjugation, where appropriate feedback loops operating faster than characteristic atmospheric turbulence times can alter the outgoing beacon phase front to maximize power received by the

conjugator aperture. This fade correction technique then reduces the intensity variance on the outgoing beacon leg (one-way link) over a conventional link.

## VII. APPENDIX A

### MISSION REQUIREMENTS

This appendix contains the information collected for five missions for which detailed information was available. The mission requirements are presented in tables A-1 through A-5. Table A-5 also appears in chapter 2 as table II-3.

Table A-1. Helicopter Mission Requirements (IFPS).

Mission Description:	Helicopter Air to Air; short range voice communication between helicopters, small network (fast switch between terminals is acceptable) is desirable as long term goal.	
Operating Scenario:	Helicopters fly in denied areas, operating under strict radio silence to avoid detection. These are covert "first strike" missions to take out a specific target. This communication is currently accomplished via hand signal and "wing" movements, maintaining radio silence at all costs. It is very difficult to transfer any but the most basic information or prearranged signal. With an optical communication terminal the man on board the helicopter points the transmitter toward the second helicopter and begins covert transmission. The second helicopter receives the transmission and the man on board points his transmitter back toward the first helicopter and completes the communication link. The transmission can be accomplished on an on-demand basis or at predetermined times.	
Optical vs. RF:	Optical communication meets the covert communication requirements. RF frequencies will reveal the helicopter's presence, and hand signals are inadequate.	
Nonlinear Optics Use:	Automatic tracking may decrease fades due to the atmosphere and helicopter jitter.	
Platform Type:	Helicopters - Hand held transmitter; receiver clamped to doorway or window.	
Requirement Source:	AFWAL/ MAC/ Intraformation Positioning System (IFPS). Draft of SON (approved as applicable but w/o final approval). MAC draft SON-03-88 (?); CBD appeared first quarter FY90 for a large multi-M\$ program. RFP due third quarter FY90. Joint program between Flight Dynamics Lab and Avionics Lab. DPM Major Ed Raska, Avionic Laboratory Deputy Branch Chief (513-255-2261).	
<b>Communication</b>		
Range	Nominal 4 nmi or 50% beyond visual range (e.g. 1 mi in fog).	
Altitude	50 ft to 2,000 ft.	
Digital	DR = 20 kbps voice, BER = $10^{-3}$ to $10^{-2}$ , full duplex, single channel; upgrade to data transfer with BER $10^{-7}$ to $10^{-6}$ .	
Analog	DR = 20 kbps, SNR = 9 db.	
<b>Acquisition/Tracking</b>		
	Point and shoot	
Field of Regard	Transmitter	Receiver
Azimuth	180°	360°
Elevation	45°	45°
Uncertainty Angle (Transmitter and Receiver)		
Azimuth	1° clear, TBD if beyond visual range.	
Elevation	2° clear, TBD if beyond visual range.	

Table A-1 (con't). Helicopter Mission Requirements (IFPS).

<b>Environment</b>	
Weather/Atmosphere	All Weather, poor visibility (11 or 14 nm/hr rain, medium or heavy fog).
Dynamic Environment	Helicopter, straight flight, no hard turns.
<b>System</b>	
Total Time	No constraints, real time voice comm any time on demand.
Availability	On demand.
Covertness	Extremely important; primary system driver.
Size/Weight/Volume	Hand held or mounted to door jam; small aperture.
Power	TBD
Cost	TBD
Other	Must be eyesafe. Must not impose additional limitations on personnel.



Table A-2. Situational Awareness Data Link (SADL) Mission Requirements.

Mission Description:	Situational Awareness Data Link: Fighter to Fighter Intergroup Network. Four networked fighters are directed by one commander/pilot sharing all sensor and status data in order to act as a single fighting unit. This is the JTDS (RF) mission which is still under development and having technical difficulties.	
Operating Scenario:	Four fighter aircraft (1 command, 3 subordinate) comprising a small communication network are linked into a single fighting unit with the commander directing the fire power of all four aircraft. All sensor and status data, such as weapons stores and radar threat receivers are monitored either by the command aircraft or his designee. The initial acquisition can occur in very benign conditions (well defined trajectories) but the network must be maintained once established.	
Optical vs. RF:	Optical communications narrow beamwidths will not betray the fighter presence or location. The fighters are vulnerable to detection during the entire data transfer (30 min.). Although data transfer time can be reduced by using a higher RF data rate, the relatively broad RF beams still reveal the fighter's presence.	
Nonlinear Optics Use:	The PC may reduce the fades due to jitter and the atmosphere.	
Platform Type:	Fighters.	
Requirement Source:	AFWAL/ TAC.	
<b>Communication</b>		
Link	Full duplex; network.	
Range	5 to 10 nmi.	
Altitude	≥ 500 ft.	
Digital	DR = 100 kbps, BER = 10 <sup>-7</sup> to 10 <sup>-6</sup> between aircraft (e.g. voice, weapons stores).	
Analog	Not applicable.	
<b>Acquisition/Tracking</b>		
Field of Regard (Transmitter and Receiver)		
Azimuth	360°	
Elevation	30°	
Uncertainty Angle	Transmitter and Receiver acquisition only - must maintain network once acquired.	
Azimuth	1°	
Elevation	1°	
<b>Environment</b>		
Weather/Atmosphere	All flying weather.	
Dynamic Environment	Straight flight, some evasive maneuvers. Primarily prelude to engagement and afterwards.	

Table A-2 (con't). Situational Awareness Data Link (SADL) Mission Requirements.

System	
Total Time	Maintain link while on network (< 24 hrs).
Availability	Any time on network.
Covertness	Very important.
Size/Weight/Volume	Small apertures (< 3 in) on stealth aircraft.
Power	TBD
Cost	TBD

Table A-3. Intergroup Fighter to Fighter (ITTF) Mission Requirements.

Mission Description:	Link individual Situational Awareness Data Link (SADL) fighter groups with a central command to coordinate SADL cell activities.
Operating Scenario:	The command ship transmits data updates or new instructions to individual SADL cells. This is basically a one-way link; however, two-way communication could be beneficial.
Optical vs. RF:	Optical communications narrow beamwidths will not betray the command aircraft's presence or location. However, this could probably be done with RF.
Nonlinear Optics Use:	The PC may reduce the fades due to jitter and the atmosphere and provide some automatic tracking capability.
Platform Type:	Fighters.
Requirement Source:	AFWAL/ TAC.
<b>Communication</b>	
Link	One-way.
Range	$\leq 50$ nmi.
Altitude	$\geq 500$ ft.
Digital	DR = 20 kbps, BER = $10^{-3}$ , voice only.
Analog	DR and SNR - Not applicable.
<b>Acquisition/Tracking</b>	
Field of Regard (Transmitter and Receiver)	
Azimuth	360°
Elevation	15°
Uncertainty Angle (Transmitter and Receiver)	
Azimuth	360°
Elevation	15°
<b>Environment</b>	
Weather/Atmosphere	All flying weather.
Dynamic Environment	Straight flight.
<b>System</b>	
Total Time	Maintain link while on network.
Availability	Any time on network.
Covertness	Important.
Size/Weight/Volume	Small apertures (< 4 in) since there is no room for larger apertures.
Power	TBD
Cost	TBD

Table A-4. Airborne Command Post (ACP) Mission Requirements.

Mission Description:	Airborne Command Post. Update data base between airborne command posts. Command Post spends eight to twelve hours on station, twenty-four hour coverage.
Operating Scenario:	<p>The Airborne Command Post (ACP), flying above friendly territory, is in constant contact with the permanent ground command post. The ACP provides a command post that is relatively secure from missile attack. This security is achieved by randomly flying an ACP within a 200 nmi by 300 nmi area, while maintaining radio silence. An individual aircraft stays on station for eight to twelve hours, with other ACP coming on station as needed to maintain twenty-four hour coverage. At this time the on-board data base is updated. Several of these command regions, spaced at intervals of 100 mi to 150 nmi, are used to cover large areas, such as CONUS. Periodically the individual ACPs need to exchange information and update their data bases.</p> <p>The current update uses RF and takes 30 min at 20 kbps, revealing the presence and location of the ACPs. During an optical data transfer (estimated &lt; 2 min) the ACPs could fly close to each other at the edge of their command area and complete a fast, covert data transfer.</p>
Optical vs. RF:	Optical communications narrow beamwidths will not betray the ACP's presence or location. The ACPs are vulnerable to detection during the entire data transfer (30 min.). Although data transfer time can be reduced by using a higher RF data rate, the relatively broad RF beams still reveal the ACP presence.
Nonlinear Optics Use:	The PC may reduce the fades due to jitter and the atmosphere.
Platform Type:	C135, 707, 747.
Requirement Source:	AFWAL/ SAC/ Program Manager of Airborne Command Post.
<b>Communication</b>	
Link	Full Duplex.
Range	100 nmi to 335 nmi.
Altitude	25,000 to 35,000 ft.
Digital	DR = 36 Mbps, BER = $10^{-6}$ to $10^{-7}$ . Current RF system transfers 20 kbps for 30 min.
Analog	DR, SNR - Not applicable.

Table A-4 (con't). Airborne Command Post (ACP) Mission Requirements.

<b>Acquisition/Tracking</b>	
Field of Regard	
Azimuth	360° desired. 20° to 160° and 200° to 340° coverage acceptable (bow tie pattern).
Elevation	2.5°
Uncertainty Angle (Transmitter and Receiver)	
Azimuth	56°
Elevation	2.5°
<b>Environment</b>	
Weather/Atmosphere	Very little weather at these altitudes, may have to contend with some clouds.
Dynamic Environment	Stable airplanes.
<b>System</b>	
Total Time	< 1 min.
Availability	At prearranged times.
Covertiness	Very Important.
Size/Weight/Volume	Small (3 - 4 in diameter); semi-spherical pods are OK.
Power	TBD
Cost	TBD

Table A-5. Collection Sentry Aircraft (CSA) Mission Requirements.

Mission Description:	Collection Sentry Aircraft (similar in range and data rate to Airborne Command Post Mission). Update database or transfer sensor data from a sentry aircraft or a remote piloted vehicle (RPV) patrolling over hostile territory.
Operating Scenario:	A patrol aircraft or RPV has collected a variety of sensor data. The interrogating aircraft, approximately 100 nmi. away, approaches the patrol area and initiates a data transfer. The data transfer must be very covert, not revealing the presence or location of the patrol aircraft or RPV. The interrogating aircraft is a sentry aircraft going on station and receiving the latest data or a command aircraft monitoring the RPV. A real time video relay is desired but not required (potentially an upgrade).
Optical vs. RF:	Optical communications narrow beamwidths will not betray the CSA presence or location. The CSA are vulnerable to detection during the entire data transfer (30 min.). Although data transfer time can be reduced by using a higher RF data rate, the relatively broad RF beams still reveal the CSA presence.
Nonlinear Optics Use:	The PC may reduce the fades due to jitter and the atmosphere.
Platform Type:	Large Lear Jets (between a Fighter and C135 in size).
Requirement Source:	AFWAL/ Army/ CSA Program Manager.
<b>Communication</b>	
Link	Potentially asymmetric.
Range	50 to 100 nmi, clear atmosphere - may reduce range with clouds.
Altitude	25,000 to 35,000 ft.
Digital	DR = 30 to 60 Mbps, BER = $10^{-7}$ .
Analog	DR and SNR - Not applicable.
<b>Acquisition/Tracking</b>	
Field of Regard (Transmitter and Receiver)	
Azimuth	360°
Elevation	2°
Uncertainty Angle (Transmitter and Receiver)	
Azimuth	60°
Elevation	2°
<b>Environment</b>	
Weather/Atmosphere	Very little weather at these altitudes, may have some clouds.
Dynamic Environment	Normal environment, straight flight (No dog fighting or steep turns).

Table A-5 (con't). Collection Sentry Aircraft (CSA) Mission Requirements.

System	
Total Time	< 1 min.
Availability	On demand.
Covertness	Very important.
Size/Weight/Volume	Keep it small, CSA aircraft are loaded with equipment.
Power	TBD
Cost	TBD

## VIII. APPENDIX B

### PROPAGATION EQUATION DERIVATION

In section B.1, we present the equations showing how a Gaussian beam propagates in free space when subject to tilt, translation, and focus errors. In section B.2, we then add (1) a Gaussian reflectivity, (2) a (full or partial) tilt and focus correction, as well as (3) an additional uncorrected tilt and focus contribution, and repropagate to the receiver, which is assumed to be located in the original transmitter plane. We also present the cases that reduce to that of Lutomirski and Warren<sup>25</sup>, for comparison. Section B.3 makes the specific parameter assumptions for a phase conjugated link.

Included in section B.4 are some numerical evaluations for irradiance breakeven PC gain (IBPG). This gain is the increase in power needed at the transponder in order to compensate for the range and truncation losses for the two-way conjugated link. Stated differently, the gain is the additional factor that must be included to change a one-way power transmission link to a two-way phase conjugated calculation, keeping the same power on the receiver.

Presented in section B.5 are theoretical and numerical results for the full "power in the bucket" breakeven PC gain (PBPG), describing the gain needed to match received power to that found in the 1-way case. This power calculation assumes that the receiver has a gaussian reflectivity, formulated in the same way as the gaussian transponder in section B.2.

Finally, section B.6 presents theoretical and numerical results for a different figure of merit, the "reduction in power required by the transponder to return a signal to the receiver when it is fed and then conjugates the path aberration, as compared to the power that would be needed for the transponder to send a direct signal to the receiver". This last set of results shows most clearly the potential payoff of phase conjugation.

The general results for the beam width, displacement, and transmission loss are given in equations (A-46), (A-31) and (A-24). For the case with an originally on-axis beam ( $\vec{p}_1 = 0$ ), the displacement is given in equation (A-51). These equations can



be used in link budget calculations, with transmission factor associated with the phase conjugation given by the factor

$$L(\alpha, \beta) = \int_{\text{receiver}} d^2r \exp[ -2(\vec{r} - \vec{r}_3)^2/Q_3^2 ] \quad (\text{VIII-1})$$

As an approximation, one could use the on-axis loss factor defined in equation (A-66).

Note that this loss factor has various knobs that can be tweaked for performance enhancement. For a fixed geometry (range),

$w_1$  = transmitter beam size (1/e in "field")

$F_1^{-1}$  = transmitter curvature

$b$  = reflector (transponder) size

$F_2^{-1}$  = reflector curvature added (i.e. not conjugated)

appear to be the most likely parameters to vary in order to optimize performance.

### Irradiance Breakeven PC Gain (IBPG) -- Example

As a simple limit, we treat the IBPG given by the inverse of equation (A-65) for the no-tilt ( $\vec{\rho}_1 = 0$ ) case,

$$\vec{\theta}_1 = 0.$$

The gain is then

$$\begin{aligned} G_{10} &= L_{10}^{-1} \\ &= \frac{(1 + v\delta)^2 + \gamma^2 - 2v\gamma\delta^2\epsilon + \delta^2(1 + \gamma^2)\epsilon^2}{(\delta/v)(v^2 + \delta^2\gamma^2)} \end{aligned} \quad (\text{VIII-2})$$

where  $\delta$ ,  $v$ ,  $\gamma$ , and  $\epsilon$  are given in equations (A-39), (A-40), (A-41), and (A-57). A typical case is that range and aperture sizes are fixed, and one hopes to adjust  $F_2$  to minimize the required gain. This occurs by optimizing equation (VIII-2) at

$$\epsilon = \epsilon_0 = \frac{v\gamma}{(1 + \gamma^2)} \quad (\text{VIII-3})$$

which reduces the required gain by

$$X = \frac{G(\epsilon = \epsilon_0)}{G(\epsilon = 0)} = 1 - \frac{v^2\gamma^2\delta^2}{(1 + \gamma^2)[\gamma^2 + (1 + v\delta)^2]} \quad (\text{VIII-4})$$

The  $F_2$  control knob thus helps only when  $\gamma \neq 0$  (i.e. when  $F_1 \neq R$  which occurs when the transmitter beam has not been properly focused).

The offset angle part of the gain, as in equations (A-63) and (A-64), is

$$\exp(G_{11})$$

where

$$G_{11} = \frac{-2r_2^2}{Q_2^2} + \frac{2r_2^2}{(Q_2^2 + b^2)} + \frac{2r_3^2}{Q_3^2} \quad (\text{VIII-5})$$

where the first term is evaluated for the one-way link from the transponder to the receiver ( $w_1 \rightarrow b$ ), giving

$$\begin{aligned}\hat{G}_{11} &\equiv \frac{G_{11}}{2(R\theta_1/w_1^2)} \\ &= \frac{(v^2[(v\delta^2 + \delta - v)(\delta\gamma^2 - v - v^2\delta) + 2v^2\delta^3\gamma\epsilon + \delta^2\epsilon^2(v - \delta)(v - \delta\gamma^2)]}{(v^2 + \delta^2\gamma^2)[\gamma^2 + (1 + v\delta)^2 - 2v\gamma\delta^2\epsilon + \delta^2(1 + \gamma^2)\epsilon^2]}\end{aligned}\quad (\text{VIII-6})$$

For  $\gamma = 0$  (focused beacon), this becomes

$$\begin{aligned}\hat{G}_{11} &\equiv \frac{G_{11}}{2(R\theta_1/w_1^2)} \\ &= \frac{v(v - \delta - v\delta^2)(1 + v\delta) + v(v - \delta)\delta^2\epsilon^2}{(1 + v\delta)^2 + \delta^2\epsilon^2}\end{aligned}\quad (\text{VIII-7})$$

So, for large tilt offsets ( $\bar{\theta}_1$ ), some return wave control ( $\epsilon \neq 0$ ) might pay off (i.e. there is still an " $\epsilon$ " term remaining that can be used for control).

For simplicity, consider the case with  $\gamma = 0$  and  $v = \delta$  (i.e. focused and with equal transceiver and transponder sizes). Then,

$$\hat{G}_{11} = \frac{v^4(1 + v^2)}{(1 + v^2)^2 + v^2\epsilon^2}\quad (\text{VIII-8})$$

so that increasing  $\epsilon^2$  (the transponder decollimation) brings  $\hat{G}_{11}$  closer to zero, and increases the IBPG,  $G_i$ . From equation (VIII-2), when  $\gamma = 0$  increasing  $\epsilon^2$  increases  $G_{i0}$  (the zero tilt offset value of gain) and  $G_i$  (the total gain, including a contribution from the transmitter-plane tilt offset). Thus, in this simple case,

- with the transceiver path in focus and with  $b = w_1$ , the best performance (minimum breakeven gain) is achieved with a collimated transponder ( $\epsilon = 0$ ).

## Propagation Equation Derivation

### 1.0 ONE-WAY PROPAGATION

In this appendix, I will evaluate the propagated field for tilted, defocused, and decentered infinite gaussian beams.

Let

$$k = 2\pi/\lambda$$

$$\lambda = \text{wavelength}$$

$$R = \text{range}$$

$$a = k/R$$

$$F = \text{focal range}$$

$$w = \text{gaussian field } 1/e \text{ radius in transmitter plane}$$

$$Q = \text{gaussian field } 1/e \text{ radius in receiver plane}$$

$$\vec{\rho}_0 = \text{transmitter plane decentration}$$

$$\vec{r}_0 = \text{receiver plane decentration}$$

$$P = \text{power}$$

$$U_0 = \text{peak transmitter field}$$

$$\vec{\theta} = \text{transmitter tilt angle}$$

$$\vec{\phi} = \text{receiver tilt angle}$$

$$\vec{\rho} = \text{transmitter plane coordinate}$$

$$\vec{r} = \text{receiver plane coordinate}$$

Then the transmitter plane scalar field is

$$U(\vec{\rho}) = U_0 \exp(-(\vec{\rho} - \vec{\rho}_0)^2/w^2) \quad (\text{A-1})$$

The power is given by

$$\begin{aligned} P &= \int U(\vec{\rho})^2 d^2\vec{\rho} \\ &= \frac{\pi}{2} U_0^2 w^2 \end{aligned} \quad (\text{A-2})$$

The receiver plane field is given in the Fresnel approximation by<sup>(6)</sup>

$$V(\vec{r}) = \frac{c_o}{\lambda R} \int_{-\infty}^{\infty} \int U(\vec{\rho}) \exp \left[ + \frac{ik}{2R} (\vec{r} - \vec{\rho})^2 - \frac{ik}{2F} \rho^2 - ik\vec{\theta} \cdot \vec{\rho} \right] d^2\vec{\rho} \quad (A-3)$$

$$= \frac{C}{\lambda R} \int_{-\infty}^{\infty} \int U_o \exp \left[ -A(\vec{\rho} + \frac{\vec{B}}{2A})^2 + \frac{B^2}{4A} \right] d^2\vec{\rho} \quad (A-4)$$

where

$$c_o = -i \exp(ikR) \quad (A-5)$$

$$A = \frac{1}{w^2} + \frac{ik}{2} \left( \frac{1}{F} - \frac{1}{R} \right) \quad (A-6)$$

$$\vec{B} = ik \left( \vec{\theta} + \frac{\vec{r}}{R} \right) - \frac{2\rho_o}{w^2} \quad (A-7)$$

$$C = c_o \exp \left[ \frac{ikr^2}{2R} - \frac{\rho_o^2}{w^2} \right] \quad (A-8)$$

Completing the integration, we find

$$V(\vec{r}) = \frac{c_o U_o}{\lambda R} \frac{\pi}{A} \exp \left[ \frac{B^2}{4A} + \frac{ikr^2}{2R} - \frac{\rho_o^2}{w^2} \right] \quad (A-9)$$

Now A and B are complex. Thus, the field is

$$V(\vec{r}) = \frac{DU_o w}{Q} \exp \left[ - \frac{ik}{2G} r^2 - ik\vec{\phi} \cdot \vec{r} - \frac{(\vec{r} - \vec{r}_o)^2}{Q^2} \right] \quad (A-10)$$

where we have defined

- D = (unimportant) r-independent phase
- Q = propagated spot size
- G = propagated curvature
- $\vec{\phi}$  = propagated tilt angle
- $\vec{r}_o$  = propagated displacement

and (after much tedious algebra) find

$$Q^2 = \frac{4R^2}{w^2 k^2} + w^2 R^2 \left( \frac{1}{F} - \frac{1}{R} \right)^2 \quad (A-11)$$

$$G^{-1} = -R^{-1} + \frac{w^2}{Q^2} \left( R^{-1} - F^{-1} \right) \quad (A-12)$$

$$\vec{\phi} = \frac{4R\vec{\rho}_0}{k^2 w^2 Q^2} - \frac{w^2 R}{Q^2} \left( \frac{1}{F} - \frac{1}{R} \right) \vec{\theta} \quad (A-13)$$

$$\vec{r}_0 = -R\vec{\theta} - R \left( \frac{1}{F} - \frac{1}{R} \right) \vec{\rho}_0 \quad (A-14)$$

$$D = c_0 \exp \left\{ -i\psi - \frac{iR^2}{kQ^2} \left[ \frac{4\vec{\rho}_0 \cdot \vec{\theta}}{w^2} + \left( \frac{2\rho_0^2}{w^2} - \frac{k^2 w^2 \theta^2}{2} \right) \left( \frac{1}{F} - \frac{1}{R} \right) \right] \right\} \quad (A-15)$$

$$\tan\psi = \frac{kw^2}{2} \left( \frac{1}{F} - \frac{1}{R} \right) \quad (A-16)$$

(where D and  $\psi$  are irrelevant).

Some of these equations have obvious interpretations:

Equation (A-11): The spot width is the root-mean-square of a diffraction spot

$$Q_D = \frac{2R}{wk} = \left( \frac{2}{\pi} \right) \left( \frac{\lambda}{2w} \right) R$$

and a focusing spot

$$Q_F = w \left( \frac{R}{F} - 1 \right)$$

where the diffraction spot size is the gaussian beam version of the Airy equation

$$Q_{D,Airy} = 1.22 \left( \frac{\lambda}{D} \right) R$$

Since  $2/\pi \sim .7$ , infinite gaussian beams spread less than uniform beams. (But who has an infinite mirror?)

Equation (A-12): This equation gives the curvature on the beam after propagation. Note that the limit  $R \rightarrow 0$  must be taken with care, noting that

$$w^2/Q^2 \xrightarrow{R \rightarrow 0} 1 + 2R/F$$

so that

$$G^{-1} \xrightarrow{R \rightarrow 0} -R^{-1} + (1 + 2F^{-1}R) (R^{-1} - F^{-1})$$

$$\xrightarrow{\quad} F^{-1}$$

as one would expect.

Equation (A-13): The tilt angle has two components. A tilt angle in the transmitter plane causes tilt which vanishes in the focal plane, while translation in the transmitter plane induces a tilt angle in the receiver plane. In the focal plane,

$$Q \rightarrow \frac{2R}{wk}$$

so that

$$\vec{\theta} \rightarrow \vec{\rho}_0/R$$

Equation (A-14): Translation in the receiver plane is produced by tilt and translation in the transmitter plane. In the focal plane ( $R=F$ ), transmitter plane translation is irrelevant, and the standard

$$\vec{r}_0 = -R\vec{\theta}$$

result is found.

## 2.0 TWO-WAY PROPAGATION

The discussion above is applicable to a one-step propagation. We now apply these formulae to the two-way calculation.

We now express equations (A-11) to (A-14) in terms of values at the transmitter/receiver (transceiver) and transponder planes with subscripts 1 and 2, respectively. Then, in this notation, the field hitting the transponder, or second optic, has characteristics

$$Q_2^2 = \frac{4R^2}{k^2 w_1^2} + w_1^2 S_1^2 \quad (A-17)$$

$$S_1 = 1 - R/F_1 \quad (A-18)$$

$$R/G_2 = -1 + S_1 w_1^2/Q_2^2 \quad (A-19)$$

$$\vec{\phi}_2 = (w_1^2/Q_2^2) S_1 \vec{\theta}_1 + 4R\vec{\rho}_1/(k^2 w_1^2 Q_2^2) \quad (A-20)$$

$$\vec{r}_2 = S_1 \vec{\rho}_1 - R\vec{\theta}_1 \quad (\text{A-21})$$

A reflection of the field at the second plane of the form

$$\exp(-r^2/b^2)$$

$b = 1/e$  effective transponder radius

adds an effective width term to the reflected beam, giving the beam an outgoing width

$$w_2^2 = Q_2^2 b^2 / (Q_2^2 + b^2) \quad (\text{A-22})$$

as well as modifying the displacement of the outgoing beam to

$$\vec{\rho}_2 = \vec{r}_2 b^2 / (b^2 + Q_2^2) \quad (\text{A-23})$$

In addition to the power loss factor induced by the beam spread

$$\tau_1 = w_2^2 / Q_2^2 \text{ (beam truncation power loss - spread)} \quad (\text{A-24a})$$

the gaussian reflection gives a beam truncation transmission loss factor due to pointing error of

$$\tau_2 = \exp[-r_2^2 / (Q_2^2 + b^2)] \quad (\text{A-24b})$$

At the second optic, we now impose a phase conjugation, parametrized by

$\alpha$ : tilt correction factor  
 $\beta$ : focus correction factor

so that

$$R/G_2 \rightarrow \beta R/G_2$$

$$\vec{\phi}_2 \rightarrow \alpha \vec{\phi}_2$$

This parametrization permits us to treat full conjugation ( $\alpha = \beta = -1$ ) or no conjugation ( $\alpha = \beta = 1$ ). We then propagate through the uncompensated tilt and focus which we permit to be added (for generality) by the second optic

$$F_2^{-1}: \text{ added curvature at second optic}$$

$$\vec{\theta}_2: \text{ added tilt at second optic}$$

so that combining with the correction factors, the curvature and tilt on leaving the second optic are changed from their input values to



$$R/G_2 \rightarrow \beta R/G_2 + R/F_2 \quad (A-25)$$

$$\vec{\phi}_2 \rightarrow \alpha \vec{\phi}_2 + \vec{\theta}_2 \quad (A-26)$$

After propagation back to the receiver, assumed co-located with the transmitter, and which we call the transceiver, at range R, we find that entering this third optic, the beam is characterized by

$$Q_3^2 = \frac{4R^2}{k^2 w_2^2} + S_2^2 w_2^2 \quad (A-27)$$

$$S_2 = 1 - R/F_2 - \beta R/G_2 \quad (A-28)$$

$$R/G_3 = -1 + S_2 w_2^2 / Q_3^2 \quad (A-29)$$

$$\vec{\phi}_3 = (w_2^2 S_2 / Q_3^2) (\alpha \vec{\phi}_2 + \vec{\theta}_2) + 4R \vec{r}_2 / [k^2 Q_2^2 Q_3^2] \quad (A-30)$$

$$\vec{r}_3 = S_2 [b^2 / (b^2 + Q_2^2)] \vec{r}_2 - R(\alpha \vec{\phi}_2 + \vec{\theta}_2) \quad (A-31)$$

After going through the third optic with

$F_3^{-1}$ : added curvature at third optic

$\vec{\theta}_3$ : added tilt at third optic

we find that exiting the third optic, the curvature and tilt are changed to

$$R/G_4 = R/G_3 + R/F_3 \quad (A-32)$$

$$\vec{\phi}_4 = \vec{\phi}_3 + \vec{\theta}_3 \quad (A-33)$$

where, typically, we expect the first and third optics to be the same, so that

$$\vec{\theta}_3 = -\vec{\theta}_1 \quad (A-34)$$

$$F_3 = -F_1 \quad (A-35)$$

We now integrate over the receiver to determine the received power. We assume a receiver of radius, c. This power integral is modeled by

- o multiplying the field by a gaussian transmission  $\exp(-r^2/c^2)$
- o integrating over the infinite gaussian

This takes a beam characterized by size, displacement and power of  $Q_3^2$ ,  $\vec{r}_3$ , and  $P_3$  (where  $P_3$  is the power leaving the transponder and thus entering the transceiver plane), and converts it to a beam with size, displacement, and power (actually received by the transceiver):

$$w_3^2 = Q_3^2 c^2 / (Q_3^2 + c^2) \quad (A-36)$$

$$\vec{\rho}_3 = \vec{r}_3 c^2 / (c^2 + Q_3^2) \quad (A-37)$$

$$P_3' = P_3 \frac{w_3^2}{Q_3^2} \exp[-2r_3^2 / (Q_3^2 + c^2)] \quad (A-38)$$

Equation (A-38) is the crucial equation which completes the calculation of "power in the receiver bucket".

#### Simplified Notation

We now define scaling variable notation

$$\delta = kb^2 / (2R) \quad (A-39)$$

$$\nu = kw_1^2 / (2R) \quad (A-40)$$

$$\gamma = \nu S_1 \quad (A-41)$$

In this notation,

$$Q_2^2 / w_1^2 = (1 + \gamma^2) / \nu^2 \quad (A-42)$$

$$b^2 / w_1^2 = \delta / \nu \quad (A-43)$$

$$w_2^2 / w_1^2 = \delta (1 + \gamma^2) / [\nu(\nu\delta + 1 + \gamma^2)] \quad (A-44)$$

$$R/G_2 = [\nu\gamma - 1 - \gamma^2] / (1 + \gamma^2) \quad (A-45)$$

$$Q_3^2 / w_1^2 = \frac{(\nu\delta + 1 + \gamma^2)}{\nu\delta (1 + \gamma^2)} + S_2^2 \frac{\delta (1 + \gamma^2)}{\nu (\nu\delta + 1 + \gamma^2)} \quad (A-46)$$

$$R/G_4 = R/F_3 - \frac{(1 + \nu\delta)^2 + \gamma^2 - \gamma\nu\delta^2 + (\beta + 1) \delta^2 [\gamma\nu - (1 + \gamma^2)]}{(1 + \nu\delta)^2 + \gamma^2} \quad (A-47)$$

#### On-axis Starting Point

For the simplified case with no decentration on the transmitter beam

$$\vec{\rho}_1 = 0$$

the scaling variables can be inserted easily to give

$$\vec{\phi}_2 = \frac{\nu\gamma}{1 + \gamma^2} \vec{\theta}_1 \quad (\text{A-48})$$

$$\vec{r}_2 = -R\vec{\theta}_1 \quad (\text{A-49})$$

$$\vec{\phi}_3 = S_2 \left( \vec{\theta}_2 + \frac{\alpha\nu\gamma\vec{\theta}_1}{1 + \gamma^2} \right) \frac{w_2^2}{Q_3^2} - \frac{w_1^4 \vec{\theta}_1}{\nu^2 Q_2^2 Q_3^2} \quad (\text{A-50})$$

$$\vec{r}_3 = -R \left( \vec{\theta}_2 + \frac{\alpha\nu\gamma\vec{\theta}_1}{1 + \gamma^2} \right) - \frac{Rb^2 S_2 \vec{\theta}_1}{b^2 + Q_2^2} \quad (\text{A-51})$$

#### Special Test Case

Lutonirski and Warren<sup>(2)</sup> treated the special case with

$$F_2^{-1} = 0$$

$$\vec{\theta}_2 = 0$$

$$\beta = -1$$

$$\alpha = -1$$

With these additional assumptions, and ignoring the  $F_3$  contribution (which was ignored in reference 2), we find

$$S_2 = \nu\gamma/(1 + \gamma^2) \quad (\text{A-52})$$

$$Q_3^2/w_1^2 = \frac{(1 + \nu\delta)^2 + \gamma^2}{\delta\nu(1 + \nu\delta + \gamma^2)} \quad (\text{A-53})$$

$$R/G_3 = - \frac{(1 + \nu\delta)^2 + \gamma^2 - \gamma\nu\delta^2}{(1 + \nu\delta)^2 + \gamma^2} \quad (\text{A-54})$$

The  $Q_3^2$  equation agrees with equation (23) of reference (2). The  $R/G_3$  result does not, which is due to an (alleged) typographical error in that paper.

The linear terms in reference (2) do include the return pass contribution,  $\vec{\theta}_3 = \vec{\theta}_1$ , so we get

$$\begin{aligned}\vec{\phi}_4 &= \vec{\theta}_1 \left\{ - \frac{\nu\delta(1+\nu\delta)}{(1+\nu\delta)^2 + \gamma^2} \right\} + \vec{\theta}_1 \\ &= \vec{\theta}_1 \left\{ \frac{1+\nu\delta+\gamma^2}{(1+\nu\delta)^2 + \gamma^2} \right\}\end{aligned}\quad (A-55)$$

$$\vec{r}_3 = R\vec{\theta}_1 \left\{ \frac{\nu\gamma}{1+\gamma^2 + \nu\delta} \right\} \quad (A-56)$$

and agree with reference (2) (up to the sign of each term), again after correction of a second error in reference (2). (Note that in reference (2), the last  $\theta$  in equation (22) should be  $i\theta$ , and the  $\delta^2 \nu(\gamma-\nu)$  and  $i\nu\delta\gamma$  factors in equation (23) are off by a sign.)

### 3.0 PC Link Model Case

For a phase conjugated link calculation, we will use a form with  $F_2^{-1}$  not set to zero, but with

$$\begin{aligned}\vec{\rho}_1 &= 0 \quad (\text{transmitted beam on-axis}) \\ \alpha &= -1 \quad (\text{phase-conjugated tilt}) \\ \beta &= -1 \quad (\text{phase-conjugated focus}) \\ \vec{\theta}_2 &= 0 \quad (\text{no tilt added at transponder})\end{aligned}$$

With these assumptions, and defining

$$\epsilon = R/F_2 \quad (A-57)$$

we find

$$S_2 = \frac{\nu\gamma}{1+\gamma^2} - \epsilon \quad (A-58)$$

$$\vec{r}_3 = R\vec{\theta}_1 \frac{\nu}{1+\nu\delta + \gamma^2} [\gamma + \delta\epsilon] \quad (A-59)$$

$$Q_3^2/w_1^2 = \frac{\gamma^2 + (1+\nu\delta)^2 - 2\nu\gamma\delta^2\epsilon + \delta^2(1+\gamma^2)\epsilon^2}{\nu\delta(1+\nu\delta + \gamma^2)} \quad (A-60)$$

Note that by setting

$$\epsilon = -\gamma/\delta = -\frac{w_1^2}{b^2} \left(1 - \frac{R}{F_1}\right)$$

the return offset can be reduced to zero. (A special case of this is  $F_1 = R$  and  $1/F_2 = 0$ , the focused probe, collimated return case.) Unfortunately, the beam spread ( $Q_3^2$ ) is increased. The loss component

$$\Lambda = \exp(-2r_3^2/Q_3^2)$$

is given by

$$-\ln \Delta = \frac{2 R^2 \theta_1^2 \nu^3 \delta (\gamma + \delta \epsilon)^2}{w_1^2 (1 + \nu \delta + \gamma^2) [(1 + \nu \delta)^2 + \gamma^2 - 2\nu\gamma\delta^2\epsilon + \delta^2(1 + \gamma^2)\epsilon^2]} \quad (\text{A-61})$$

with minimum at the solution of the quadratic

$$\begin{aligned} \epsilon^2 [\gamma \delta^3 (1 + \gamma^2) + \nu \gamma \delta^4] + \epsilon [\delta^2 (1 + \gamma^2) (\gamma^2 - \delta^2)] \\ - \gamma [\nu \gamma^2 \delta^2 + \delta \gamma^2 + \delta (1 + \nu \delta)^2] = 0 \end{aligned} \quad (\text{A-62})$$

I leave further manipulation of this to the interested reader. (I didn't get to it!)

Note that as  $b \rightarrow \infty$ ,  $\vec{r}_3 \rightarrow 0$ .

#### Link Model - Near Field

In the near field,  $\delta$ ,  $\nu$  and  $\gamma$  all go to infinity, and

$$\frac{r_3^2}{R^2 \theta_1^2} \rightarrow \left( \frac{w_1^4}{w_1^2 b^2 + b^4} \right) \left( s_1 + \frac{b^2 \epsilon}{w_1^2} \right)^2$$

As is obvious, for a large reflector,  $b^2 \gg w_1^2$ , and if  $\epsilon = 0$ ,  $r_3^2 = 0$ , i.e. no offset is produced if you conjugate on a large reflector. If you defocus at the reflector, however, then the limit is

$$\frac{r_3^2}{R^2 \theta_1^2} \rightarrow \epsilon^2$$

The loss factor limit (for  $\epsilon \rightarrow 0$ ) is

$$-\ln \Delta \approx 2R^2 \theta_1^2 / b^2$$

which goes to zero for a large reflector.

## Link Model - Far Field

In the far field,  $\delta$ ,  $\nu$  and  $\gamma$  all go to zero, so that the loss factor is

$$- \ln \Delta = \frac{2R^2 \theta_1^2 \nu^3 \delta (\gamma + \delta \epsilon)^2}{w_1^2 [1 - 2\nu\gamma\delta^2\epsilon + \delta^2(1 + \gamma^2)\epsilon^2]}$$

When  $\epsilon \rightarrow 0$ , and  $b$  is finite, the factor is

$$- \ln \Delta = \frac{\theta_1^2 w_1^4 b^2 k^3}{8R}$$

Clearly, the case of

$$\epsilon = -\gamma/\delta = -\frac{w_1^2}{b^2} (1 - R/F_1)$$

offers the potential for eliminating the link loss, at the expense of broadening the beam.

## 4.0 IRRADIANCE BREAK-EVEN PC GAIN (IBPG)

A useful figure of merit for the performance of a phase conjugated link is the ratio of the irradiance delivered with a transmitter power,  $P$  (see Equation (A-2)), in a 1-way link, compared to that delivered in a 2-way phase conjugated link also starting with power,  $P$ . This ratio is found by squaring the equivalent of equation (A-10), so that (with  $\alpha = \beta = -1$ ,  $\vec{r}_1 = 0$ ,  $\vec{r}_2 = 0$ ), the two irradiances are:

$$I_{1\text{-way}}(\vec{r}) = \frac{|U_o|^2 w_1^2}{Q_2^2} \exp \left[ -2(\vec{r} - \vec{r}_2)^2 / Q_2^2 \right] \quad (\text{A-63})$$

$$I_{PC}(\vec{r}) = \frac{|U_o|^2 w_1^2}{Q_2^2} \frac{w_2^2}{Q_3^2} \exp \left[ -2r_2^2 / (Q_2^2 + b^2) - 2(\vec{r} - \vec{r}_3)^2 / Q_3^2 \right] \quad (\text{A-64})$$

We define the Irradiance Breakeven PC loss as

$$\begin{aligned} L_I &= \frac{I_{PC}(0)}{I_{1\text{-way}}(0)} \\ &= L_{I0} \exp L_{I1} \end{aligned} \quad (\text{A-65})$$

where the size of the transmitter ( $w_1^2$ ) in the 1-way link should be identified with the radius of the transponder in the 2-way link, while the transmitter radius  $w_1^2$  in the 2-way PC link is that of the transceiver. In calculations, this means that in the 1-way formulae,  $\nu \rightarrow \delta$  and  $\gamma \rightarrow \delta\gamma/\nu$  for the 1-way irradiance.

Using the notation given earlier, one can show that for  $\vec{\theta}_1 = 0$ ,

$$L_I \rightarrow L_{I0} = \frac{(\nu^2 + \delta^2 \gamma^2)(\delta/\nu)}{(1 + \nu\delta)^2 + \gamma^2 - 2\nu\gamma\delta^2\epsilon + \delta^2(1 + \gamma^2)\epsilon^2} \quad (\vec{\theta}_1 = 0) \quad (A-66)$$

For the trivial return collimated / outgoing focused case,

$$\gamma = \epsilon = 0$$

and

$$L_{I0} \rightarrow \frac{\nu\delta}{(1 + \nu\delta)^2}$$

Assuming  $\delta = \nu$  (since we are comparing to 1-way transmission from an aperture characterized by  $\delta$ , and use of equal aperture sizes simplifies the algebra), then when  $\nu \rightarrow 0$  (far field),  $L_I \rightarrow \nu^2$ , i.e. the relative link loss is small. When  $\nu \rightarrow \infty$  (near field),  $L_I \rightarrow 1/\nu^2$ , i.e. the relative link loss is also small.  $L_I$  is maximized (and the breakeven gain minimized) when

$$\nu = 1$$

If  $\delta$  is fixed,  $L_I$  is maximized when  $\nu \rightarrow \infty$  (near field), i.e. for fixed transponder diameter, the best performance of the PC link is when the transceiver is largest, a rather obvious result.

The Irradiance Breakeven PC gain (IBPG), is the retroreflection gain (as obtained with a nonlinear optic system with gain) needed to offset this loss. It is given by

$$G_I = L_I^{-1} = G_{I0} \exp G_{I1} \quad (A-67)$$

An intuitive interpretation of this gain is found by the following considerations. The 1-way link efficiency is

$$\epsilon_1 = T_T T_A T_R T_J$$

where

- $T_T$  = transmission through the transmitter (clipping)
- $T_A$  = atmospheric losses
- $T_R$  = receiver clipping
- $T_J$  = jitter transmission (1-loss)

For the 2-way link, the efficiency is

$$\epsilon_2 = T_T T_A T_{TP} T_{PC} T_A T_R$$

where

$T_{TP}$  = transponder clipping

$T_{PC}$  = losses due to imperfect correction of the jitter (and turbulence) by the phase conjugator

So, the Irradiance Breakeven PC Gain as defined in this Appendix is

$$G_I = L_I^{-1} = \frac{\epsilon_1(\text{peak})/T_A}{\epsilon_2(\text{peak})/T_A^2} = T_A \epsilon_1 / \epsilon_2$$

i.e. the IBPG is the ratio of the 1-way and 2-way link efficiencies. We have ignored the effect of atmospheric transmission losses in the present calculation only for calculational convenience. They must eventually be included.

For the case in which there is no tilt at the transceiver ( $\vec{\theta}_1 = 0$ ), and no uncompensated refocus at the PC transponder ( $\epsilon = 0$ ), the IBPG is

$$G_I = G_{I0} = \frac{(1 + \nu\delta)^2 + \gamma^2}{(\nu^2 + \delta^2 \gamma^2)(\delta/\nu)} \quad (\text{A-68})$$

For the simple case of equal transceiver and transponder diameters, i.e.  $w_1 = b$ , we get  $\nu = \delta$ , and

$$G_{I0} = \frac{(1 + \nu^2)^2 + \gamma^2}{\nu^2(1 + \gamma^2)} \quad (\text{A-69})$$

Special Cases, assuming  $\nu = \delta$ :

Two limit cases for  $\nu = \delta$  are:

1. Far Field ( $\nu \sim 0$ ):  $G_{I0} = 1/\nu^2$
2. Near Field ( $\nu \sim \infty$ ):  $G_{I0} = \nu^2/(1 + \gamma^2)$

So in the near field, poor focusing can reduce the required breakeven PC gain. For example, severe turbulence can produce some defocusing which reduces  $G$  (referenced to the aberrated 1-way propagation case).

#### Description of Figures

Figures A-1 through A-5 present  $G_I$  (including  $G_{I0}$  and  $\vec{\theta}$  effects, i.e.  $G_{I1} \neq 0$ ) versus the normalized transmitter tilt angle

$$T - \vec{\theta} w_1/\lambda \quad 179$$

where  $\vec{\theta}$  is the transmitter tilt angle. These figures include results for



- o five values of Fresnel Number ( $= \nu = \delta$ ) (in figures A-1 through A-5 for  $\nu = 10^{-4}, 10^{-2}, 10^0, 10^2, \text{ and } 10^4$ )
- o three values of transmitter focus ( $F = 1.1R, R, 0.9R$ ) in each figure
- o three values of unconjugated transponder focus ( $F_2 = \infty, 4R, -4R$ ) in each figure

These figures support the following conclusions:

1. Shown in the figure is the maximum value of  $\vec{T}$  for which the curve is really appropriate, estimated by

$$T_{\text{MAX}} \sim \frac{\lambda}{2w_1} + \frac{b}{R} \quad (\text{A-70})$$

to indicate that if the beam tilt is larger than the diffraction size and the receiver size, then not much power hits the receiver in either the 1-way or phase conjugated 2-way paths, and estimates of irradiance breakeven PC gain are severely affected by the "infinite gaussian reflector" assumption.

2. There is substantial change in gain relative to the  $\vec{\theta} = 0$  case, as defined in equations (A-68) and (A-69), as long as

$$\vec{T} < 0.1 \text{ for } \nu > 1, F = R$$

which is a rather small value of tilt to expect. The impact of  $\vec{T}$  is less important for small values of  $\nu$  (far field)

3. Use of an unconjugated transponder focus ( $F_2$ ) contribution does not offer any obvious benefit (as is only vaguely visible in the figures, but evident from the actual numerical values of G).

Another interesting set of figures (figures A-6 through A-14) shows the dependence of  $G_I$  on range. Note that the maximum range of validity (given by inverting equation A-70) is also given in each figure. From these figures, the following conclusions are drawn.

1. Very little dependence on  $F_2$  is evident.
2. The range of validity of the formulation (in terms of maximum range) is small for the larger tilt angles.
3. Irradiance breakeven PC gains of less than 1 are common. In particular, the realistic Figure A-10 case, while only quantitatively reliable for  $R < 1.5 \text{ km}$ , shows PC gains of less than -100 dB. For the in-focus ( $F=R$ ) case, very tiny breakeven PC gain is needed to provide enhanced performance in a PC link.

## Summary of IBPG Calculations

1. Ranges of confidence in the formalism (due to equation (A-70)) are limited. A hard aperture transponder should be analyzed to better define limits of applicability. (The formalism may be valid far beyond the "confidence" regime in equation (A-70)).
2. The utility of  $F_2 \neq \infty$  (unconjugated transponder focus) has not yet been demonstrated.
3.  $F = \infty$ , a typical laser diode case with collimated transmitter, needs to be explored with this model.

### 5.0 POWER BREAK EVEN PC GAIN (PBPG)

The breakeven PC gain may also be defined by comparing power in the bucket calculations. This case is more realistic than the IBPG calculations, as it better represents the performance enhancement expected from a physical laser link. In this case, the received power in a one-way link is given by

$$P_{1\text{-way}}/P_o = \frac{w_2^2}{Q_2^2} \exp [-2r_2^2/(Q_2^2 + c^2)] \quad (\text{A-71})$$

while for the phase conjugated "PC" link, we get

$$P_{PC}/P_o = \frac{w_2^2 w_3^2}{Q_2^2 Q_3^2} \exp [-2r_2^2/(Q_2^2 + b^2) - 2r_3^2/(Q_3^2 + c^2)] \quad (\text{A-72})$$

As in the discussion after equation (A-65), one must take care in using the 1-way calculation to use "b" as the transmitter size parameter and "c" as that of the receiver. We define the Power Breakeven PC gain (PBPG) as

$$G = P_{1\text{-way}}/P_{PC} = G_o \exp G_1 \quad (\text{A-73})$$

Then

$$G_o = \frac{[w_2^2/Q_2^2]_{1\text{-way}}}{[w_2^2 w_3^2/(Q_2^2 Q_3^2)]_{PC}} \quad (\text{A-74})$$

Now in the 1-way link

$$Q_{2(1\text{-way})}^2 = \frac{b^2}{\delta^2} + \frac{b^2 \gamma^2}{\nu^2} \quad (\text{A-75})$$

since the transmitter has size "b" (i.e. the PC transponder size). The  $\nu^2$  in the second term is unexpected, since it has the transceiver radius in it. This occurs in this equation merely to remove the  $\nu$  which is included in the definition of  $\gamma$  from equation (A-41). So

$$\begin{aligned} w_2^2/Q_2^2 (1\text{-way}) &= \frac{c^2}{c^2 + Q_2^2} \\ &= \frac{c_o \delta \nu^3}{c_o \delta \nu^3 + \nu^2 + \gamma^2 \delta^2} \end{aligned} \quad (\text{A-76})$$

where we define

$$c_o = c^2/w_1^2 \quad (\text{A-77})$$

After a little algebra, we find

$$G_0 = \frac{(1 + \nu\delta)^2 + \gamma^2 - 2\nu\delta^2\epsilon + \delta^2\epsilon^2(1 + \gamma^2) + c_o \nu\delta (1 + \nu\delta + \frac{2}{\gamma})}{\nu\delta + \gamma^2\delta^3/\nu + c_o\delta^2\nu^2} \quad (\text{A-78})$$

For the trivial return-collimated/outgoing-focused case,

$$\gamma = \epsilon = 0$$

and for equal transmitter and receiver apertures,

$$c = w_1, \text{ i.e. } c_o = 1$$

we get

$$G_0 \rightarrow \frac{1 + 2\nu\delta}{\nu\delta}$$

Assuming  $\delta = \gamma$  (i.e. equal transceiver and transponder apertures sizes), then

$$G_0 \rightarrow \frac{1 + 2\nu^2}{\nu^2}$$

so that  $G_0 \rightarrow 1/\nu^2$  in the far field ( $\nu \rightarrow 0$ ), i.e. the required gain is large, while in the near field ( $\nu \rightarrow \infty$ ), the required gain goes to 2. (Note that as  $c \rightarrow \infty$ ,  $G_0 \rightarrow (1 + \nu\delta)/(\nu\delta)$ , so the expected  $\nu \rightarrow \infty$  limit of  $G_0 = 1$  is obtained in that case. The  $G_0 \rightarrow 2$  limit comes from the dual truncation, at the transponder and at the receiver.)

The exponential factor of the breakeven PC gain is

$$G_1 = \frac{2 r_3^2}{Q_3^2 + c^2} + \frac{2 r_2^2}{Q_2^2 + b^2} - \left( \frac{2 r_2^2}{Q_2^2 + c^2} \right)_{1\text{-way}} \quad (\text{A-79})$$

which vanishes in the limit of zero pointing error ( $\vec{\theta}_1 = 0$ ).

#### Description of Figures

Figures A-15 through A-19 present the Power Breakeven PC Gain (PBPG),  $G$ , including  $G_0$  and  $G_1$  (i.e.  $\vec{\theta} \neq 0$ ) effects, plotted versus the normalized tilt angle

$$T = \vec{\theta} w_1 / \lambda$$

where  $\vec{\theta}$  is the transmitter tilt angle. These figures include:

- o five values of Fresnel Number ( $= \nu = \delta$ ) in figures A-15 to A-19 for  $\nu = 10^{-4}, 10^{-2}, 10^0, 10^2$  and  $10^4$
- o three values of transmitter focus ( $F = 1.1R, R, 0.9R$ ) in each figure
- o three values of unconjugated transponder focus ( $F_2 = \infty, 4R, -4R$ ) in each figure

These figures support the following conclusions:

1. Shown in the figure is the maximum value of  $\vec{T}$  for which the curve is really appropriate, estimated by

$$T_{\text{MAX}} \sim \frac{\lambda}{2w_1} + \frac{b}{R} \quad (\text{A-80})$$

to indicate that if the beam tilt is larger than the diffraction size and the receiver size, then not much power hits the receiver in either the 1-way or phase conjugated 2-way paths, and estimates of PBPG are severely affected by the "infinite gaussian reflector" assumption.

2. For  $\nu > 1$ , the PBPG grows significantly with  $T$ , especially beyond  $T_{\text{MAX}}$ , when the reliability of the results are of concern.

Another interesting set of figures (figures A-20 through A-28) shows the dependence of  $G$  on range. The maximum range of validity (given by inverting equation A-80) is also given in each figure. From these figures, we see:

1. Very little dependence on  $F_2$ , especially for  $R < R_{\text{MAX}}$

2. Power breakeven is always  $> 3$  dB. Three is the proper  $R=0$  limit for gaussian truncated beams, since the beam width is increased by  $\sqrt{2}$  by interaction with the reflector, resulting in more clipping losses at the receiver.
3. At close range (large Fresnel number), not much gain is needed to make PC appear to offer payoff.
4. The payoff is at long range, where PC and 1-way range losses cancel. The PC then takes what's left and sends it back on axis to the receiver.
5. The interesting region of  $R > R_{MAX}$  needs to be explored using wave optics.

#### 6.0 REDUCTION IN REQUIRED POWER

The PBPG is a useful design parameter, in that it gives a first estimate (i.e. ignoring atmospheric and optical transmission losses) of the gain required by the phase conjugator to compensate for 2-way "range" losses.

The crucial advantage of phase conjugation is that it will allow the transponder size to be reduced. Most of the link losses will occur in the first path from the transmitter (with radius  $w_1$ ) to the transponder (b) with very efficient reimaging of the conjugated beam back to the transceiver.

To estimate this effect, i.e. that the power needed on the transponder is reduced relative to the one-way requirement, we define a new parameter.

$M$  = power that needs to be transmitted from the transponder in a PC link relative to that which needs to be transmitted in a 1-way link (ignoring atmospheric losses and phase conjugation inefficiency).

The power received by the transponder is

$$P_{TP}/P_o = \frac{w_2^2}{Q_2^2} \exp \left[ - 2r_2^2 / (Q_2^2 + b^2) \right] \quad (A-81)$$

so that  $M$  may be found by taking the ratio of the path losses:

$$\begin{aligned} M &= \frac{P_{1-way}/P_o}{P_{PC}/P_{TP}} \\ &= M_o \exp (M_1) \end{aligned} \quad (A-82)$$

After a little algebra, we find

$$M_0 = \frac{(w_2^2/Q_2^2)_{1\text{-way}}}{(w_3^2/Q_3^2)_{\text{PC}}} = \frac{c_0 \nu^2 [(1+\nu\delta)^2 + \gamma^2 - 2\nu\gamma\delta^2\epsilon + \delta^2\epsilon^2(1+\gamma^2) + c_0\nu\delta(1+\nu\delta+\gamma^2)]}{(c_0\delta\nu^3 + \nu^2 + \gamma^2\delta^2)(1 + \nu\delta + \gamma^2)} \quad (\text{A-83})$$

and also

$$M_1 = 2r_3^2/(Q_3^2 + c^2) - 2r_2^2/(Q_2^2 + c^2)_{1\text{-way}} \\ = 2 \left( \frac{R\theta_1}{w_1} \right)^2 \left[ \frac{\nu\delta(1+\nu\delta + \gamma^2)}{(1 + \nu\delta)^2 + \gamma^2 - 2\nu\gamma\delta^2\epsilon + \delta^2\epsilon^2(1 + \gamma^2) + C_0 \nu\delta(1+\nu\delta+\gamma^2)} - \frac{\nu^3\delta}{\nu^2 + \delta^2\gamma^2 + c_0\delta\nu^3} \right] \quad (\text{A-84})$$

As an example, if

$$\begin{aligned} c_0 &= 1 && (\text{i.e. } c = w_1) \\ \delta &= \nu && (\text{i.e. } b = w_1) \\ \gamma - \epsilon &= 0 && (\text{i.e. } F_1 = R, F_2 = \alpha) \end{aligned}$$

then

$$M_0 \rightarrow (1 + 2\nu\delta)/(1 + \nu\delta) \quad (\text{A-85})$$

$$M_1 \rightarrow -2(R\theta_1/w_1)^2 \nu^2\delta^2/[(1 + \nu\delta)(1 + 2\nu\delta)] \quad (\text{A-86})$$

The fact that the PC link requires less power at the transponder is evident in Figures A-29 through A-33 in plots vs.  $\theta_1/(\lambda/w_1)$ , and in Figures A-34 through A-42 in plots vs. range. This benefit is more significant for larger pointing errors.

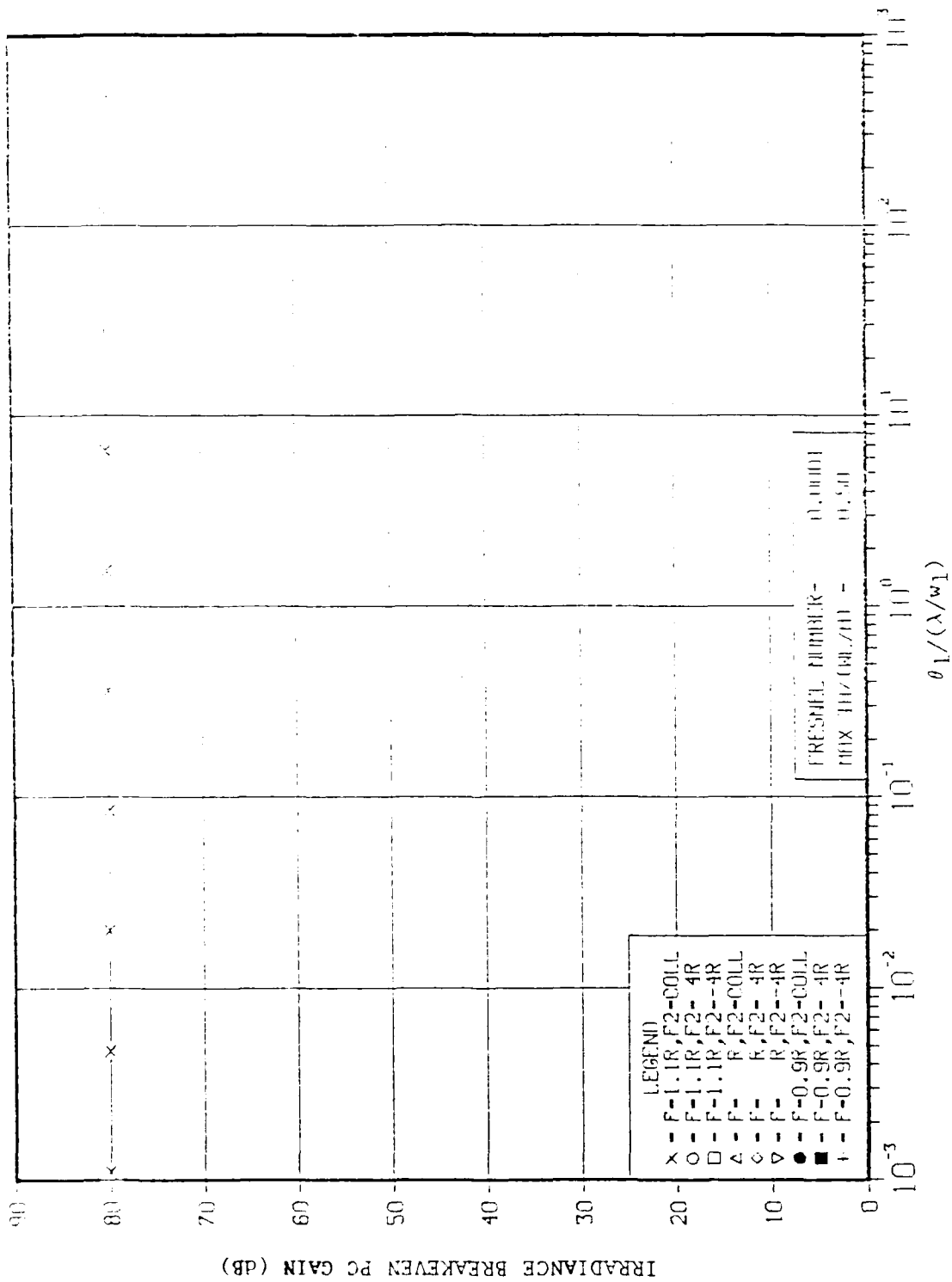


Figure A-1.  $G_1$  vs.  $\theta_1 \rightarrow w_1 \theta_1 / \lambda$  for  $\nu = 0.0001$

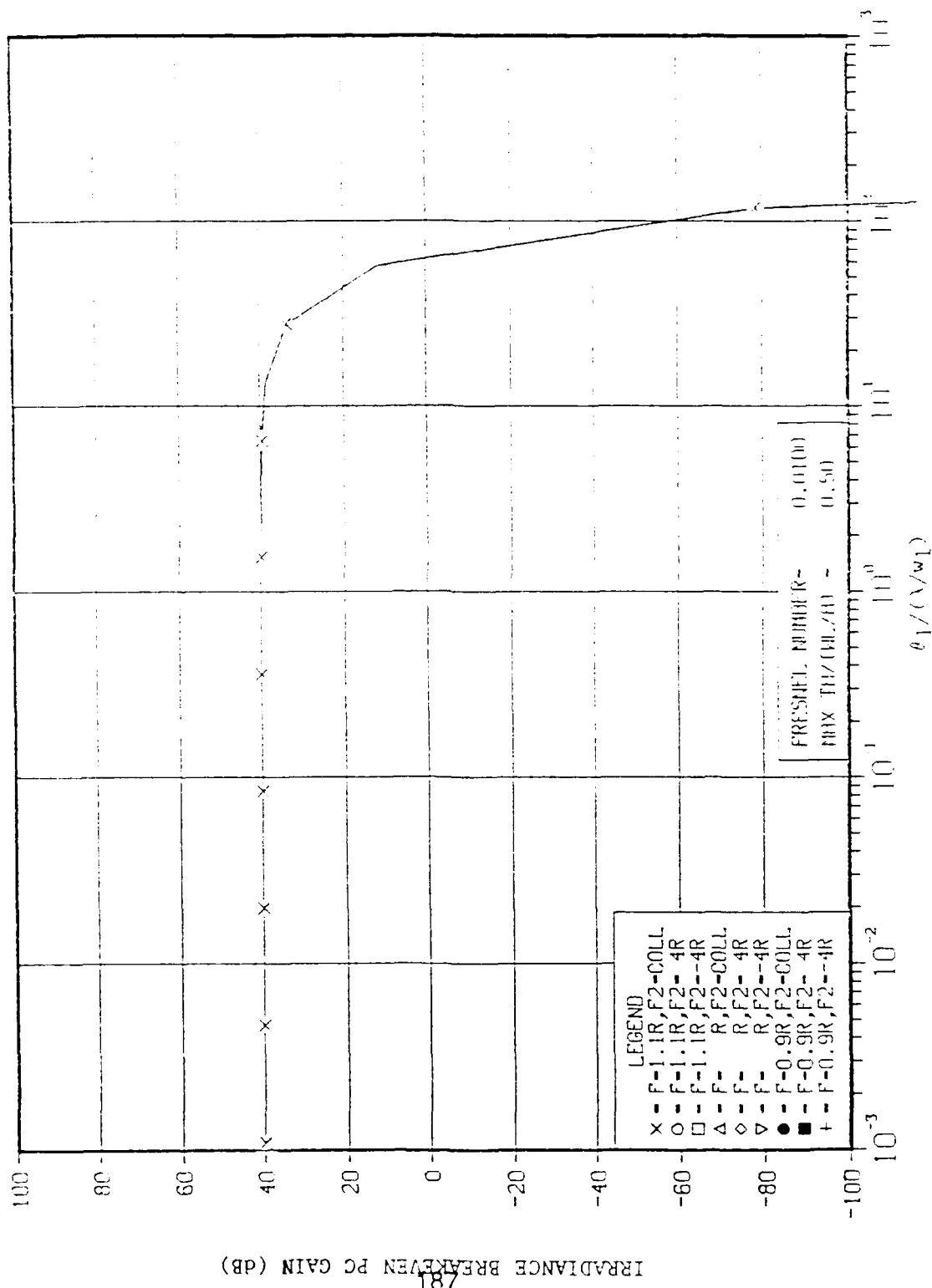


Figure A-2.  $G_1$  vs.  $\theta_1 = w_1 \theta_1 / \lambda$  for  $\nu = 0.01$



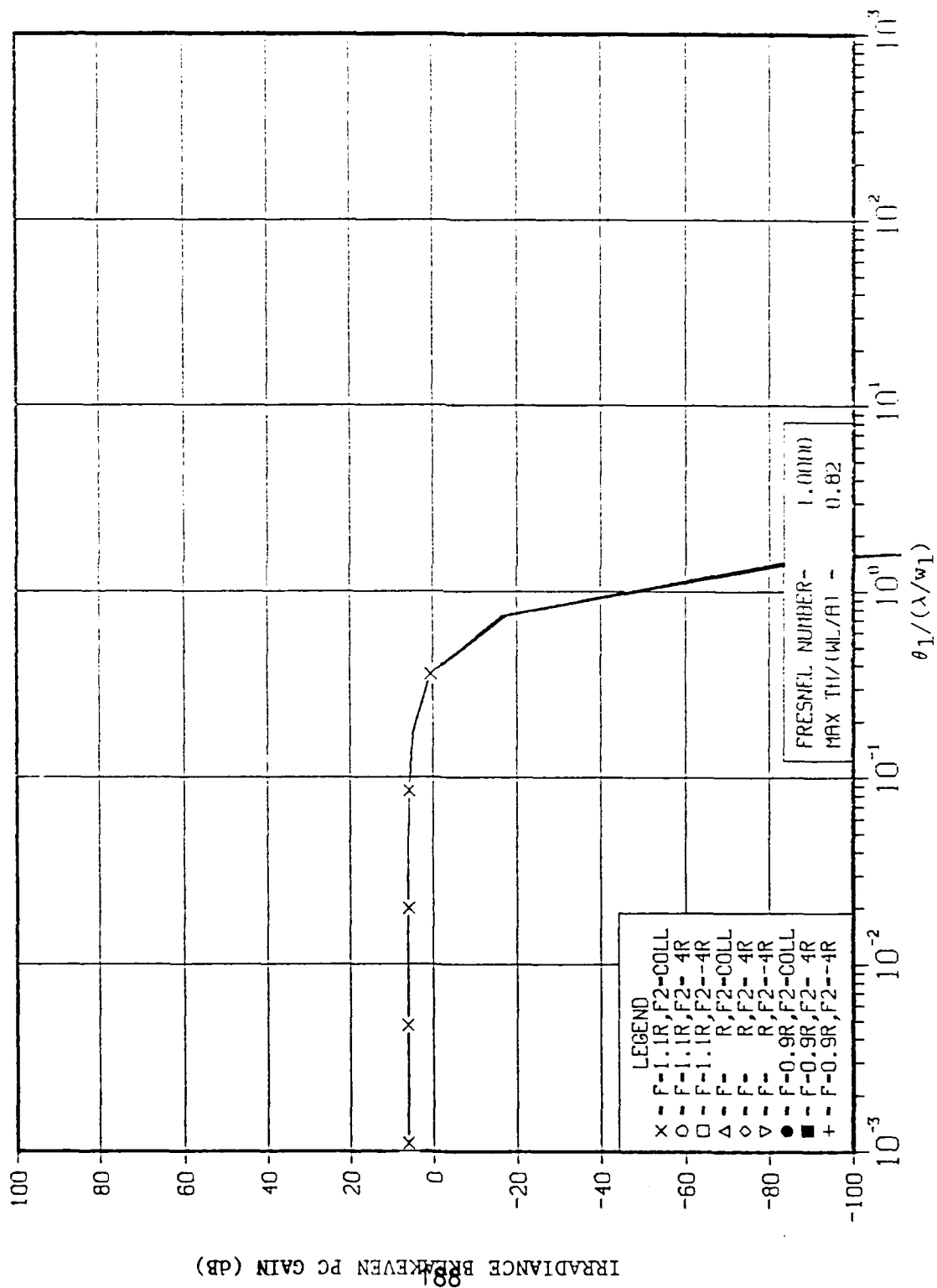


Figure A-3.  $G_I$  vs.  $\vec{T} = w_1 \vec{\theta}/\lambda$  for  $\nu = 1$

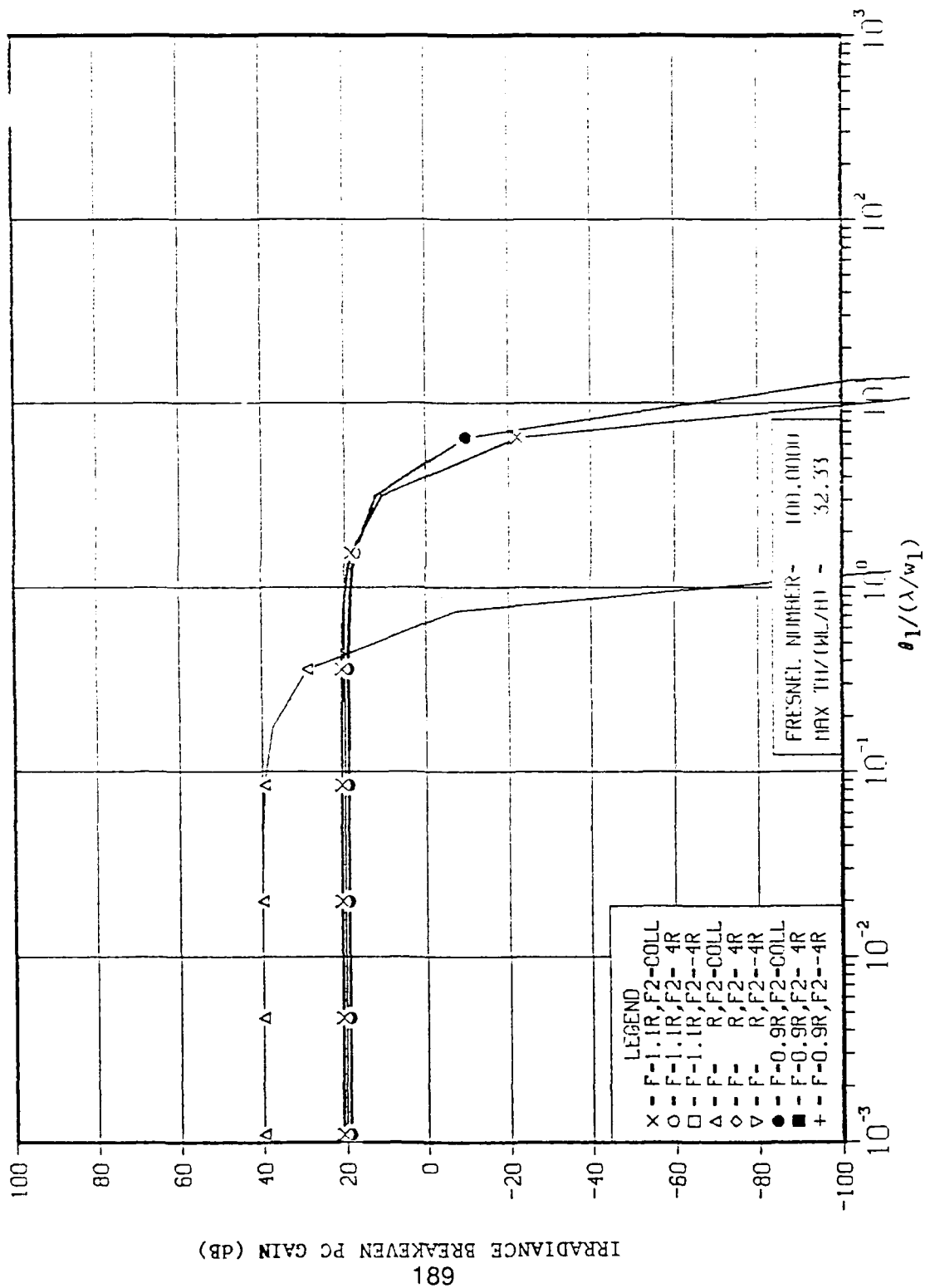


Figure A-4.  $G_I$  vs.  $\vec{T} = w, \vec{\sigma}, \lambda$  for  $\nu = 100$

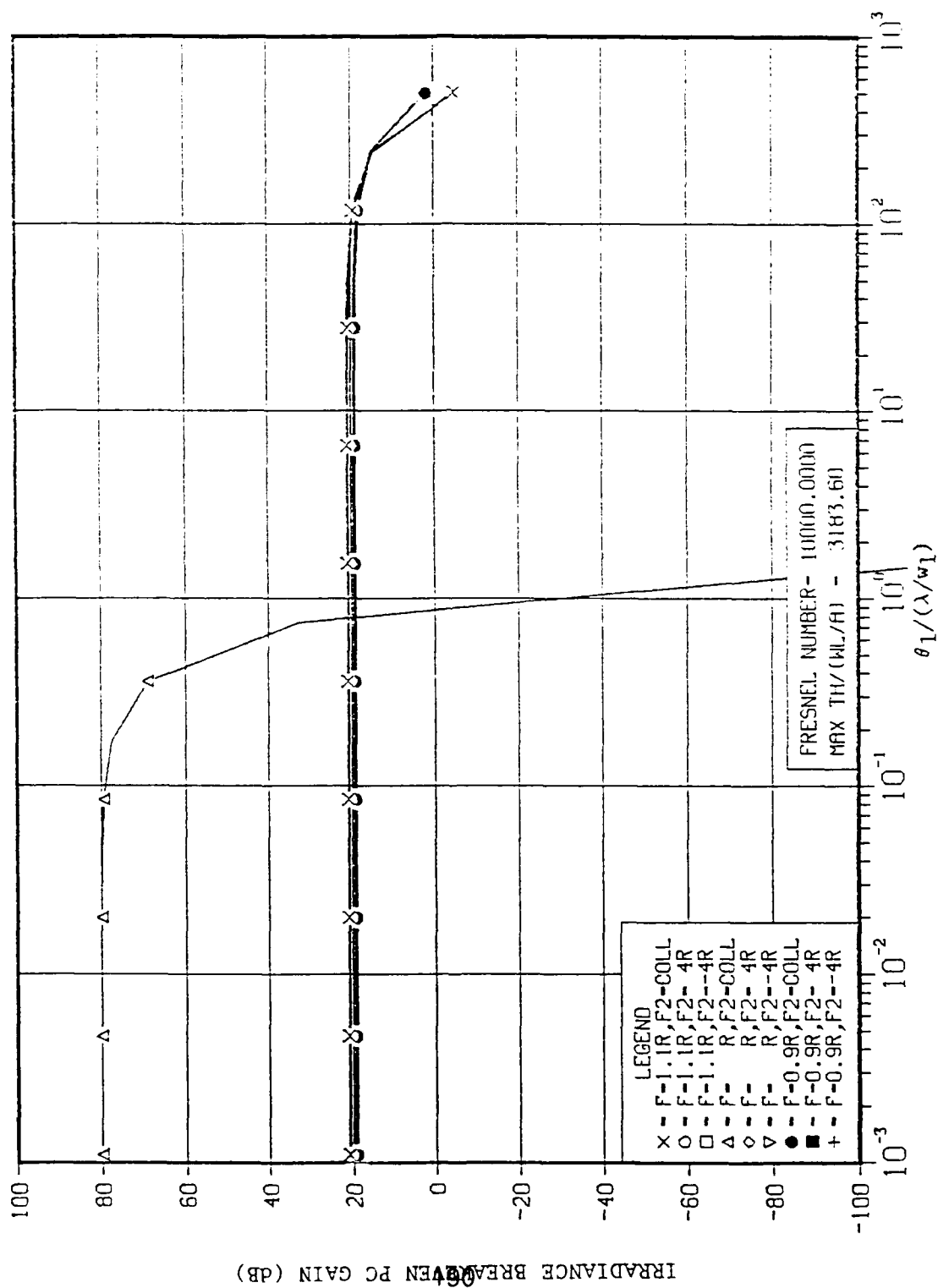


Figure A-5.  $G_I$  vs.  $\vec{T} = w_1 \vec{\theta}/\lambda$  for  $\nu = 10,000$

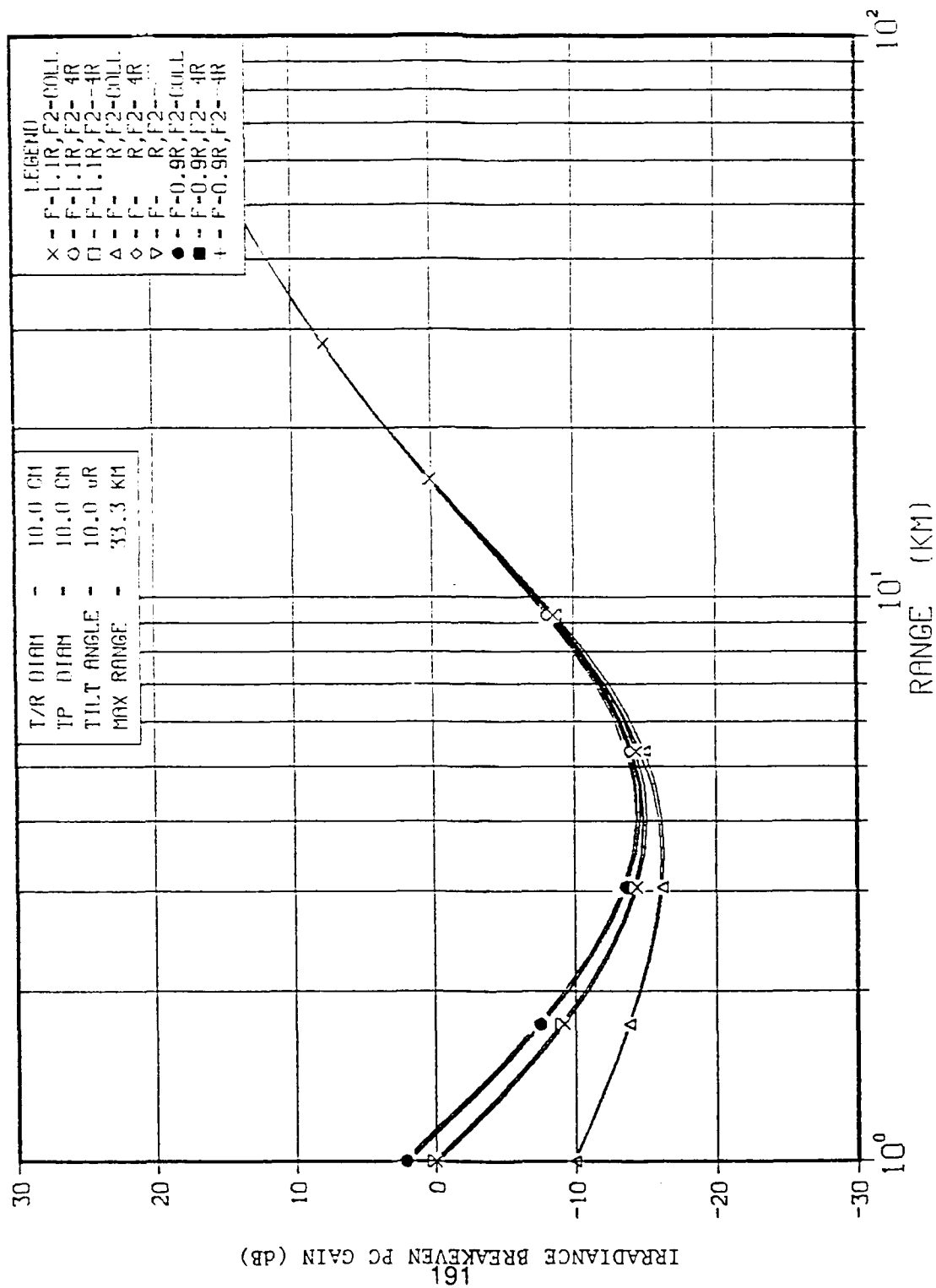


Figure A-6.  $G_I$  vs.  $R$  for  $\theta_I = 10\mu\text{rad}$ ,  $w_I = b = 5 \text{ cm}$

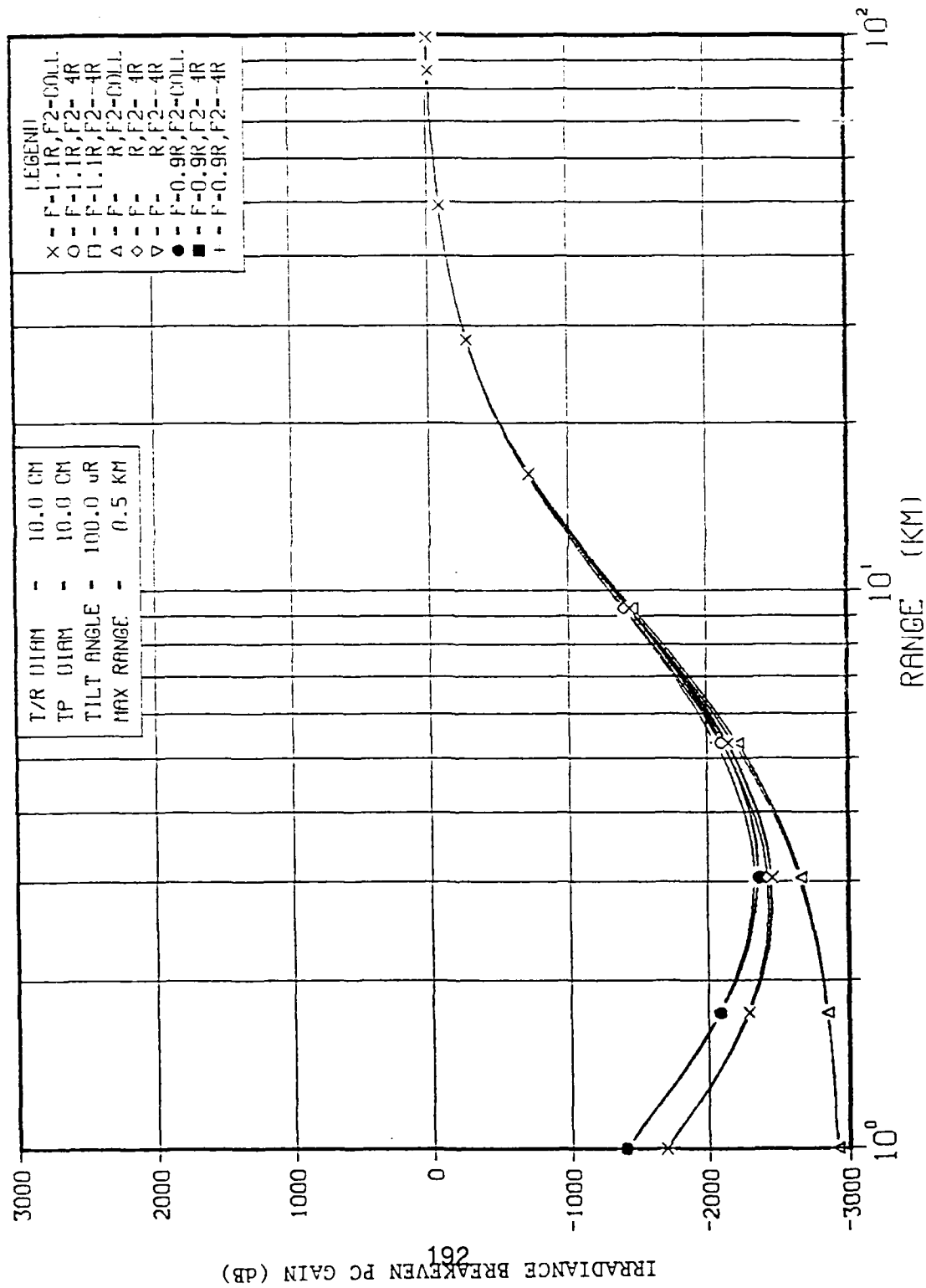


Figure A-7.  $G_1$  vs.  $R$  for  $\theta_1 = 100\mu\text{rad}$ ,  $w_1 = b = 5$  cm

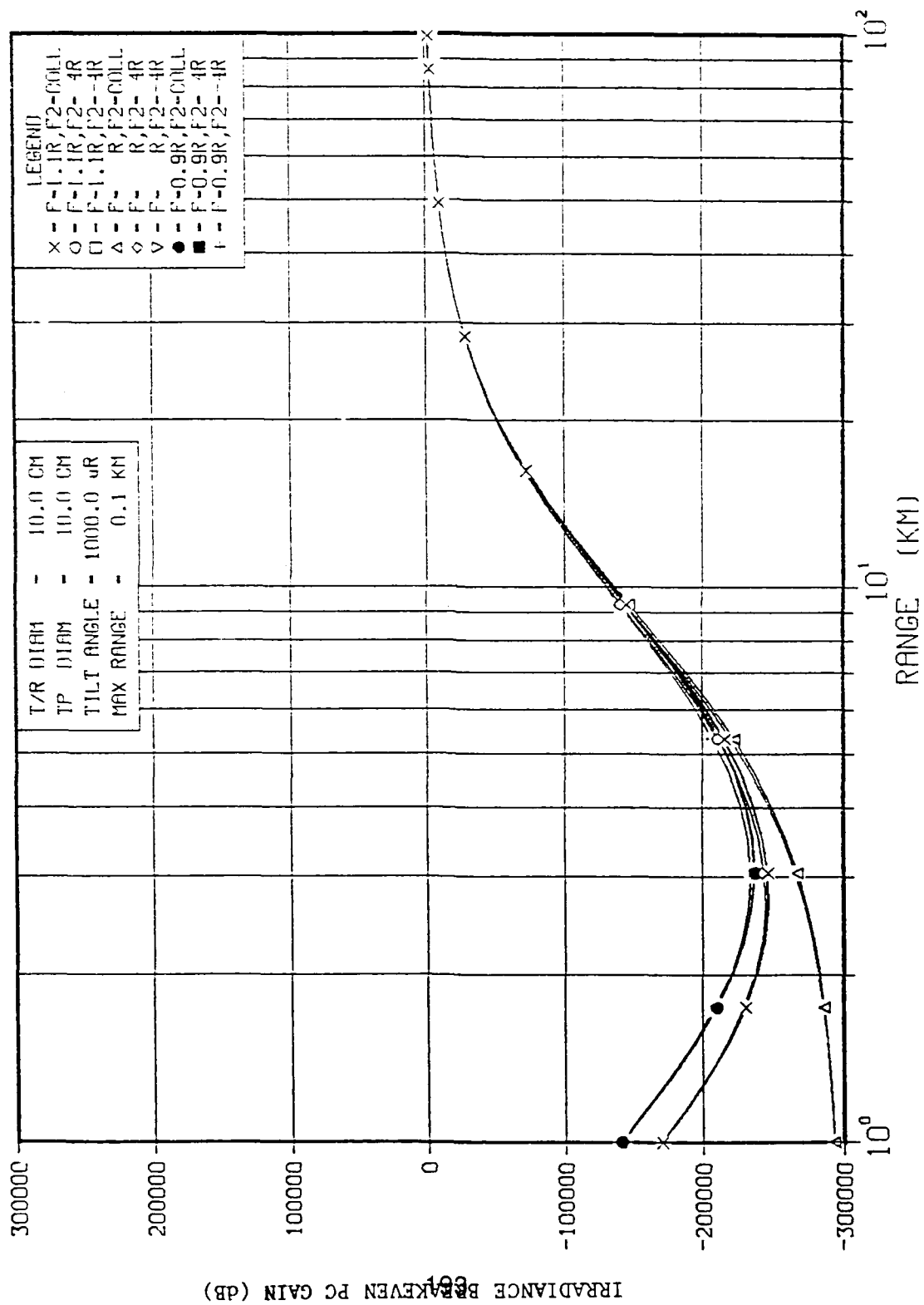


Figure A-8.  $G_I$  vs.  $R$  for  $\theta_I = 1000\mu\text{rad}$ ,  $w_I = b = 5$  cm

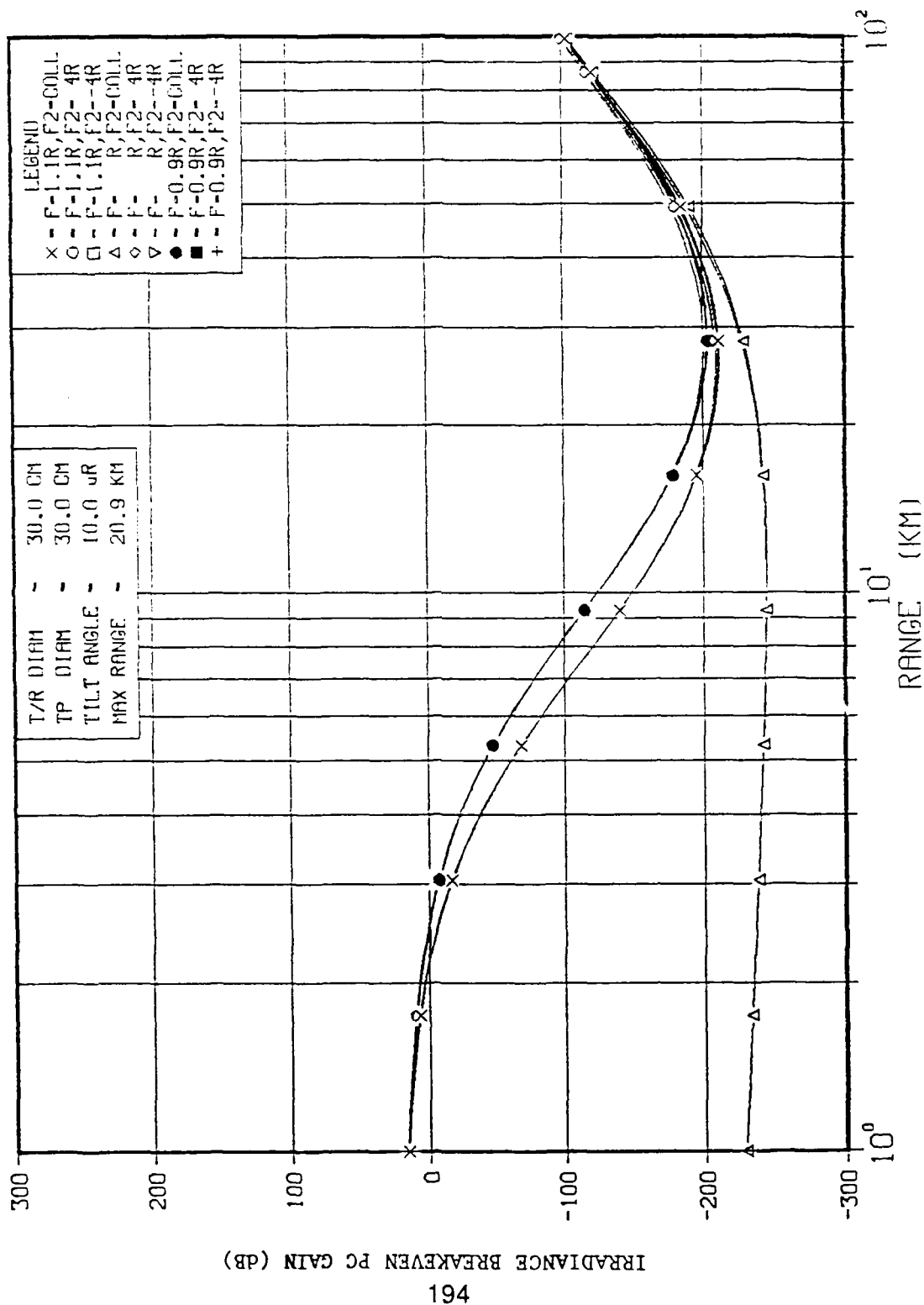


Figure A-9a.  $G_1$  vs.  $R$  for  $\theta_1 = 10\mu\text{rad}$ ,  $w_1 = b = 15$  cm

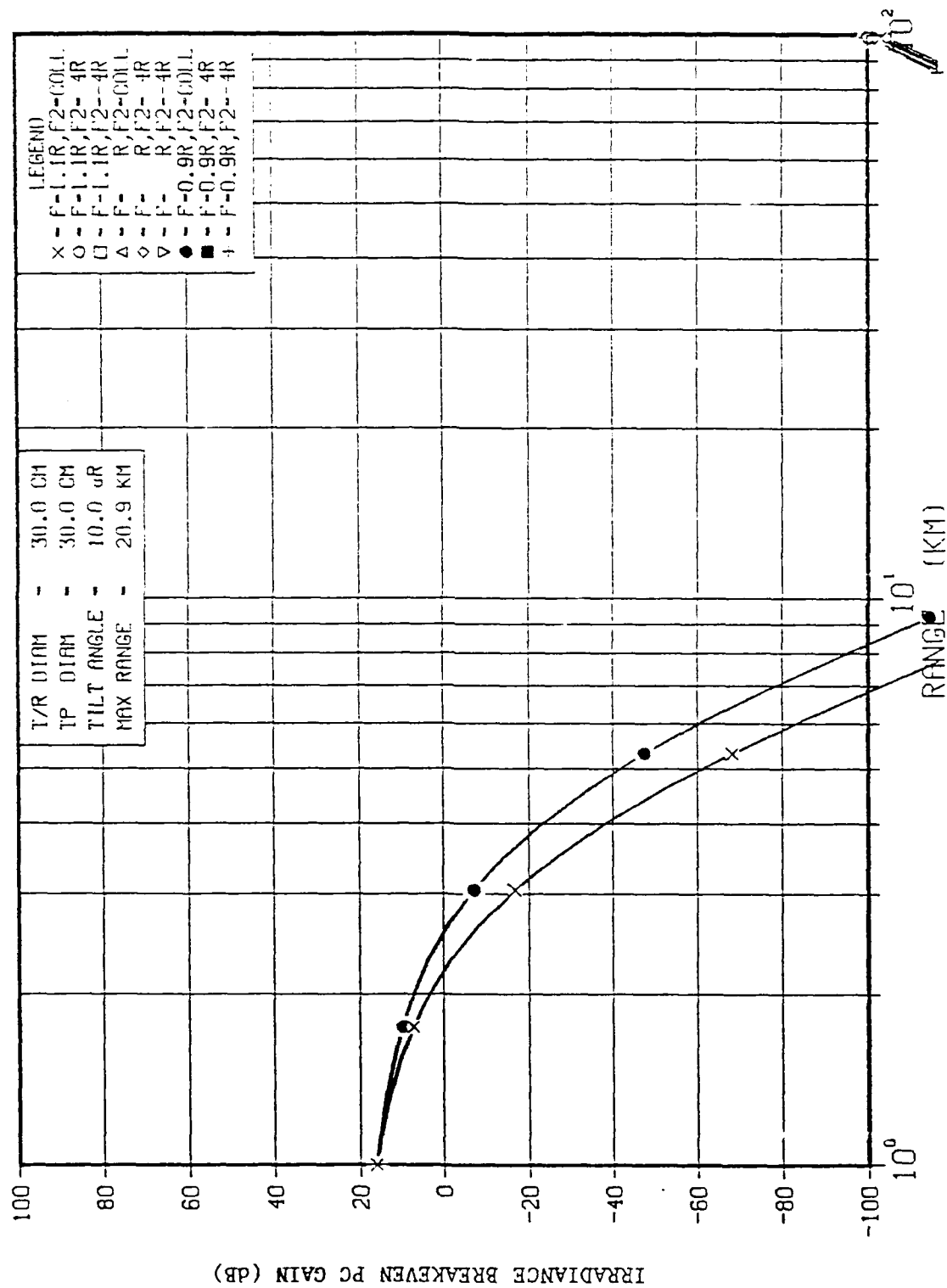


Figure A-9b.  $G_1$  vs.  $R$  for  $\vec{\theta}_1 = 10\text{rad}$ ,  $w_1 = b = 15\text{ cm}$  (expanded view)



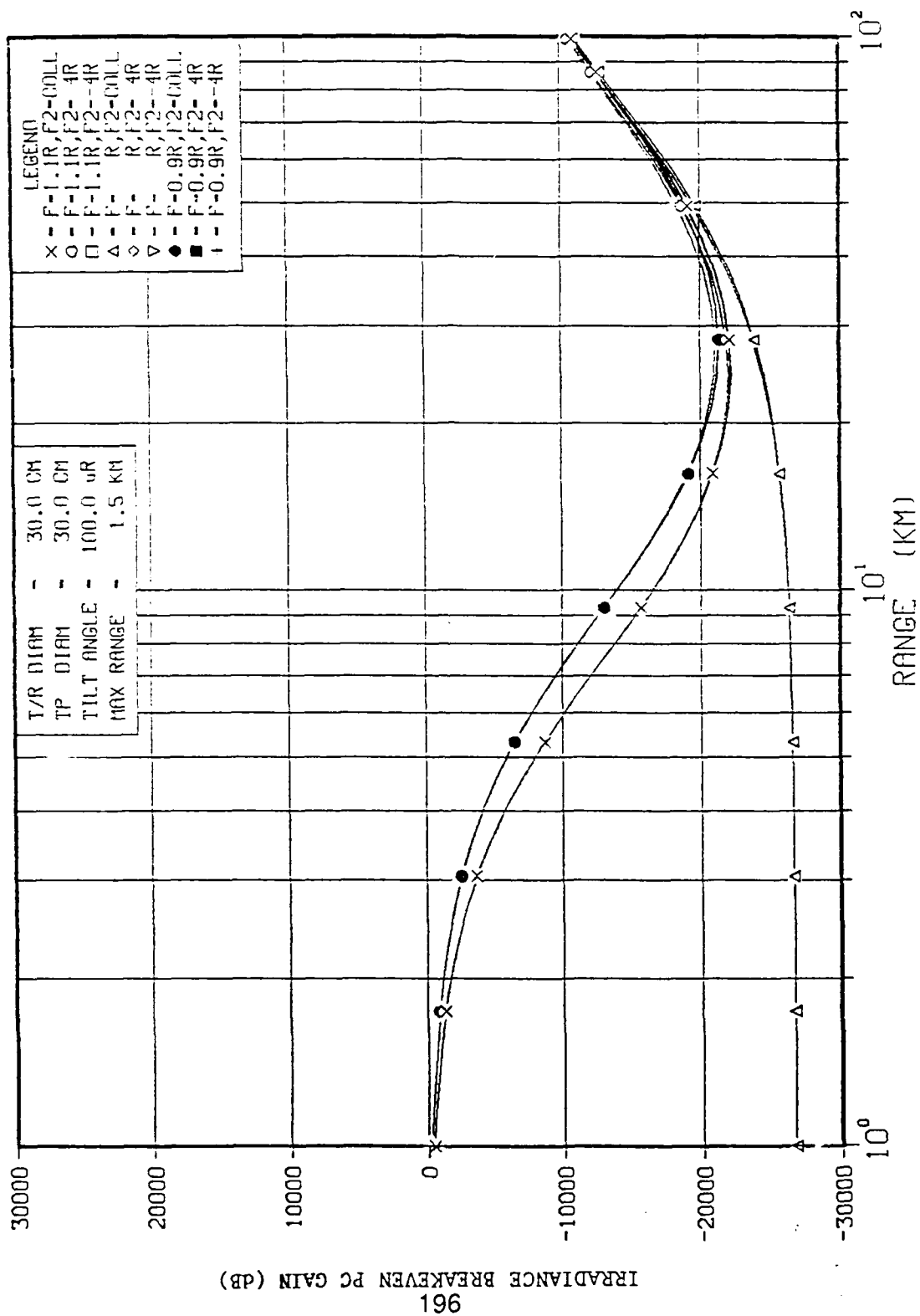


Figure A-10.  $G_I$  vs.  $R$  for  $\vec{\theta}_I = 100\mu\text{rad}$ ,  $w_I = b = 15 \text{ cm}$

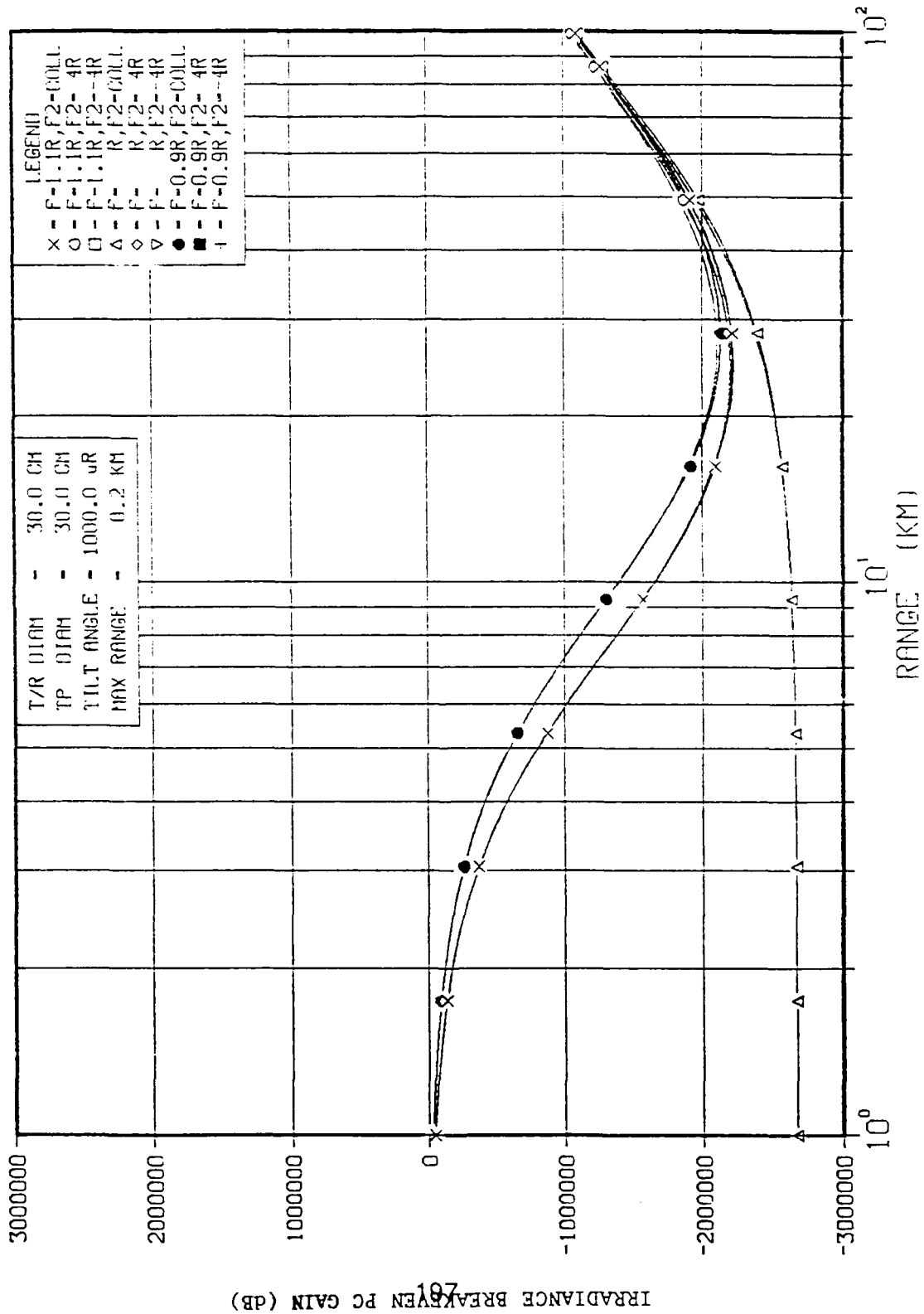


Figure A-11.  $G_I$  vs.  $R$  for  $\theta_1 = 1000\mu\text{rad}$ ,  $w_1 = b = 15 \text{ cm}$

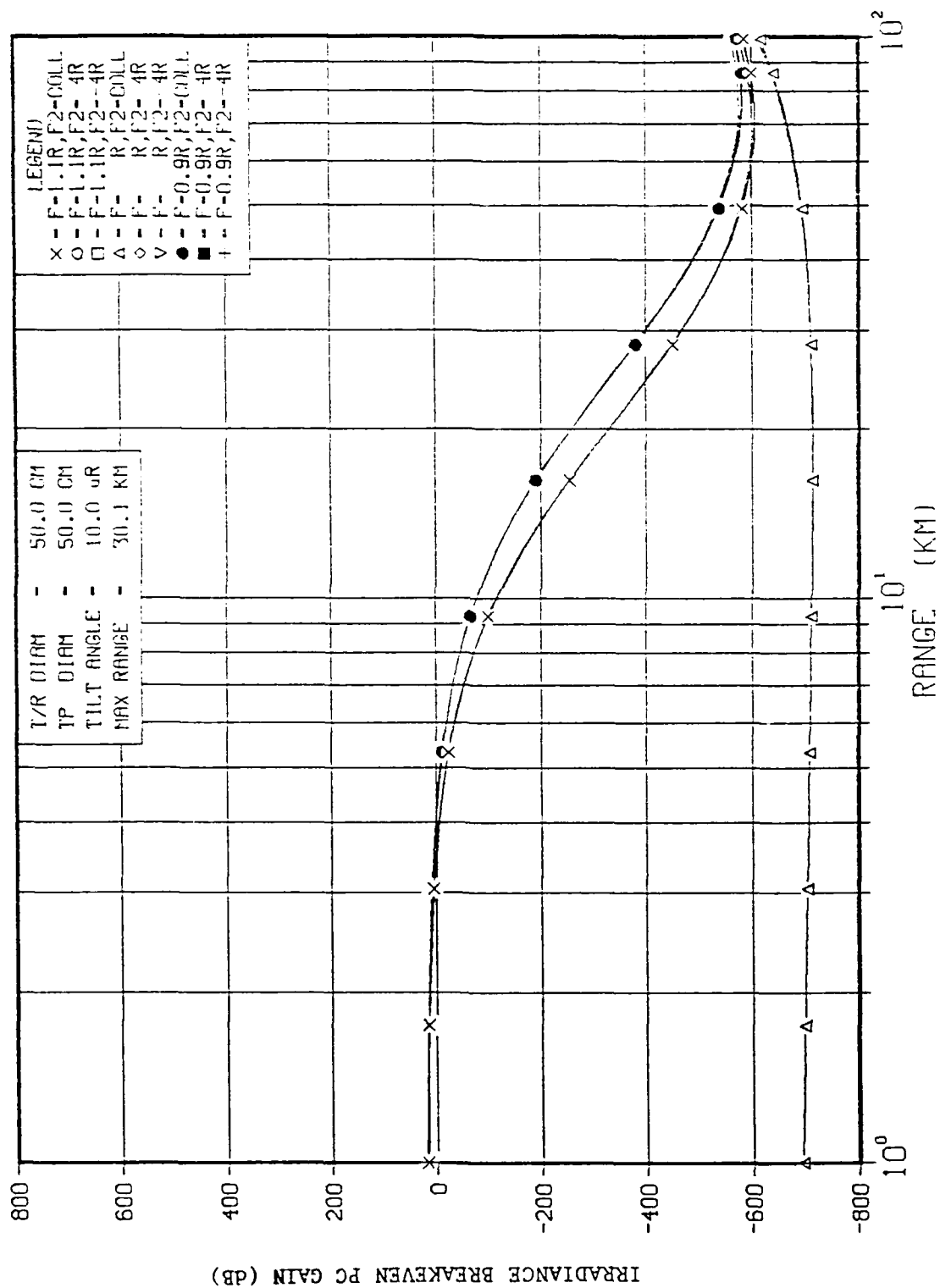


Figure A-12a.  $G_I$  vs.  $R$  for  $\theta_1 = 10\mu\text{rad}$ ,  $w_1 = b = 25$  cm

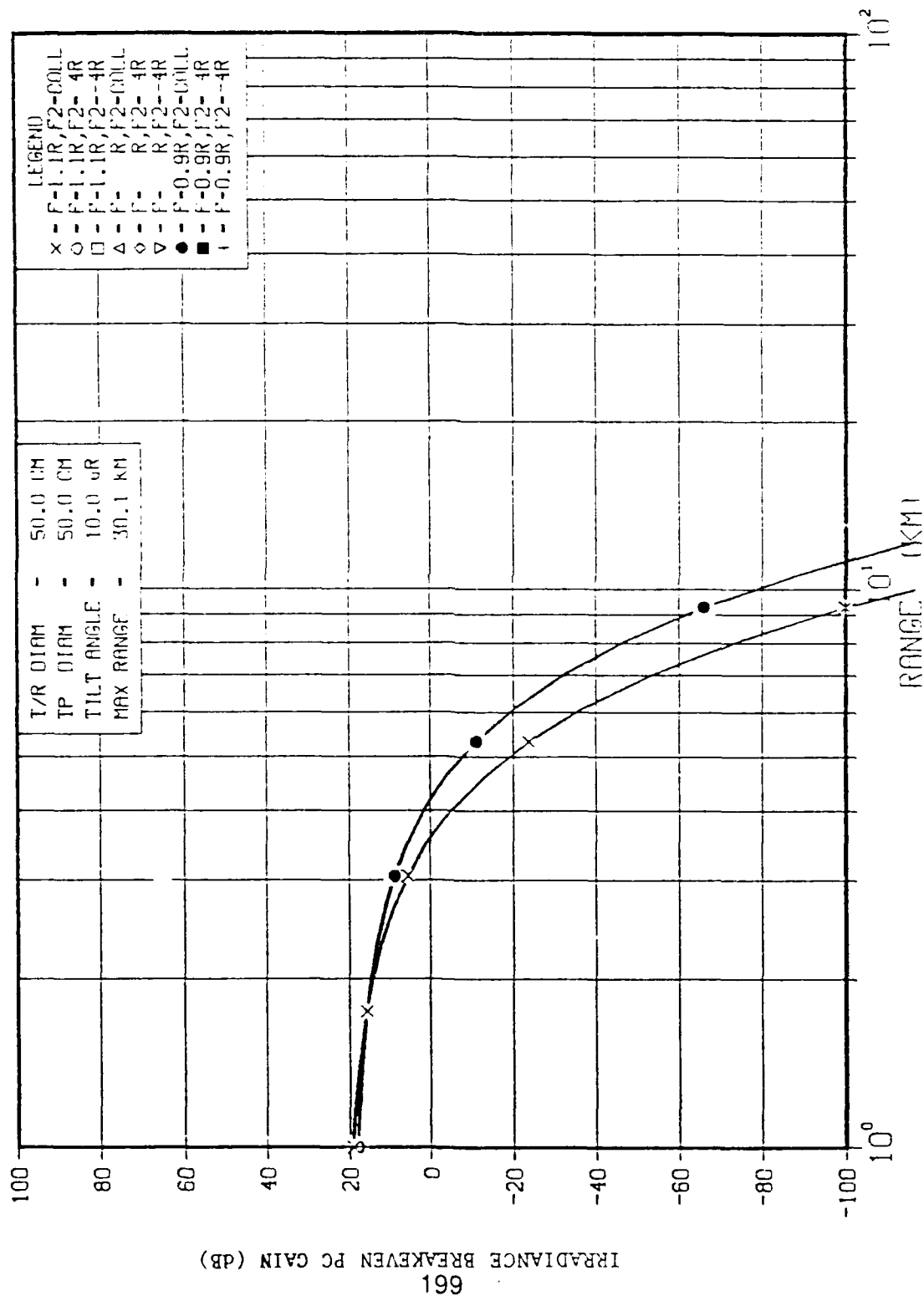


Figure A-12b.  $G_I$  vs.  $R$  for  $\theta_1 = 10^\circ$ ,  $w_1 = b = 25$  cm (expanded view)

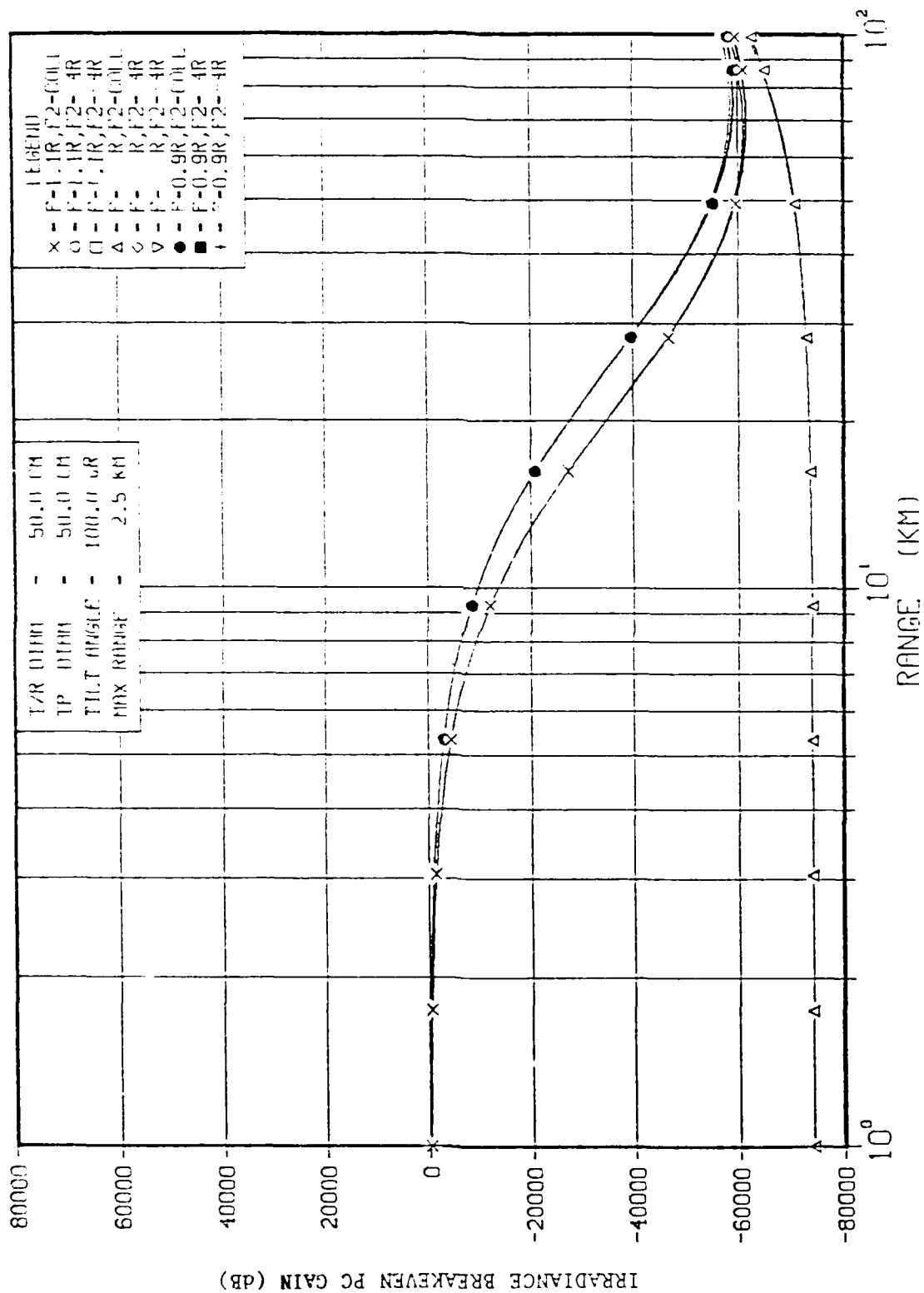


Figure A-13.  $G_1$  vs.  $R$  for  $\theta_1 = 100\mu\text{rad}$ ,  $w_1 = b = 25$  cm

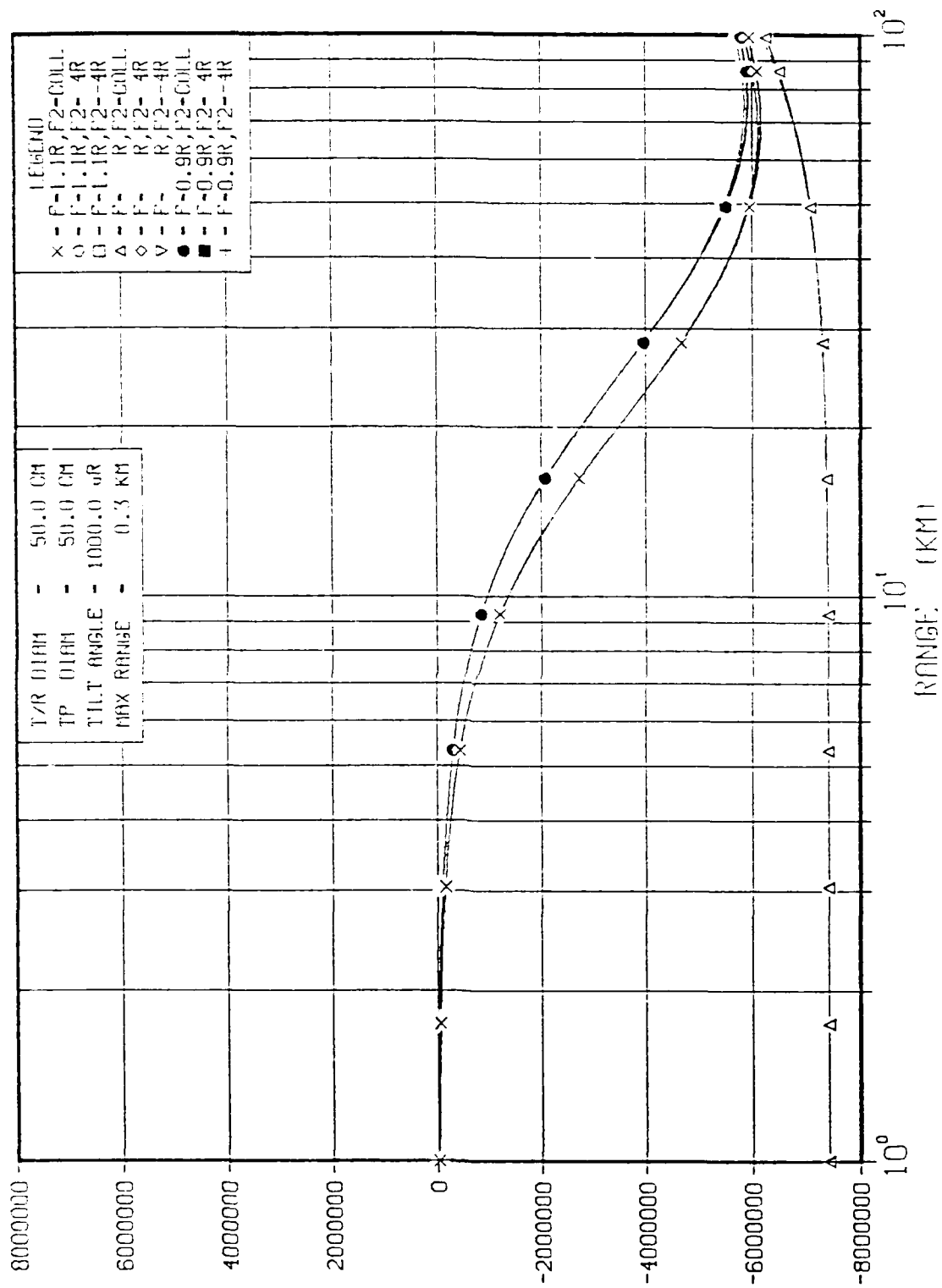


Figure A-14.  $G_1$  vs.  $R$  for  $\dot{\theta}_1 = 1000 \mu\text{rad}$ ,  $w_1 = b = 25 \text{ cm}$

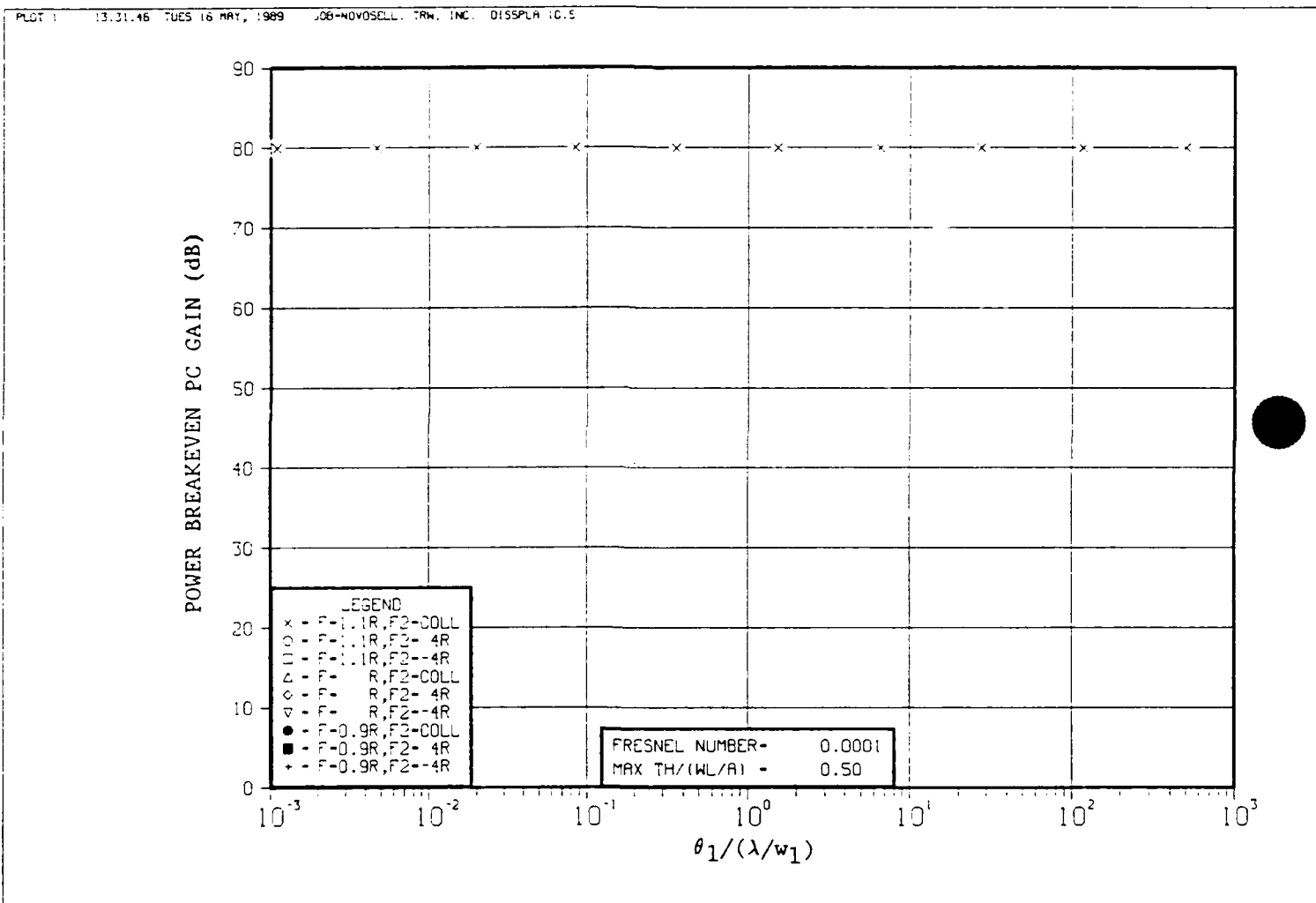


Figure A-15.  $G$  vs.  $T = w_1 \theta_1/\lambda$  for  $\nu = 0.0001$

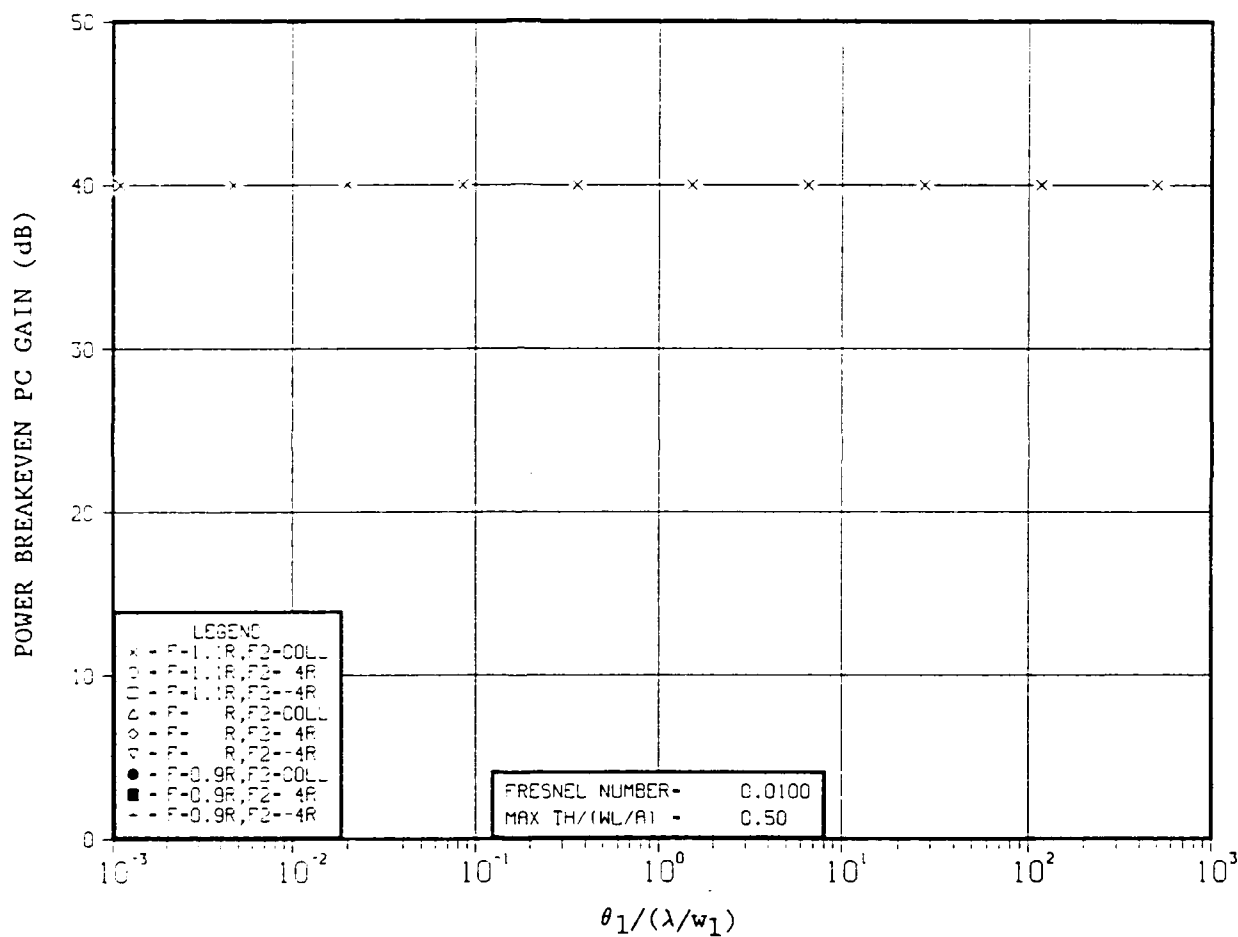


Figure A-16.  $G$  vs.  $T = w_1 \theta_1/\lambda$  for  $\nu = 0.01$



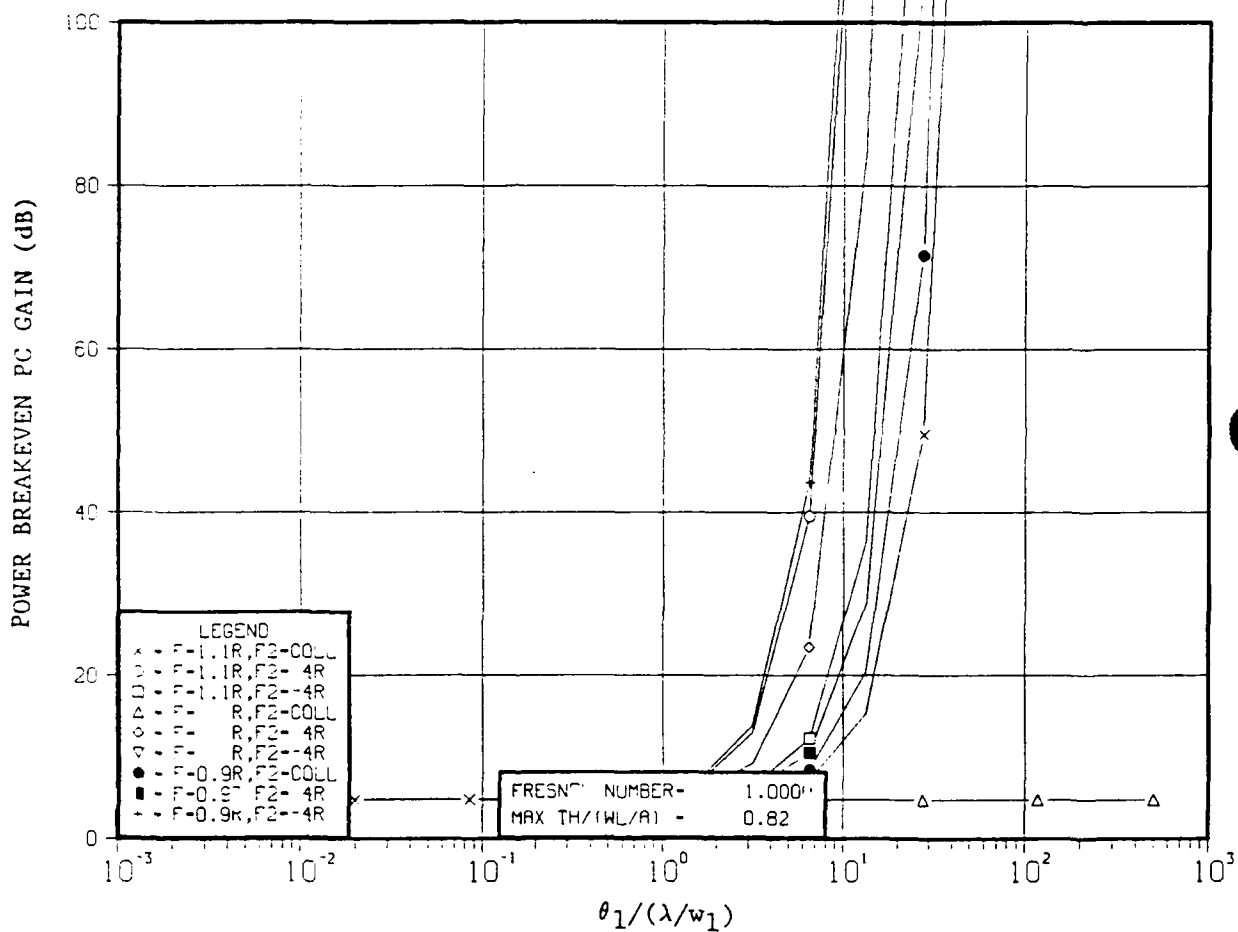


Figure A-17.  $G$  vs.  $T = w_1 \theta_1/\lambda$  for  $\nu = 1$

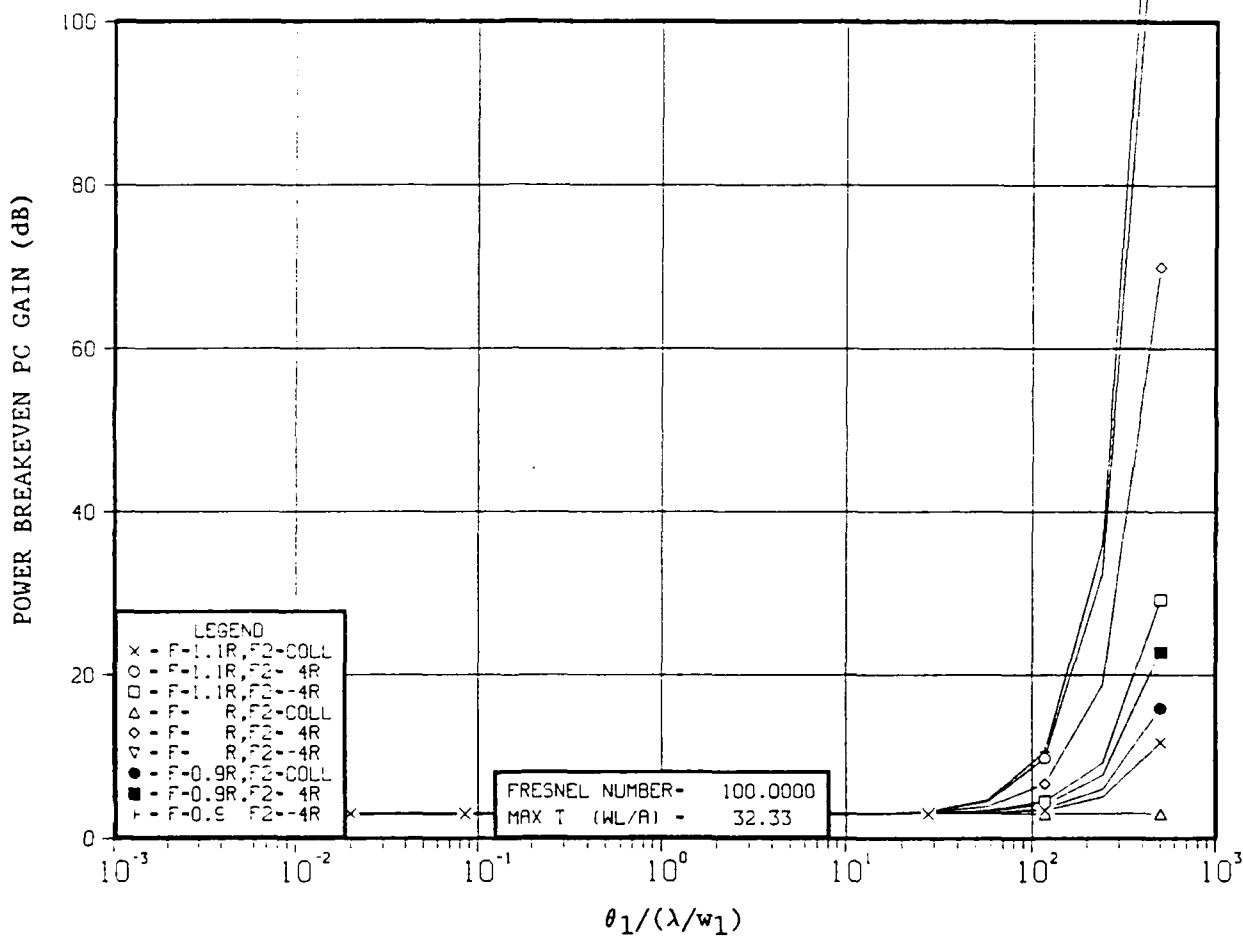


Figure A-18.  $G$  vs.  $T = w_1 \theta_1/\lambda$  for  $\nu = 100$

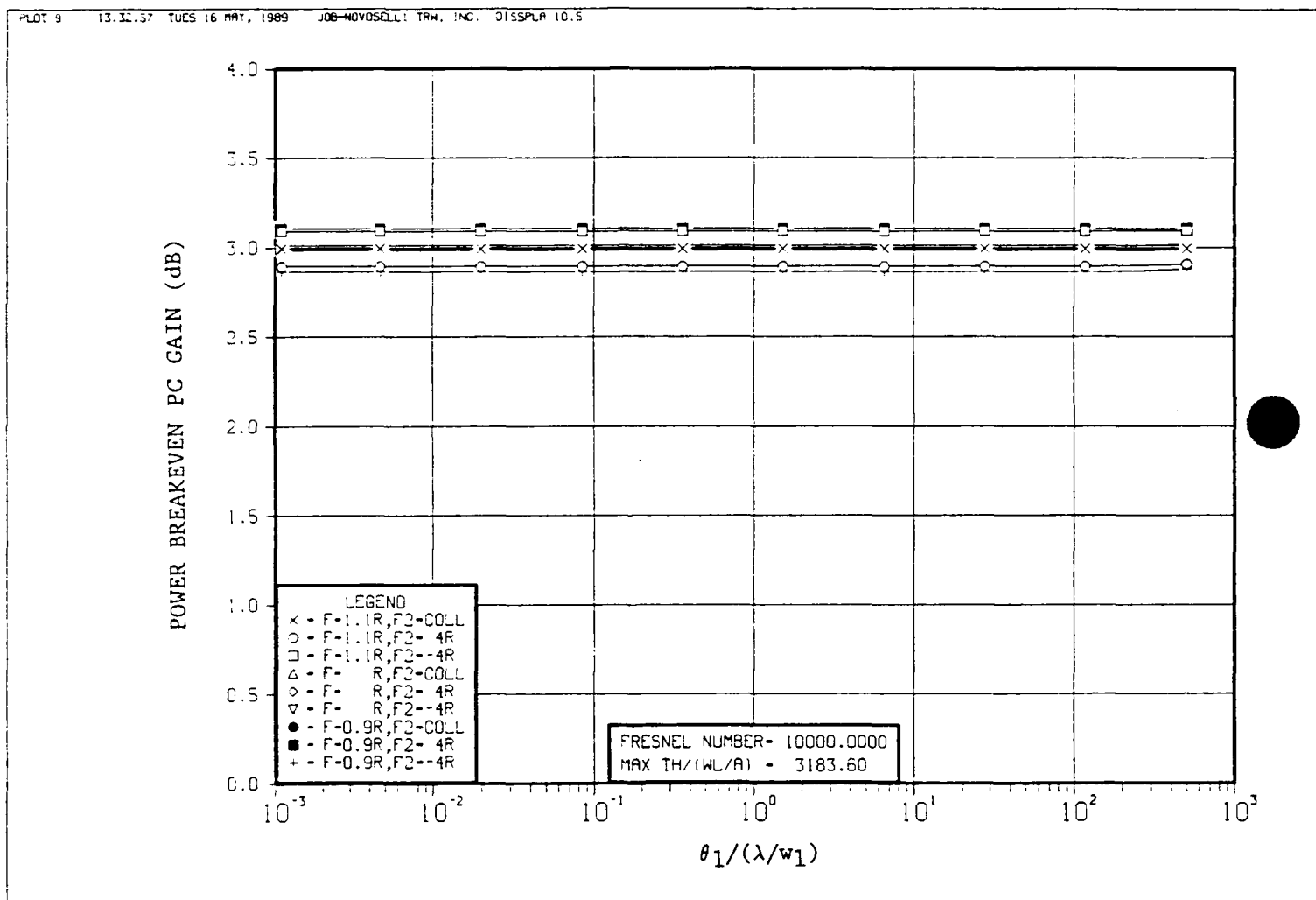


Figure A-19.  $G$  vs.  $T = w_1 \theta_1/\lambda$  for  $\nu = 10,000$

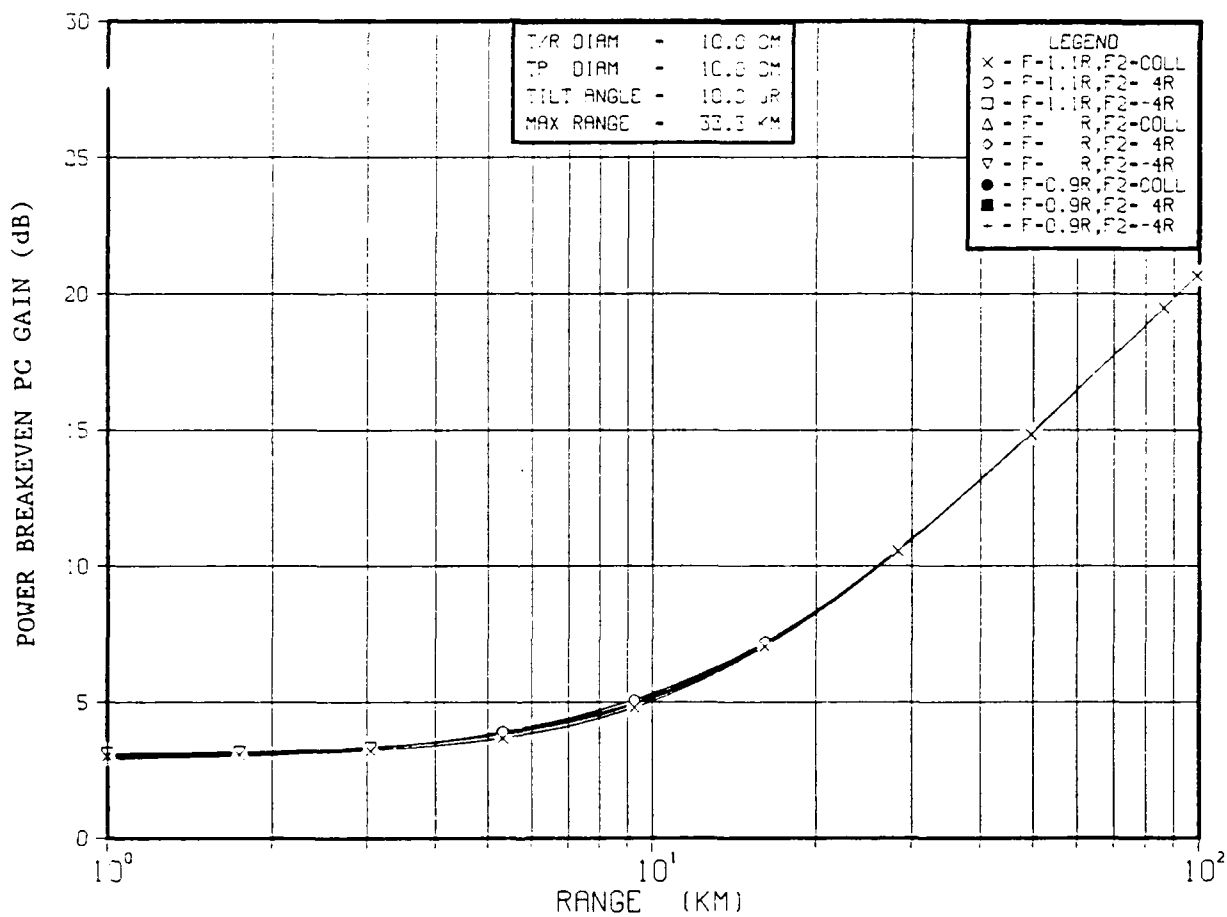


Figure A-20.  $G$  vs.  $R$  for  $\theta_1 = 10\mu\text{rad}$ ,  $w_1 = b = 5$  cm

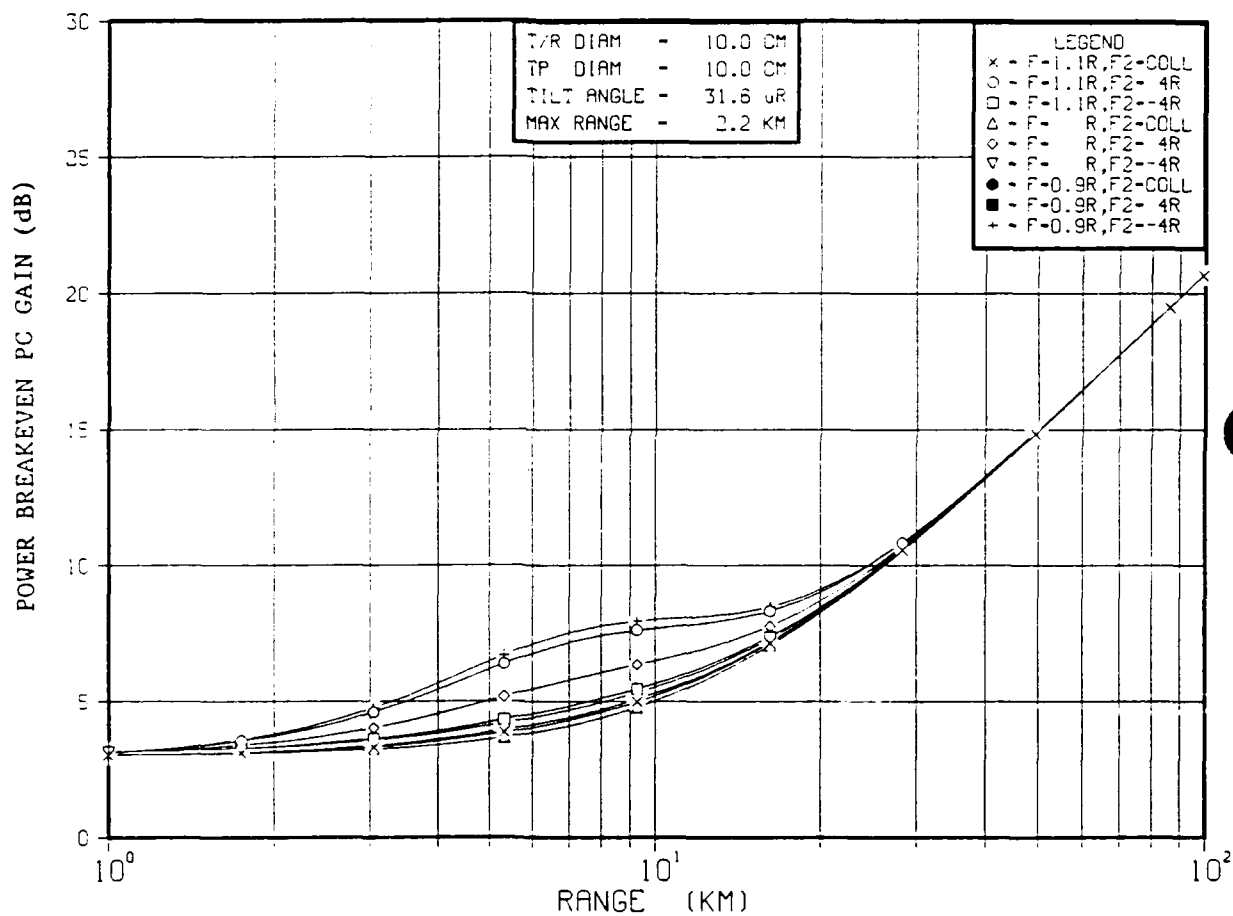


Figure A-21. G vs. R for  $\theta_1 = 32\mu\text{rad}$ ,  $w_1 = b = 5 \text{ cm}$

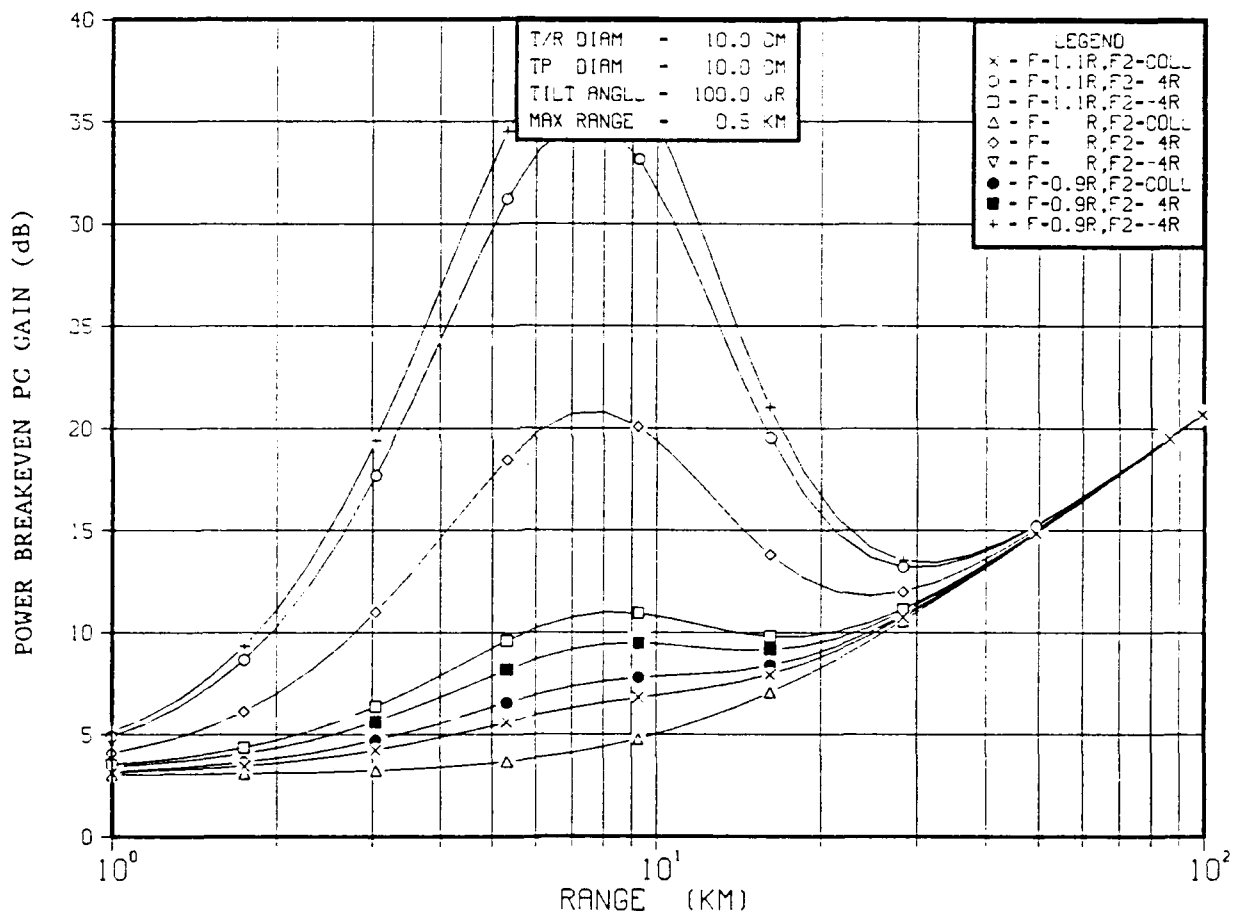


Figure A-22. G vs. R for  $\theta_1 = 100\mu\text{rad}$ ,  $w_1 = b = 5 \text{ cm}$

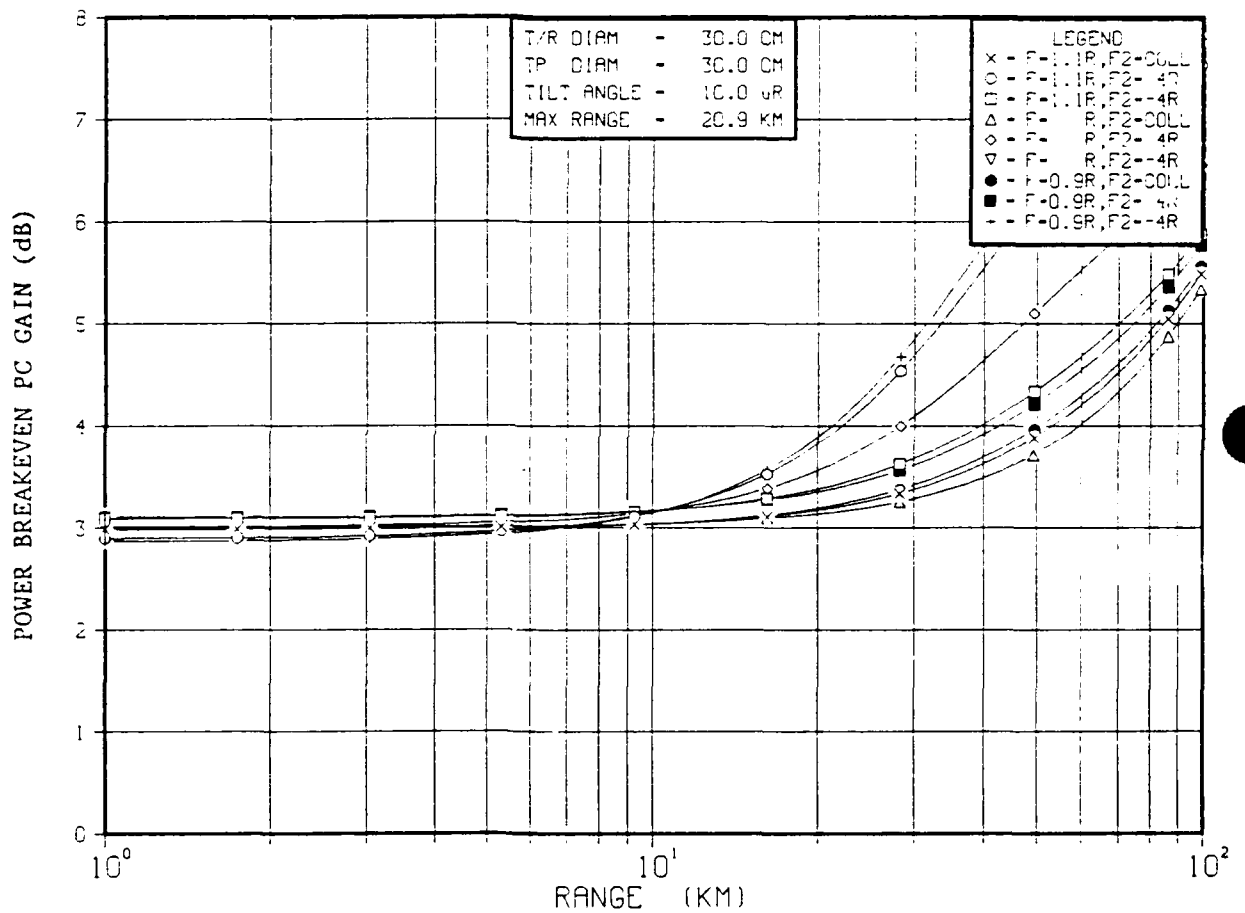


Figure A-23.  $G$  vs.  $R$  for  $\theta_1 = 10\mu\text{rad}$ ,  $w_1 = b = 15$  cm

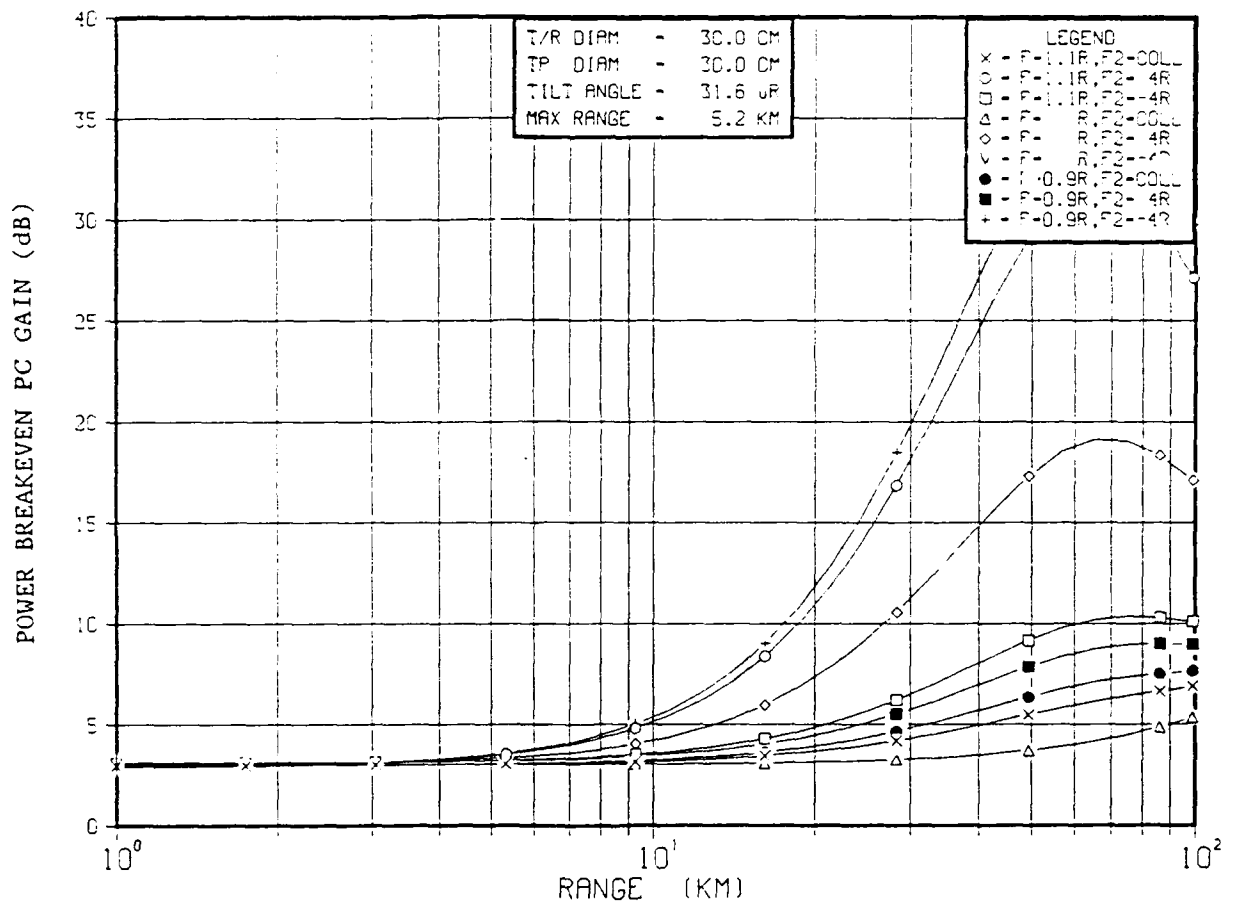


Figure A-24.  $G$  vs.  $R$  for  $\theta_1 = 32\mu\text{rad}$ ,  $w_1 = b = 15$  cm



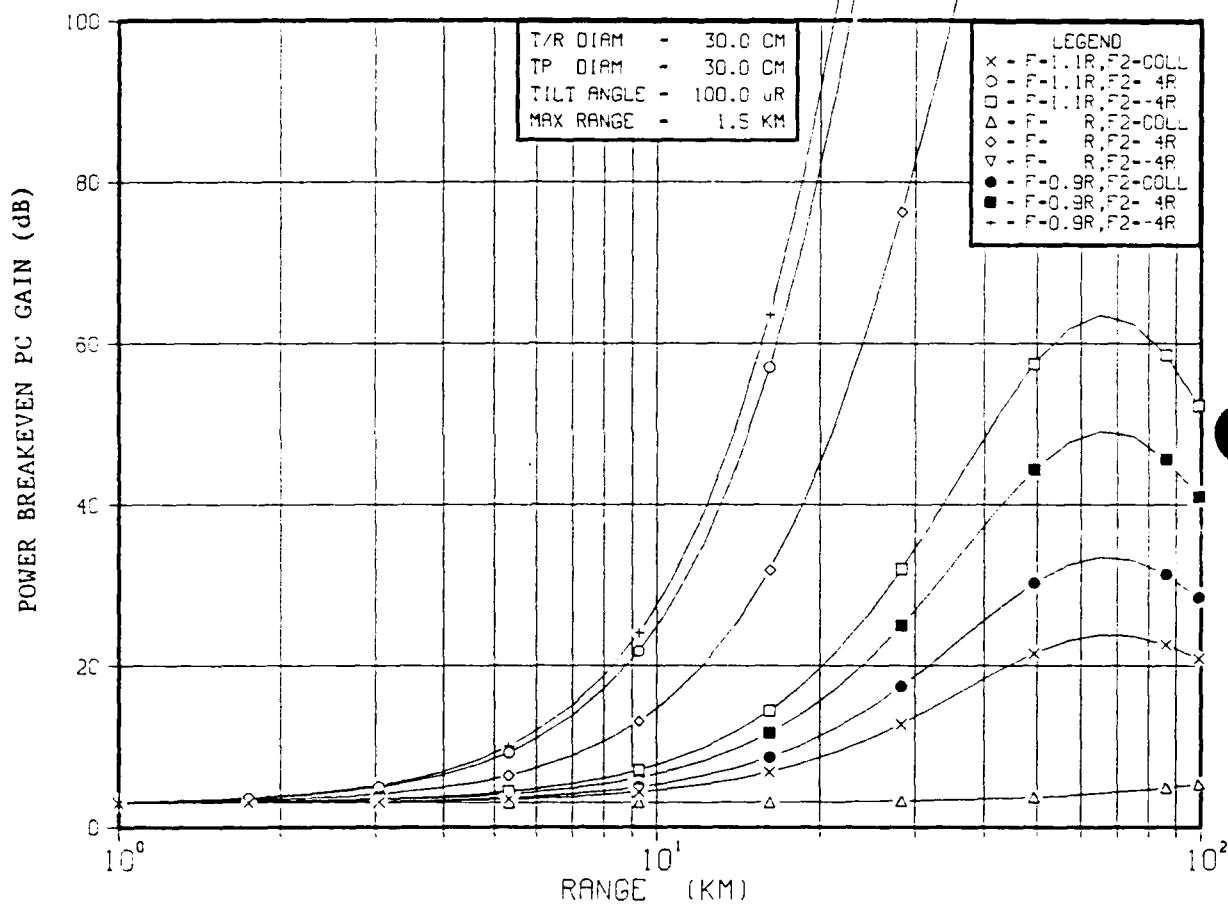


Figure A-25.  $G$  vs.  $R$  for  $\theta_1 = 100\mu\text{rad}$ ,  $w_1 = b = 15$  cm

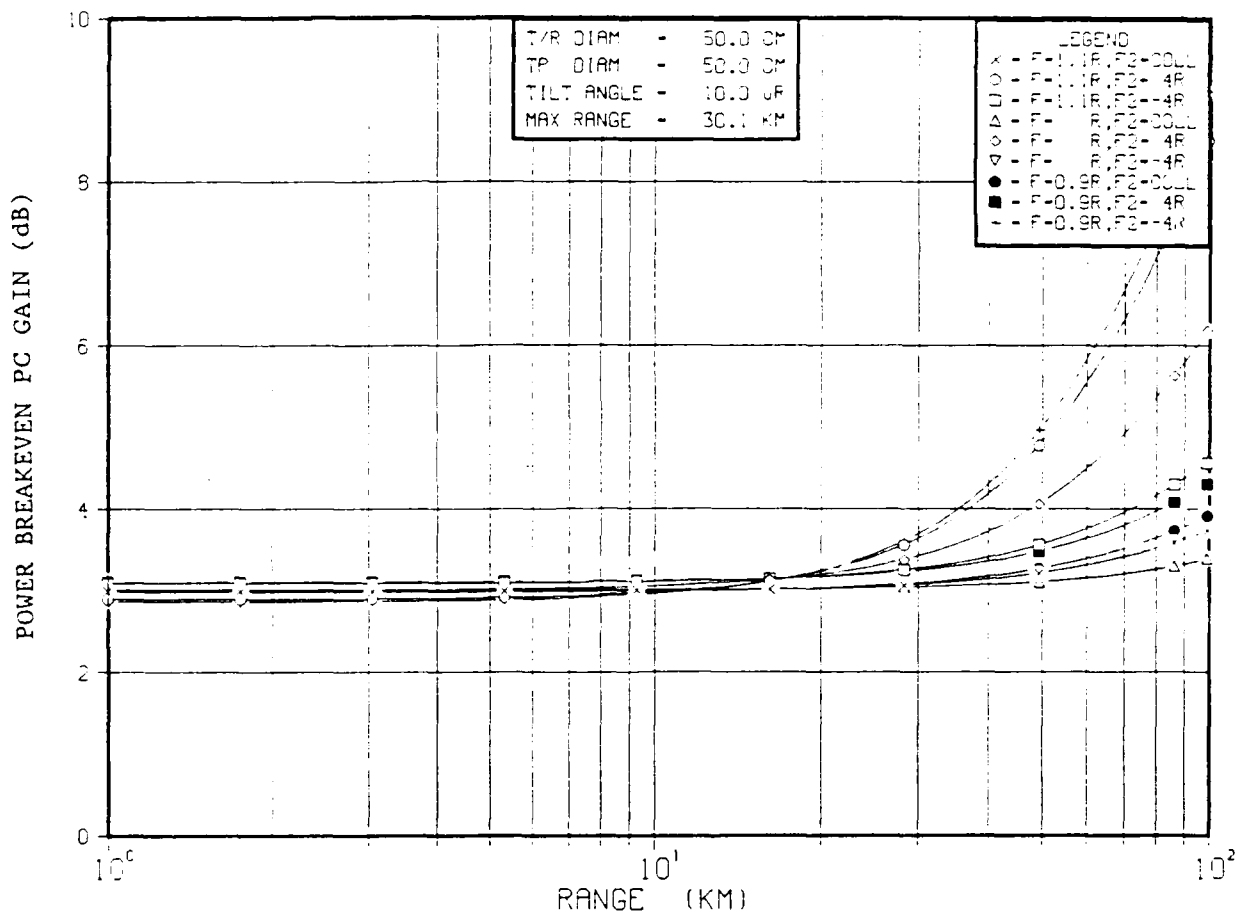


Figure A-26.  $G$  vs.  $R$  for  $\theta_1 = 10\mu\text{rad}$ ,  $w_1 = b = 25$  cm

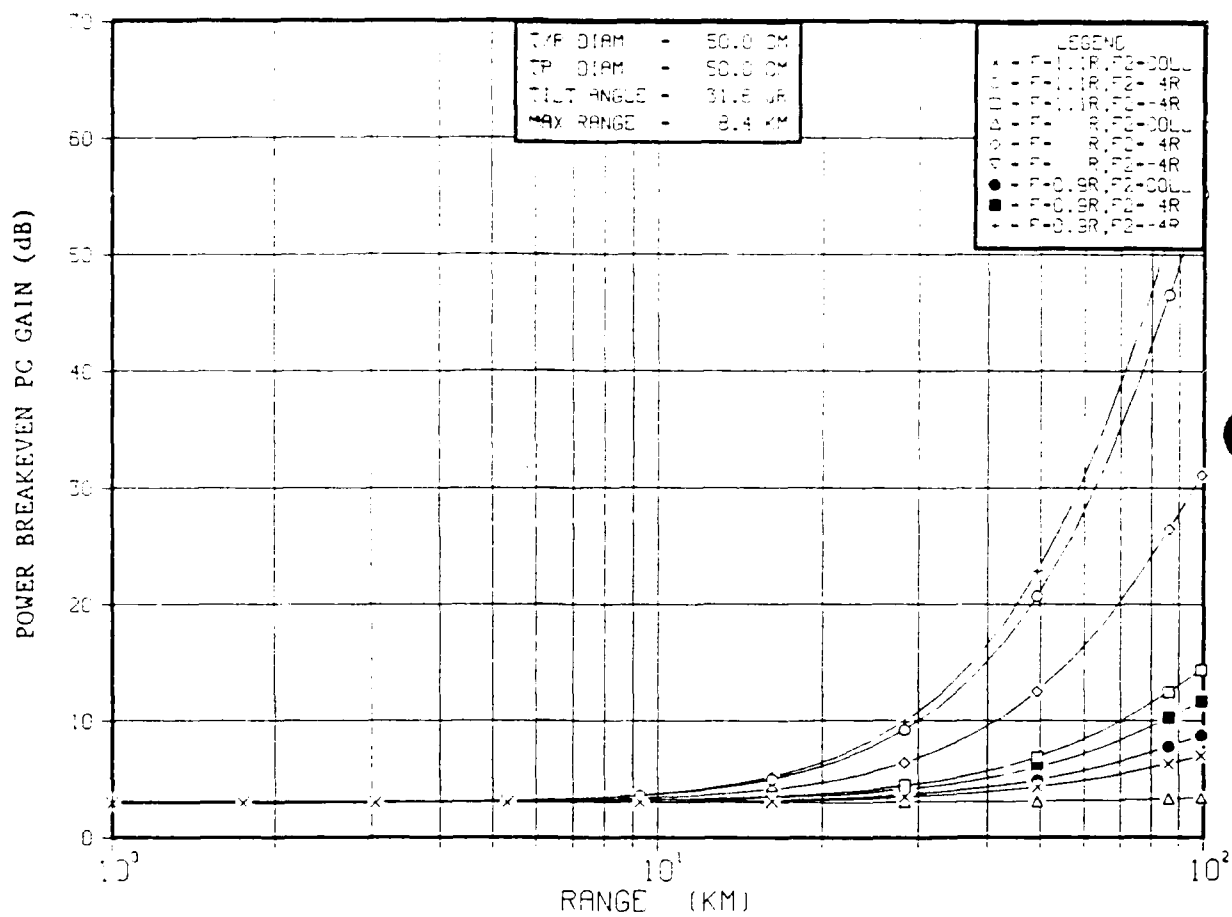


Figure A-27.  $G$  vs.  $R$  for  $\theta_1 = 32\mu\text{rad}$ ,  $w_1 = b = 25$  cm



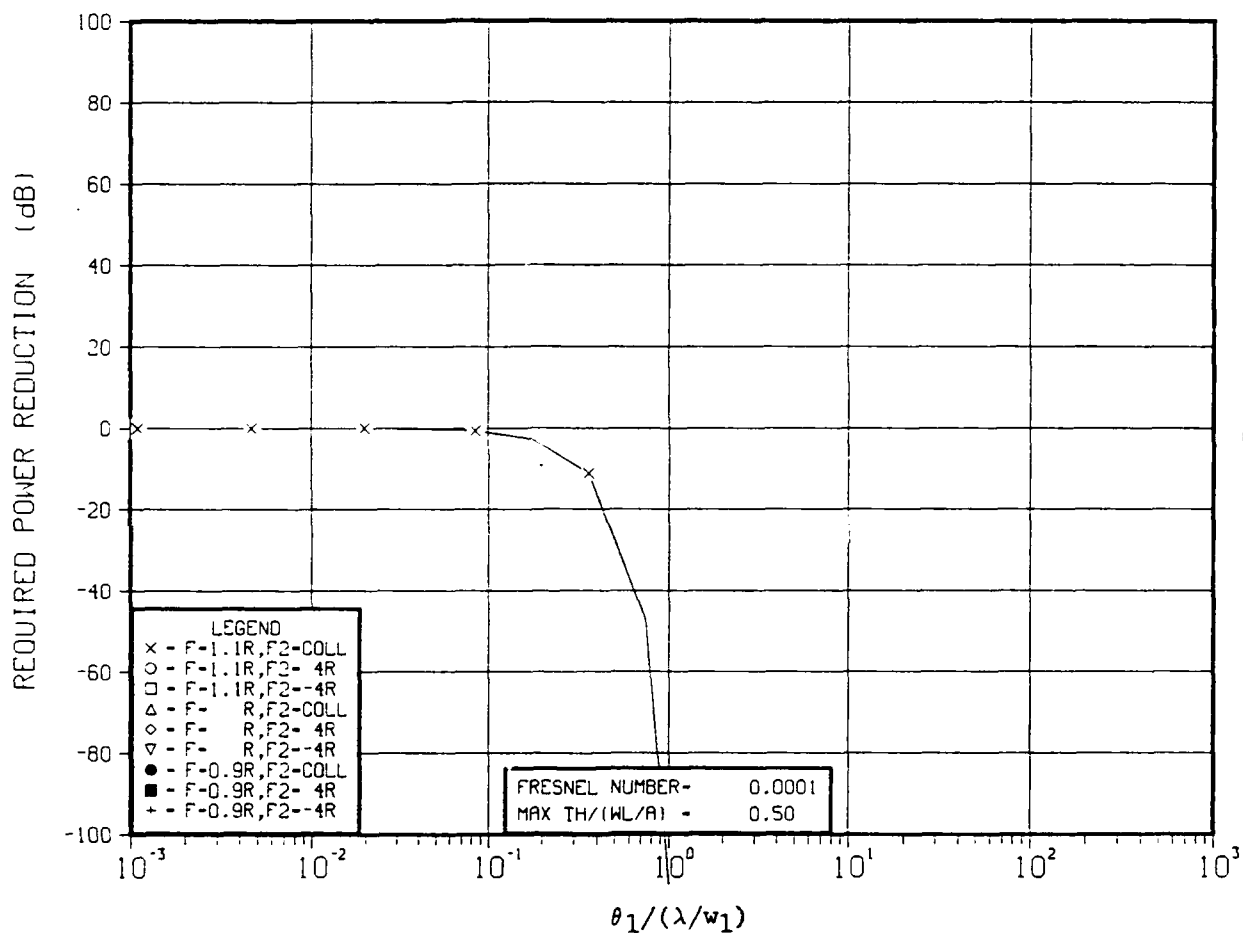


Figure A-29.  $M$  vs.  $T = w_1 \theta_1/\lambda$  for  $\nu = 0.0001$

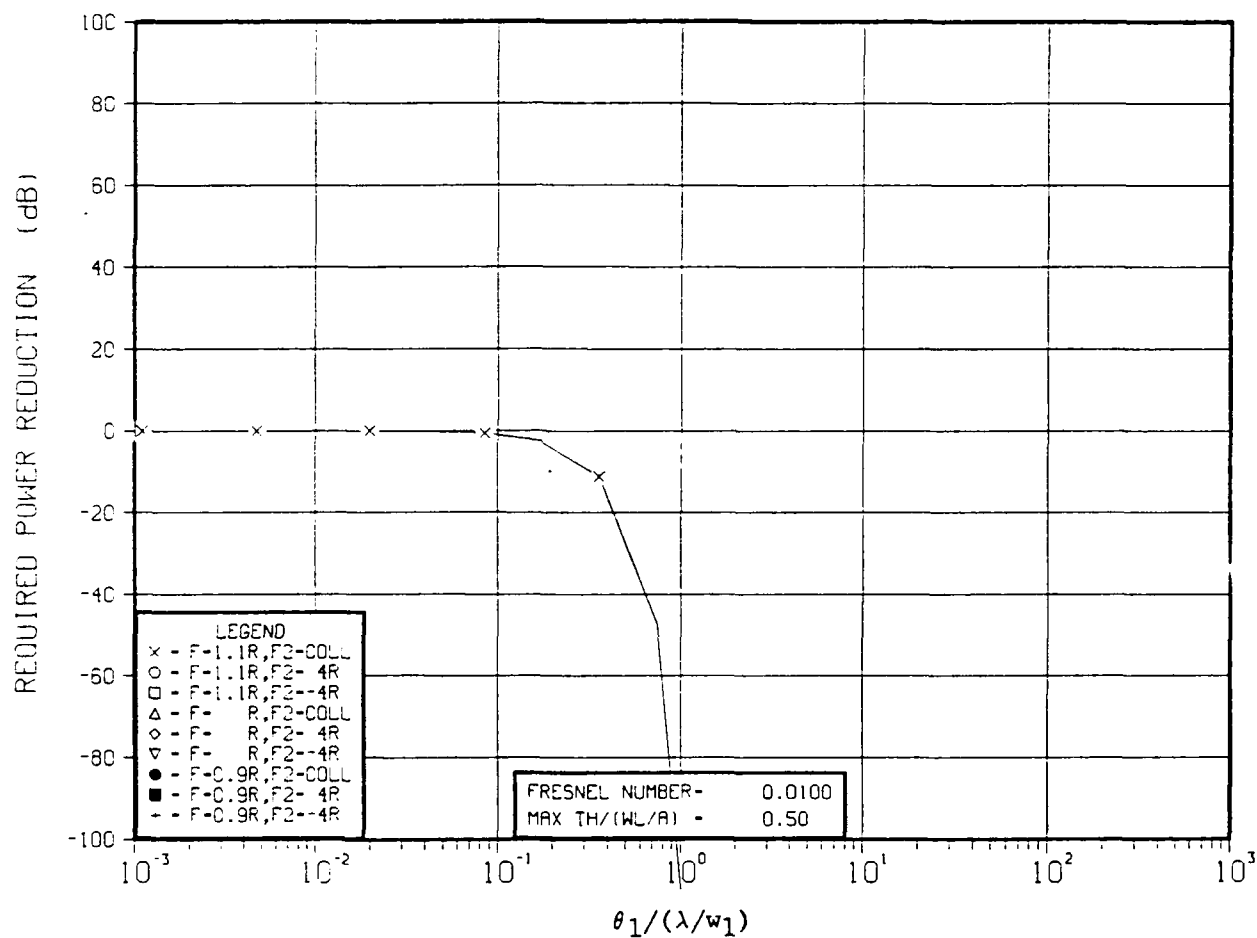


Figure A-30.  $M$  vs.  $T = w_1 \theta_1/\lambda$  for  $\nu = 0.01$

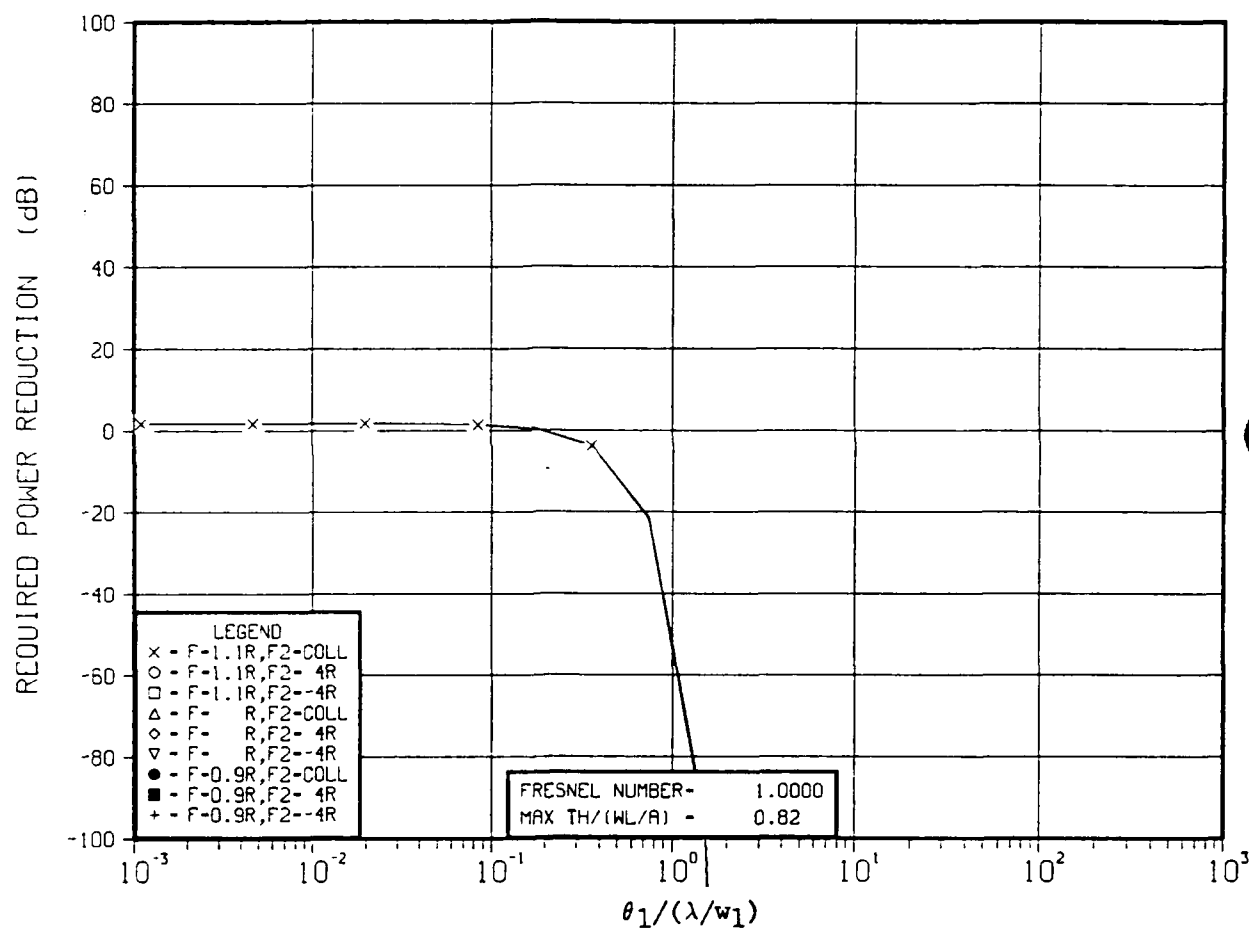


Figure A-31.  $M$  vs.  $T = w_1 \theta_1/\lambda$  for  $\nu = 1$

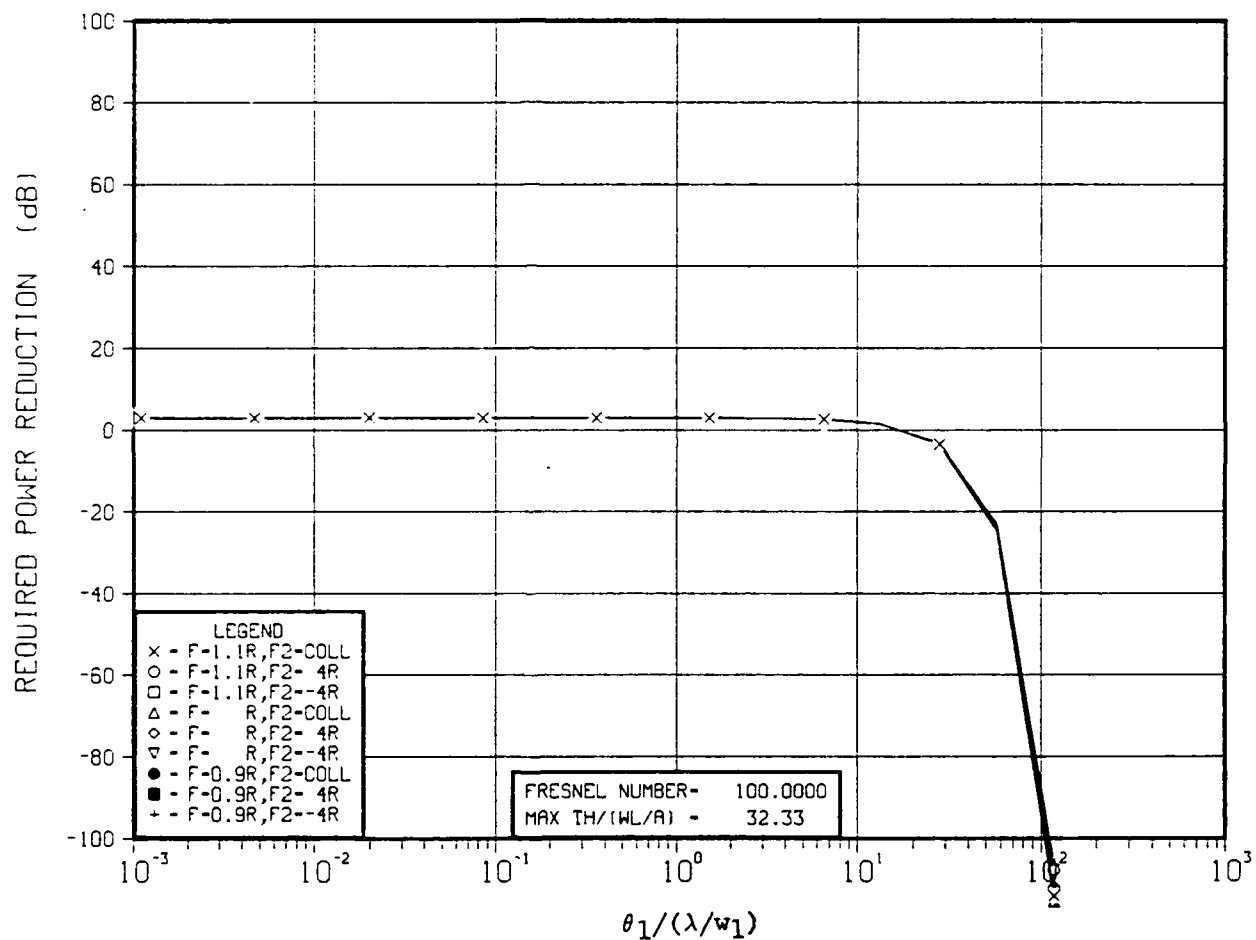


Figure A-32.  $M$  vs.  $T = w_1 \theta_1/\lambda$  for  $\nu = 100$



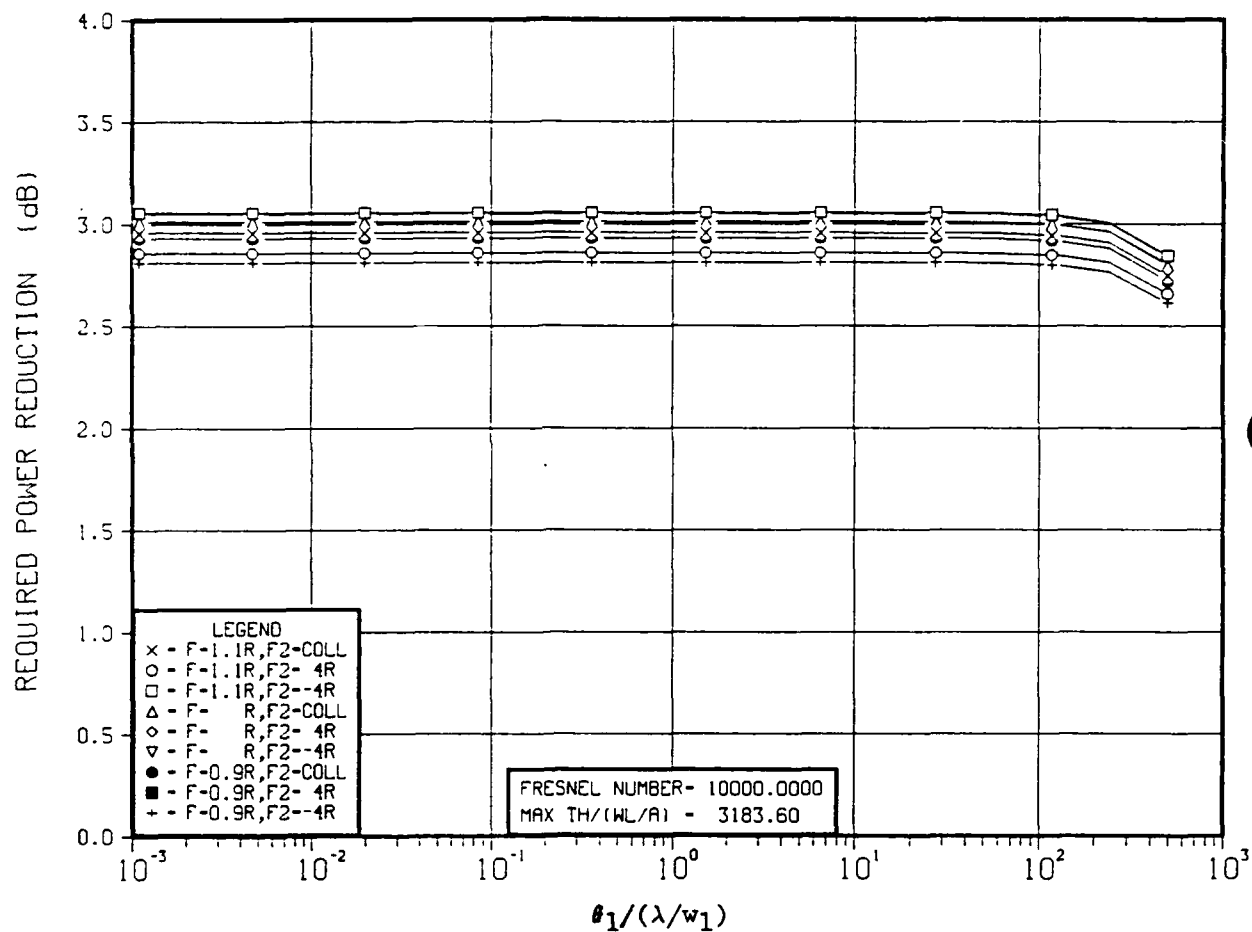


Figure A-33.  $M$  vs.  $T = w_1 \theta_1/\lambda$  for  $\nu = 10,000$

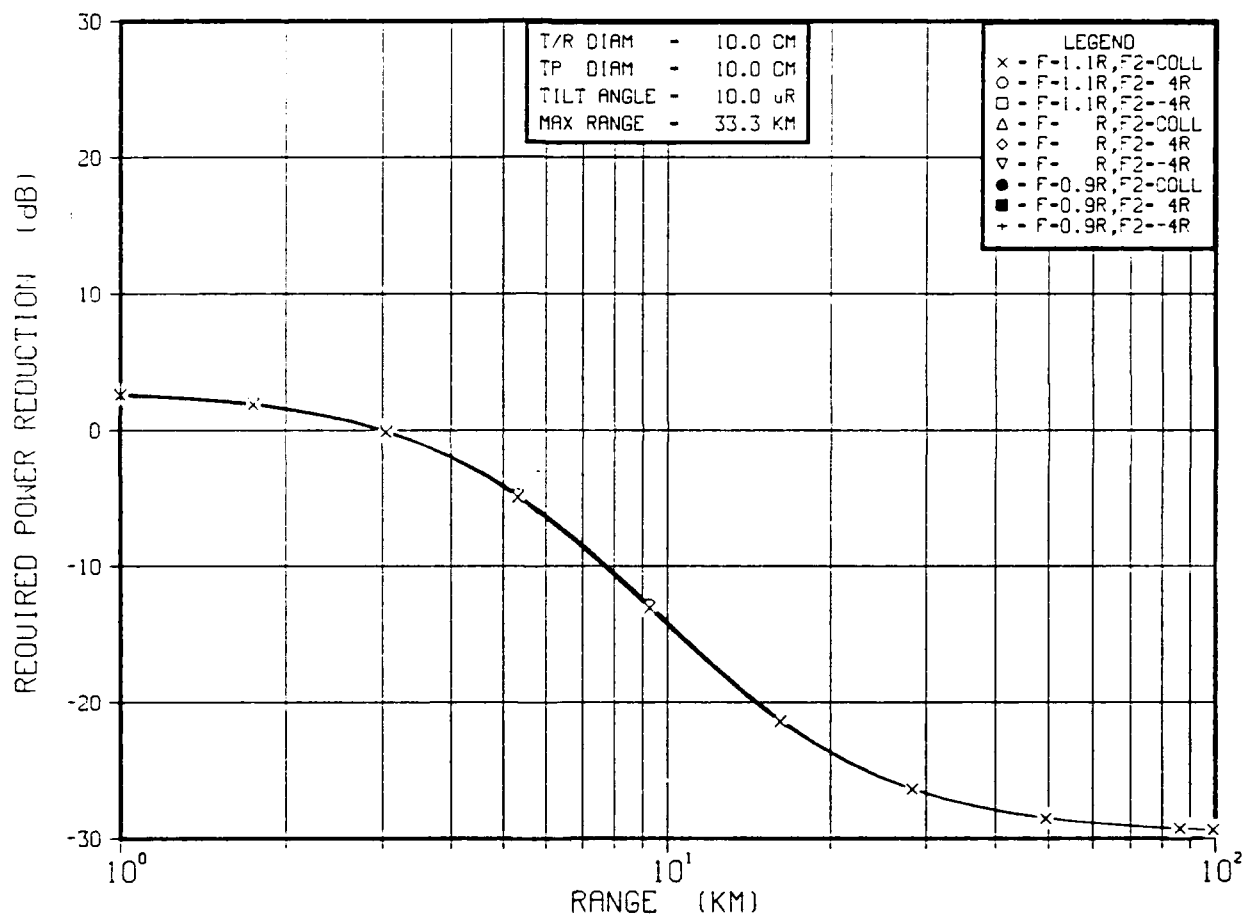


Figure A-34. M vs. R for  $\theta_1 = 10 \mu\text{rad}$ ,  $w_1 = b = 5 \text{ cm}$

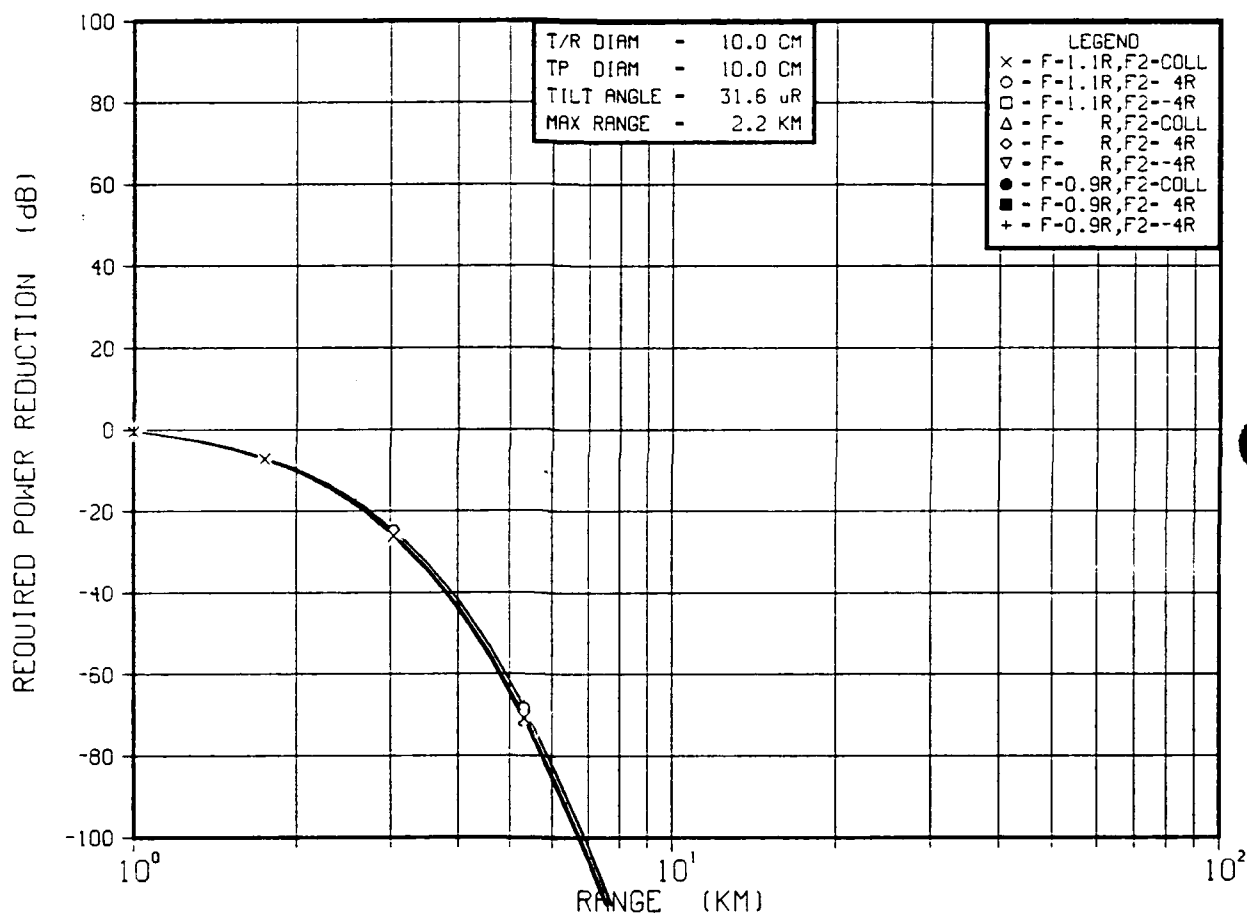


Figure A-35. M vs. R for  $\theta_1 = 32 \mu\text{rad}$ ,  $w_1 = b = 5 \text{ cm}$

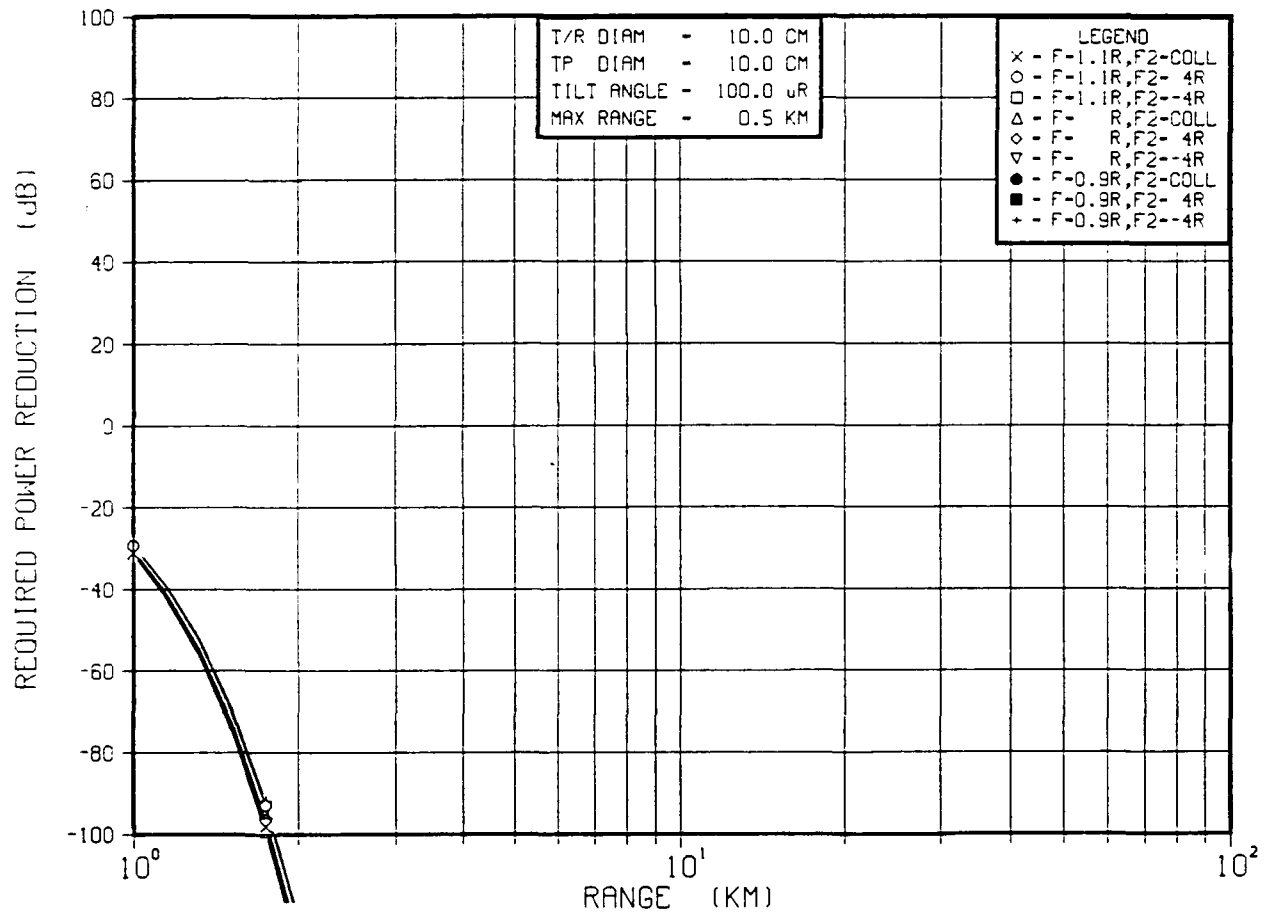


Figure A-36. M vs. R for  $\theta_1 = 100 \mu\text{rad}$ ,  $w_1 = b = 5 \text{ cm}$

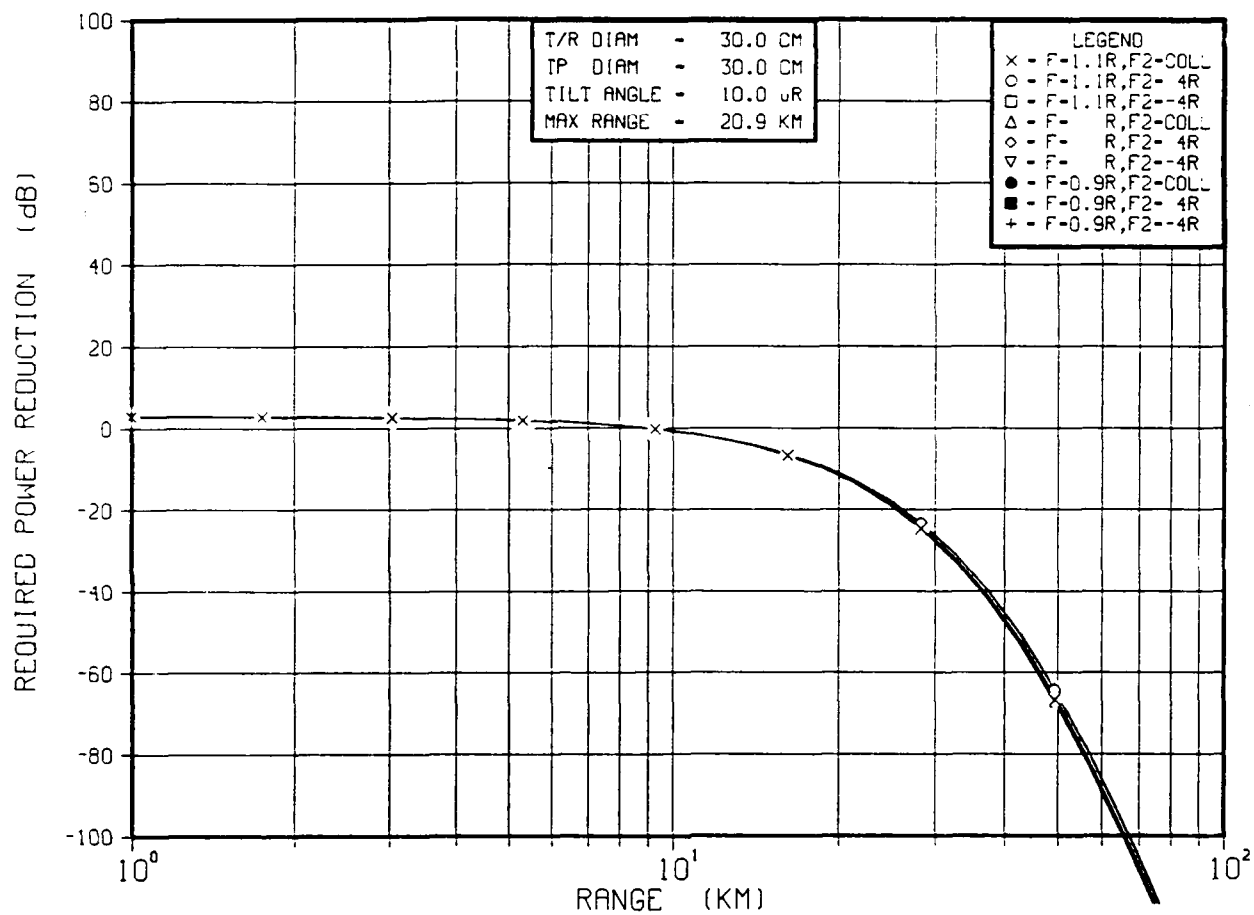


Figure A-37. M vs. R for  $\theta_1 = 10 \mu\text{rad}$ ,  $w_1 = b = 15 \text{ cm}$

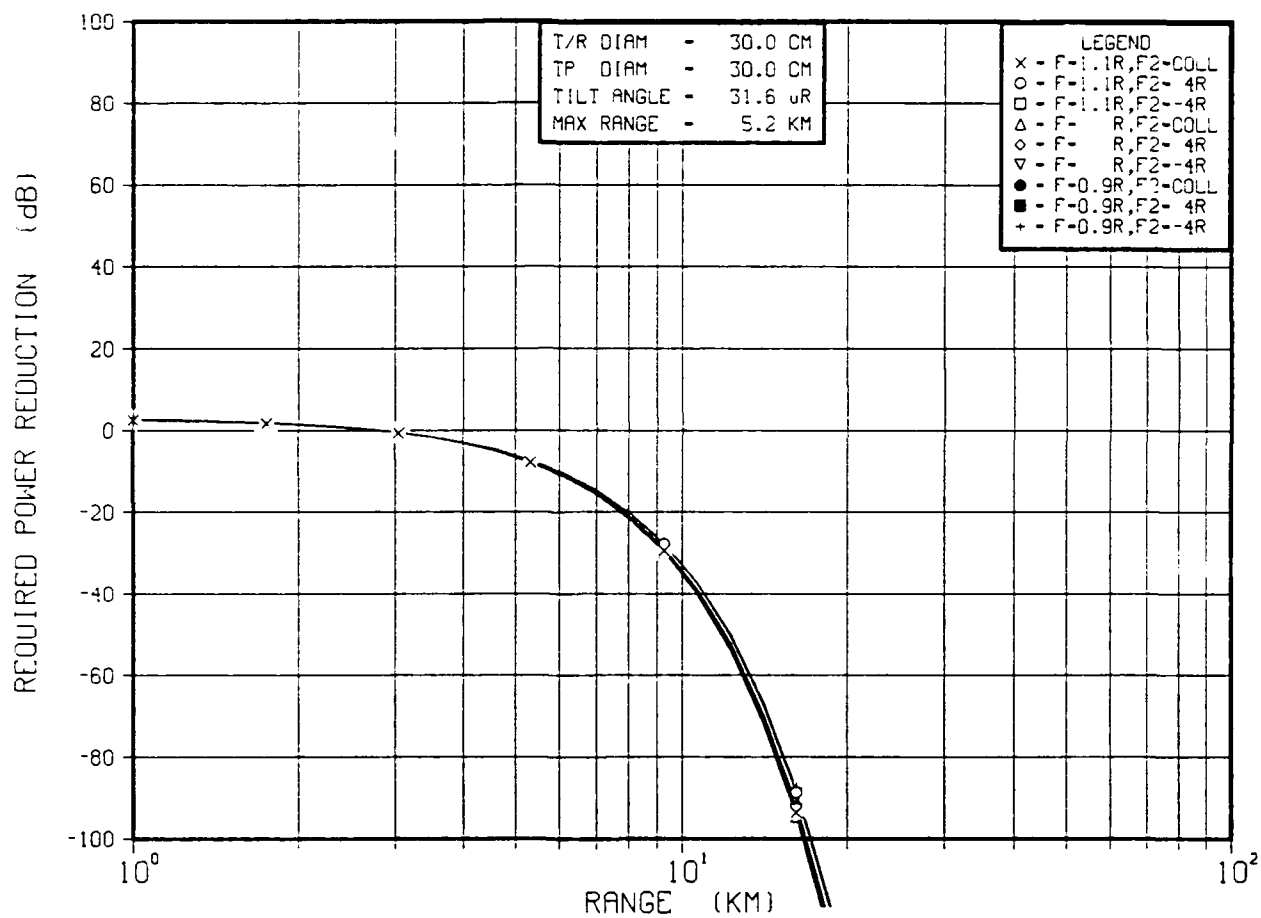


Figure A-38.  $M$  vs.  $R$  for  $\theta_1 = 32 \mu\text{rad}$ ,  $w_1 = b = 15 \text{ cm}$

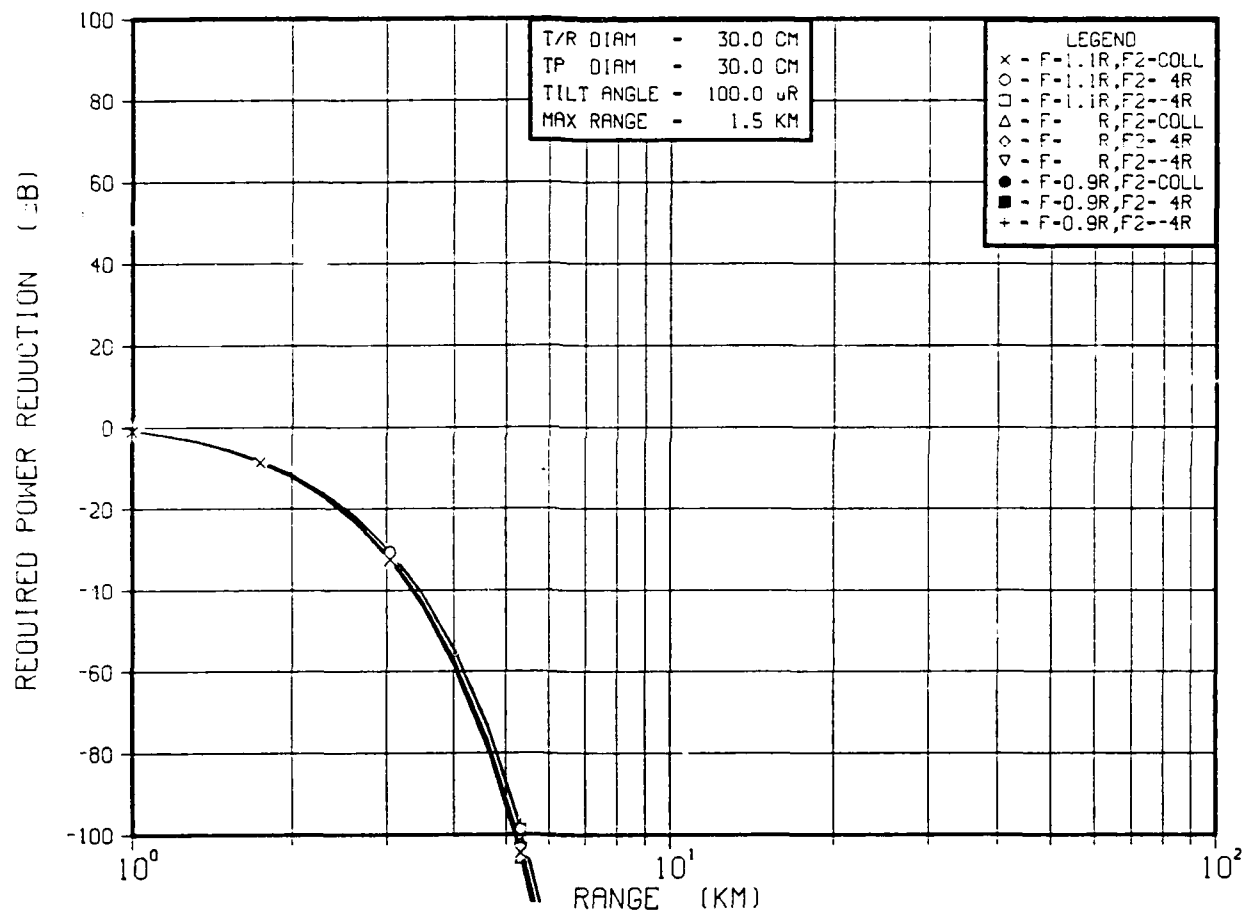


Figure A-39. M vs. R for  $\theta_1 = 100 \mu\text{rad}$ ,  $w_1 = b = 15 \text{ cm}$

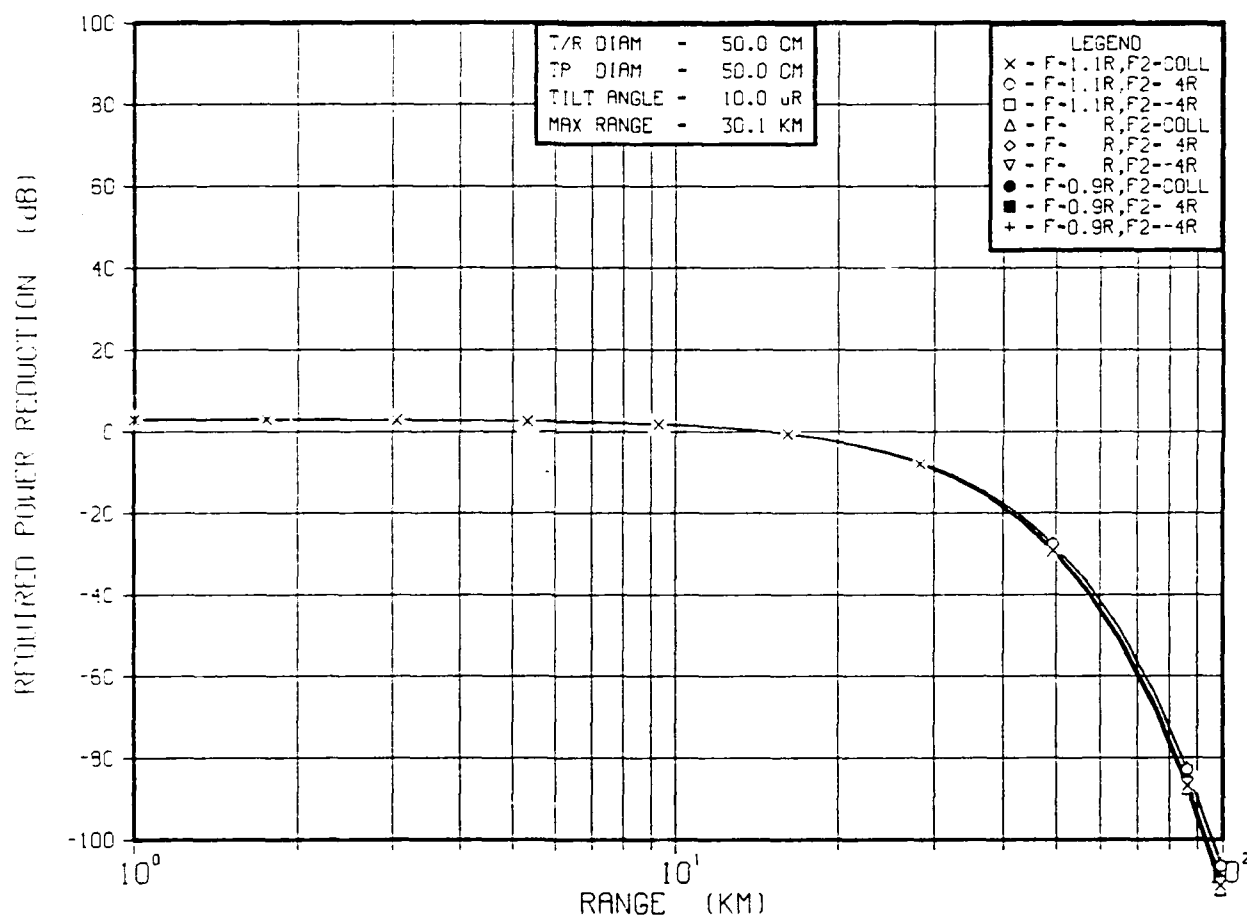


Figure A-40. M vs. R for  $\theta_1 = 10 \mu\text{rad}$ ,  $w_1 = b = 25 \text{ cm}$



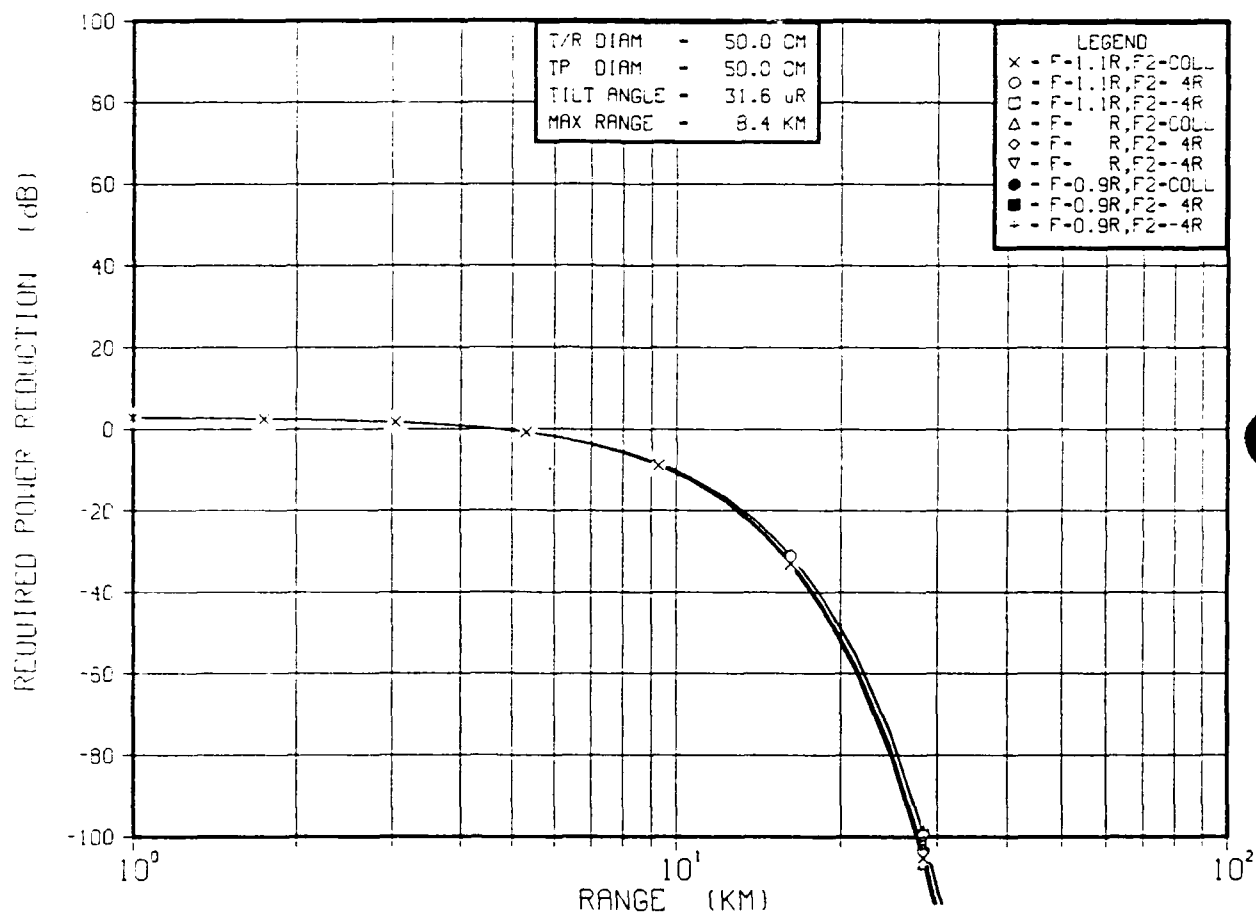


Figure A-41. M vs. R for  $\theta_1 = 32 \mu\text{rad}$ ,  $w_1 = b = 25 \text{ cm}$

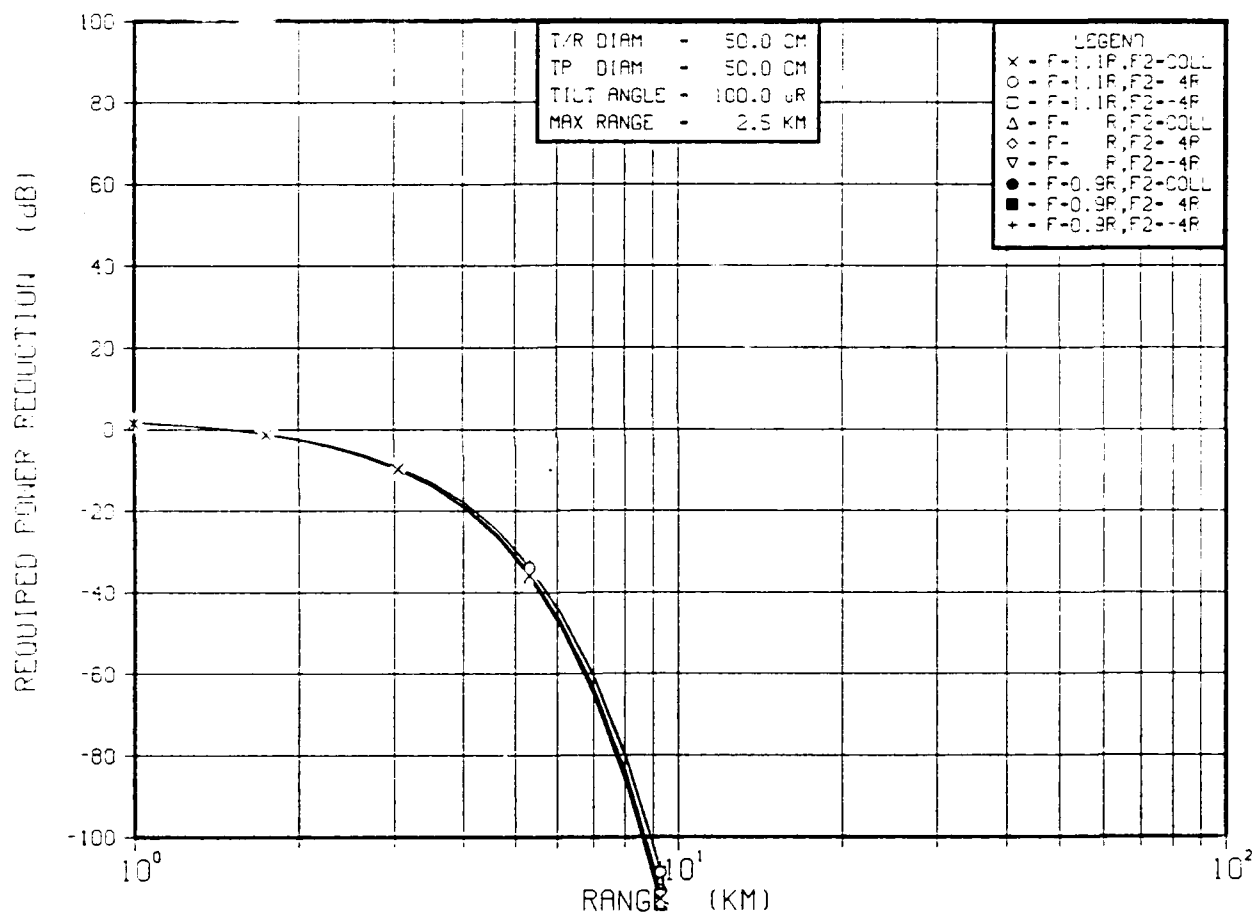


Figure A-42. M vs. R for  $\theta_1 = 100 \mu\text{rad}$ ,  $w_1 = b = 25 \text{ cm}$

## IX. REFERENCES

1. R. A. Fisher, ed., Optical Phase Conjugation, Academic Press, New York, (1983).
2. J. Brock, G. Holleman, F. Patterson, J. Fukumoto, L. Frantz, and M. Valley, "Nonlinear Optics Technology, Area I: FWM Technology", Final Report, ONR-TR-86-xx, (1986).
3. V. I. Tatarskii: Wave Propagation in a Turbulent Medium, English Translation (McGraw-Hill, New York, 1961).
4. V. I. Tatarskii: The Effects of the Turbulent Atmosphere on Wave Propagation, English Translation, U S. Dept. of Commerce, NTIS, Springfield, VA, (1971).
5. A. Ishimaru, Wave Propagation and Scattering in Random Media, Vol. 2, (Academic Press, New York, 1978).
6. R. R. Mills, Jr., A. L. Kistler, V. O'Brien, and S. Corrsin, "Turbulence and Temperature Fluctuations Behind a Heated Grid", NACA-TN-4288 (1958).
7. J. W. Strohbehn, ed., Laser Beam Propagation in the Atmosphere, Topics in Applied Physics, Vol. 25, (Springer-Verlag, New York 1978).
8. G. R. Ochs, R. R. Bergman, and J. R. Snyder, "Laser-Beam Scintillation over Horizontal Paths from 5.5 to 145 kilometers", J. Opt. Soc. Am. 59,231 (1969).
9. G. R. Ochs, T-i. Wang, and E. J. Goldenstein, "An Optical System for Profiling Wind and Refractive-Index Fluctuation", AD-A051-434 (1977).
10. G. R. Ochs, R. F. Quintana, and G. F. Miller, "An Optical Device for Measuring Refractive-Index Fluctuation in the Atmosphere", AD-A051-435 (1977).
11. G. R. Ochs, W. D. Cartwright, and D. D. Russell, "Optical  $C_n^2$  Instrument Model II", PB80-209000 (1979).
12. G. R. Ochs, W. D. Cartwright, and P. S. Endow, "Optical System Model III for Space-Averaged Wind Measurements", PB80-160302 (1979).
13. G. R. Ochs and W. D. Cartwright, "Optical System Model IV for Space-Averaged Wind and  $C_n^2$  Measurements", PB80-208101 (1980).

14. B. W. Guderian and G. R. Ochs, "A Calibrator for Optical Instruments that Measure  $C_n^2$  and Crosswind", PB82-188020 (1981).
15. G. R. Ochs and R. J. Hill, "A Study of Factors Influencing the Calibration of Optical  $C_n^2$  Meters", PB83-171082 (1982).
16. G. R. Ochs, D. S. Reynolds, and R. L. Zurawski, "Folded-Path Optical  $C_n^2$  Instrument", PB85-216398 (1985).
17. G. R. Ochs and W. D. Cartwright, "Optical System Model IV for Space-Averaged Wind and  $C_n^2$  Measurements", Revised, PB86-144086/XAB (1985).
18. G. R. Ochs and S. F. Clifford, "Remote Probing of Wind and Refractive-Index Structure Using Optical Scintillation Techniques", N87-17272/2/XAB (1986).
19. GLAD-386 is a copyrighted software developed by G. Lawrence, Applied Optics Research, 655 N. Alvernon, Suite 226, Tucson AZ. Versions 2.1, 3.5, and 3.7 were employed on this program.
20. M. Sargent III, M. O. Scully, and W. E. Lamb, Jr., Laser Physics, (Addison-Wesley, MA, 1974.)
21. D. Atlas, R. M. Cunningham, R. J. Donaldson, Jr., G. Kantor, and P. Newman, "Some Aspects of Electro-Magnetic Wave Propagation" in Handbook of Geophysics and Space Environments, edited by S. L. Valley, Ch 9, (Air Force Cambridge Research Labs, MA, 1965).
22. D. E. Novoseller, private communication "Turbulence Modeling EOI Final Report", 88.K004.DEN-146.
23. Spatial Filter With Gain, U. S. Patent No. 4803686, Feb. 1989.
24. F. M. Davidson and L. Boutsikaris, "Homodyne Detection Using Photorefractive Materials as Beamsplitters", Opt. Eng. 29, 369 (1990).
25. R. F. Lutomirski and R. E. Warren, "Atmospheric Distortions in a Retroreflected Laser Signal", App Opt 14, 840 (1975).